



HAL
open science

Interfacial phenomena involved in the manipulation of drops and bubbles

Xiaofeng Jiang

► **To cite this version:**

Xiaofeng Jiang. Interfacial phenomena involved in the manipulation of drops and bubbles. Chemical and Process Engineering. Université de Lorraine, 2017. English. NNT: 2017LORR0260. tel-01822383

HAL Id: tel-01822383

<https://theses.hal.science/tel-01822383>

Submitted on 25 Jun 2018

HAL is a multi-disciplinary open access archive for the deposit and dissemination of scientific research documents, whether they are published or not. The documents may come from teaching and research institutions in France or abroad, or from public or private research centers.

L'archive ouverte pluridisciplinaire **HAL**, est destinée au dépôt et à la diffusion de documents scientifiques de niveau recherche, publiés ou non, émanant des établissements d'enseignement et de recherche français ou étrangers, des laboratoires publics ou privés.



AVERTISSEMENT

Ce document est le fruit d'un long travail approuvé par le jury de soutenance et mis à disposition de l'ensemble de la communauté universitaire élargie.

Il est soumis à la propriété intellectuelle de l'auteur. Ceci implique une obligation de citation et de référencement lors de l'utilisation de ce document.

D'autre part, toute contrefaçon, plagiat, reproduction illicite encourt une poursuite pénale.

Contact : ddoc-theses-contact@univ-lorraine.fr

LIENS

Code de la Propriété Intellectuelle. articles L 122. 4

Code de la Propriété Intellectuelle. articles L 335.2- L 335.10

http://www.cfcopies.com/V2/leg/leg_droi.php

<http://www.culture.gouv.fr/culture/infos-pratiques/droits/protection.htm>

UNIVERSITÉ DE LORRAINE
École Nationale Supérieure des Industries Chimiques
Laboratoire Réactions et Génie des Procédés
École Doctorale RP2E

THÈSE

Présentée pour obtenir le grade de

Docteur de l'Université de Lorraine
Spécialité : Génie des Procédés et des Produits

Par

Xiaofeng JIANG

Sujet :

PHÉNOMÈNES INTERFACIAUX DANS LA MANIPULATION DES GOUTTES ET DES BULLES

Soutenue publiquement le 14 Novembre 2017

Membres du jury

Président

M. Jean-Claude CHARPENTIER, Directeur de recherche Émérite (LRGP - ENSIC, Nancy)

Rapporteurs

Mme. Cécile MONTEUX, Chargée de recherche CNRS (SIMM - ESPCI, Paris)

M. Christian RUYER-QUIL, Professeur (LOCIE - Université Savoie Mont Blanc, Chambéry)

Examineurs

M. Xavier FRANK, Chargé de recherche INRA (IATE - Centre de recherche Occitanie-Montpellier)

M. Huai-Zhi LI, Professeur (directeur de thèse, LRGP - ENSIC, Nancy)

Acknowledgement

My deepest gratitude goes first and foremost to my supervisor, Prof. Huai-Zhi Li, for his constant encouragements and illuminating instructions. He provides me very valuable technical guidance through all stages of this thesis. I appreciate all his contributions of time, advice, and patience to make my PhD experience meaningful and fulfilling. His innovative spirit, rigorous scientific approaches and matter-of-fact attitude motivate me to be a better researcher and his amiable and knowledgeable character stimulates me to improve myself continuously.

I would like to express my heartfelt gratitude to Denis Funfschilling, Rainier Hertz, Yining Wu, and Jiankai Jiang, who help me in the beginning of my thesis. I am also greatly indebted to Chunying Zhu, who assists me in preceding part of experiments. Similarly, I would like to express my gratitude to all my colleagues in Syspol (LRGP-CNRS) who help and encourage me during three years.

Special thanks should be given to the staff in the mechanical workshop and technique service department. I thank David Brunello and Franck Giovanella in electronic service department (SIEL) as they help me to prepare the ultra-high-speed acquisition system. I am grateful to Charly Koenig, Christian Blanchard and Alain Chérèque in mechanical workshop who help me to fabricate the high-precision experimental devices. I also thank Jean-François Remy for all his help in SEM and AFM measurements.

I thank Cécile Monteux, Christian Ruyer-Quil, Xavier Frank, Jean-Claude Charpentier for their kind presence and valuable suggestions.

Lastly, my thanks would go to my beloved family for their kind considerations and great confidence in me all through these years.

Table of Contents

Acknowledgement.....	i
Résumé étendu	1
General Introduction.....	9
PART I: Pinch-off of drops and bubbles.....	11
I.1 Literature review.....	12
I.1.1 Bubble pinch-off.....	14
I.1.2 Drop pinch-off.....	15
I.2 Experimental details	21
I.2.1 Experimental setup and method.....	21
I.2.2 Physical properties of working fluids.....	24
I.2.3 Imaging analysis	27
I.3 Bubble pinch-off in liquid	29
I.3.1 Air bubble pinch-off in Newtonian fluids	29
I.3.2 Air bubble pinch-off in non-Newtonian fluids	32
I.3.3 Modeling and simulations.....	36
I.4 Drop pinch-off in a surround fluid.....	39
I.4.1 Drop pinch-off in air.....	39
I.4.2 Drop pinch-off in liquid.....	45
I.5 Ferrofluid drop formation and pinch-off in air.....	52
I.5.1 Shape evolution	52
I.5.2 Formation volume and frequency.....	58
I.5.3 Breakup mechanism of neck.....	59
I.6 Droplet pinch-off at microscale	68
I.6.1 Breakup dynamics of liquid thread.....	68
I.6.2 Velocity distribution in the liquid neck	71
I.7 Conclusion	75
PART II: Drop manipulation by superhydrophobicity	77
II.1 Literature review	78
II.1.1 Wetting and superhydrophobicity	78
II.1.2 Drop motion on barrier-attached surface.....	81
II.1.3 Liquid marble	82
II.1.4 Slope motion through superhydrophobic interphase.....	84
II.2 Experimental details	86

II.2.1 Experimental method for drop hurdling.....	86
II.2.2 Experimental method for undressing water marbles.....	88
II.2.3 Experimental method for slope motion.....	89
II.2.4 Physical properties of working fluids.....	90
II.2.5 Imaging analysis.....	91
II.3 Drop hurdling barriers of various geometries.....	93
II.3.1 Hurdling dynamics.....	93
II.3.2 Hurdling time.....	97
II.3.3 Energy dissipation.....	100
II.4 Undressing water marbles on oil film.....	103
II.5 Slope motion of liquid drops and liquid marbles.....	110
II.5.1 Drops downhill on superhydrophobic surface.....	110
II.5.2 Liquid marbles downhill on a glass slide.....	114
II.5.3 Stable velocity and deformation.....	116
II.6 Conclusion.....	119
PART III: Manipulation of dripping-on-substrate (DoS).....	121
III.1 Literature review.....	122
III.1.1 Drop spreading.....	122
III.1.2 Bottleneck of pinch-off investigation.....	124
III.2 Experimental details.....	126
III.3 Results and discussion.....	133
III.3.1 Initial contact and spreading.....	133
III.3.2 Pinch-off of Newtonian fluids.....	140
III.3.3 Filament thinning of non-Newtonian fluids.....	145
III.4 Conclusion.....	158
PART IV: General conclusions and perspectives.....	159
IV.1 General conclusions.....	160
IV.2 Perspectives.....	162
Nomenclature.....	166
References.....	171
Annexes.....	191
Publications issued from this thesis.....	194

Résumé étendu

L'interface est la frontière entre les différentes phases. En Génie des Procédés, les interfaces affectent le transfert de chaleur et de matière, l'écoulement des fluides, la cinétique de réactions et la dispersion entre les phases. Les phénomènes interfaciaux tels que le mouillage, l'étalement, l'extraction, la rectification, le séchage, la sédimentation, l'agitation, l'émulsification, la réaction, la catalyse hétérogène, etc. ont été largement utilisés dans divers domaines comme la physique, la biologie, la médecine et l'ingénierie. Les phénomènes interfaciaux couplés aux écoulements polyphasiques, constituent un domaine multidisciplinaire et attirent d'intenses attentions. Les travaux pionniers ont accompli de nombreux progrès, tels que l'instabilité de Rayleigh-Plateau, le cône de Taylor, le phénomène de Leidenfrost et l'effet Marangoni. Les gouttes et les bulles sont les exemples interfaciaux typiques et font l'objet d'intenses travaux de recherche depuis des décennies. Ainsi, l'étude d'une goutte ou d'une bulle individuelle est une approche efficace pour comprendre les phénomènes complexes polyphasiques et interfaciaux impliqués dans de nombreuses applications telles qu'émulsification, dévolatilisation, absorption, impression par jet d'encre, fermentation, fabrication de verre, éruption volcanique, électrospray. etc.

L'hydrodynamique de gouttes ou de bulles fait l'objet d'une attention particulière, notamment pour la formation, le mouvement et la manipulation, en raison des champs d'applications industrielles très étendus et de riches phénomènes physiques. Cette thèse se concentre principalement sur les phénomènes interfaciaux impliqués dans des gouttes et des bulles, y compris le pincement des gouttes et des bulles dans un liquide, la manipulation de gouttes sur des surfaces superhydrophobes et le contact initial suivi de l'étalement d'une goutte sur une surface solide. Ces études de la manipulation de gouttes ou de bulles approfondissent non seulement la compréhension des phénomènes interfaciaux, mais facilitent également les applications éventuellement industrielles comme le revêtement par pulvérisation, l'impression par jet d'encre et le transport de liquide. Les principaux résultats de cette thèse sont présentés en trois parties distinctes.

- *Partie I met l'accent sur l'instabilité interfaciale, à savoir la dynamique de pincement locale des gouttes et des bulles au voisinage du point de singularité de la rupture.*

Au cours du processus du pincement d'un fluide, l'équation de Navier-Stokes ne peut décrire le point de la rupture qui est une singularité. Dans le voisinage immédiat de la singularité, l'évolution du cou montre des comportements auto-similaires et toute la mémoire des conditions initiales est perdue. Au cours des dernières décennies, l'attention s'est concentrée sur la dynamique du pincement, que ce soit à l'échelle macroscopique ou microscopique. Premièrement, son mécanisme sert à diverses applications: impression jet d'encre, décodage d'ADN, émulsification, dépôt de réactifs sur des bandes de diagnostic, fabrication de particules et de microcapsules et pipetage automatique de fluides dans la découverte massivement parallélisée de médicaments. Prenant l'exemple de l'impression par jet d'encre, la génération de millions de gouttelettes à très haute cadence permet d'imprimer des textes et des images et cette technique s'étend même à la production de cellules photovoltaïques et à la fabrication de tissus biologiques imprimés en 3D. Deuxièmement, son comportement physique complexe, comme l'auto-similarité et la singularité universelles, fascine beaucoup de scientifiques de différentes disciplines. Bien que de nombreuses études aient été consacrées à ce domaine, les connaissances sur la singularité restent encore très limitées. Dans cette partie, la dynamique du pincement a été étudiée de manière exhaustive dans différentes conditions expérimentales : du gaz-liquide au liquide-liquide, des fluides homogènes aux fluides hétérogènes, de la macro-échelle à la micro-échelle, sans un champ externe ou avec champ externe, la gravité superposée ou la gravité compensée. L'étape finale du pincement se révèle affectée par des interactions entre les fluides internes et externes. Les résultats détaillés sont les suivants :

Tout d'abord, une buse submergée a été utilisée pour générer des bulles et une caméra numérique rapide Phantom v7.11 a été adoptée pour visualiser la dynamique du pincement de bulles dans les fluides tant newtoniens que non-newtoniens. Les résultats montrent que la force d'Archimède prend effet à l'instant initial, mais à la fin du pincement, l'inertie, la traînée visqueuse liquide et la tension superficielle atteignent un certain équilibre. L'exposant de la loi de puissance indique que le pincement des bulles dans les fluides newtoniens et les fluides non newtoniens de faible viscosité est auto-similaire, mais le pincement des bulles dans les fluides newtoniens et non newtoniens de haute viscosité s'écarte du caractère auto-similaire. Ces résultats expérimentaux ont été validés par une simulation numérique basée sur l'ascension verticale et l'extension radiale.

Deuxièmement, un pincement d'un liquide dans une seconde phase liquide a été étudié. Les fluides de gouttes vont de l'eau pure aux fluides newtoniens visqueux ainsi qu'aux fluides non newtoniens. L'effet du rapport de viscosité λ entre les fluides interne et externe sur le pincement a été quantifié. Pour des gouttes de fluides newtoniens, nous avons démontré que le comportement auto-similaire universel dépend en grande partie du rapport de viscosité : à λ intermédiaire ($55,56 \leq \lambda \leq 638,89$), le pincement est universel et auto-similaire avec les caractéristiques de deux points distincts de pincement suivis de la formation d'une seule chaîne de gouttelettes; lorsque $\lambda < 0,061$ et $\lambda \geq 3305,56$, le pincement n'est plus universel ni auto-similaire avec divers points de pincement le long du filament. Des gouttelettes satellites de différente taille sont formées et ce sans régularité. L'effet de viscosité est principalement dû à l'interaction entre les fluides externe et interne. De plus, nos expériences révèlent que le pincement d'une goutte non-newtonienne dans l'air et dans les fluides externes visqueux présente un comportement particulier : la formation de filaments exceptionnellement longs et de perles de gouttelettes satellites sur le filament.

En outre, par rapport aux fluides mentionnés ci-dessus, nous avons testé un fluide hétérogène - ferrofluide, qui se compose de particules magnétiques solides, substrat liquide et tensioactifs. Un champ magnétique externe a été ajouté pour manipuler la formation et la rupture du ferrofluide solide-liquide hétérogène. En faisant varier la direction du champ magnétique et la force appliqués, la gravité est compensée (UM) et superposée (DM) et les points du pincement primaire sous UM et DM ont été observés pour être invariants à la direction appliquée de la force magnétique. Les résultats montrent que le volume, la forme ainsi que la fréquence de formation de gouttes de ferrofluide pourraient être activement contrôlés par le champ magnétique externe. Nous démontrons qu'il existe trois régimes au cours du processus de la rupture du cou: régime linéaire, régime transitoire et régime de pincement final auto-similaire. La présence du champ magnétique raccourcit la durée du régime transitoire et prolonge le régime linéaire en particulier à une densité de flux magnétique plus élevée. Pour l'amincissement radial, l'exposant du pincement primaire est compris entre 0,70 et 0,80 alors que pour l'allongement axial, l'exposant du pincement primaire reste proche de l'unité. Ceci implique que la vitesse d'allongement axial est supérieure à celle d'amincissement radial. Dans l'ensemble, le processus de formation et la dynamique de rupture en présence d'un champ magnétique diffèrent significativement de

leurs homologues sans champ magnétique et nous excluons l'effet des conditions initiales, en particulier la direction du champ magnétique, sur le pincement auto-similaire.

Enfin, compte tenu de la limitation de la résolution spatiale de la caméra ($\sim 20 \mu\text{m}$), nous sommes allés plus loin pour étudier le pincement des gouttelettes à micro-échelle où la gravité est négligeable. Un dispositif microfluidique du type flow-focusing avec des dimensions submillimétriques (largeur = hauteur = $400 \mu\text{m}$) a été fabriqué en fraisant les canaux dans une plaque plane de polyméthacrylate de méthyle (PMMA). De l'eau déionisée a été utilisée comme phase dispersée. La phase continue, huile minérale avec 2% de Span 20, était guidée par deux branches latérales égales sur le point de flow-focusing. Une petite quantité de particules de latex (Merck, France) avec un diamètre étalonné de $0,88 \mu\text{m}$ a été ajoutée dans la phase dispersée comme traceur. Le diamètre minimum du cou peut être abaissé jusqu'à $\sim 1 \mu\text{m}$ et le pincement final est mis à l'échelle avec une loi d'exposant $b = 1$. Le champ d'écoulement a été obtenu par notre système de vélocimétrie par images des particules (μ -PIV, Dantec Dynamics, Danemark). L'écoulement inverse dans le cou de la gouttelette près du point de rupture a été trouvé, car des particules de traceur dans la gouttelette d'eau sont rejetées des deux côtés. On obtient ensuite le diagramme d'écoulement, montrant que l'écoulement inverse dépend de façon sensible du débit de la phase aqueuse dispersée. Dans l'ensemble, la dynamique du pincement à micro-échelle est assez similaire à celle à macro-échelle malgré l'absence de la gravité. A macro-échelle, le champ d'écoulement pour les ferrofluides en suspension ne peut être mesuré en raison de l'opacité. Ici, le pincement des gouttelettes à micro-échelle peut donner quelques pistes intéressantes aux phénomènes proches du point critique de la rupture.

➤ *Partie II présente la manipulation des gouttes sur des surfaces superhydrophobes.*

Le mouvement de gouttes et leur manipulation sur une surface solide sont un sujet tant scientifique qu'applicatif. De nombreuses applications existent dans ce domaine : matériaux autonettoyants ou antigivrants, biomédicaux, revêtement par pulvérisation, impression par jet d'encre, condensation goutte à goutte, transport de liquide, etc. La manipulation de gouttes et leur mobilité dépendent fortement des interactions entre des gouttes et des surfaces de support. Des surfaces communes comme le verre, le bois et le sol sont souvent

hydrophiles et il n'est pas possible de manipuler une goutte d'eau sur une surface mouillable. Afin de manipuler une goutte intacte, une surface superhydrophobe est requise et bénéficie d'une attention croissante dans de nombreux domaines académiques et industriels. La feuille de lotus est une surface non mouillante la plus commune qui présente un état de Cassie-Baxter pour des gouttes d'eau. Les structures locales sur une feuille de lotus emprisonnent l'air en forment des poches d'air entre la surface solide et le liquide, menant au mécanisme superhydrophobe. À côté de feuilles de lotus, il y a de nombreuses surfaces superhydrophobes dans la nature, comme des pattes d'araignée, des ailes de papillon, etc. De nos jours, la superhydrophobicité artificielle peut être obtenue en modifiant les structures de surface à nano-échelle pour créer des gouttes superhydrophobes ressemblant à des perles qui sont en réalité des perles blindées. Dans cette partie, la manipulation de gouttes a été réalisée en modifiant, soit la surface solide, soit l'interface liquide. La stabilité des interfaces a été obtenue par des propriétés superhydrophobes puis manipulées dans différents contextes: saut de gouttes sur des barrières de haies superhydrophobes et de déshabillage de perles liquides habillées de particules superhydrophobes. Le mouvement de gouttes liquides et de perles liquides est comparé sur une pente inclinée en ce qui concerne deux types d'interfaces superhydrophobes. Les résultats sont détaillés dans ce qui suit :

D'une part, à travers les surfaces rendues superhydrophobes par un revêtement, la dynamique complexe de gouttes franchissant différentes barrières de haies a été étudiée expérimentalement dans diverses conditions, y compris des gouttes de différente nature et des barrières de haies de différentes géométries. Par rapport à une sphère rigide, la déformation de gouttes liquides, un mécanisme d'auto-ajustement, permet leur franchissement des haies. Cependant, il est encore difficile de quantifier la déformation spatio-temporelle d'une goutte lors du saut au-dessus d'une haie, car la structure de la déformation est tridimensionnelle et particulièrement complexe. Deux corrélations empiriques sont proposées pour décrire les principaux paramètres du saut, à savoir le temps de saut et la perte d'énergie cinématique, qui révèlent l'efficacité dynamique du franchissement et la déformation de la forme pendant le saut. Ces surfaces superhydrophobes avec des obstacles de différentes géométries donnent un cadre intéressant pour étudier la dynamique d'une ligne triple. Le saut de haies par des gouttes liquides en se déformant constitue non seulement un sujet académique fascinant, mais promet aussi de nombreuses applications industrielles, telles que le transport directionnel de liquide,

l'autopropulsion, les surfaces autonettoyantes et antigivrage, le revêtement et la pulvérisation.

D'autre part, en enveloppant des particules superhydrophobes sur la surface d'une goutte d'eau, la cinétique du déshabillage de ces particules de la surface d'eau a été menée à bien sur un mince film d'huile. Dans tous les cas, ces perles, des gouttes d'eau enrobées par des particules superhydrophobes, commencent d'abord un mouvement linéaire pour éliminer progressivement de particules extérieures; suivi de l'étape transitoire où des particules compactes sont encore déshabillées; enfin, les perles d'eau sont immobilisées et adhèrent au film d'huile lorsque presque toutes les particules superhydrophobes à la base de la perle sont éliminées. L'angle de contact des perles capturées après le déshabillage est comparable à celui des gouttes d'eau pures posées sur le même film d'huile, ce qui prouve que la base des perles d'eau est presque vide de particules superhydrophobes pour exhiber un contact direct eau-huile. De plus, nous avons constaté que plus le volume d'une perle liquide est grand, plus longue est la distance à parcourir; plus la viscosité de l'huile est grande dans le film, plus le régime transitoire est court pour immobiliser des perles liquides. Nos résultats expérimentaux permettent de mieux comprendre les mécanismes de revêtement rapide d'une interface liquide pour former des perles et de leur déshabiller en enlevant des particules. Ainsi, on peut envisager de développer des applications potentielles dans les domaines de la médecine, des produits pharmaceutiques, des cosmétiques et des produits de soins.

En outre, dans le but de comparer deux différents types de superhydrophobicité, le mouvement sur la pente du même angle d'inclinaison a été étudié : des gouttes aqueuses sur une surface superhydrophobe et des perles aqueuses sur une surface hydrophile. Des gouttes liquides et des perles liquides commencent une phase d'accélération vers un régime stationnaire. Peu importe des gouttes liquides et des perles liquides, la vitesse stationnaire de descente diminue avec la viscosité du liquide. Plus la viscosité est faible, plus la déformation est grande. Fait important, la vitesse stationnaire des perles liquides est inférieure à celle des gouttes et vice versa pour la déformation maximale F_{max} . Nos résultats expérimentaux démontrent que des gouttes liquides se différencient des perles liquides pour des raisons de l'état de surface du plan incliné : la superhydrophobicité du revêtement par pulvérisation s'avère plus efficace pour le mouvement des gouttes, tandis que des particules superhydrophobes enveloppant des perles produisent des frottements solide-solide avec le plan.

- *Partie III entreprend l'étude des phénomènes interfaciaux du contact initial entre une goutte et une surface métallique ainsi que l'amincissement du cou de gouttes.*

Le contact initial suivi du mouillage et de l'étalement d'une goutte liquide sur un substrat et le pincement d'un film liquide sont des phénomènes très rapides qui trouvent de nombreuses applications, comme gouttes de pluie sur un pare-brise, enlèvement de salissures par des détergents, impression par jet d'encre, peinture, condensation goutte-à-goutte et dépôt de pesticides. Le contact initial et l'étalement d'une goutte liquide sur une surface solide concernent le pontage entre les deux phases différentes tandis que le pincement d'un film liquide évolue vers la rupture du cou. Comment le point de singularité de contact ou de rupture est-il établi à l'échelle microscopique ou même moléculaire? Compte tenu de la limite de résolution des caméras rapides, une approche électrique a été mise au point pour conduire aux informations quantitatives à proximité du point de rupture ou de contact à une cadence ultra-rapide. Dans cette partie, le contact initial, l'étalement sur une surface plane métallique, le pincement des fluides newtoniens et l'amincissement des filaments de fluides non-newtoniens ont été étudiés grâce à la combinaison des approches électriques et optiques sur un système goutte-à-substrat (DoS).

En raison de la constance de l'intensité de courant continu $I = 0,1$ mA, la tension électrique décroissante reflète la résistance électrique décroissante du pont de liquide. Mais la résistance dépend en grande partie de la partie la plus étroite du liquide où le mouvement des électrons est largement obstrué, c'est-à-dire que plus la largeur minimale du col est petite, plus la résistance est grande. Ainsi, le système goutte-à-substrat (DoS) a été conçu pour étudier le contact initial et l'étalement, le pincement des fluides newtoniens et l'amincissement du filament des fluides non newtoniens en ajustant la distance entre la sortie de la buse et la surface métallique.

Pour le contact initial et l'étalement, nous définissons le temps zéro comme le moment où le premier contact est observé dans l'image et le premier point de la tension décroissant dans les signaux électriques. L'acier inoxydable et le bronze ont été utilisés comme deux surfaces métalliques. Une loi d'échelle permet d'exclure l'effet du matériau des surfaces métalliques et des propriétés du fluide, en particulier la conductivité, sur l'exposant pour l'étalement à

très court temps. En appliquant la loi de puissance, l'exposant de $-0,08$ à $-0,15$ est obtenu à partir des signaux électriques ultra-rapides.

En ce qui concerne le pincement des fluides newtoniens, l'exposant varie de $0,6$ à $0,7$ pour les fluides newtoniens de faible viscosité. Mais un plus grand exposant de 1.2 est observé pour les fluides newtoniens de haute viscosité. Alors qu'en appliquant la loi de similitude, la tension électrique de 20% Emkarox évolue avec un exposant de $-0,02$ et les autres fluides présentent un exposant allant de $-0,07$ à $-0,10$. Ici, le changement de loi d'échelle est observé aussi bien dans les images que les signaux électriques, ce qui est dû à l'effet de la viscosité du fluide.

Pour le pincement des fluides non newtoniens, on a déjà observé le long filament et des gouttelettes satellites sur un filament, mais un phénomène spécial existe dans les signaux électriques. Les pics se produisent régulièrement pendant l'amincissement du filament des fluides non newtoniens. Le temps entre les pics reste constant et plus la conductivité est grande, plus l'amplitude de pics sont importante. Nous avons essayé d'ajouter du chlorate de sodium (NaCl) dans des solutions aqueuses de polyacrylamide (PAAm) et nous avons constaté que le nombre de pics augmente et que l'extremum global de la tension électrique diminue fortement. De plus, il a été démontré que le temps pour l'ensemble du processus d'amincissement était directement lié à la viscosité et que l'extremum global de la tension était déterminé par la conductivité des fluides.

Au total, à l'exception de la forte variation du signal électrique au contact initial et à la rupture du filament, la dynamique obtenue de l'étalement et du pincement à court temps est similaire entre la méthode de visualisation par caméra rapide et la méthode électriques. Cependant, les pics électriques sont trouvés lors de l'amincissement de filament de fluides non-newtoniens. En raison d'une relation quantitative difficile à établir pour l'instant entre les signaux électriques et les images, une étude complémentaire sera nécessaire pour élucider le point de rupture d'un film liquide en particulier.

General Introduction

Interface is the boundary between two phases and it is usually about 10 nm in thickness. Interfaces affect the heat or mass transport, fluid flow, reaction rate, phase distribution between the phases due to the different properties from the bulk phase. Thus interfacial phenomena like spreading, wetting, extraction, rectification, drying, sedimentation, stir, adsorption, emulsification, reaction, heterogeneous catalysis etc., have been widely applied in a variety of domains, like physics, biology, medicine and engineering.

Interfacial phenomenon coupled together with multi-phase flow, is a multi-disciplinary field and has attracted enormous attentions. Previous pioneers introduce some breakthrough progresses, for example, Laplace and Young's functions, Rayleigh-Plateau instability, Taylor cone, Lendenfrost phenomenon and Marangoni effect etc. Drops and bubbles are the typical interfacial problems and have been the main concern for numerical, theoretical and experimental investigations during the past years. Thus, studying an individual drop or bubble is an effective and bottom-up approach to understand complex multiphase and interfacial phenomena involved in numerous applications such as emulsification, polymer devolatilization, absorption, inkjet printing, fermentation, glass manufacture, volcanic eruption, electrospray and so on.

Drop or bubble based hydromechanics has gained extensive attention, especially formation, motion and manipulation, due to the wide-ranging applications and rich physical phenomena. In this thesis, the dynamics of the formation, pinch-off, motion and spreading of drops (bubbles) in different circumstances were studied. The content of the thesis is arranged as follows:

PART I focus on the interfacial instability, i.e. local pinch-off dynamics of drops and bubbles in the vicinity of the singularity point. Firstly, bubble pinch-off in Newtonian and non-Newtonian fluids was studied and a simulation analysis was proceeded to confirm the experimental results. Secondly, liquid drops pinch-off in both air and viscous fluids were experimentally investigated. The drop fluids ranged from pure water to viscous fluids and to non-Newtonian fluids. The effect of viscosity ratio between internal and external fluid on the pinch-off of two-fluid flow was mainly justified. Thirdly, the pinch-off of heterogeneous ferrofluid drops at a nozzle in air was experimentally investigated with an external magnetic field (downward or upward). The gravity-superimposed and gravity-compensated effect was

verified and the universal scaling law was extended to the heterogeneous fluid. Lastly, the investigation of pinch-off went further into the confined microchannel coupling with μ -PIV system. The particles' motion in the liquid thread at the very vicinity of singularity point was obtained.

PART II studied the active control and manipulation of liquid drops either through superhydrophobic coating on a substrate or on a liquid drop. Drop mobilization on a solid surface has received widespread attention. In this part, we firstly introduced liquid drops hurdling the preconditioned barriers with various geometries displaying superhydrophobic surface. We demonstrated that both the external factors like barriers' geometry and size and internal factors such as drops' initial motion velocity, volume, surface tension and dynamic viscosity, could affect their hurdling dynamics. The hurdling difficulty was quantified through the consuming time and kinetic energy and two empirical relationships were proposed. On the other hand, through wrapping superhydrophobic particles on liquid drops, the dynamical behavior of a rolling liquid marble on oil film was studied. Three stages were observed during the undressing process and the dynamics was obtained. In addition, the two kinds of superhydrophobic interface were compared through the slope motion of both liquid drops and liquid marbles.

PART III further investigates the dripping-on-substrate (DoS) phenomenon of initial contact and spreading and final pinch-off through the ultra-high-speed electric device and high-speed optical camera. By controlling the distance between the nozzle and the substrate, three behaviors of dripping-on-substrate (DoS) were obtained. The effect of fluid properties on short-time spreading, pinch-off of Newtonian fluids and filament thinning of non-Newtonian fluid was demonstrated.

PART I: Pinch-off of drops and bubbles

I.1 Literature review

The raindrop falling down from the sky, the water drop trickling from a faucet, the atomized droplets releasing from a sprayer and the soap bubble blew by a child, they are all ubiquitous phenomena in our daily life. Figure I.1 shows commonly-encountered: a single drop *vs.* numerous droplets (mist); a single bubble *vs.* countless bubbles (foam).



Figure I.1. Typical examples of drop and bubble formation. (a) water drop, (b) water mist, (c) soap bubble, (d) soap foam.

Drop or bubble formation and breakup mechanism plays a significant role in gas-liquid (liquid-liquid) contacting and reaction processes which are widely used in chemical industry, petrochemical industry, biotechnology and mineral processing, etc. (Liontas et al., 2013). A typical drop-based application in medicine is to encapsulate the bio-active reagent into a drop in order to improve the reaction kinetic or avoid the cross-contamination. Another bubble-based technique in flotation is to capture particles by small rising bubbles through the suspension (Chen et al., 2015). Thus to study an individual drop or bubble is an

effective and bottom-up approach to understand the complex phenomena such as inkjet printing, emulsion and spray coating, etc.

Over the last decades, drop or bubble formation has been intensively investigated due to the wide-ranging applications and rich-underlying physics. For drop formation, numerous works have been dedicated to break-up mechanisms and resulting drop size, ranging from pure liquid (Shi et al., 1994) to suspension (Miskin and Jaeger, 2012), from gas-liquid phases (Dietrich et al., 2013a) to liquid-liquid phases (Hemmati et al., 2015; Zhang and Stone, 1997), from macro-drops (Corkidi et al., 2012) to micro-droplets (Fu et al., 2012b; Josephides and Sajjadi, 2015; Leshansky and Pismen, 2009), from Newtonian fluids (McCreery and Stoots, 1996) to non-Newtonian fluids (Mounir et al., 2013), without (Rueger and Calabrese, 2013) or with (Lee et al., 2006; Xu et al., 2014a) an external field. And even the influencing factors, like density, viscosity, surface tension, to name only a few also have been exhaustively studied by previous authors (Roché et al., 2009; Wehking et al., 2013). For bubble formation, a lot of previous studies (Lind and Phillips, 2010; Simmons et al., 2015; Tzounakos et al., 2001; Yang et al., 2007; Yuan et al., 2014) have been devoted to the global characteristics such as the bubble shape, size, rising velocity and frequency, considering the fluid parameters (density, viscosity and surface tension), design parameters (nozzle diameter, geometry and wettability) and operating parameters (flowrate and pressure). More comprehensive information about bubble formation could be referred to a review by Kulkarni and Joshi (Kulkarni and Joshi, 2005).

Conventional theory (Rayleigh, 1892) predicts that the capillary instability to perturbations exists with wavelengths greater than the circumference of the thread. And subsequent nonlinear growth leads to disintegration of the thread into droplets or satellite droplets by secondary instabilities (Brenner et al., 1994; Henderson et al., 1997; Lister and Stone, 1998a). However, the focus of researchers' attention now has switched to the final pinch-off region due to the complexity of underlying physics (Burton et al., 2005; Cohen et al., 1999; Day et al., 1998; Kuo and Dennin, 2013; Louvet et al., 2014; Rothert et al., 2001; Zhang and Lister, 1999a). Firstly, pinch-off is a singularity where the dynamical description breaks down and the curvature, velocity and pressure all diverge to infinity. Fluid pinch-off, black-hole formation and crack propagation, are typically physical singularities that fascinates many scientists (Herbst, 2012). Secondly, the dynamics both spatially and temporally in the vicinity of pinch-off exhibits self-similar behavior due to the large, i.e., orders of magnitude, disparity between local length and time scales and corresponding global scales (Herbst and Zhang, 2011). The shape of pinching neck at different times and

positions can be superimposed onto a single shape after appropriate scaling (Cohen et al., 1999; Day et al., 1998; Eggers, 1997; Zhang and Lister, 1999b). Thus the pinch-off from a gas thread (bubble) or a liquid thread (drop) is frequently investigated. Peregrine *et al.* (Peregrine et al., 2006) studied the pinch-off of drops and bubbles and found that the pinch-off of a bubble occurred much faster than that of a drop. In this section, we will summarize the bubble and drop pinch-off, respectively.

I.1.1 Bubble pinch-off

When a bubble grows from a nozzle where the gas is pumped at a constant flow rate, the increasing bubble volume definitely leads to the increasing buoyancy. Once the buoyancy and inertia overcomes the surface tension and liquid viscous drag, a gas neck occurs and continuously thins to be a thread (Figure I.2). Eventually, the thread pinches off into two parts due to the Kelvin-Helmholtz instability (Bergmann et al., 2006; Burton et al., 2005). Though, a lot of attention have been devoted to the global characteristics of bubble formation, the local dynamics of bubble pinch-off is not yet well-understood and well-documented due to the very fast phenomena evolved.

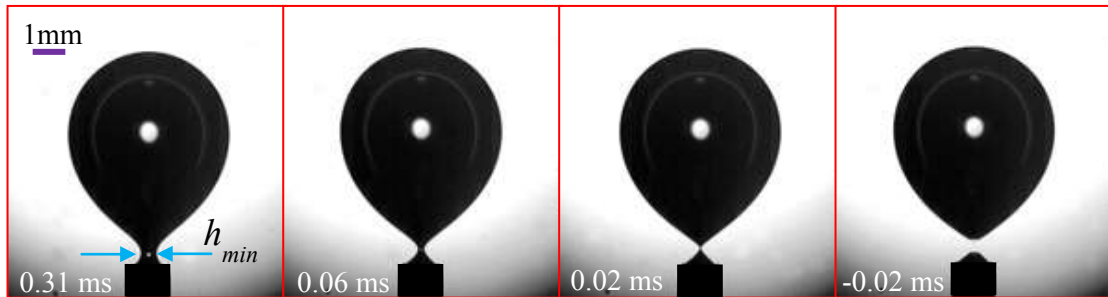


Figure I.2. Air bubble pinch-off in water.

By assuming a power-law relationship, $h_{\min} = a\tau^b$, where h_{\min} is the minimum neck diameter and τ is the time-to-pinch-off ($\tau = t_0 - t$, here t_0 is breakup time and t is real time), bubble pinch-off can be studied in terms of the universal self-similarity. The early studies of Louquet-Higgins *et al.* (Louquet-Higgins et al., 1991) and Oguz and Prosperetti (Oguz and Prosperetti, 1993) proved that air bubble detaches from an underwater nozzle with an exponent of $b = 0.5$. Burton *et al.* (Burton et al., 2005) experimentally studied the nitrogen bubble pinch-off in liquids like acetone and glycerol solutions and found that when the external liquid viscosity η_{ext} is lower than 10 cP, the exponent b equals 0.5; while η_{ext} is

larger than 100 cP, the exponent b remains 1. Gordillo *et al.* (Gordillo et al., 2005) proposed a modified relationship $h_{\min} (-\log h_{\min})^{1/4} \propto \tau^{1/2}$, and $h_{\min} \propto \tau^{1/3}$ for symmetric and asymmetric air bubble pinch-off in water at high Reynolds numbers. Keim *et al.* (Keim et al., 2006) experimentally demonstrated that air bubble pinch-off in water with an exponent $b = 0.56$. Thoroddsen *et al.* (Thoroddsen et al., 2007) conducted a comprehensive experimental study on bubble pinch-off and found that air, helium and SF6 bubbles pinch-off in water all shows an exponent in the range of $b = (0.56 - 0.60)$ which is also a little bit larger than 0.5. Egger *et al.* (Eggers et al., 2007) used slender body theory to successfully deduce the time-dependent exponent $b = 0.5 + 1/[4\sqrt{-\ln(\tau)}]$. Recently, Ray *et al.* (Ray et al., 2012) investigated the air bubble pinch-off during the liquid drop impacting on liquid pool and demonstrated that Weber number (We) only affects the coefficient a and the exponent b remains as a constant 0.5.

Moreover, bubble pinch-off in confined microchannel has been investigated in both Newtonian and non-Newtonian fluids (Fu et al., 2012a; van Hoeve et al., 2011). Despite some experimental analyses and empirical correlations, the mechanism of bubble pinch-off in unconfined systems is far from well-understood, especially in non-Newtonian fluids. Our group has already numerically and experimentally investigated the bubble formation in both Newtonian and non-Newtonian fluids, either in macroscopic columns or microscopic channels (Dietrich et al., 2013b; Dietrich et al., 2008; Fu et al., 2011; Fu et al., 2012a; Li, 1999; Li et al., 2002; Lu et al., 2014). As a continuous study to further understand the bubble formation, we here focus on the final and local pinch-off region in an unconfined system and investigate the bubble pinch-off dynamics in the background fluids ranging from Newtonian fluids to non-Newtonian fluids.

I.1.2 Drop pinch-off

When a flowing fluid passes through a vertical nozzle, once beyond a critical volume, a neck occurs, thins and finally pinches off which results in two disjointed masses, sometimes accompanying with one or more satellite drops. Figure I.3 shows the dynamics of drop pinch-off in dripping regime. In order to investigate the singularity point, ‘pinch-off’ means the temporal neighborhood in the vicinity of detachment.

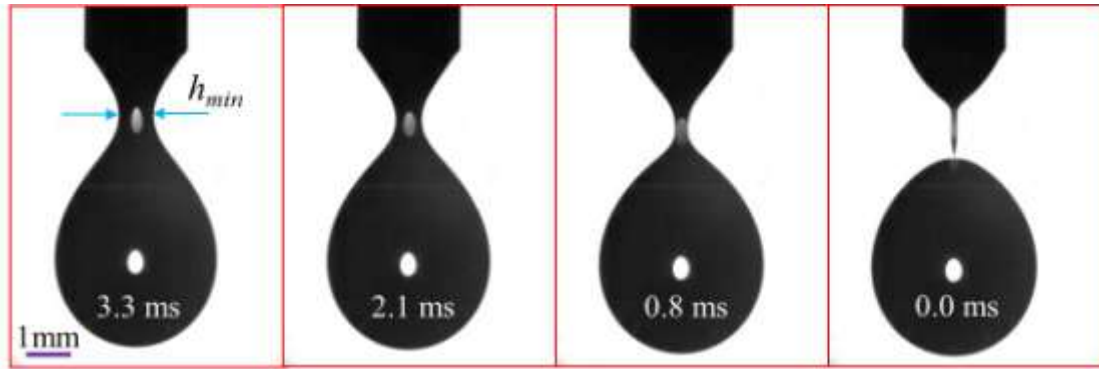


Figure I.3. Water drop pinch-off from a nozzle. h_{min} means the minimum neck diameter of the thread.

During the pinch-off process, the continuous Navier-Stokes equation fails in describing the coming breakup that is nothing but a singularity. In the immediate neighborhood of singularity, the neck evolution exhibits self-similar behaviors and all the memory of the initial conditions is lost. Over the past few decades, resurgent attention has focused on the pinch-off region no matter on macroscale (Henderson et al., 1997; Nooranidoost et al., 2016; Zhang and Lister, 1999b) or on microscale (Du et al., 2016; Fu et al., 2012b; Wu et al., 2015; Zhu et al., 2016). Firstly, its mechanism serves for various applications: ink-jet printing, DNA arraying, emulsification, deposition of reagents on diagnostic strips, manufacture of particles and microcapsules and automatic pipetting of fluids in massively parallel drug discovery. Taking the inkjet printing as an example, the generation of millions of droplets at a very short time makes it possible to print texts and images and this technique even extends to the production of solar cells (Krebs, 2009) and in the fabrication of 3D printed biological tissue (Visconti et al., 2010; Xu et al., 2014b; Zhao et al., 2016). Secondly, its complex physical behavior, like universal self-similarity and singularity, fascinates and puzzles a lot of scientists from different disciplines (Chen and Steen, 1997; Doshi et al., 2003; Henderson et al., 1997; Jiang and Li, 2015; Lister and Stone, 1998a; Milosevic and Longmire, 2002; Savage et al., 2010; Smolka and Belmonte, 2003; Zhang and Lister, 1999b). Though massive studies have been devoted to this area, the knowledge about the singularity still remains elusive. In this section, we will mainly discuss three kinds of drop pinch-off situations: a free and homogenous surface flow, an extensional flow under external magnetic field and a confined microfluidic flow in micro-channel.

1.1.2.1 Drop pinch-off of a free and homogenous surface flow

The breakup or rupture of a free surface flow draws a lot of interest from scientists and engineers because of the widely applications as well as the occurrence of finite-time singularities and self-similar behavior near breakup (Brenner et al., 1997; Eggers, 1997; Eggers and Villermaux, 2008). In 1983, Keller and Miksis (Keller and Miksis, 1983) first proposed a scaling theory describing the self-similar recoil of a liquid sheet upon its rupture. They indicated that the interface thickness varies as the $2/3$ power of time remaining to the pinch-off and this is lately demonstrated as ‘Inertial regime (I)’ as the dominant balance exists between inertia and capillary force. In 1993, Eggers (Eggers, 1993) theoretically demonstrated the self-similar behavior of moderately viscous fluid threads using jet approximation. This is known as ‘Inertial - Viscous regime (IV)’ as the capillary force is balanced by the inertia and viscous stress. In 1995, Papageorgious (Papageorgiou, 1995) investigated the breakup of highly viscous filaments by theory and verified the self-similar behavior with unity exponent. This is known as ‘Viscous regime (V)’ as the dominant balance exists between viscous force and capillary force. Since their pioneering work, the self-similar pinch-off in the inertial regime (I) and viscous regime (V) was validated by several following researchers (Chen and Steen, 1997; Day et al., 1998; Henderson et al., 1997; Rothert et al., 2003).

Actually, as a thread of a low (high) viscosity fluid initially thins according to the I (V) regime, viscous (inertial) forces eventually become important and the dynamics ultimately enter into the IV regime so long as the effect of the outer fluid may be neglected (Basaran, 2002; Lister and Stone, 1998b). Then, the crossover from Inertial regime (I) to Inertial – Viscous regime (IV) was firstly confirmed computationally by Notz *et al.* (Notz et al., 2001) and experimentally by Chen *et al.* (Chen et al., 2002). The transition from Viscous regime (V) to Inertial – Viscous regime (IV) was confirmed by Castrejón-Pita *et al.* (Castrejon-Pita et al., 2015) through experiments and simulations. These intermediate transitory regimes made the overall picture more complex and were summarized and developed by Li and Sprittles (Li and Sprittles, 2016).

The minimum neck radius of liquid neck typically follows a power-law behavior in the remaining time, $h_{min} \propto \tau^n$, where the exponent n is between 0 and 1 (Burton et al., 2007). So far, there exist two basic types of drop pinch-off mechanism: inviscid pinch-off (Chen and Steen, 1997) with a $2/3$ exponent and viscous pinch-off (Henderson et al., 1997; Mounir et al., 2013) with a unity exponent in regards to the dependence of minimum neck diameter

on the time-to-pinch-off. However, with the development of measurement techniques, the down-scale investigation on the final pinch-off is more and more demanding (Burton et al., 2004).

1.1.2.2 Drop formation and pinch-off of a heterogeneous ferrofluid

Nowadays, external field-driven system, such as electrical, thermal, acoustic and magnetic, can actively alter the drop formation process, for example the Marangoni effect under a thermal field and the Taylor cone under an electric field. Similarly, magnetic interference has displayed enormous potential in manipulating magneto-fluid drops. Magneto-fluid is a general name given to the colloidal suspension which consists of solid magnetic particles, liquid substrate and surfactant and belongs to a kind of typical ‘smart’ materials. It possesses the characteristics of magnetism of solid and flowability of liquid. Among the family of magnetofluid, ferrofluid, with the nanoscale ferromagnetic oxide as the magnetic particles, has gained increasing prevalence both in research and industry owing to its favorable properties such as nanoscale particles, easy access, no hysteresis and small dependence on the pH, temperature and concentration of the system. The cutting-edge applications of ferrofluids include the drug delivery, cell sorting, bioassays, pump, valve, magnetic carrier, surface detection, nanoscale particles, electronic device, hyperthermia, etc. More information about ferrofluid can be obtained from a pioneer introduction by Rosensweig (Rosenweig, 1985) and a recent review by Torres-Díaz and Rinaldi (Torres-Díaz and Rinaldi, 2014).

Numerous studies have been dedicated to the horizontal behavior of ferrofluid drops under an applied magnetic field, for example, deformation (Séro-Guillaume et al., 1992; Stone et al., 1999; Zhu et al., 2011) and magnetowetting (Nguyen et al., 2010a). Chen *et al.* (Chen et al., 2009) investigated the breakup instability of a ferrofluid drop passing through a narrow zone under an applied magnetic field. The generation and manipulation of ferrofluid droplets in microfluidic devices under a magnetic field have been recently studied by our group (Wu et al., 2013; Wu et al., 2015) and by Tan *et al.* (Tan et al., 2010). However, to our best knowledge, few works have been reported on the perpendicular behavior of ferrofluid drops under a magnetic field. Afkhami *et al.* (Afkhami et al., 2008) investigated the field-induced motion of ferrofluid droplets in a viscous media. Rothert and Richter (Rothert and Richter, 1999) studied the liquid-bridge breakup of ferrofluids between two electro-magnets. Habera *et al.* (Habera et al., 2013) analyzed the effect of a magnetic field

generated by Helmholtz coils on the breakup of ferrofluid jet. Kazhan and Korovin (Kazhan and Korovin, 2003) theoretically studied the capillary instability of a cylindrical interface of viscous magnetic and nonmagnetic fluids subjected to an axial magnetic field.

The final pinch-off of a free homogenous surface flow displays the self-similar behavior and finite-time singularities and the memory of the initial conditions disappears. But the so-called universal scaling of self-similar dynamics was proved not always valid and the specific information of the initial conditions could be retained in the last pinch-off region (Doshi et al., 2003; Louvet et al., 2014; Miskin and Jaeger, 2012; Suryo et al., 2004). Whether it survives for the ferrofluid drop pinch-off in air and whether the gravity-superimposed and gravity-compensated magnetic fields can make a difference are still open questions to be answered. Furthermore, the volume of satellite drops resulting from the pinch-offs is usually less than 1% of the primary drop, which directly leads to the multi-scale distributions (Moon et al., 2014). The scarcity of the information about the primary drops as well as satellite drops under an applied magnetic field would hinder the progress of new technology and applications. Thus, the formation and pinch-off dynamics of ferrofluid drops through a vertical nozzle will be studied in air under two unidirectional magnetic fields.

1.1.2.3 Drop pinch-off in confined microchannel

During the past decades, microfluidics is a rapidly growing interdisciplinary field of research combining biomedicine, biochemistry, soft matter physics, fluid engineering and microreaction engineering etc. (Fujii, 2002; Otten et al., 2005; Sackmann et al., 2014; Theberge et al., 2010; Whitesides, 2006). The research of microfluidics was firstly conducted by S.C. Terry of Stanford University (Terry et al., 1979). In the 1980s, the trend of molecular biology such as genomes, DNA and protein, stimulated the development of microanalysis devices integrated with different assay operations. Then the Micro Total Analysis System (μ TAS) or Lab-on-Chip (LoC) spring up and meanwhile, various chips of microfluidic sensors were reported due to the different applications (Zhang et al., 2011). Thus, microfluidic devices have attracted a lot of attention in both academia and industry. Compared with traditional production equipment, microfluidic devices display the advantages of the small size, large specific surface/volume ratio, easy controllability, high efficiency and producing monodispersed droplets (Dietrich et al., 2008; Lan et al., 2014). For example, micro-devices like micro-reactor and micro-mixer, are very famous for

processing intensification in chemical engineering, due to the high-efficient mass and heat transfer (Aubin et al., 2009; Ghaini et al., 2010).

Droplets are always encountered in the application of microfluidics and have attracted a lot of attention. The formation of monodispersed droplets can be well-controlled in micro-channel (Ozen et al., 2006). On the one hand, the small length scale of the channel is comparable to the size of the droplets and the geometrical confinement could suppress the instability (Garstecki et al., 2005a). On the other hand, the gravitational force is neglected and the flow regime in micro-channel is usually laminar, which is highly stable (Afzal and Kim, 2014). The two-phase flow in micro-channels is determined by the flow conditions, channel geometry, wetting state and properties of both fluids, especially the interfacial tension (Bashir et al., 2014; Waelchli and Rudolf von Rohr, 2006). And the breakup mechanism of droplets in micro-channel is different from their unconfined counterpart (Garstecki et al., 2005b).

The main geometries of micro-channel that are intensively studied include: co-flowing, flow-focusing, T junctions (Carrier et al., 2014; Christopher and Anna, 2007; Fu et al., 2010). The flow-focusing geometry is proved to be powerful and versatile in achieving monodispersed droplets and bubbles (Dollet et al., 2008). Though a lot of studies have been devoted to the drop size and flow regime (Cubaud and Mason, 2008; Utada et al., 2007; Utada et al., 2005), little information is to our best knowledge concerning the final pinch-off of droplets in flow-focusing micro-channel. By assuming a power-law relationship between the minimum neck width and remaining time, Fu *et al.* (Fu et al., 2012b) experimentally demonstrated the exponent is around $1/3$ at low Reynolds numbers; while at high Reynolds numbers, the exponent is larger than $1/3$ and depends on the Capillary number (Ca). But their studies only reach to the scale of $\approx 100 \mu\text{m}$, which is still far from the final pinch-off point. Therefore, further investigation at micro-scale is still required.

I.2 Experimental details

I.2.1 Experimental setup and method

Bubble pinch-off experiment was conducted in a cubic poly(methyl methacrylate) (PMMA) tank (inside three dimensions: $5 \times 5 \times 6.5$ cm) filled with various solutions. Air bubbles were generated through a submerged nozzle (inner diameter $d = 0.5$ mm and outside diameter $d' = 0.81$ mm) which located at the bottom center of the cube in order to avoid the wall effect. The air was injected through a syringe pump (Hamilton, Germany). The nozzle diameter was also photographed as a reference length.

A scheme of the experiment setup for drop pinch-off is illustrated in Figure I.4 and for drop-pinch-off in air, the liquid tank was just removed. The stainless steel nozzle I (inner diameter $d = 0.6$ mm and outside diameter $d' = 0.97$ mm) and nozzle II (inner diameter $d = 1.8$ mm and outside diameter $d' = 2.5$ mm) were used to generate drops. The syringe pump (Hamilton, Germany) was adopted to change the flowrate (Q). All images were recorded after the formation process reaching a steady state.

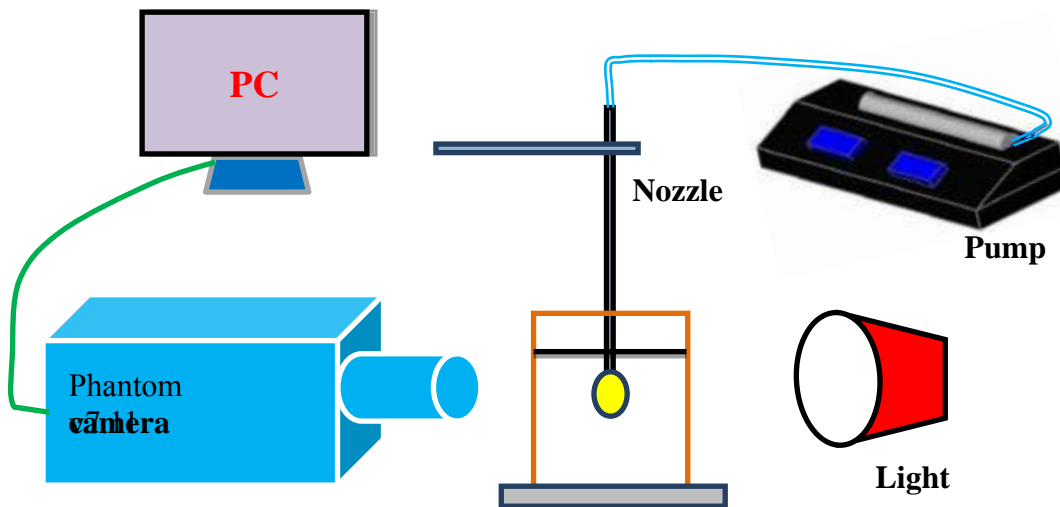


Figure I.4. Scheme of the experimental setup for drop pinch-off. The tank (made of PMMA with inside three dimensions: $5 \times 5 \times 6.5$ cm) was filled with silicone oil for drop-pinch-off in fluid system.

In order to visually study the ferrodrops behavior under a magnetic field, a schema of experiment setup was designed and displayed in Figure I.5. The above nozzle I and nozzle II were applied to generate drops. The nozzle was placed vertically above a couple of neodymium iron boron (NdFeB) magnets (Φ 60 mm, Supermagnete, France) to produce a downward-growing drop. While for the upward-growing drop, the nozzle was laid upside down to be vertically below the center of the magnet (Figure I.5, inset). The nozzle and the magnet were aligned coaxially for the sake of the maximum magnetic flux density. Through a hand lifting platforms, we could easily adjust the distance between the magnet and the nozzle. A Gaussmeter (GM07, Hirst, UK) with a precision of 0.01 mT was employed to measure the magnetic flux densities.

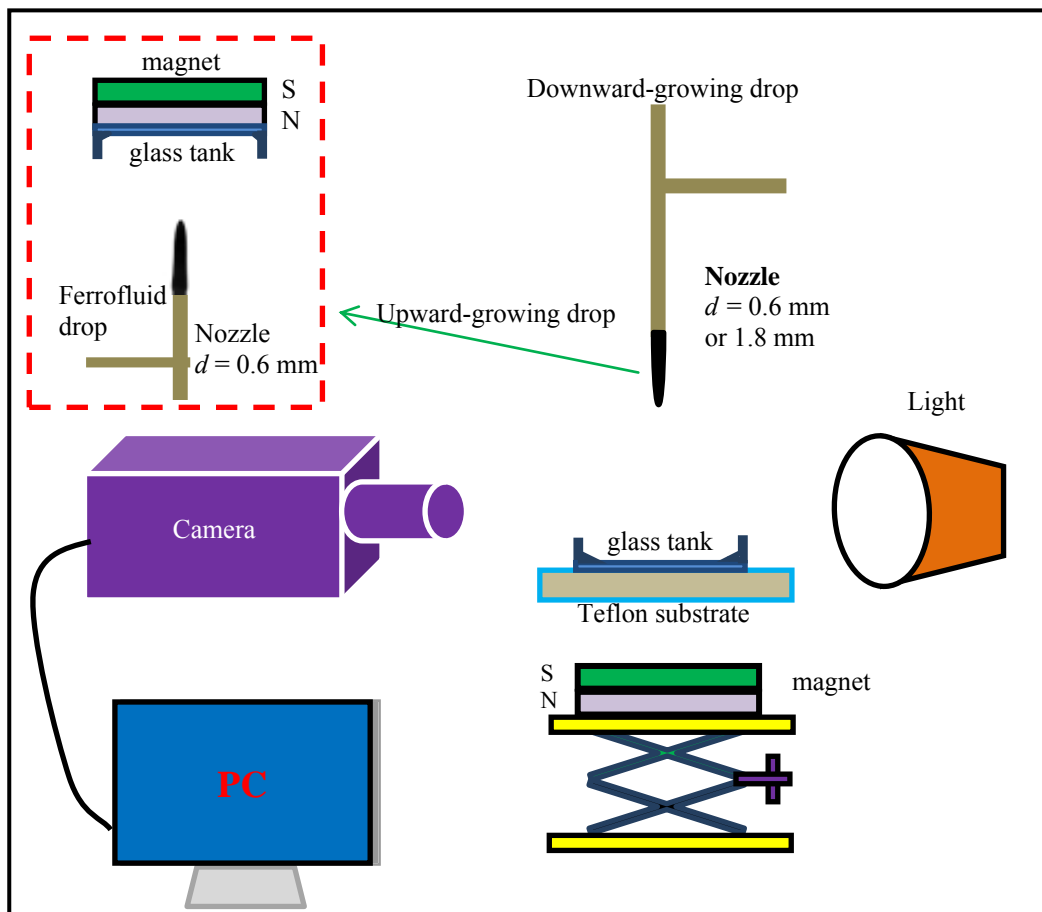


Figure I.5. Scheme of experimental setup for ferrofluid drop formation and pinch-off.

A flow-focusing microfluidic device with sub-millimeter dimensions (width = height = $400 \mu\text{m}$) was fabricated by milling the channels in a flat plate of poly (methyl

methacrylate) (PMMA), shown in Figure I.6a. PMMA is a rigid thermoplastic that is optically transparent. Our focus was given to the droplet breakup and pinch-off at the intersection, as indicated in Figure I.6a. The experimental setup is presented in Figure I.6b. Two syringe pumps (Hamilton, Germany) was adopted to control the flowrate ratio (Q_c/Q_d) between the continuous phase and the dispersed phase. Illumination was provided by a 100 W halogen lamp for bright field applications and phase contrast. A micro-particle image velocimetry system (μ -PIV, Dantec Dynamics, Denmark) was used to obtain the velocity field. A small amount of Latex particles (Merck, France) with calibrated diameter of $0.88 \mu\text{m}$ was added into dispersed phase. By tracking the shadow of seeding particles in a focus plane, the velocity can be quantified through a pair of images.

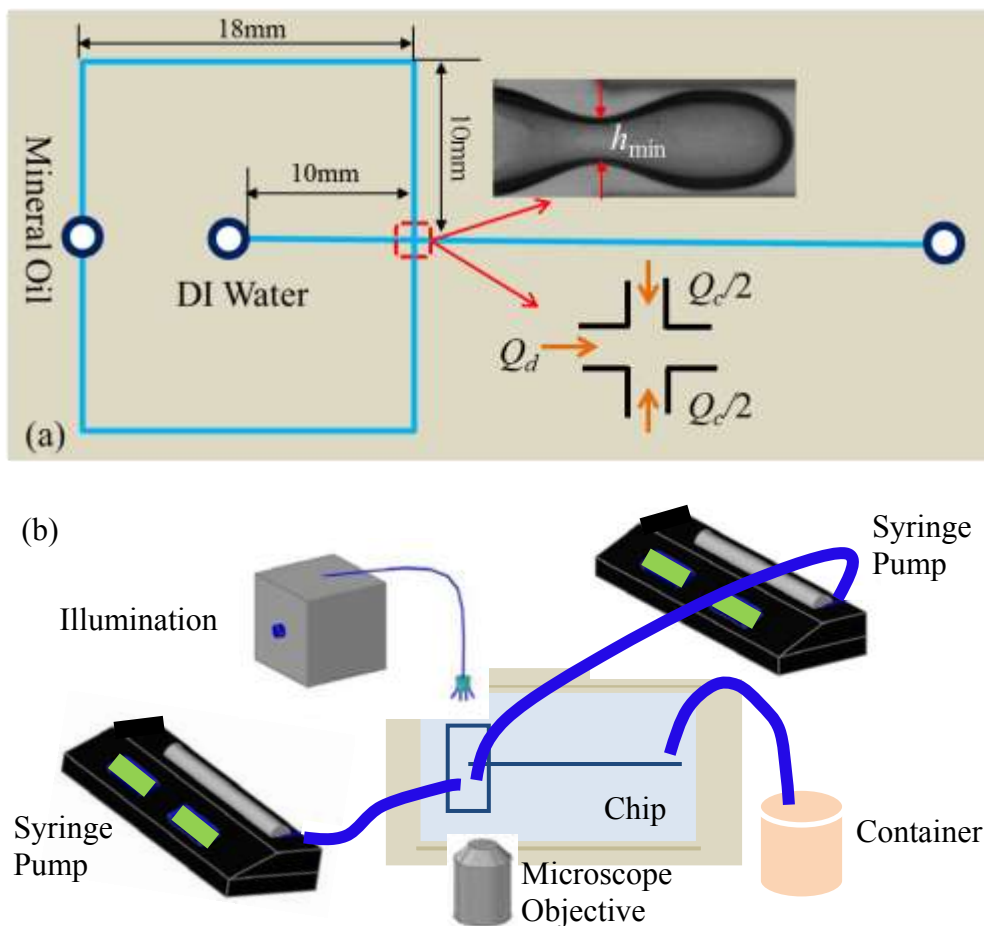


Figure I.6. (a) Microfluidic devices; (b) Scheme of the experimental setup.

I.2.2 Physical properties of working fluids

I.2.2.1 Bubble pinch-off in liquids

Table I.1 gives the basic properties of the investigated Newtonian fluids. The sodium dodecyl sulfate (SDS) and glycerol were added into water to change the surface tension and viscosity, respectively.

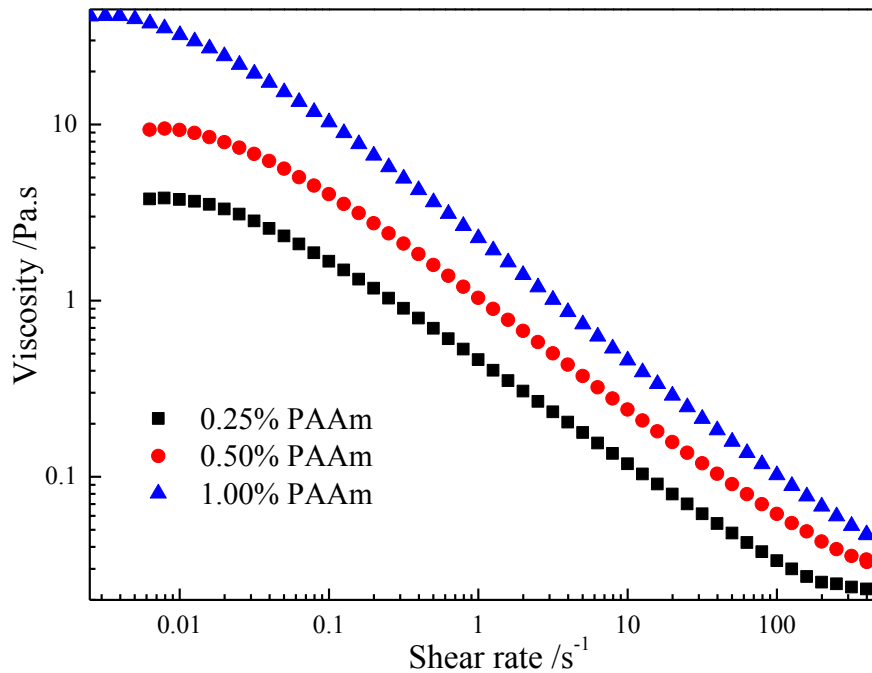
Table I.1. Properties of Newtonian fluids at 293.15 K.

	Density, $\rho /(\text{kg}\cdot\text{m}^{-3})$	Viscosity, $\eta /(\text{mPa}\cdot\text{s})$	Surface tension, $\sigma /(\text{mN}\cdot\text{m}^{-1})$
Water	996.0	1.0	72.5
0.10wt% SDS + Water	996.0	1.0	50.3
0.15wt% SDS + Water	996.0	1.0	40.6
61.23wt% Glycerol + water	1156.6	13.4	67.6
86.73wt% Glycerol + water	1227.1	138.7	65.3
100wt% Glycerol	1261.1	1407.0	63.4

0.25 wt%, 0.50 wt% and 1.00 wt% polyacrylamide (PAAm) (AN 905 SH, SNF Floerger, France) in deionized water were used as non-Newtonian fluids. These PAAm solutions were viscoelastic fluids and exhibited a shear-thinning effect. The rheological properties of PAAm solutions measured by a Rheometer (AR-G2, TA, USA) were shown in Figure I.7 and could be fitted with a power-law model for the shear-thinning part ($\eta = K\dot{\gamma}^{n-1}$), where η is the viscosity, K is the consistency, $\dot{\gamma}$ is the shear rate and n is the flow index. These values together with the density and surface tension of PAAm solutions were given in Table I.2.

Table I.2. Properties of PAAm solutions at 293.15 K.

	Density, $\rho / (\text{kg}\cdot\text{m}^{-3})$	Surface tension, $\sigma / (\text{mN}\cdot\text{m}^{-1})$	Consistency, $K / (\text{Pa}\cdot\text{s}^n)$	Flow index, n
0.25wt% PAAm	996.0	70.3	0.46	0.41
0.50wt% PAAm	996.0	69.6	1.03	0.37
1.00wt% PAAm	996.0	67.7	3.34	0.32

**Figure I.7.** Rheological properties of PAAm solutions.

1.2.2.2 Drop pinch-off in a surround fluid

Drops in our experiments were formed in surround fluids of air and silicone oils. The drops consisted of both Newtonian and non-Newtonian fluids: water, sodium dodecyl sulfate (SDS) solutions, emkarox HV 45 (Emkarox) solutions, silicone oil (SO) and polyacrylamide (PAAm, AN 905 SH, SNF Floerger, France) solutions. The physical properties of drop-in-air and drop-in-liquid systems were given in Table I.3 and Table I.4, respectively. 0.25wt%, 0.50wt% and 1.00wt% PAAm solutions were prepared as non-Newtonian fluid and the rheological properties were shown in Table I.2 and Figure I.7.

Table I.3. Fluid properties of drop-in-air system in our experiment at 293.15K.

Drop-in-air system	$\rho/(\text{kg}\cdot\text{m}^{-3})$	$\sigma/(\text{mN}\cdot\text{m}^{-1})$	$\eta/(\text{mPa}\cdot\text{s})$	$\lambda = \eta / \eta_{\text{air}}$	$l_{\eta} = \eta^2 / (\sigma\rho)$
Water	996	72.50	1.0	55.56	13.85 nm
0.10wt% SDS+Water	996	50.30	1.0	55.56	19.96 nm
0.25wt% SDS+Water	996	38.10	1.0	55.56	26.35 nm
0.50wt% Emkarox+water	996	70.00	2.0	111.11	57.37 nm
4.50wt% Emkarox+water	998	68.00	3.6	200.00	190.97 nm
Silicone oil 10 (SO 10)	920	19.70	11.5	638.89	7.30 μm
Silicone oil 50 (SO 50)	955	20.10	59.5	3305.56	187.43 μm
Silicone oil 100 (SO 100)	960	20.20	112.8	6266.67	656.14 μm

Table I.4. Fluid properties of drop-in-liquid system in our experiment at 293.15K.

Drop-in-liquid system	In SO 50		In SO 100	
	$\sigma_1/(\text{mN}\cdot\text{m}^{-1})$	$\lambda_1 = \eta / \eta_1$	$\sigma_2/(\text{mN}\cdot\text{m}^{-1})$	$\lambda_2 = \eta / \eta_2$
Water	20.20	0.017	17.60	0.009
0.10wt% SDS+Water	17.70	0.017	14.40	0.009
0.25wt% SDS+Water	11.50	0.017	10.00	0.009
0.50wt% Emkarox+water	20.10	0.034	17.70	0.018
4.50wt% Emkarox+water	19.70	0.061	17.50	0.032
0.25wt% PAAm+Water	29.70	--	29.81	--
0.50wt% PAAm+Water	30.20	--	30.05	--
1.00wt% PAAm+Water	30.00	--	29.87	--

1.2.2.3 Ferrofluid drop formation and pinch-off in air

An oil-based ferrofluid (EMG 911, Ferrotech, Germany) with density $\rho = 1200 \text{ kg}\cdot\text{m}^{-3}$ and viscosity $\eta = 11.25 \text{ mPa}\cdot\text{s}$, respectively, at 25°C , was employed. The effect of outer gas can be neglected owing to the small density and viscosity of air. The ferro-particles' volume concentration of EMG 911 is 1.8% and the initial susceptibility $\chi = 0.39$. The magneto-viscous effect could be ignored (Pamme, 2006) due to the fact that the average diameter of

colloidal particles is around 10 nm. The surface tension of the ferrofluid in air measured by a dynamical tensiometer (IT Concept, France) is $\sigma = 23.6 \pm 0.1 \text{ mN}\cdot\text{m}^{-1}$.

1.2.2.4 Drop pinch-off at micro-scale

Deionized water was used as disperse phase and filled through the main channel at a flow rate of Q_d . The continuous phase, mineral oil with 2% Span 20, was guided by two equal lateral branches with the same flow rate $Q_c/2$. The nonionic surfactant — Span 20, was added to decrease the interfacial tension. The three liquid streams could converge at the intersection and then form discrete droplets. The density and viscosity of water are $996 \text{ kg}\cdot\text{m}^{-3}$ and $1 \text{ mPa}\cdot\text{s}$; those of mineral oil are $838 \text{ kg}\cdot\text{m}^{-3}$ and $35.21 \text{ mPa}\cdot\text{s}$. The interfacial tension between these phases is $3.0 \text{ mN}\cdot\text{m}^{-1}$.

1.2.3 Imaging analysis

Bubble and drop pinch-off behavior at macro-scale was visualized and recorded with a Phantom v7.11 camera (Vision Research, USA), which is at rate up to 1000,000 frames per second (fps). The imaging details are as follows:

(1) The visualized speed was 160000 fps with a field of view 144×120 pixels for air bubble pinch-off in Newtonian fluids; While 110032 fps with a resolution 144×176 pixels for bubble pinch-off in non-Newtonian fluids. The exposure time remains as low as $2 \mu\text{s}$. This high-intensive local magnification almost reaches the limit of the present optical equipment, leading to a pixel resolution of $4 \mu\text{m}/\text{pixel}$.

(2) For drop-in-air system, the resolutions were 192×400 pixels with 51012 fps and 304×400 pixels with 39013 fps for nozzle I and nozzle II, respectively. For drop-in-fluid system, the resolution maintained 304×264 pixels, 50000 fps and 432×480 pixels, 20000 fps for nozzle I and nozzle II, respectively. The exposure time is as low as $3 \mu\text{s}$.

(3) With regard to the ferrofluid drop formation and pinch-off, the resolution maintains 400×800 pixels (nozzle I) or 600×800 pixels (nozzle II) for the downward-growing drops and 352×800 pixels (nozzle I) for the upward-growing drops. Depending on the formation frequency, the visualization speed was adjusted from 2000 to 19005 fps.

(4) Droplet pinch-off at micro-scale was visualized by an inverted microscope system (Leica, Germany) which connected to our Phantom v7.11 camera. The visualized speed is 10000 fps and the resolutions are 1280×504 pixels.

The obtained images were analyzed frame by frame through the self-programmed Matlab, with the assumption of cylindrical symmetry for drops and bubbles neck. Firstly, convert the gray image into black-and-white image by applying a threshold value which is manually tried and verified with the real pixels. Secondly, the interested liquid or gas neck is selected and the neck diameter is counted row by row. The minimum neck diameter in each image is then obtained. However, the images in microchannel were processed and the related flow fields were computed through the software DynamicStudio (Dantec Dynamics, Denmark).

I.3 Bubble pinch-off in liquid

I.3.1 Air bubble pinch-off in Newtonian fluids

During the bubble formation, the initial quasi-static expansion stage is mainly the result of the balance between buoyancy and surface tension. When the balance collapses, there come the necking and pinch-off stages. The Bond number, $Bo = \frac{\Delta\rho d^2 g}{\sigma}$, characterizes the relative importance of buoyancy and surface tension, here $\Delta\rho$ is the density difference between the gas and liquid, d is the nozzle inner diameter, g is the gravitational acceleration, σ is the surface tension. For the three investigated Newtonian fluids: water, SDS aqueous solutions and glycerol aqueous solutions, the Bo number is far below unity, which implies that surface tension plays a very important role in the initial stage of bubble formation. But when it approaches the pinch-off region, the gas inertia, the viscous drag and the surface tension reach a certain equilibrium (Lesage and Marios, 2013). This point is detailed in the modeling section as follows.

The experimental snapshots of air bubble pinch-off in various Newtonian fluids are shown in Figure I.8. For pure water, the bubble neck exhibits a symmetric shape with two symmetrical parabolic curves outside (Figure I.8a). With time evolution, the two parabolic curves approach to the centerline and the minimum neck width decreases into a short thread connecting two conical ends. When adding some surfactant into water (Figure I.8b and c), the shape evolution undergoes nothing different but the reduced surface tension will accelerate the pinch-off process. This can be argued that in presence of a surfactant, the liquid molecule cohesion is lower which facilitates the gas enter into the surfactant solutions (Loubière and Hébrard, 2004). Additionally, in Figure I.8a, b and c, two conical ends after pinch-off all recoil to be flat which is in a good agreement with the previous study (Thoroddsen et al., 2007). This flat shape derives from the instant release of surface energy which erases the memory of the cylindrical-shaped gas thread.

However, more viscous water-glycerol mixture shows a relatively longer thread before pinch-off and whose length increases with the concentration of glycerol solutions (Figure I.8d, e and f). During the experiments, the bubble pinch-off process in glycerol solutions is prolonged compared to the other Newtonian liquids and the larger the viscosity of glycerol solutions, the longer the pinch-off process undergoes. This can be explained by the larger

viscosity of external liquid leads to a higher viscous drag which gains weight in the force competition and hinders the bubble pinch-off (Davidson and Schuler, 1960).

Furthermore, it can be observed in Figure I.8d that a short moment after pinch-off, the two pieces in 61.23% glycerol solutions are approximately flat while those in viscous liquids – 86.73% and 100% glycerol solutions (Figure I.8e and f), remain the intact conical shape. This can be rationalized that viscous force significantly offsets the energy release from the pinch-off and this cushioning effect increases with the increase of external fluid viscosity.

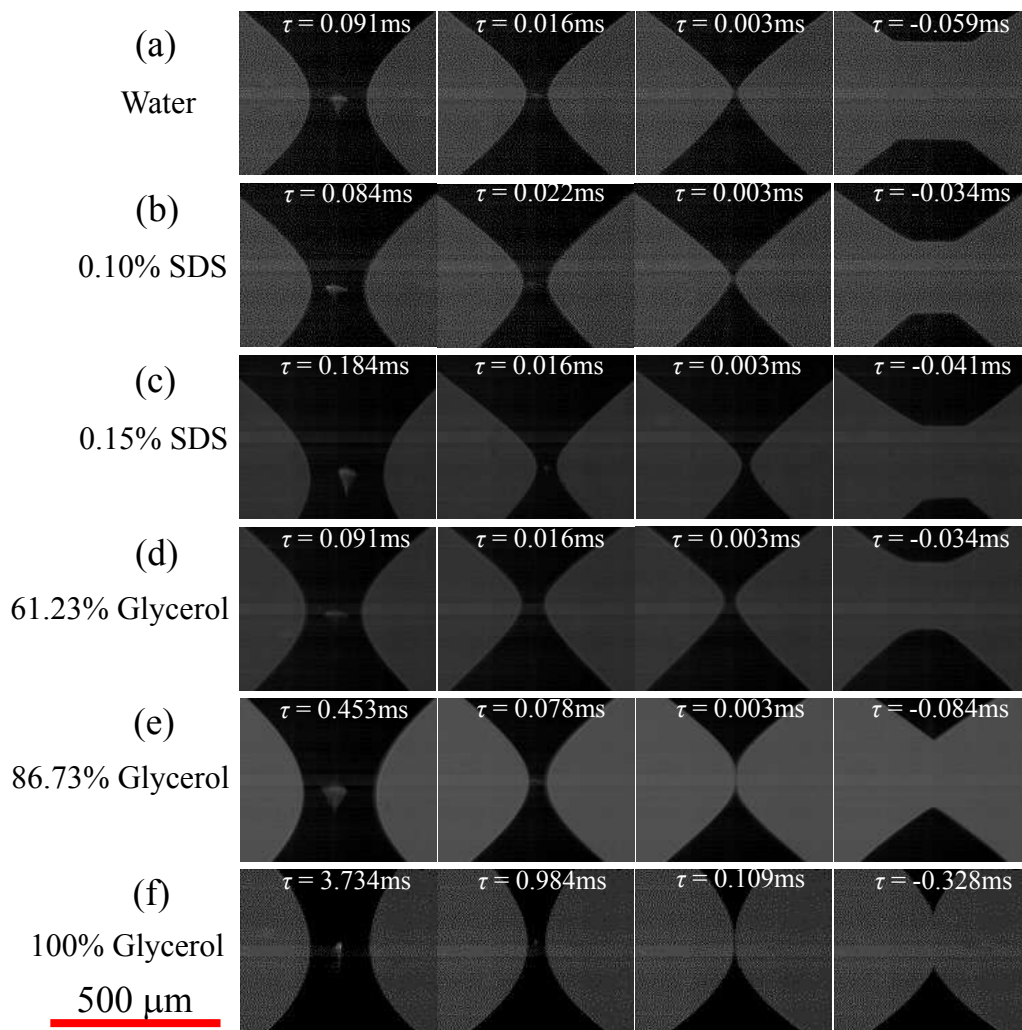
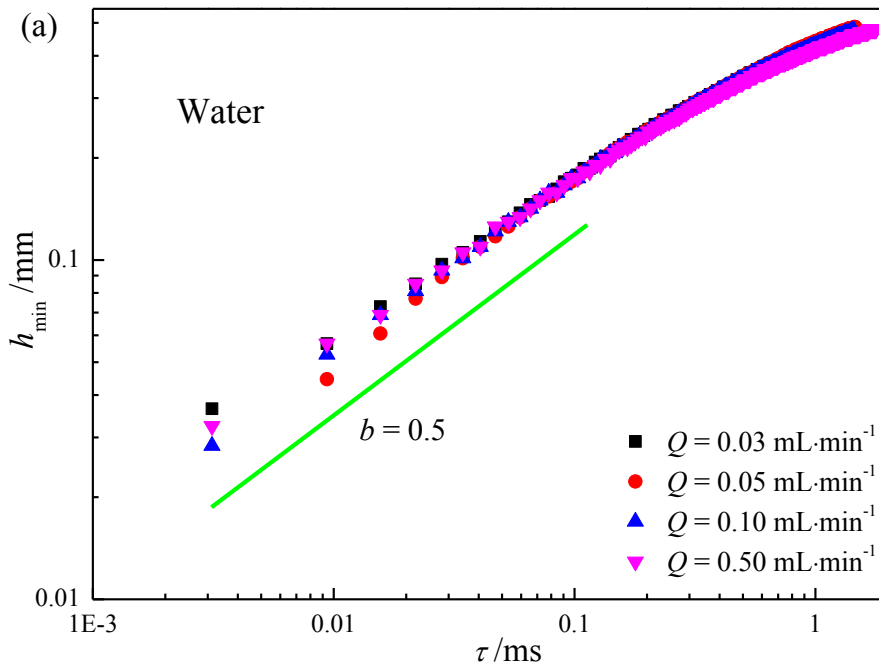


Figure I.8. Air bubbles pinching off in various Newtonian fluids. They all share the same scaling bar.

A power law ($h_{\min} = a\tau^b$) can be used to fit the evolution of the minimum neck diameter, h_{\min} , as a function of time-to-pinch-off τ . The determination of time-to-pinch-off is the average value between the last frame before and first frame after the primary pinch-off (Burton et al., 2005). From Figure I.9a, the curves with different flowrates superimpose and the exponent b of the pinch-off region shows a constant value 0.5. Moreover, in Figure I.9b, the bubble pinch-off in fluids with a lower surface tension and intermediate viscosity also show an exponent 0.5. However, for much higher viscosity, the exponent b remains unity. In fact, the pinch-off dynamics under inviscid conditions is governed by a local balance of surface tension and inertia (Gordillo et al., 2005). Albadawi *et al.* (Albadawi et al., 2013) have once numerically demonstrated the detachment stage with an exponent of 0.36 consistent with a flow where the influence of both the surface tension and gas inertia inside the neck region is of similar magnitude. Gordillo *et al.* (Gordillo et al., 2005) found that an exponent of $1/3$ occurs when the gas inertia effect in the neck is significant. Dollet *et al.* (Dollet et al., 2008) and Fu *et al.* (Fu et al., 2010) obtained an exponent $b = 1/3$ for bubbles pinch-off in confined microfluidic channels, where the collapse is mainly driven by the gas and liquid inertia rather than by capillary forces. However, for bubbles in viscous fluids, the viscous force increases at the final pinch-off stage and becomes a dominant driving force (Burton et al., 2005). Our scaling results with the exponent $b = 0.5$ and 1 show a good agreement with the previous work of Burton *et al.* (Burton et al., 2005).



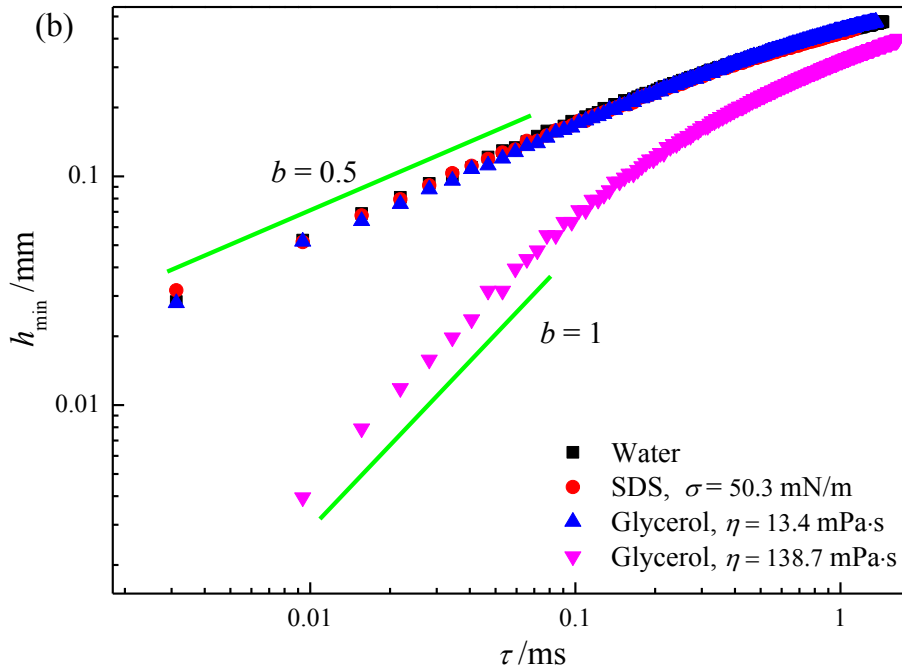


Figure I.9. The neck evolution of air bubbles pinching off in Newtonian fluids. (a) Bubble pinch-off in water, (b) bubble pinch-off in aqueous solution added with SDS and glycerol.

I.3.2 Air bubble pinch-off in non-Newtonian fluids

Non-Newtonian fluids due to their rheological properties always show special and complicated behaviors. Under the same apparent viscosity, bubbles in non-Newtonian liquids were proved to be larger than those in Newtonian liquids and in particular of quite different shape (Davidson and Schuler, 1960). Another characteristic feature is that gas bubble in viscoelastic non-Newtonian fluids rises with a pointed tail accompanied by a negative wake (Amirnia et al., 2013; Frank et al., 2012; Frank et al., 2003; Fu et al., 2012a; Funfschilling and Li, 2001). Here, we attempt to investigate the bubble pinch-off in non-Newtonian fluids.

Three representative sequences of air bubble pinch-off in different concentrations of PAAm solutions are shown in Figure I.10. At the first sight, the shape of necking and pinching off of bubbles in PAAm solutions is similar to that observed in Newtonian fluids. But several major characteristics can be further observed. Firstly, the length of gas thread as well as the curvature diameter (third image in each sequence of Figure I.10) near the pinch-off point increases with the increasing concentration of PAAm solutions. This elongation of

gas thread can be attributed to the high shearing effect on the spatial distribution of viscosity and elastic stress (Fu et al., 2012a). Secondly, accompanied with the elongated gas thread, the gas volume around the nozzle diminishes with the increasing concentration. That is because when the concentration of PAAm is higher, the viscous drag on the forming bubble at the nozzle will be more pronounced. Last but not least, two pointed tails instead of flat surfaces are observed for all PAAm solutions after the thread pinches off and their size increases with the concentration of PAAm solutions. The pointed tails accompanied by the concave boundary, especially in the upper end, mainly come from the competition between the shear and normal stresses in PAAm solutions (Funfschilling and Li, 2001). During the thread pinch-off process, the rapid necking leads the viscosity to decrease with the decreasing distance from the gas thread. That is why in PAAm solutions, two pointed tails occur at centerline after pinch-off. In fact, the upper tail will retain during the rising process while the bottom tail will be flatted to be spherical attached to the nozzle.

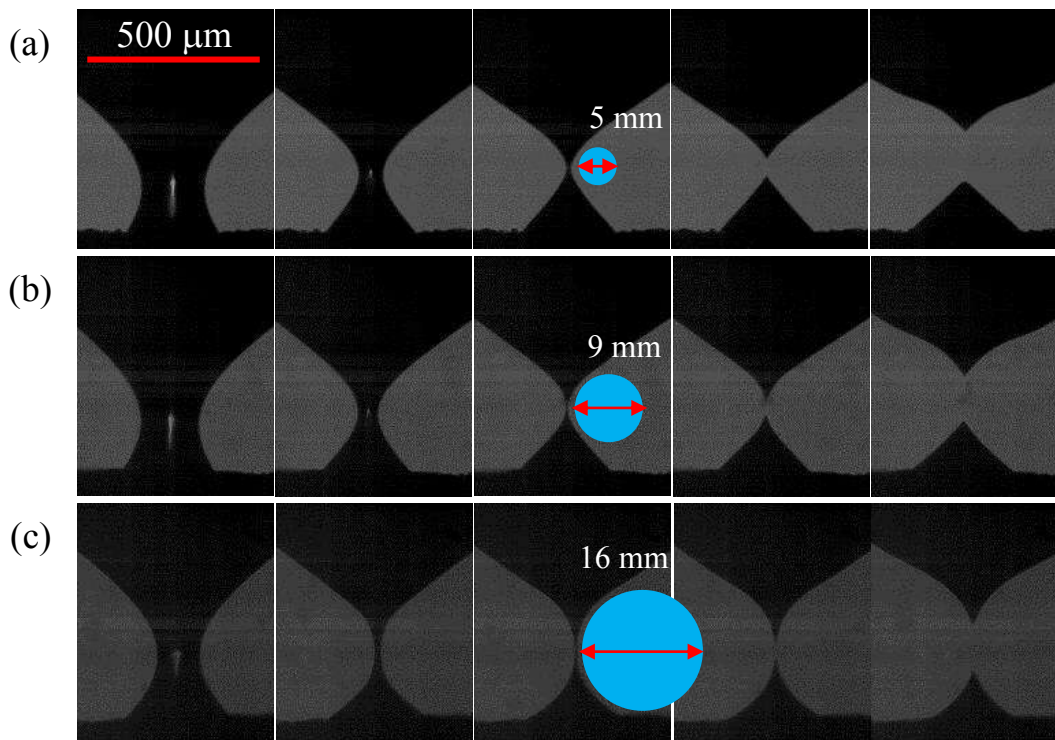
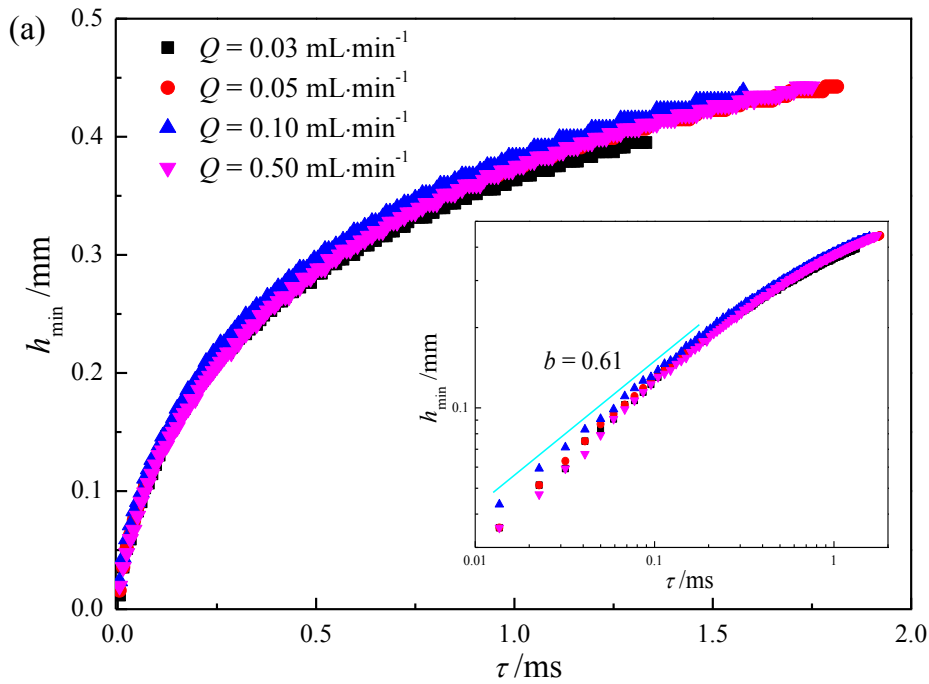


Figure I.10. Air bubbles pinching off in PAAm solutions, (a) 0.25wt% PAAm, (b) 0.50wt% PAAm, (c) 1.00wt% PAAm. The time-to-pinch-off (τ) for the three concentrations is the same as from left to right: 0.186 ms, 0.041 ms, 0.005 ms, - 0.005 ms and - 0.077 ms. Obviously, the larger the PAAm concentration, the longer the pinch-off process. The above images all share the same scaling bar.

Similarly, the minimum neck diameter *vs.* the time-to-pinch-off is fitted with the similar power law ($h_{\min} = a\tau^b$) in Figure I.11. Obviously, the final pinch-off is independent of the initial flowrate as all curves converge when the time-to-pinch-off approaches to zero. And the exponent b in Figure I.11a is 0.61 while in Figure I.11b is 0.73, compatible with the conventional range (0.5 - 1). Fu *et al.* (Fu et al., 2012a) once investigated the bubble pinch-off in non-Newtonian fluids in confined microchannel and proposed a small exponent 1/6. However, a special phenomenon can be seen in Figure I.11c which shows a transition in the final pinch-off regime. This feature is in accord with the non-self-similar profile – a long cylindrical thread near the pinch-off point. Compared to 0.25% and 0.50% PAAm solutions, the non-universal character of 1.00% PAAm solution probably comes from both an elastic behavior and in particular as the stronger shear-thinning effect with a lower flow index.



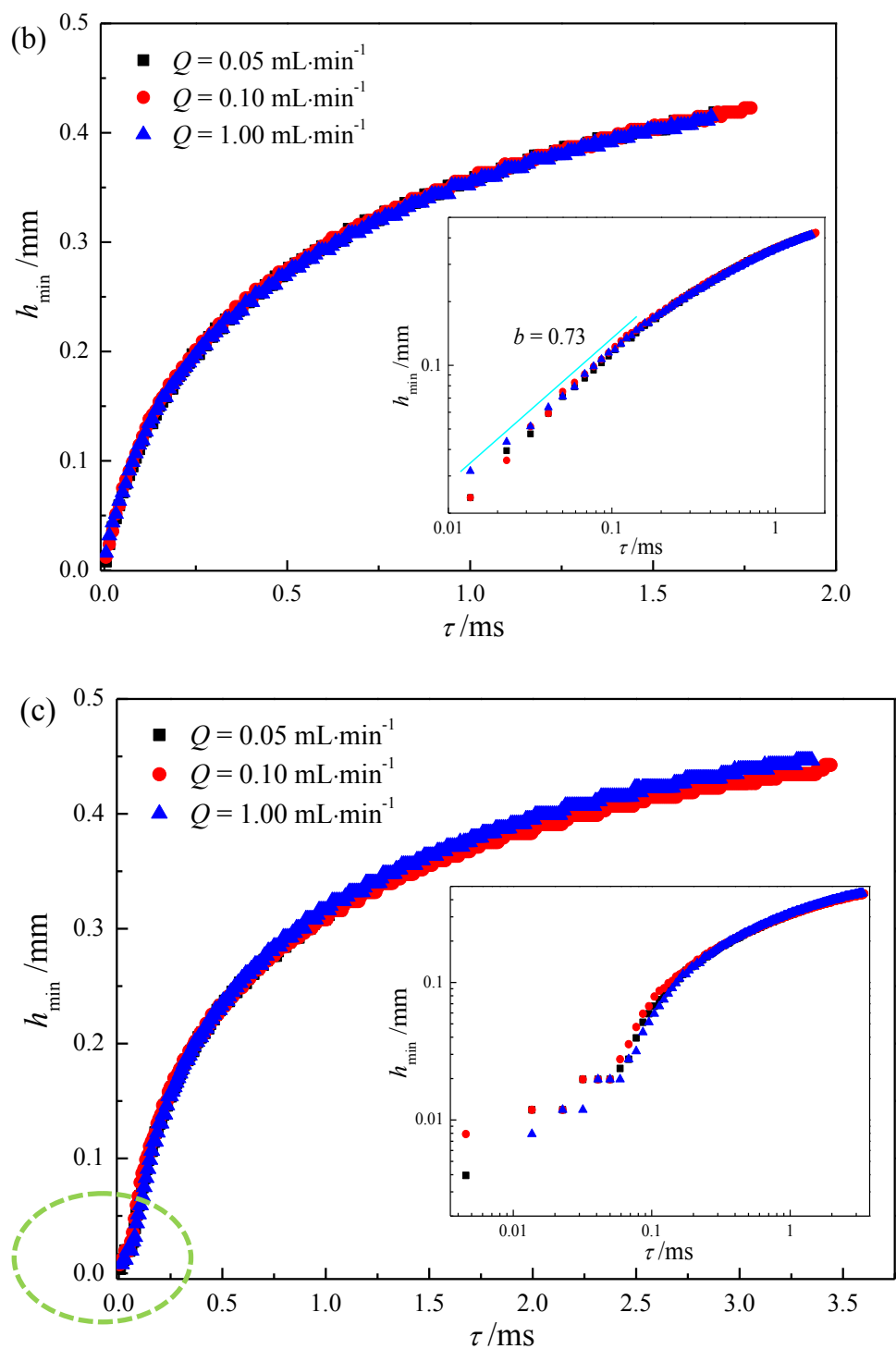


Figure I.11. Scaling law of air bubbles pinching off in non-Newtonian fluids. (a) 0.25wt% PAAm; (b) 0.50wt% PAAm; (c) 1.00wt% PAAm.

I.3.3 Modeling and simulations

Owing to the axisymmetric shape, the 2D modelling of bubble pinch-off mechanism was based on the following main assumptions: the liquid around the bubble is incompressible and of infinite extent; the gas flow is adiabatic; the gas pressure inside the bubble is uniform (Li et al., 2002). Both Newtonian and non-Newtonian properties were taken into account in this modelling approach. An equivalent radius, R , for any point on the bubble surface was defined by using two local radii of curvature R' and R'' . $2/R = 1/R' + 1/R''$. The motion of that point was expressed in terms of the equivalent radius. The non-spherical bubble shape could then be taken into account with a sufficient number of grid points. The modelling consisted essentially of two motion equations that described respectively the radial expansion and the vertical ascension of the bubble.

The association of the Navier-Stokes equation describing the conservation of momentum for the fluid around the bubble in the radial direction and the continuity equation for the purely extensional, incompressible and irrotational flow leads to

$$R\ddot{R} + \frac{3}{2}\dot{R}^2 = \frac{P_L - P_\infty}{\rho_L} - \frac{1}{\rho_L} \int_R^\infty (\text{div } \tau)_r dr \quad (\text{I.1})$$

The static liquid pressure at the level of bubble P_L is related to the gas pressure in the bubble P_B through the following equilibrium condition at the interface:

$$P_L + \tau_{rr}|_{r=R} + \frac{2\sigma}{R} = P_B \quad (\text{I.2})$$

Combining Eqs (I.1) and (I.2) leads to the equation that governs the radial expansion:

$$P_B = P_L + P_L \left(R\ddot{R} + \frac{3}{2}\dot{R}^2 \right) + \frac{2\sigma}{R} + P_\mu \quad (\text{I.3})$$

Here, the term $P_\mu = 3 \int_R^\infty \frac{\tau_{rr}}{r} dr$ can be considered as the pressure due to the viscous drag of fluid. In the case of non-Newtonian fluids obeying the power-law, we have

$$P_\mu = \frac{4K(2\sqrt{3})^{n-1}}{n} \left(\frac{\dot{R}}{R} \right)^n \quad (\text{I.4})$$

It is worth noting that PAAm solutions used display viscoelastic properties. If the shear-thinning viscosity can effectively be described by the above-mentioned power law, both the first difference of normal force and the relaxation time are experimentally measured on the rheometer. For example, the typical relaxation time is approximately 12 s, 20 s and 30 s in

0.25%, 0.50% and 1.00% PAAm solutions respectively. In our previous studies (Frank et al., 2012; Frank and Li, 2005, 2006), it was demonstrated that if the elasticity does play a major role in the complex negative wake behind a rising bubble in a viscoelastic liquid such as PAAm solutions after its detachment from an orifice, a forming bubble at the orifice exhibits axisymmetric shape and neck so that the effect of the fluid elasticity is negligible for the whole formation process. In fact, the neck elongation during the pinch-off induces radially normal forces which are orthogonal to the axial shear fields in the PAAm solutions and then annihilated due to the axisymmetry. Regarding the use of a simplified power law to describe the viscosity evolution, the shear rate range corresponding to the bubble formation at an orifice around 1 mm is well located in the power law and far from two Newtonian plateaus (Funfschilling and Li, 2001; Li. Huai Z. et al., 2002). The motion equation governing the vertical bubble ascension was based on a balance of different forces: inertial, buoyancy and viscous drag forces, the vertical component of surface tension acting on bubble surface as well as eventually gas momentum rate through the orifice:

$$\left(\rho_G + \frac{11}{16} \rho_L \right) \frac{d}{dt} (V_B U_B) = (\rho_L - \rho_G) g V_B - \frac{\pi D_{\max}^2}{8} C_D \rho_L U_B^2 - 4\pi\sigma \int_0^{\theta'} \frac{R'^2}{R} \cos \theta \sin \theta d\theta + \frac{4\rho_G Q_o^2}{\pi D_o^2} \quad (I.5)$$

Eqs (I.1) - (I.5) were then solved numerically at each element using a proper constitutive relation to obtain the bubble shape at each time interval by means of a finite-difference method. A peculiar attention was paid to the bubble neck to follow the pinch-off dynamics. The simulation was finished when the bubble neck is closed: in this case, the bubble was considered as formed and detached from the orifice.

The theoretical shape evolution given in Figure I.12 compares well the experimental observation. In particular, the pinch-off mechanism through the variation of the minimum neck diameter, h_{\min} with the remaining time τ follows effectively a power-law: $h_{\min} = a\tau^b$ when the neck is below a threshold. The theoretical value gives $b = 0.58, 0.98$ and 0.70 respectively for bubbles pinch-off in water, 86.73% glycerol solution and 0.50% PAAm solution. These values are of comparable order with the above experimental data.

It is worth mentioning that as for the experiments exhibiting spatial resolution limitation, the numerical simulation has its own shortcoming due to mainly the very fast pinch-off mechanism. A compromise is required to balance a global large bubble size and a locally fine neck. Therefore, the modelling should be more carefully validated as for

Newtonian fluids. Besides the experimental investigation at finer scale such as micro-PIV within a microchannel, a much more rigorous rheological model including the elastic effect and deeply smaller meshing as the Lattice Boltzmann approach (Frank and Li, 2005, 2006) would be helpful.

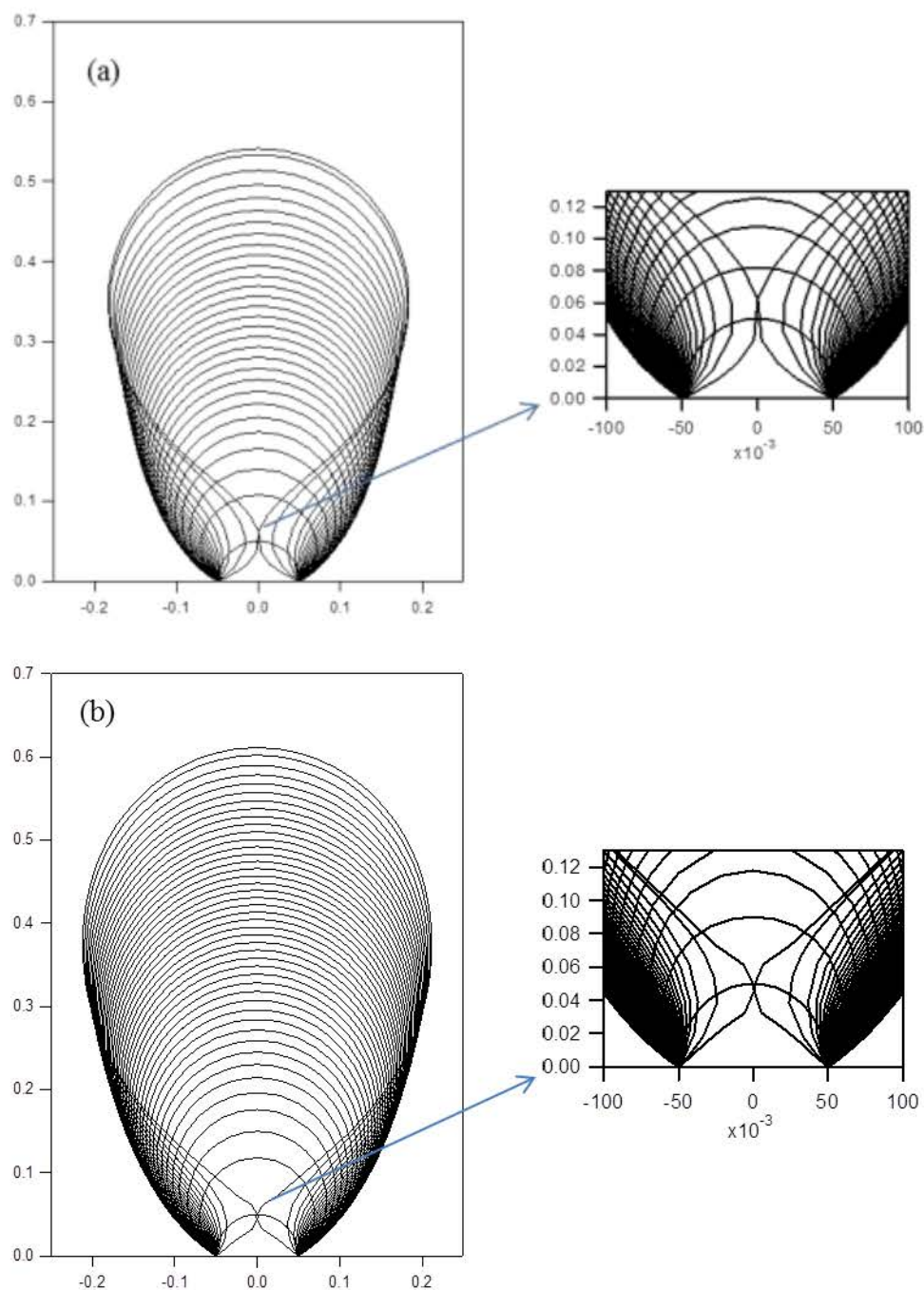


Figure I.12. Numerical simulation of the pinch-off dynamics for a bubble forming at an orifice. (a) 86.73% glycerol solution. (b) 0.50% PAAm solution.

I.4 Drop pinch-off in a surround fluid

I.4.1 Drop pinch-off in air

Figure I.13a presents the sequence of a water drop pinch-off in air. When the surface tension is surpassed by the inertial force and gravity, the neck occurs and rapidly increases in length and decreases in width, which evolves into a conical thread. The thread loses its uniformity and continuously elongates until a critical length where it pinches off first at the bottom and then at the upper end. Liao *et al.* (Liao et al., 2004) once indicated that when $We = \rho u^2 R / \sigma \gg 1$, the pinch-off process switched from a “bottom breakup first” pattern to “upper breakup first” pattern. In our experiments, We number is far below unity, so the pinch-off exhibits a “bottom breakup first” pattern.

Compared to the pure water, the slightly increased viscosity by Emkarox (Figure I.13b and c) and the lowered surface tension by SDS (Figure I.13d and e) lead to a negligible effect on the critical thread length but results in a slightly smaller size of newly-formed drops. However, a small difference can be observed in SO 10 with thin micro-threads up and down as shown in Figure I.13f. The micro-threads rebound into the primary thread in an extremely short period. In fact, Shi *et al.* (Shi et al., 1994) proposed the cascade structure of micro-threads when largely magnified the space and time resolution near the pinch-off point and Henderson *et al.* (Henderson et al., 1997) experimentally demonstrated the transition of primary thread to the secondary thread at the drop. In addition, both the bottom of the nozzle fluid and the top of the newly drop after two pinch-offs develop into plane surfaces due to the liberation of surface energy. This typical characteristic was already observed by previous authors in both drop and bubble pinch-off (Burton and Taborek, 2008). Furthermore, the thread evolves into a chain of droplets (indicated in the right side of Figure I.13a - e) which quickly merge into one large satellite drop while only two end drops on the thread evolve into one satellite drop in Figure I.13f. The shape analyses imply different mechanisms between the low-viscosity fluids (like water, SDS and Emkarox) and the relatively high-viscosity SO 10.

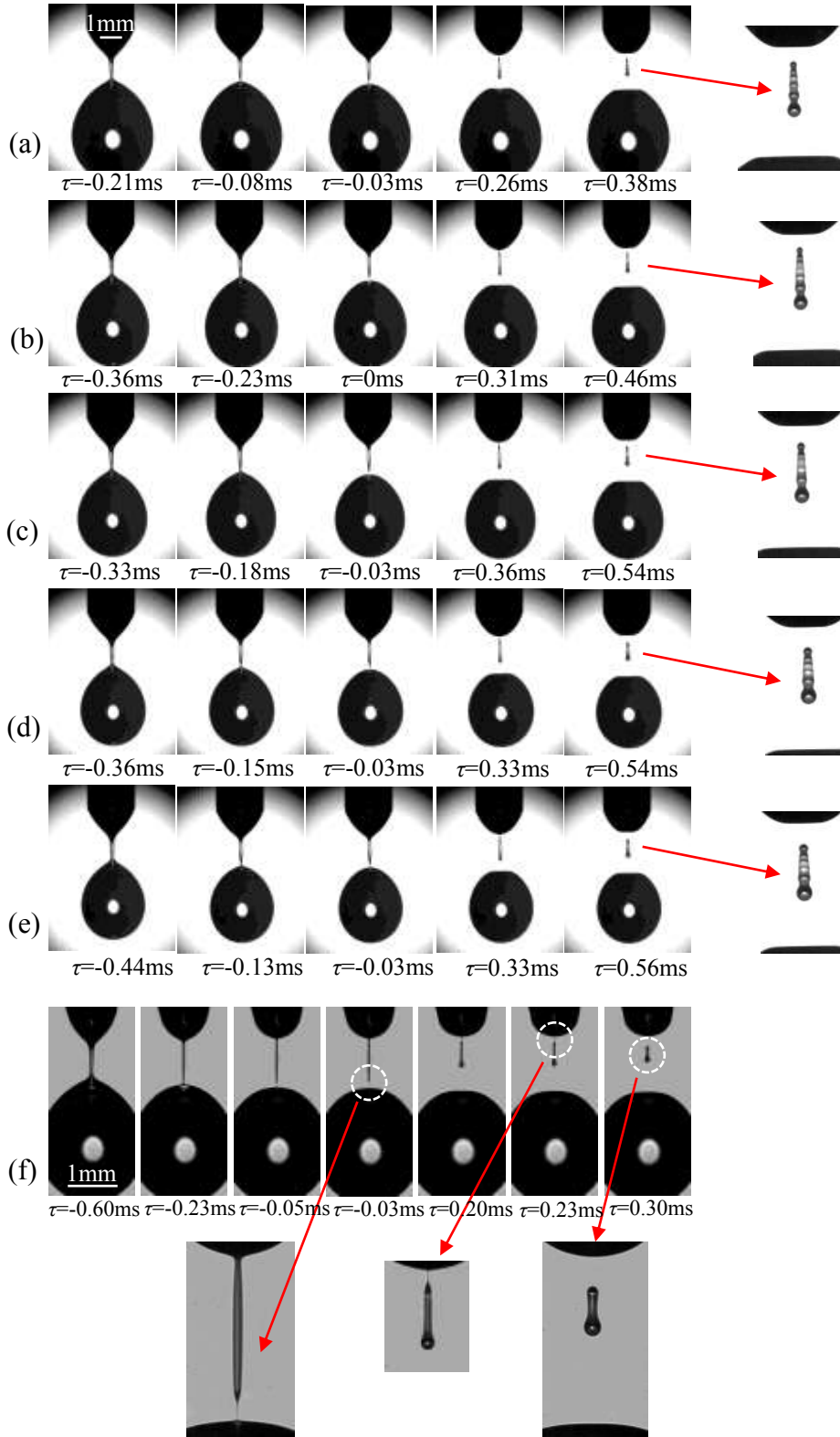
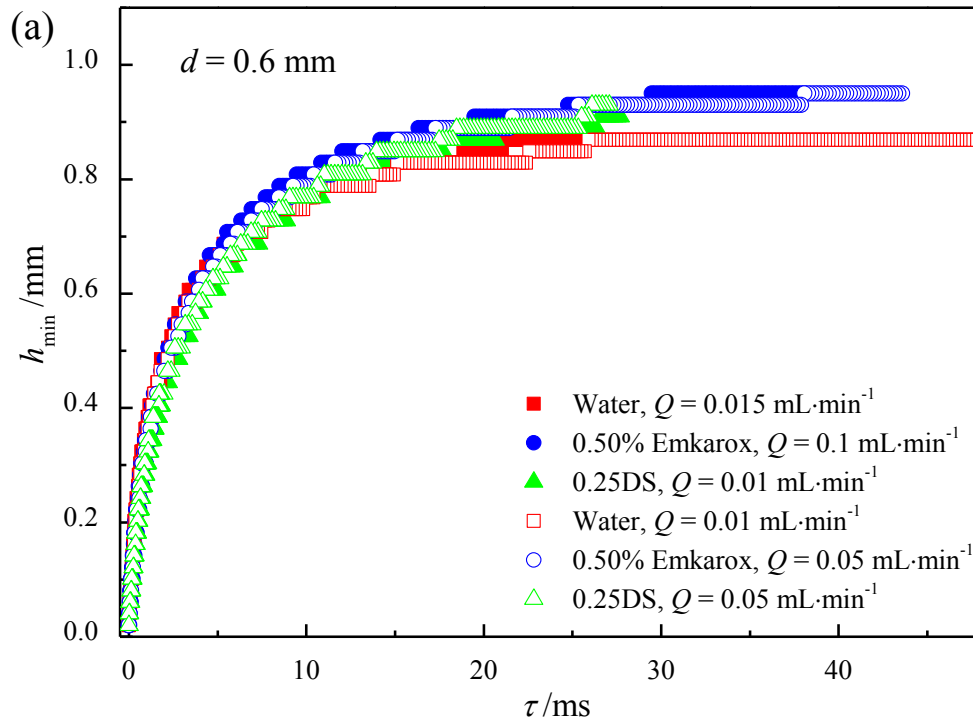


Figure I.13. Pinch-off sequences for different solutions in air. (a) $\lambda = 55.56$, $l_\eta = 13.85$ nm; (b) $\lambda = 55.56$, $l_\eta = 19.96$ nm; (c) $\lambda = 55.56$, $l_\eta = 26.35$ nm; (d) $\lambda = 111.11$, $l_\eta = 57.37$ nm; (e) $\lambda = 200.00$, $l_\eta = 190.97$ nm; (f) $\lambda = 638.89$, $l_\eta = 7.30$ μm . (a) – (e) share the same scaling bar.

In order to verify the universal scaling law $h_{\min} \propto \tau^b$, we plot the minimum neck diameter h_{\min} as a function of time-to-pinch-off τ in Figure I.14. With regard to the strong dependence of exponent b on the breakup time, here we set the time τ to zero at the last frame before first detachment is observed.

Figure I.14a and I.14b show that the final pinch-off is independent of initial conditions, such as flowrate, nozzle diameter and even the fluid properties. But a bifurcation could be observed in Figure I.14c: for relatively low viscosity ratio λ , the pinch-offs exhibit a classical exponent of $2/3$; while the pinch-off of SO 10 shows an exponent of 1. These exponents are compatible with the previous results and together with the shape evolution, it convinces the universal pinch-off character to some extent.



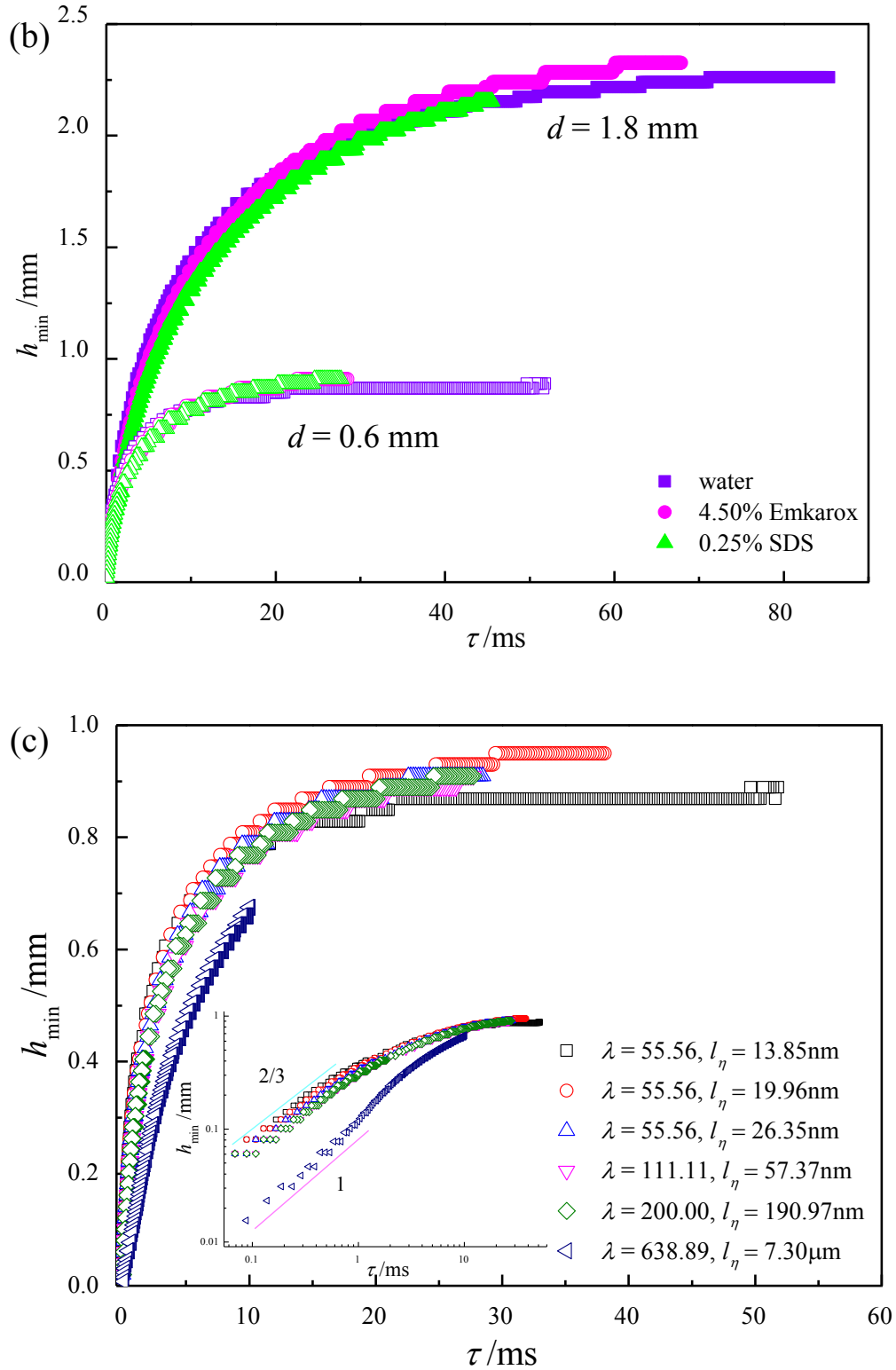


Figure I.14. Minimum neck diameter (h_{\min}) as a function of the time-to-pinch-off (τ) for various fluids in air. (a) Different flowrates; (b) Different nozzle diameters; (c) Scaling law under different conditions, inset is the corresponding log-log plot.

The viscosity ratio of internal and external fluids is the governing parameter for pinch-off process (Longmire et al., 2001). Cohen *et al.* (Cohen et al., 1999) once studied the two-viscous-fluid pinch-off and identified the universal pinch-off behavior with the viscosity ratio between internal and external fluids ($\lambda = \eta_{in} / \eta_{ex}$) ranging from 0.02 to 30. Zhang *et al.* (Zhang and Lister, 1999b) numerically investigated the capillary instability of a fluid thread in a surround fluid with $1/16 \leq \lambda \leq 16$ and proved that universal similarity scaling is effectively preserved. Here, the universal self-similarity is demonstrated for drop pinch-off in air for the range $55.56 \leq \lambda \leq 638.89$.

The viscosity of internal fluid is an important factor for drop pinch-off in air at length scale smaller than the viscous length scale $l_\eta = \eta^2 / (\sigma\rho)$ (Burton and Taborek, 2008; Shi et al., 1994). For fluids of low viscosity – water, SDS and Emkarox solutions used in this work, the viscous length scale l_η is typically of order of nanometer (out of present optical resolution) and thus they can be described as inviscid pinch-off. The value of l_η for SO 10 is several micrometers (relatively close to the present optical resolution) and usually it's called viscous pinch-off. But for the much higher viscosity like SO 50 and SO 100, the value of l_η is several hundred micrometers which are close to the order of millimeter (comparable to the nozzle diameter). Once the neck width is smaller than l_η , the viscous stresses gain weight and compete with other forces in presence. Figure I.15a and b present the sequences for SO 50 ($\lambda = 3305.56$) and SO 100 ($\lambda = 6266.67$) pinch-off in air. For the relatively lower viscosity fluid – SO 10, it was proved to be self-similar with two pinch-off points and two nearly flat surfaces. However, in Figure I.15a and b, SO 50 and SO 100 form a uniform cylinder near the singularity and then pinch off in the way of spinning which is reminiscent of the cascade structure discovered by Shi *et al.* (Shi et al., 1994). The critical thread length of the filament is found to increase with the viscosity, which was already observed in bubble pinch-off by Thoroddsen *et al.* (Thoroddsen et al., 2007). However, two major differences need to be outlined: firstly, several random pinch-off points with some bulges and separate satellite droplets; secondly, the small tails attached to the nozzle fluid and the newly-formed drop, as indicated in the blowup of Figure I.15a and b. These multiple pinch-off points as well as varying-sized satellite droplets were also observed by Henderson *et al.* (Henderson et al., 1997) in a viscous drop pinch-off.

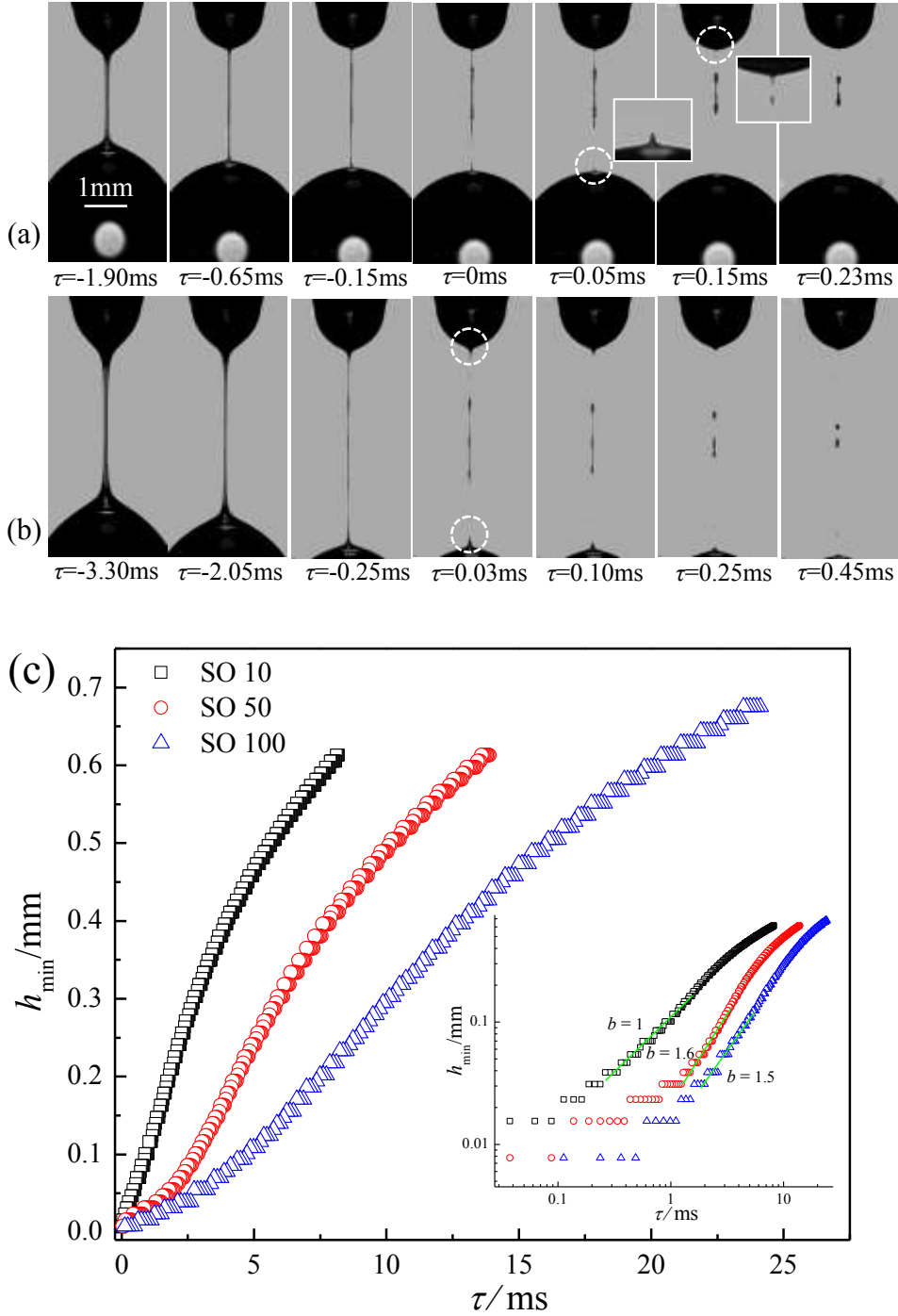


Figure I.15. Shape evolution and thinning mechanism of three kinds of silicone oils in air. (a) and (b) are sequences of SO 50 ($\lambda = 3305.56$) and SO 100 ($\lambda = 6266.67$) pinch-off in air, respectively; (c) minimum neck diameter vs. time-to-pinch-off for silicone oils.

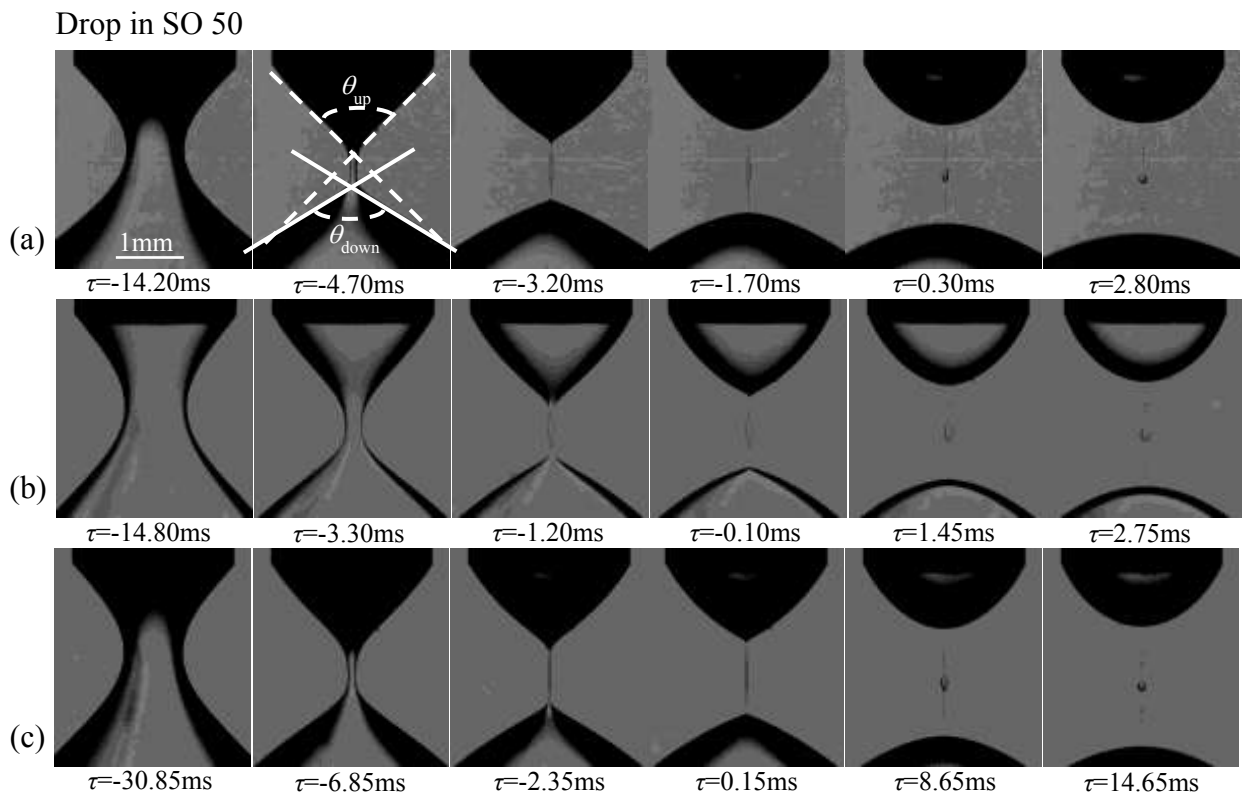
The particular shape evolution of viscous Newtonian fluids in air deserves to inquire whether it is still self-similar. Figure I.15c shows the relationship between the minimum neck diameter and time-to-pinch-off for three kinds of silicone oils pinch-off in air.

Compared to SO 10, an obvious transition can be observed in the final pinch-off region of SO 50 and SO 100, because of the long-term filament at higher viscosity. Then, the effective part in the close vicinity of pinch-off point is chosen to correlate with the scaling law, $h_{\min} \propto \tau^b$. The unity exponent of SO 10 is again observed while the larger exponent is obtained for SO 50 and SO 100. The particular exponent together with the special pinch-off shape indicates that the pinch-off dynamics of SO 50 and SO 100 deviates from the conventional self-similar pinch-off. Furthermore, we studied the pinch-off dynamics of non-Newtonian fluid – PAAm in air, and it was found that the thread evolves into a so long filament that it cannot be recorded by the camera. This increased stability of the filament is mainly due to the increased viscosity under the extensional flow (Cooper-White et al., 2002). Thus we can conclude that Newtonian fluids of higher viscosity as well as non-Newtonian fluids exhibit a non-self-similar and non-universal character owing to their spinning in the final pinch-off region.

I.4.2 Drop pinch-off in liquid

Compared to the drop pinch-off in air, the thread evolution in viscous fluids (Figure I.16) is quite different: near the detachment, the bottom of the thread first starts to thin, followed by the upper end and then both ends thin simultaneously, resulting in a bulge in the middle. With time evolution, the bulge gathers together to be ellipsoidal while the two ends of the thread gradually thin to be a needle. Once pinching off from the two ends, the thread quickly detaches again from the bulge which finally develops into a spherical and large satellite drop. The disconnected thread undergoes interfacial instabilities and then evolves into cascades of sub-satellite drops. Such kind of cascade pinch-offs was evidenced in a numerical study (Burton and Taborék, 2007), which shows the comparable shape evolution with our experiments. Intuitively, the self-similar drop pinch-off in air tends to combine the wholeness of the thread while the counterpart in viscous fluids is somewhat to divide the thread. This different behavior derives from the possible mechanisms: on the one hand much smaller viscosity ratio λ between two phases and on the other hand lower interfacial tension leading to multi-scale issues. More importantly, smooth surfaces instead of plane surfaces can be observed in the newly formed drop as well as the nozzle drop. Compared to the drop-in-air system, the highly viscous external fluid opposes a strong drag to the forming drop and hinders the pinch-off of the thread.

In addition, for a given inner drop fluid, the primary satellite drop in SO 50 is much bigger than that in SO 100. While for a given external fluid, the primary satellite drop in Emkarox aqueous solutions is found to be much bigger than that in other two solutions. It implies that the larger the viscosity ratio λ , the larger the primary satellite drop. The external fluid with a lower viscosity exerts a less viscous drag and facilitates then the satellite drop formation. While the internal fluid with a relatively higher viscosity can counteract with the external viscous drag and then grow up easily.



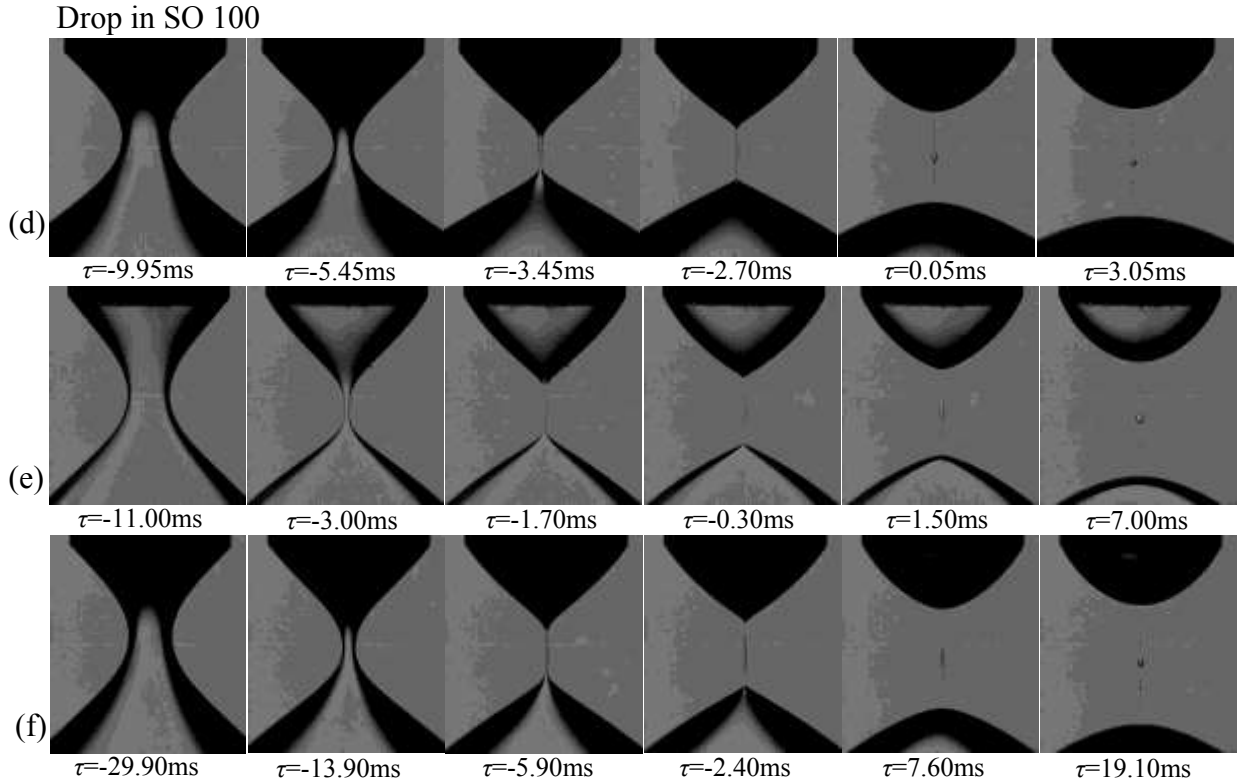


Figure I.16. Shape evolution of various aqueous drops pinching off in silicone oils. (a) Water in SO 50 ($\lambda = 0.017$); (b) 4.50 wt% Emkarox in SO 50 ($\lambda = 0.061$); (c) 0.25 wt% SDS in SO 50 ($\lambda = 0.017$); (d) Water in SO 100 ($\lambda = 0.009$); (e) 4.50 wt% Emkarox in SO 100 ($\lambda = 0.032$); (f) 0.25 wt% SDS in SO 100 ($\lambda = 0.009$). All sequences in this figure share the same scaling bar.

For the cascade of satellite drops, we estimate the area of satellite drops in the same sequence from multiplying the pixel numbers and area and plot in Figure I.17a. With time evolution ($t_1 \rightarrow t_2$), the existing satellite drops grow but the primary satellite drop remains the same. It's very difficult to quantify the size distribution of satellite drops in the mode of beads-on-string due to the instability of time and space, as well as the camera resolution. Additionally, we investigate the cone angles (shown in Figure I.16a) in the upper and bottom ends near the pinch-off point and the results are given in Figure I.17b. Obviously, the bottom cone angle (θ_{down}) is much larger than the upper one (θ_{up}) for two kinds of silicone oils. This difference of cone angle between top and bottom was also indicated by previous authors (Cohen et al., 1999). For the same internal fluid, both the upper and bottom

cone angles tend to increase with the viscosity of external fluid while for the same background fluid, they decrease with the viscosity of internal fluid.

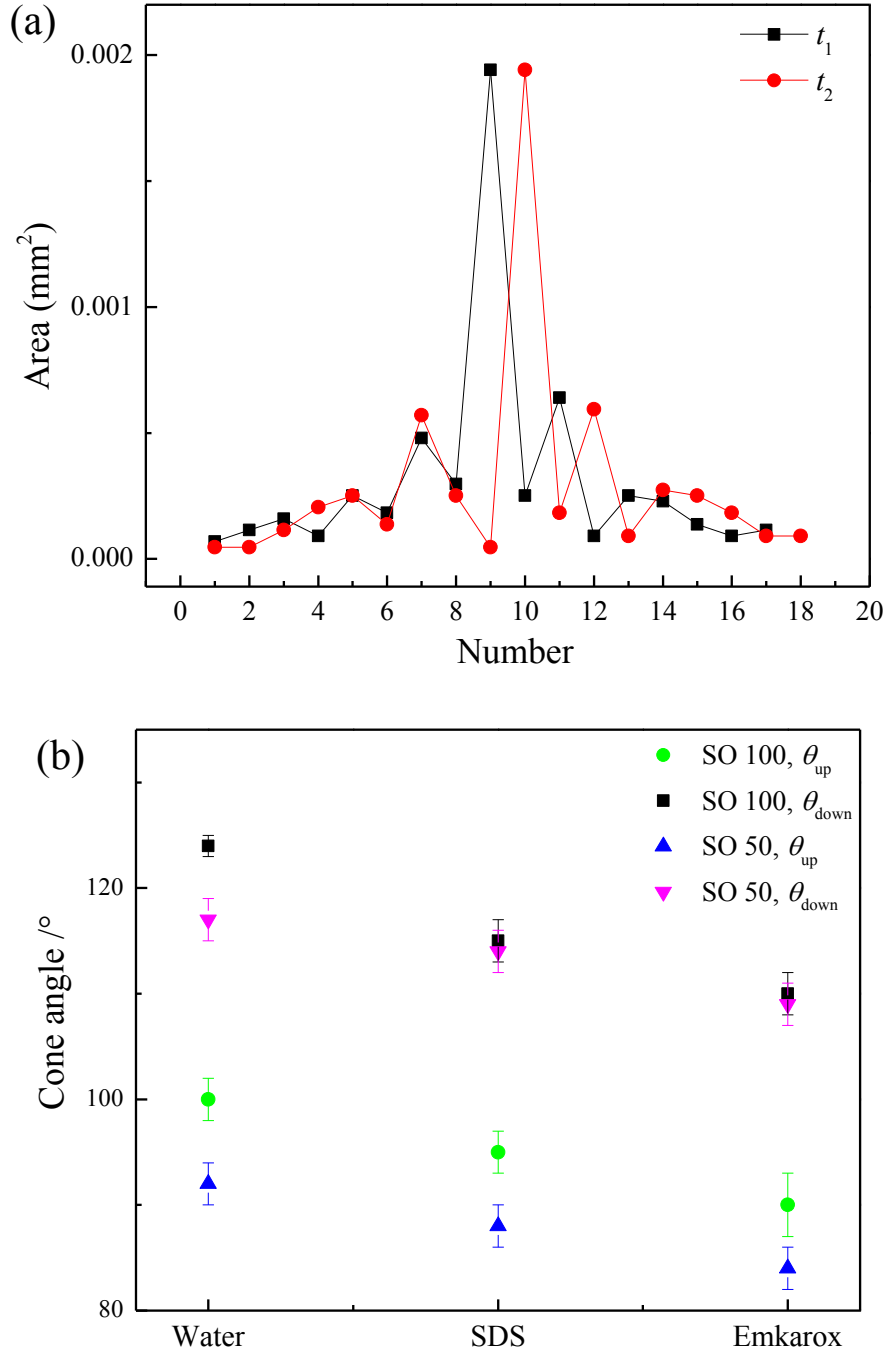
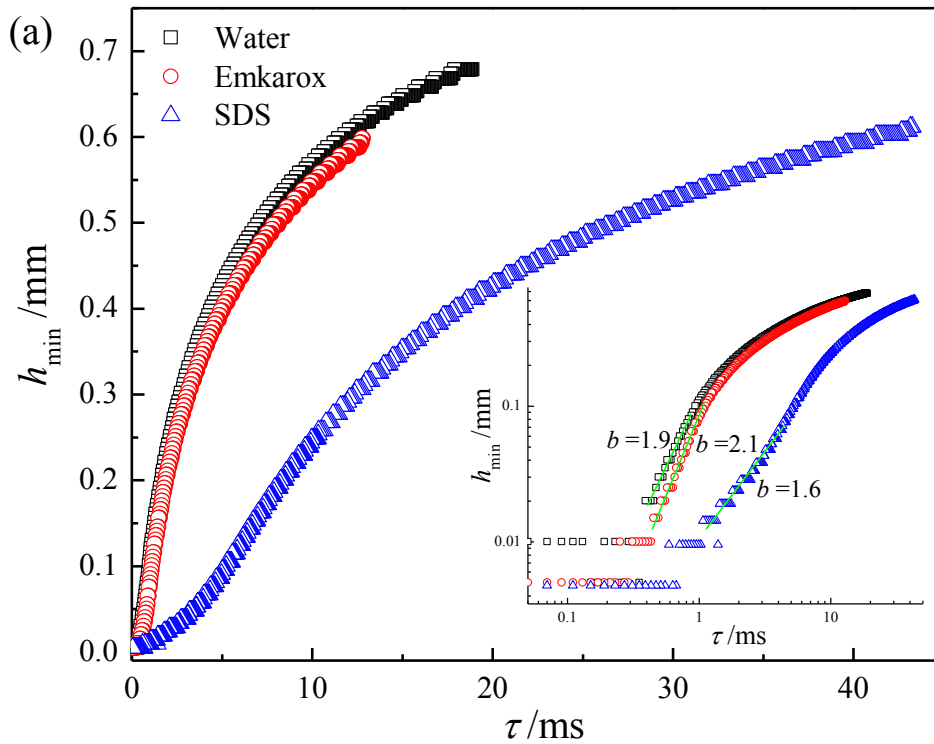


Figure I.17. (a) Area distribution of satellite drops of 0.25wt% SDS in SO 100 ($\lambda = 0.009$), $d = 0.6$ mm, $t_2 - t_1 = 0.72$ ms. Number of satellite droplets is counted from top to bottom along the thread. (b) Cone angles at upper and bottom ends near the pinch-off point.

The beads-on-string character and the smooth recoil shape of drop pinch-off in viscous fluids are quite different from that of drop pinch-off in air. Thus the power-law scaling is applied to investigate the drop pinch-off in viscous fluids and the typical results are shown Figure I.18. Obviously, the exponents are all larger than unity, implying the local spatio-temporary dynamics. This differs from the self-similar pinch-off. Firstly, compared to the drop-in-air system, the viscosity ratio λ of drop-in-liquid system is lower and the external fluid exerts a larger viscous effect on the pinch-off dynamics. Secondly, the interfacial tension of liquid-liquid system (in Table I.4) is much lower than the surface tension of liquid-gas system (in Table I.3), which enhances the interfacial instability.



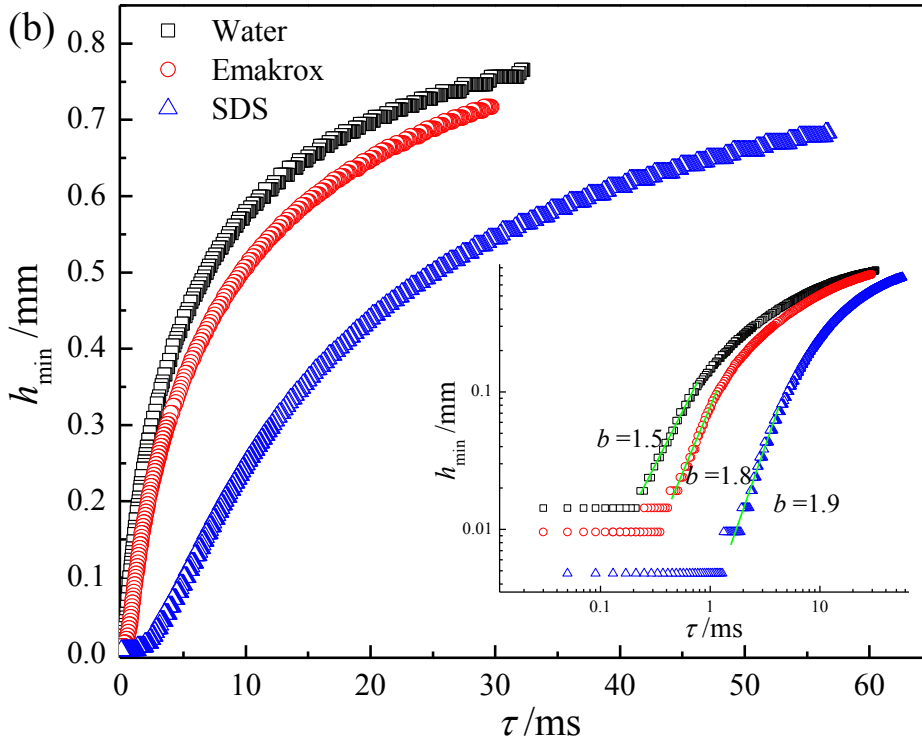


Figure I.18. Drop pinch-off of various aqueous liquids. (a) In SO 50. (b) In SO 100. Insets are the corresponding log-log plots

For the exhaustive investigation on the pinch-off mechanisms, we go further to study the drop pinch-off of a non-Newtonian fluid in viscous fluids. Figure I.19 shows the pinch-off sequence of 0.25% PAAm solution in SO 100. The neck evolves into an exceptionally long filament with beads-on-string. Also the big ‘blister’ locates at, not exactly the middle but the upper part of the filament. The small satellite drops continuously occur, especially at the lower part of the filament, but the position of the primary satellite drop almost remains the same. Similarly, it is difficult to capture the size distribution of beads on the string due to the spatio-temporary instabilities. Therefore, the shape evolution such as long-lived filament and multiple instabilities confirms that the pinch-off of a non-Newtonian drop in a viscous surrounding fluid fails to be universal and self-similar.

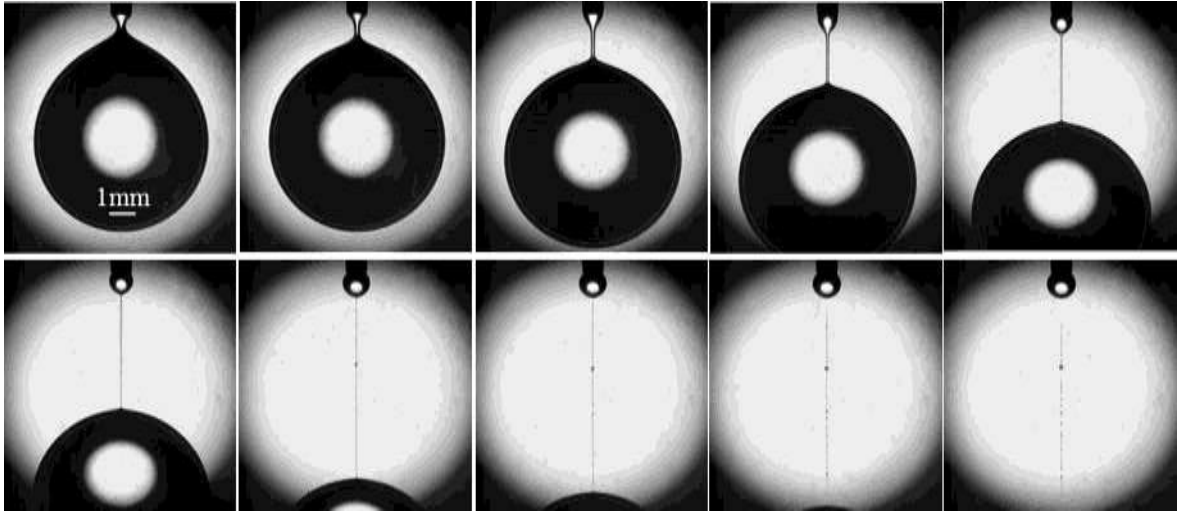


Figure I.19. Pinch-off sequence of a 0.25% PAAm drop pinch-off in SO 100, $d = 0.6$ mm. The capture times are 1.14s, 1.11s, 0.96s, 0.82s, 0.61s, 0.46s, 0.11s, 0.04s, -0.04s and -0.11s.

Until now, our experimental work demonstrates that non-Newtonian drop pinch-off deviates from the conventional universal behavior no matter in air or in viscous fluids. However, the pinch-off behavior of Newtonian fluids is significantly affected by the viscosity ratio λ . For the intermediate λ ($55.56 \leq \lambda \leq 638.89$), the drop pinch-off obeys the universal self-similar scaling law with rebounded flat surfaces and combined satellite drops, while for two extremes, $\lambda \rightarrow 0$ ($\lambda < 0.061$) and $\lambda \rightarrow \infty$ ($\lambda \geq 3305.56$), it deviates from the so-called universal self-similarity with the smooth recoiled shape and beads-on-string characteristics. In fact, these results are to some extent in a reasonable agreement with the work of Tomotika (Tomotika, 1935). Of course, fundamental mechanisms require still further investigations to explain such deviations.

I.5 Ferrofluid drop formation and pinch-off in air

I.5.1 Shape evolution

The shape evolution during the formation process reflects the interplay of various forces, especially under the conditions: no magnetic field (NM), the gravity-superimposed downward magnetic field (DM), gravity-compensated upward magnetic field (UM). Here we mainly discuss three types of shape evolution: the initial drop growing out from a nozzle, the thinning neck and the shapes after pinch-off.

I.5.1.1 Initial shapes

Figure I.20 shows several examples of ferrofluid drops in the initial quasi-steady stage of drop formation. Note that $\tau = t_0 - t$ is the remaining time defined as the difference between the breakup time t_0 and real time t . Here, we choose t_0 to be the median between the last frame before and the first frame after the detachment. The initial shape of a free drop dripping from a nozzle tends to be spherical due to the balance of surface tension and gravity (Figure I.20a). However, the presence of a downward attracting magnetic field enhances the gravity and definitely leads to a conical shape (Figure I.20c). When the magnetic force is in the opposite direction to the gravity, an upward conical shape can be formed (Figure I.20b). In contrast with the free drop falling from a nozzle, a downward magnetic field intuitively facilitates the formation process. While for the inversely growing drop, additional force is required to overcome the gravity. Figure I.20d and e show the initial shapes of upward drops under different magnetic flux densities. Compared to Figure I.20e, the exceptional long and large liquid column at $B = 39.24$ mT implies the ferrofluid struggles to grow up due to the interplay of magnetic attraction, surface tension and gravity. Magnetic force repels surface tension and gravity by attracting the fluid while surface tension and gravity counterbalance by changing the curvature (Stone et al., 1999) and accumulating larger volume, respectively. Once magnetic force surpasses surface tension and gravity, a neck occurs, thins and finally pinches off. Therefore, at relatively lower magnetic flux density, the accumulation of fluid volume is the prerequisite of generating an upward drop. In fact, there exists a threshold value of magnetic flux density below which the ferrofluid will spread on the nozzle. Our experiments revealed that $B = 39.24$ mT would approached to this threshold.

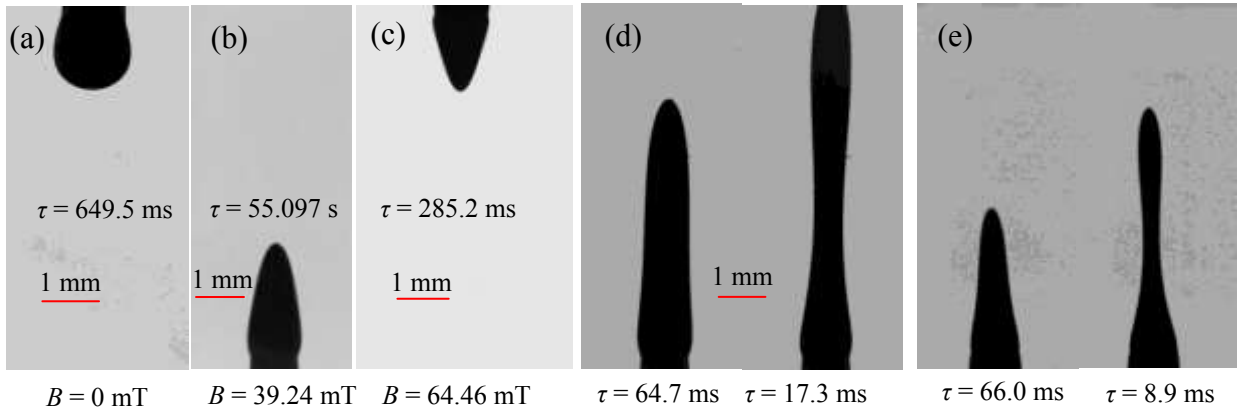


Figure I.20. Initial shapes of ferrofluid drops. (a) Without a magnetic field (NM); (b) under an upward magnetic field (UM); (c) under a downward magnetic field (DM); (d) and (e) initial growing shapes for upward ferrofluid drops at $B = 39.24$ mT and $B = 115.71$ mT, respectively. (d) and (e) share the same scaling bar.

1.5.1.2 Thinning shapes

Figure I.21a illustrates the sequences of shape evolution under NM during the breakup process. Once the gravity and inertial force overcome the surface tension, the neck appears. Immediately, the neck starts to thin and elongate into a so-called thread, connecting a nearly spherical mass of ferrofluid at the bottom and a conical mass at the nozzle end. The thread synchronously increases in axial direction and decreases in radial position until the critical pinch-off point where the lower end will be released from the thread to form a drop. Intuitively, the ferrofluid drop under NM behaves much like a water drop falling from a faucet (Shi et al., 1994).

Figure I.22b and c present the typical examples of ferrofluid drops thinning under a unidirectional magnetic field, DM and UM, respectively. Obviously, the presence of a magnetic field not only deforms the two masses connected by the thread but also significantly elongates the thread. The gravity-superimposed magnetic field (DM) adds up to the gravity and inertial force and accelerates the thinning process. However, the gravity-compensated magnetic field (UM) shown in Figure I.22c must overcome alone all other forces. That's why the magnetic flux density needed for an inversely growing drop is much higher.

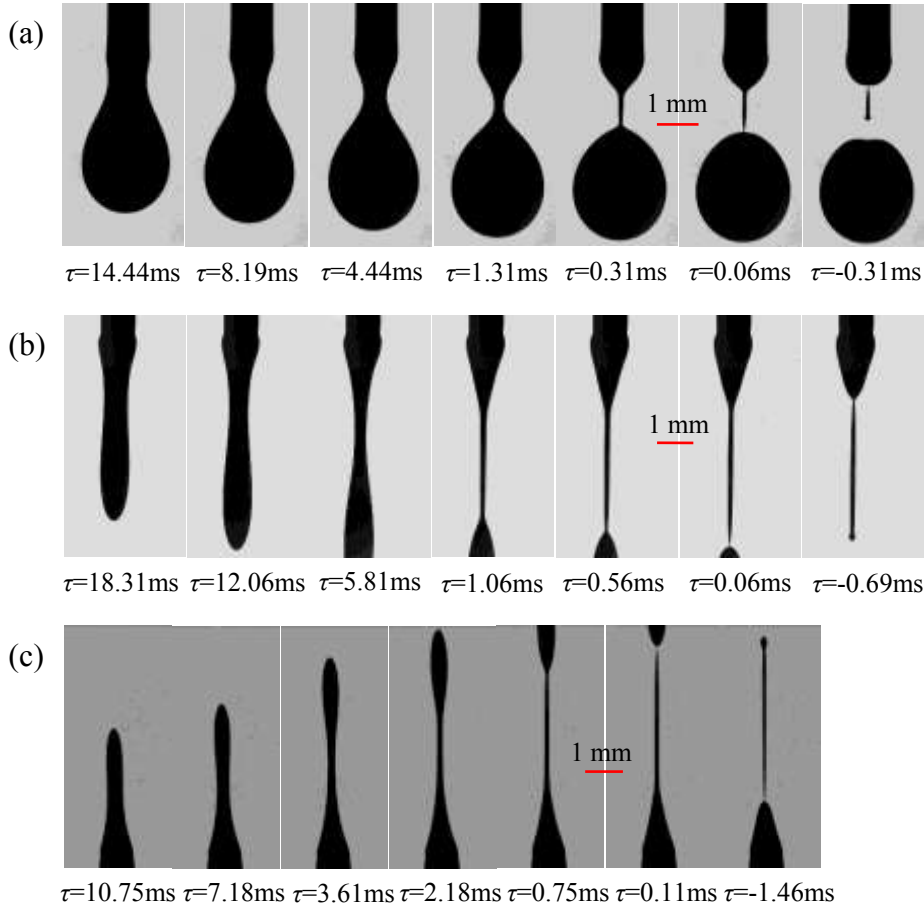


Figure I.22. Shape evolution of ferrofluid drops thinning under different conditions. (a) NM, $d = 0.6$ mm, $Q = 0.05$ mL·min⁻¹; (b) DM, $B = 29.66$ mT, $d = 0.6$ mm, $Q = 0.05$ mL·min⁻¹; (c) UM, $B = 115.71$ mT, $d = 0.6$ mm, $Q = 0.001$ mL·min⁻¹.

For the downward drop (DM or NM), the thread always detaches first from the emerging drop and then from the nozzle, accompanying usually by satellite drops. While for the upward drop (UM), the primary pinch-off point occurs in the upper end and a secondary instability at the bottom follows immediately. In practice, with respect to the breakup point, different results were reported by other authors due to the difference stemming from experimental systems used. Copper-White *et al.* (Cooper-White et al., 2002) and Yildirim and Basaran (Yildirim and Basaran, 2006) reported the rapid appearance of the lower snap-off and subsequent upper pinch-off for non-Newtonian fluids. Lee *et al.* (Lee et al., 2006) observed that the breakup of the liquid bridge occurred first at the upper end in a AC electrical field.

Furthermore, it can be found that the cone angle far from magnetic field more or less remains constant in the neighborhood of singularity due to the attraction of magnetic force. Figure I.23 shows the cone angle (θ_a) vs. the magnetic flux density (B). θ_a decreases with the increasing flowrate and increases with the increasing nozzle diameter. When B below 40 mT, θ_a decreases sharply, and beyond 40 mT it decreases slowly until a constant value ($\theta_a \approx 25^\circ$), which is quite different from the Taylor cone (98.6°) (Taylor, 1964) under an intense electric field and the small angle (36.2°) measured by Day *et al.* (Day *et al.*, 1998) for inviscid pinch-off of a liquid drop in air.

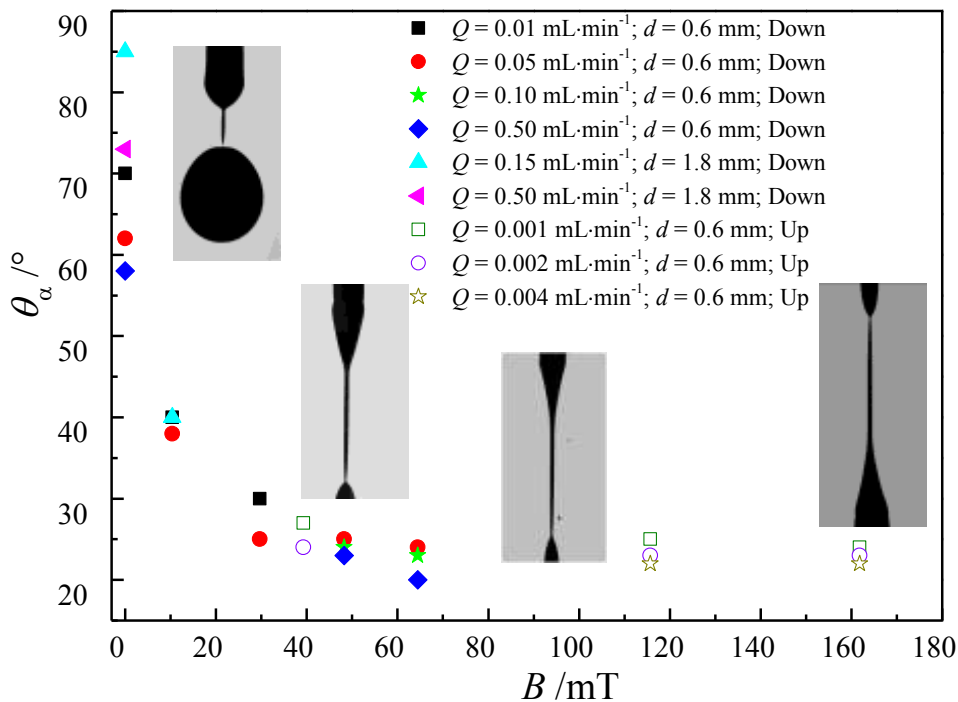


Figure I.23. The cone angle vs. the magnetic flux density for ferrofluid drops. Note that the cone angles were measured from the far end connected to the nozzle with almost the same time-to-pinch-off.

I.5.1.3 Formed shapes

Figure I.24 presents the shape evolution of the newly formed drop as well as satellite drops under various conditions. Due to the strong magnetic flux density for the upward growing drops, i.e. close distance between the glass tank and the nozzle, the newly formed drop and the satellite drops are very difficult to capture. Thus here we mainly discuss the primary drop and satellite drops under NM and DM.

In Figure I.24a, after the first pinch-off, the individual primary drop is formed and the top of which takes on a flat surface due to the instantaneous release of the surface energy. With time, the flat surface disappears and the newly formed drop undergoes several shape oscillations before reaching a nearly spherical shape. In contrast, the presence of a magnetic field shows a cushion effect on the detached drop so that no flat surface can be observed in Figure I.24d. More interestingly, the primary drop in Figure I.24d descends with a stable ellipsoidal shape without any distinct deformation. This discrepancy may be resulted from the fact that magnetic force can stabilize the primary drop by dampening the oscillations of the primary drop. Stone *et al.* (Stone et al., 1999) have adopted the slender-body theory to determine the static shape of conically ended dielectric drops under an electric field and indicated that the shape of interface is governed by the balance between interfacial tension stresses and Maxwell electric stresses.

The common features of satellite drop formation in Figure I.24a, b, c and e are as follows: two satellite drops connected by the thread first get close to each other and converge into one drop, then the combined drop oscillates towards a spherical (Figure I.24a & b) or ellipsoidal (Figure I.24c & e) shape. When the magnetic flux density is small (Figure I.22b), the satellite drop remains a spherical shape like the counterpart without a magnetic field. Interestingly, the filament in Figure I.24e behaves like a string of pearls and then produces several satellite drops. However, it can be easily found that the motion trajectory of satellite drops differs significantly between NM and DM. The converged satellite drop in Figure I.24a first rises up to touch the drop attached to the nozzle and then descends; whilst the satellite drops in Figure I.24b, c and e fall down directly without any bouncing up. In summary, the stronger magnetic flux density deforms the satellite drop more significantly and generates consecutively more satellite drops, as well as changes the motion trajectory of satellite drops.

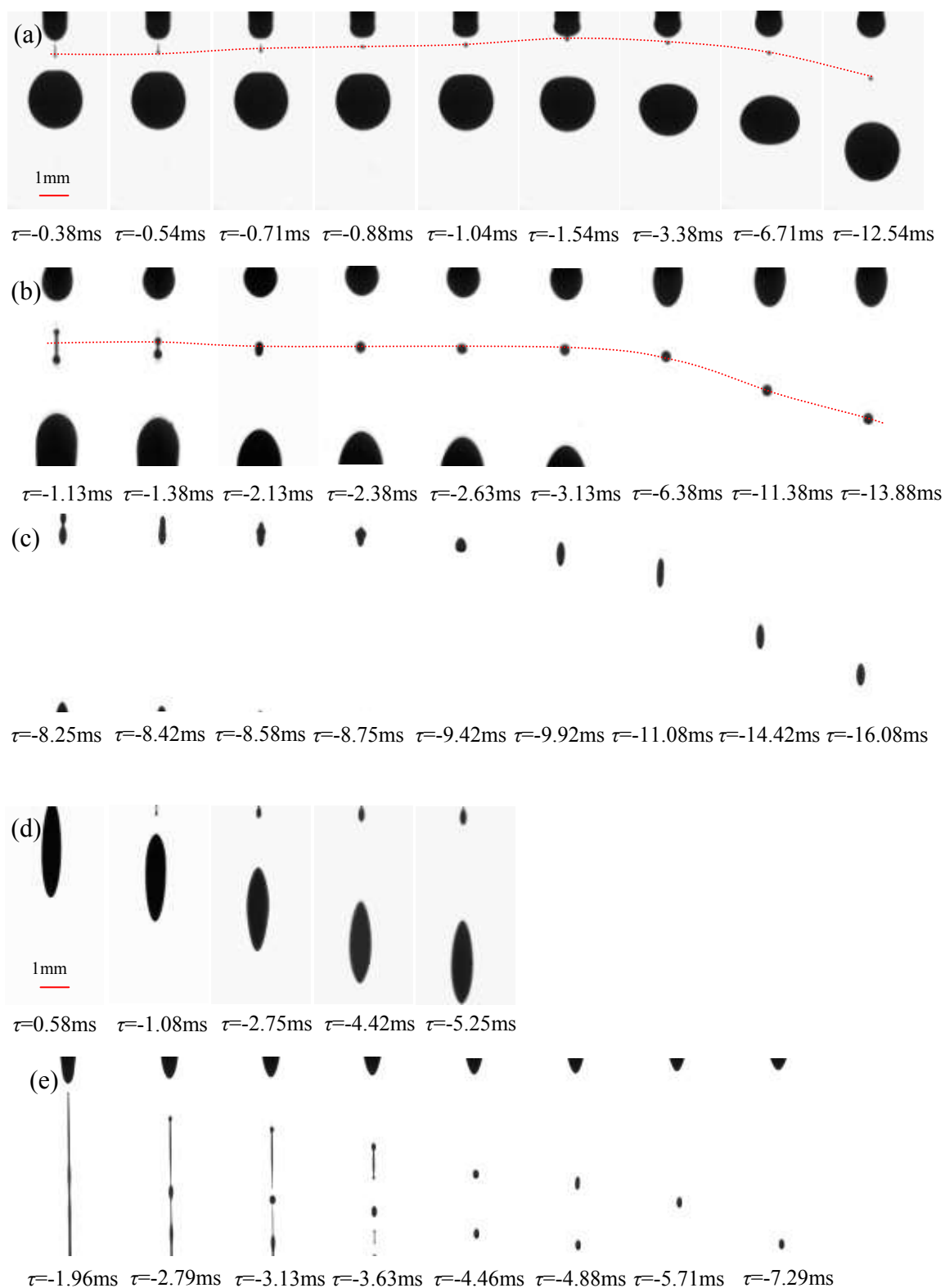


Figure I.24. Shape evolution of primary drops and satellite drops. (a) Primary and satellite drops, $B = 0$ mT, $Q = 0.5$ mL \cdot min $^{-1}$; (b) satellite drops, $B = 10.36$ mT, $Q = 0.5$ mL \cdot min $^{-1}$; (c) satellite drops, $B = 30.99$ mT, $Q = 0.5$ mL \cdot min $^{-1}$; (d) primary drops, $B = 30.99$ mT, $Q = 0.5$ mL \cdot min $^{-1}$; (e) satellite drops, $B = 64.46$ mT, $Q = 0.5$ mL \cdot min $^{-1}$. The same scaling bar applies everywhere.

I.5.2 Formation volume and frequency

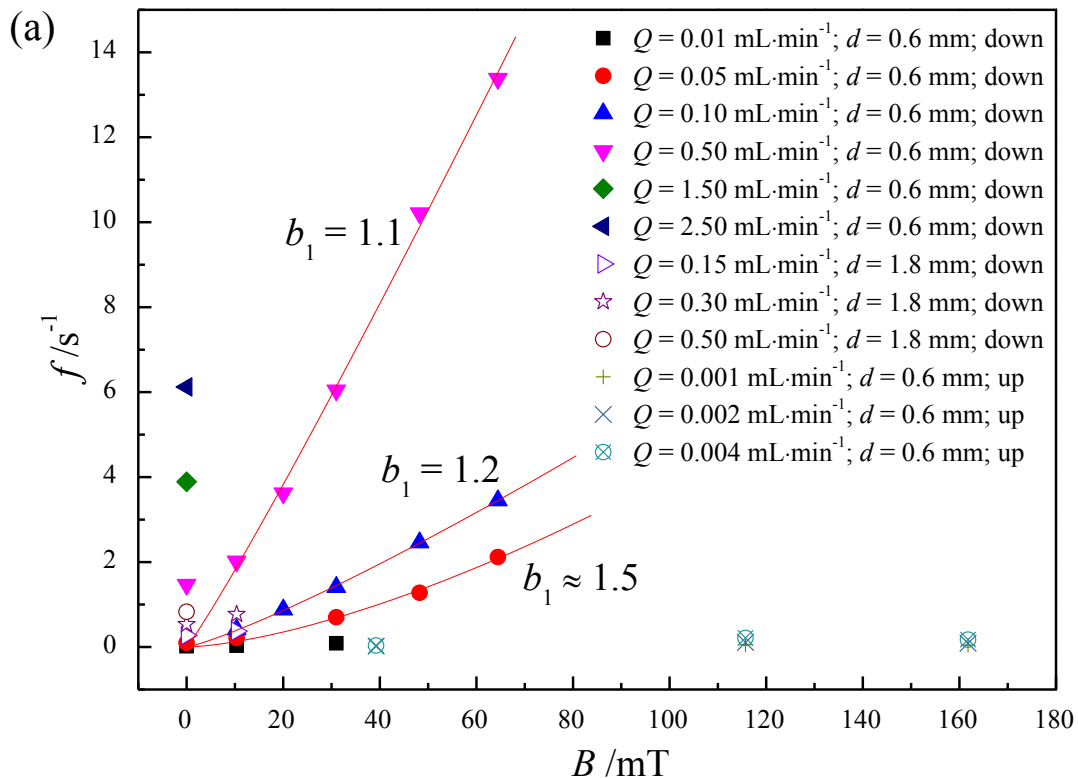
In order to quantify the effect of fluid flowrate and magnetic flux density on the drop formation, the frequency (f) and dimensionless drop volume (V/d^3) were calculated and displayed in Figure I.25.

As expected, the drop volume and formation frequency increase with flowrate, while the drop volume decreases and formation frequency increases with the magnetic flux density. At $Q = 0.5$ mL/min, the drop volume under $B = 64.46$ mT decreases by nearly 90% and the corresponding frequency is about 9 times faster compared to its counterpart without a magnetic field. From Figure I.25a and I.25b, power laws could be proposed to describe the frequency and the dimensionless volume, respectively,

$$f = a_1 \times B^{b_1} \quad (\text{I.6})$$

$$\frac{V}{d^3} = a_2 \times B^{b_2} \quad (\text{I.7})$$

Here, a_1 , a_2 , b_1 and b_2 are fitting parameters. When flowrate equals 0.05 mL/min, 0.10 mL/min and 0.50 mL/min, the corresponding values of (a_1, b_1) are (0.00, 1.51), (0.02, 1.19) and (0.15, 1.08); the corresponding values of (a_2, b_2) are (0.27, -1.15), (0.27, -1.15) and (0.20, -1.00), respectively.



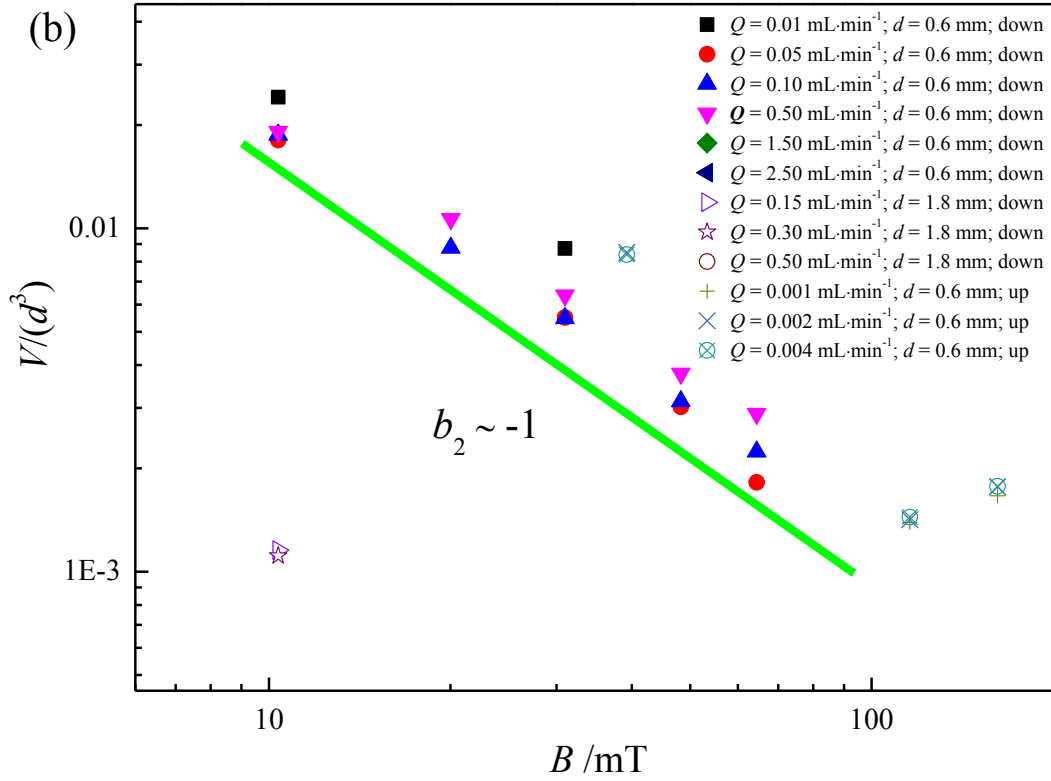


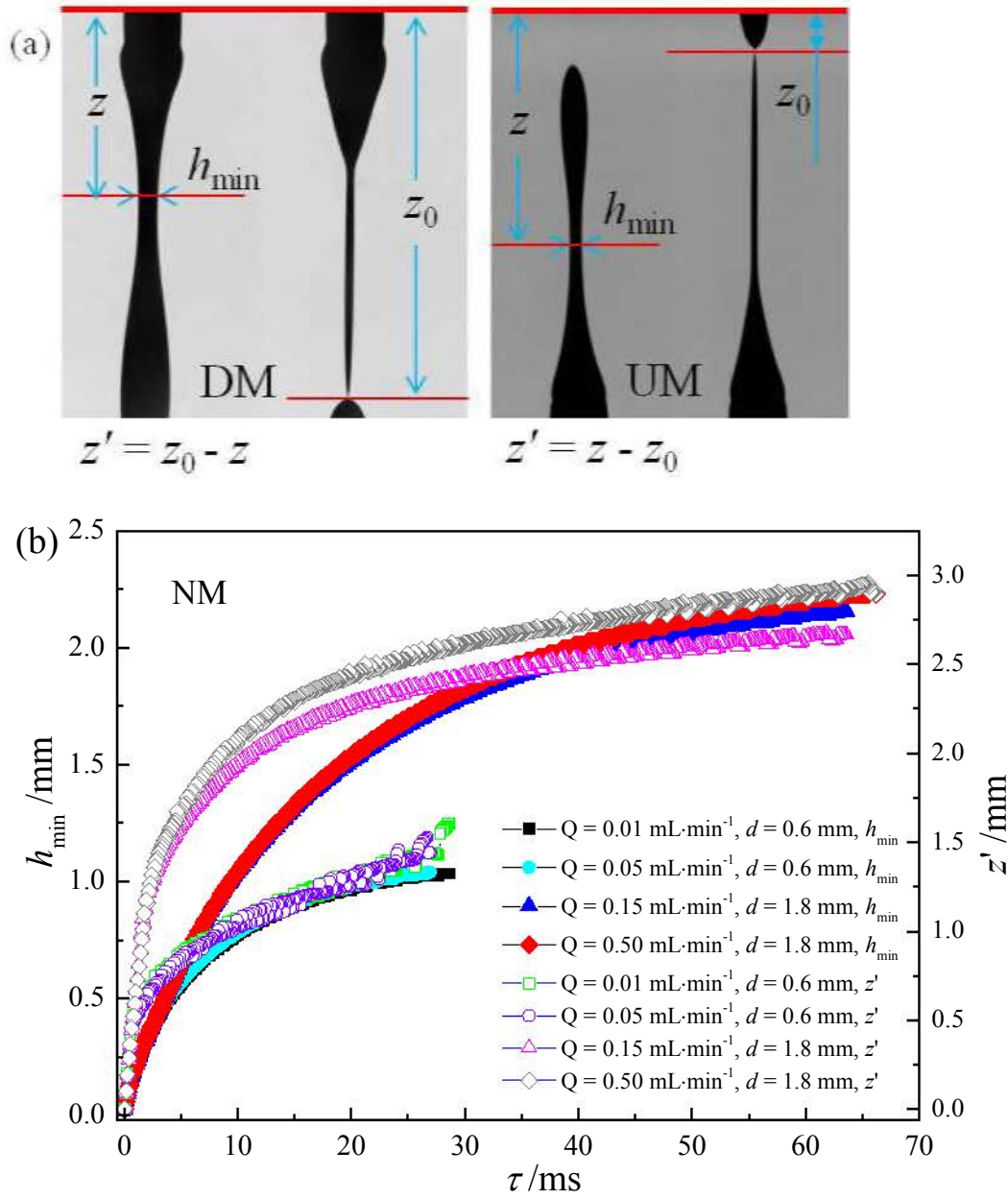
Figure I.25. (a) Frequency and (b) dimensionless volume of ferrofluid drop formation.

I.5.3 Breakup mechanism of neck

I.5.3.1 Self-similar breakup

Firstly, several examples of the minimum neck diameter h_{\min} and corresponding relative neck position z' indicated in Figure I.26a, as a function of time-to-pinch-off τ are plotted in Figure I.26.

No matter for NM, DM and UM, the flowrate and nozzle diameter only affect the initial stage of the horizontal and vertical neck evolution. The lower flowrate displays a negligible effect. Under the same magnetic flux density, both the neck minimum diameter and relative position converge rapidly into a unique curve in the immediate vicinity of pinch-off point, in spite of the initial conditions.



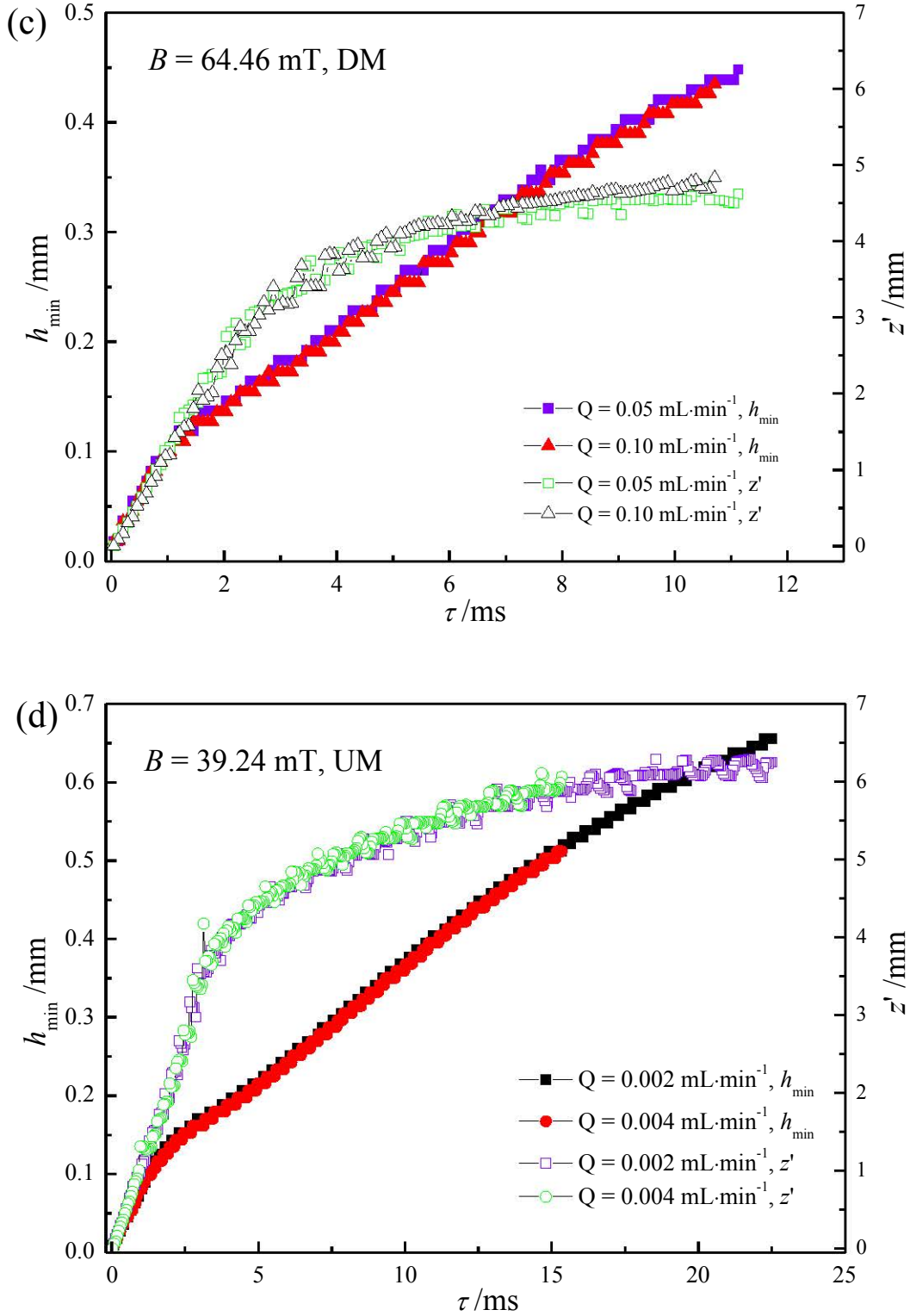


Figure I.26. Minimum neck diameter and corresponding relative position vs. time-to-pinch-off. (a) Relative position; (b) NM, $d = 0.6$ (or 1.8) mm; (c) DM, $B = 64.46$ mT, $d = 0.6$ mm; (d) UM, $B = 39.24$ mT, $d = 0.6$ mm.

1.5.3.2 Minimum neck diameter

Previous works in the literature focusing on the drop breakup mechanism reveal that there exist two, three or even four regimes during the neck evolution, depending on fluid properties (Lister and Stone, 1998a). In the absence of a magnetic field (Figure I.26b), the breakup of ferrofluid drop resembles the common water drop and exhibits three distinct regimes: linear regime, transient regime and final self-similar pinch-off regime. However, the application of magnetic field significantly shortens the duration of transient regime and prolongs the linear regime regardless of the direction of magnetic field (see Figure I.26c and d). This can be argued that for DM, the gravity superimposed by magnetic force definitely accelerates the transient regime, while for UM, the magnetic force is still large enough to overcome the gravity and to shorten the transient regime. In fact, the long-term linear regime occurs when the magnetic flux density is approximately larger than 20 mT for downward drops, below which the linear regime is replaced partially by the transient regime.

The minimum neck diameter h_{\min} vs. time-to-pinch-off τ for the primary pinch-off is plotted in Figure I.27. A scaling law $h_{\min} = a\tau^b$ was applied to correlate the radial neck evolution in the last stage. The inset in Figure I.27a indicates that under $B = 10.38$ mT, the exponent b is 0.78 for different nozzle diameters and flowrates. The exponent b remains 0.80 for DM and 0.79 for UM (Figure I.27b). In fact, the exponent b in our experiments are within the range of (0.70 – 0.80) for the primary pinch-off, regardless of the initial conditions. These results seem to indicate that ferrofluid drops exhibit a universal self-similar pinch-off behavior and the direction of magnetic field exerts only a negligible effect on this exponent. Compared to the classical $b = 2/3$ or 1, the discrepancy maybe stems from a dual compromise between the number of images with a high image acquisition and the limited resolution of these images when the thread undergoes in particular below 50 μm .

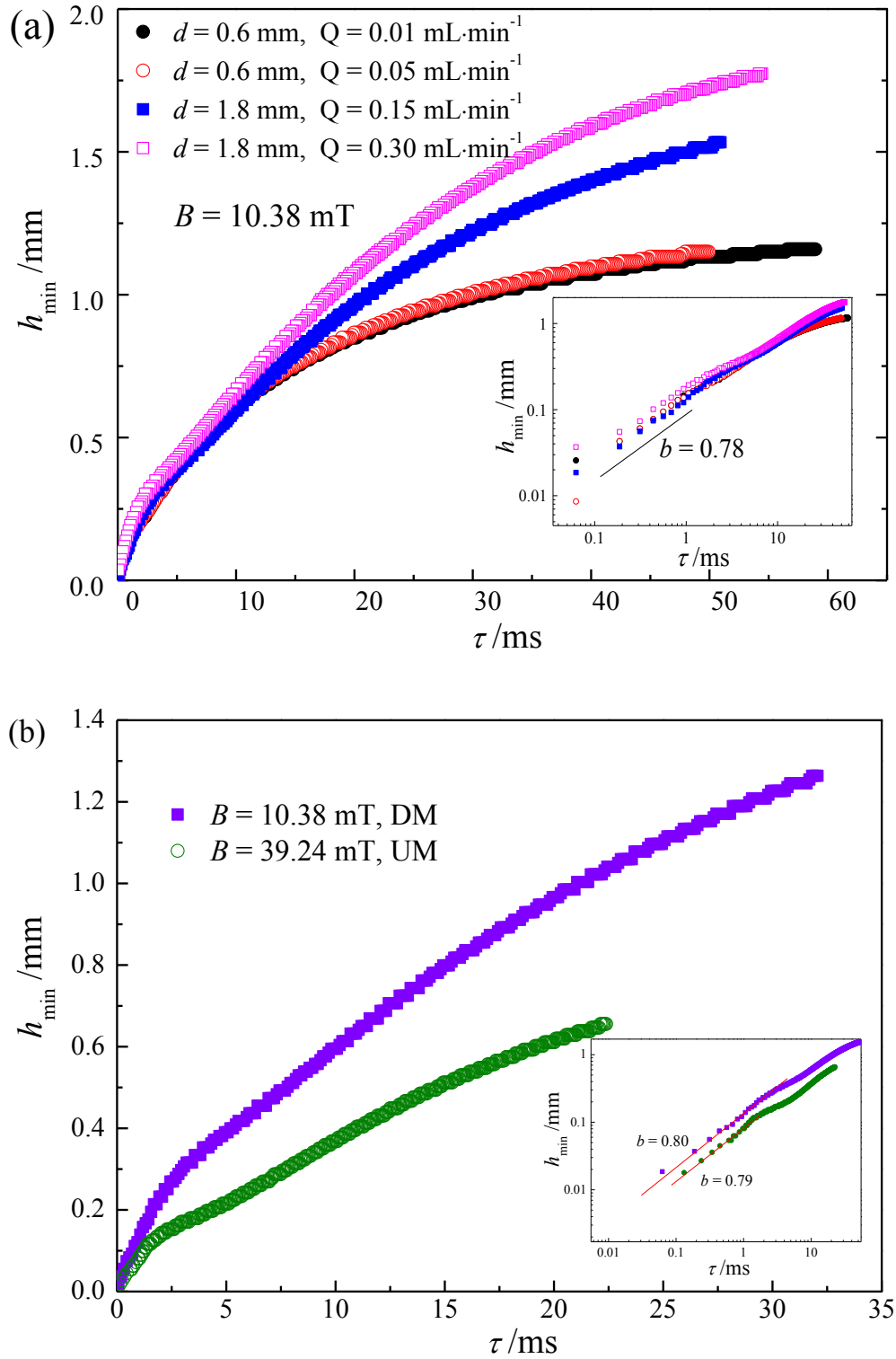


Figure I.27. Pinch-off mechanism. (a) Plots of h_{\min} vs. τ for ferrofluid drops pinch-off under DM; (b) plots of h_{\min} vs. τ for ferrofluid drops pinch-off under DM ($Q = 0.01 \text{ mL}\cdot\text{min}^{-1}$) and UM ($Q = 0.002 \text{ mL}\cdot\text{min}^{-1}$). The inset of (a) and (b) are log-log plots.

Over the past few years, emphasis was given to the primary pinch-off process. But the knowledge about the secondary pinch-off process seems to be a little bit blank. A stable phenomenon of two pinch-off points appears for all the cases investigated in our work with the occurrence of satellite drops. Thus, we here go further to compare the two singularities and obtain some instructive results. Figure I.28a and b show the secondary pinch-off process of downward and upward drops, respectively. No matter UM or DM, the end of the thread which firstly undergoes a pinch-off will rebound to be toroidal whose size increases with the second pinch-off. Surprisingly, the secondary pinch-off point starts to thin before the end of the primary pinch-off shown in Figure I.28a whilst the reverse could be observed in Figure I.28b. This non-synchronization in timing for downward and upward drops is presumably caused by the gravity-superimposed or gravity-compensated effect. In the literature (Burton et al., 2004, 2007; Chen et al., 2002; Henderson et al., 1997; Whitney, 2013), it was reported that the exponent could depend on the choice of the breakup time. In this work, the breakup time was systematically chosen as the median between the last frame before and the first frame after detachment. Owing to the high-speed camera employed, this choice induced negligible error. The main errors shown in Figure I.28c stem from two resources: one hand, the spatial resolution of the visualization system including the camera and image analyses according to the calibration; on the other hand the experimental deviation as every pinch-off point was based on 15 to 20 repetitions.

Similarly, the power law $h'_{\min} = a\tau^b$ was applied to scale the secondary pinch-off process, here h'_{\min} is the minimum neck diameter (seen the notes in Figure I.28a and b) and τ' is the remaining time, both corresponding to the secondary pinch-off point. The results together with the primary pinch-off are summarized in Figure I.28c. Only marginal difference exists between the primary and secondary pinch-off processes for the parameter a . With the increasing magnetic flux density, a first undergoes a decrease from 0.2 mm.s^{-b} to 0.1 mm.s^{-b} and then reaches a constant value 0.1 mm.s^{-b}. With respect to the exponent b , a bifurcation can be seen from the double pinch-off processes: 0.70 - 0.80 for the primary pinch-off while 0.60 - 0.70 for the secondary pinch-off. The lower value of exponent b for the secondary pinch-off could probably be attributed to the smaller volume of the thread compared to the newly formed drop, and especially to the compression effect as a spring following the primary pinch-off.

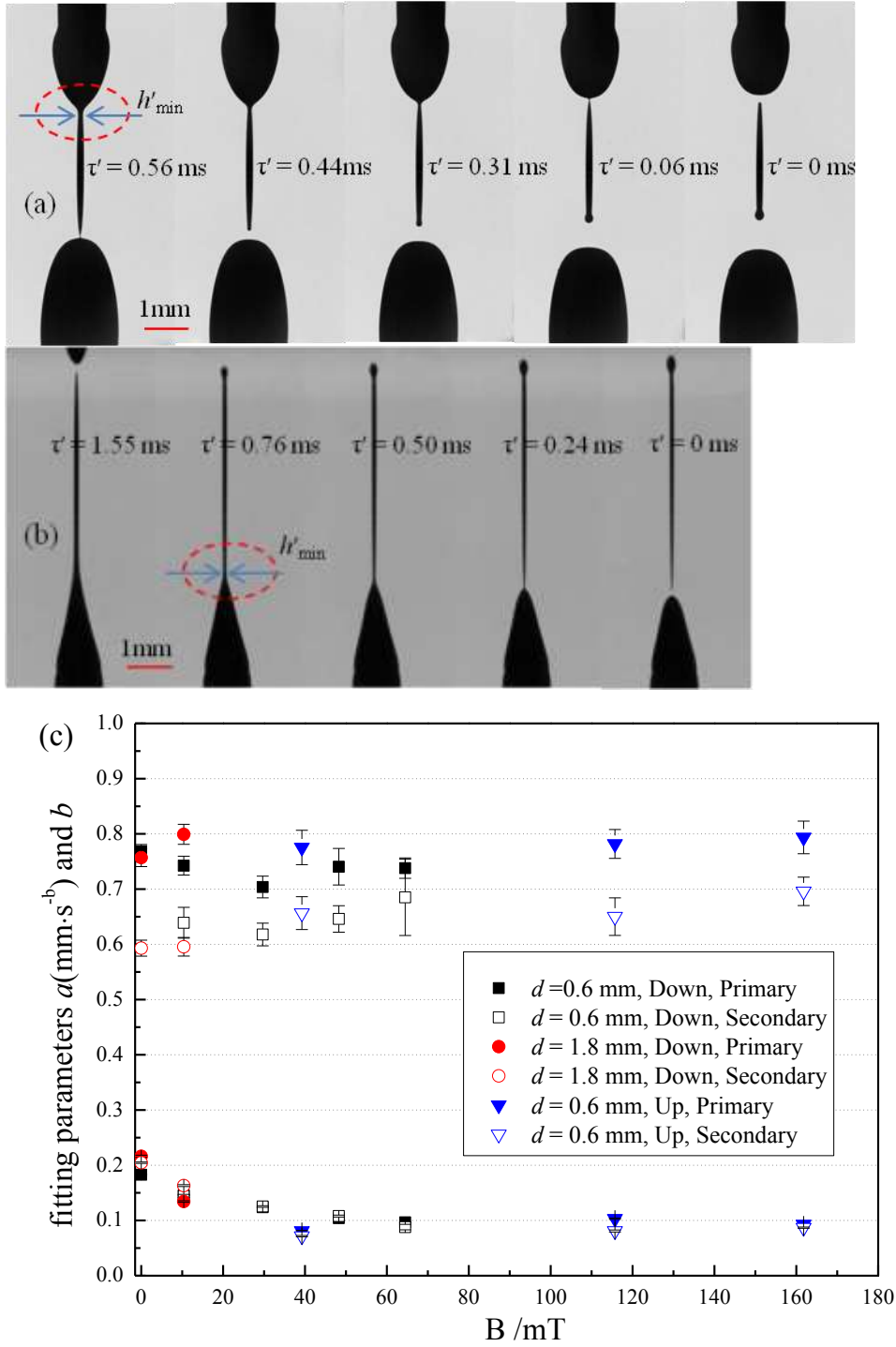


Figure I.28. (Color online). Sequences of secondary pinch-off under DM (a) and UM (b), respectively; (c) plot of the fitting parameters vs. the magnetic flux density B . The parameter a depends on the choice of the unity while the exponent b is dimensionless and characterizes the pinch-off mechanism. Here, ‘Primary’ and ‘Secondary’ mean the primary and secondary pinch-off process, respectively.

1.5.3.3 Relative neck position

The corresponding neck position can reflect the axial motion. Thus the relative neck position z' vs. the remaining time τ is plotted in Figure I.29.

A transition can also be observed in Figure I.29 no matter for NM, DM and UM. Interestingly, the initial relative position in Figure I.29a increases with the magnetic flux density while the reverse is true for that in Figure I.29b. Normally, the larger the magnetic flux density, the larger the initial relative position. The special trend in Figure I.29b mainly derives from the competition between the magnetic force and gravity which we have discussed in the previous part. Furthermore, in Figure I.29a, the initial relative position under $B = 64.46$ mT and $B = 48.25$ mT is almost superposed. This is probably due to the saturation point of magnetic field flux above which the thread can no longer be elongated.

The similar power-law ($z' = a' \times \tau^{b'}$) can be employed to correlate the relative position (z') approaching to the pinch-off point. Basically, the exponent b' remains unity for all the cases investigated. Compared to h_{\min} , the exponent in the axial direction is a little bit larger than the counterpart in the radial direction, indicating that the vertical elongating velocity is higher than the horizontal thinning velocity. The similar result was once observed for microbubbles pinching off in the flow-focusing device (van Hoeve et al., 2011).

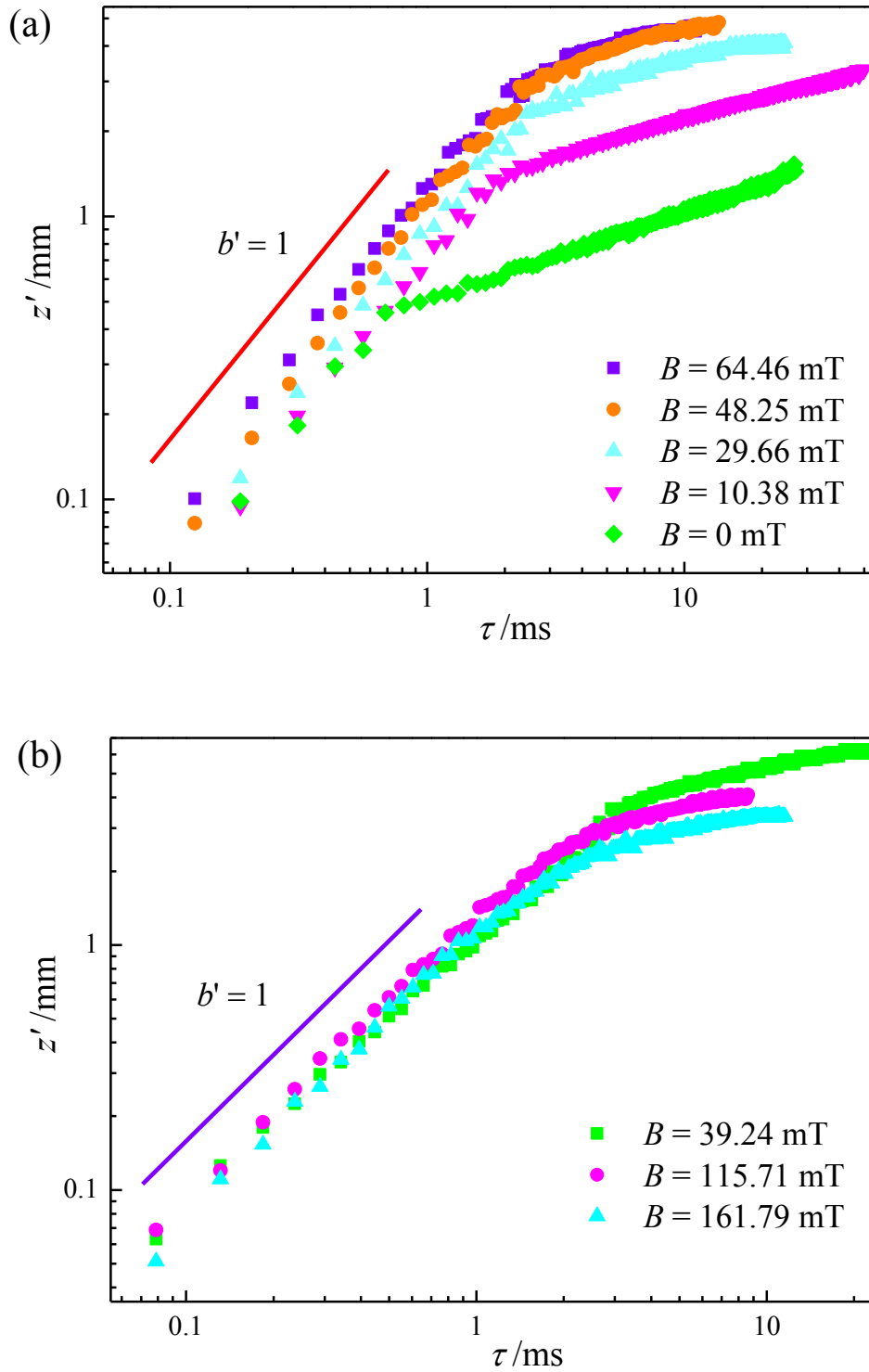


Figure I.29. Relative position of ferrofluid drops. (a) Plot of z' vs. τ for downward-growing drops, $d = 0.6$ mm, $Q = 0.05$ mL \cdot min $^{-1}$; (b) plot of z' vs. τ for upward-growing drops, $d = 0.6$ mm, $Q = 0.002$ mL \cdot min $^{-1}$.

I.6 Droplet pinch-off at microscale

The previous sections focus on the bubble or drop pinch-off dynamics at macroscale, considering the fluid properties and gravity-compensated (gravity-superimposed) effect. Now our attention moves to the droplet pinch-off at microscale. For one thing, drop pinch-off at macroscale is in the direction of gravity while that at microscale is horizontal and the gravity is negligible. For another, the multi-scale investigation is required for further understanding the pinch-off dynamics.

I.6.1 Breakup dynamics of liquid thread

When two immiscible fluids encounter at the intersection, the dispersed phase firstly undergoes the expansion stage in both axial and radial direction and the continuous phase converges to flow into the main channel, due to the inertial force. The dispersed phase grows and elongates until the occurrence of a concave curvature. Since then, a liquid neck forms due to the competition between inertial force, shear stress and interfacial tension between the continuous and dispersed phases. The liquid neck of the dispersed phase keeps narrowing and the curvature increases. Gradually, the water neck evolves into a thread whose width is distinctively smaller than the channel width. At this time, viscous force and shear stress at interface gain progressively weight in the force competition. Finally, the liquid thread pinches off and forms several satellite droplets. The pinch-off behavior of dispersed phase at two flowrate ratios is illustrated in Figure I.30. And it was found that the pinch-off point occurs first at the downstream and then upstream.

The water neck at $Q_c/Q_d = 1.25$ (Figure I.30a) locates at the edge of the intersection. While in Figure I.30b, the water neck enters into the downstream main channel. And the left part of the water neck at $Q_c/Q_d = 1.25$ is conical compared to the smooth surface at $Q_c/Q_d = 2.67$. The above two characteristics are derived from the interaction between the continuous and dispersed phases. When the flowrate ratio is much higher, the thinning effect from the continuous phase is naturally stronger, and vice versa. The thin and elongated water thread in the vicinity of pinch-off point is reminiscent of the detachment of a viscous drops in air or in another inviscid and immiscible fluid (Henderson et al., 1997; Miskin and Jaeger, 2012).

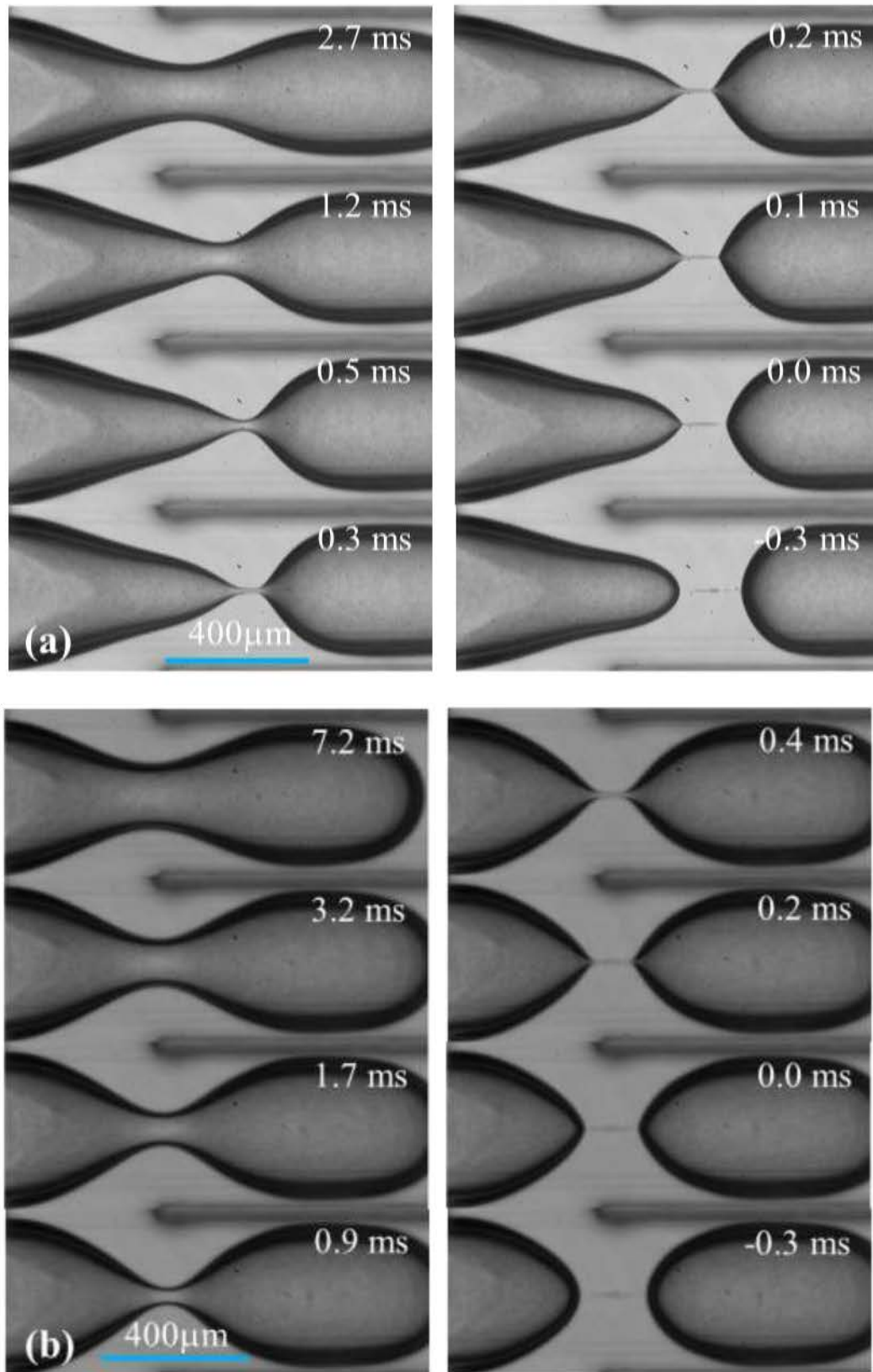


Figure I.30. Pinch-off at two flowrate ratios. (a) $Q_c/Q_d = (15 \text{ mL}\cdot\text{hr}^{-1}) / (12 \text{ mL}\cdot\text{hr}^{-1}) = 1.25$; (b) $Q_c/Q_d = (4 \text{ mL}\cdot\text{hr}^{-1}) / (1.5 \text{ mL}\cdot\text{hr}^{-1}) = 2.67$.

With regard to the scaling law $h_{\min} \propto \tau^b$, the minimum neck diameter recorded by the high-speed camera at macroscale can reach as low as $\sim 20 \mu\text{m}$. However, in microchannel, the traceable diameter could be lowered to $\sim 1 \mu\text{m}$, with the help of the microscopic magnification. More importantly, the gravity can be neglected in microchannel. Thus it is necessary to verify the scaling law of drop pinch-off at microscale. Figure I.31 presents the minimum neck diameter h_{\min} as a function of time-to-pinch-off τ . The definition of h_{\min} and τ is the same with the previous section I2, I3 and I4 at microscale. The thinning process can be divided into three stages. When $h_{\min} > 0.15 \text{ mm}$, the liquid neck of dispersed phase is relatively large and the thinning process is mainly controlled by the continuous phase (Fu et al., 2012a). When $h_{\min} \sim (0.08 - 0.15) \text{ mm}$, the interface curvature increases and the capillary pressure which scales as σ/h_{\min} plays a dominant role during this thinning stage (Lu et al., 2013, 2014; Wu et al., 2013). Through this transitional stage, the water neck thins rapidly and enters the final pinch-off region. In fact, the capillary pressure will give way to the viscous force when the neck minimum width is smaller than the viscous length scale L_{μ} ($\mu_c \mu_d / \rho \sigma = 11.8 \mu\text{m}$) proposed by Lister and Stone (Lister and Stone, 1998a). Thus in the final pinch-off stage, the viscous force becomes increasingly important. During the slow thinning period, the exponent b is 0.43 and 0.35 for low and high flowrate ratio, respectively, as shown in Figure I.31. This implies that the thinning dynamics is affected by the initial condition – flowrate ratio. In fact, Fu *et al.* (Fu et al., 2012b) showed that the exponent (0.32 – 0.72) is dependent of the conditions of the continuous phase. However, the final pinch-off stage in our experiments exhibits an exponent of unity, which is reminiscent of the viscous drop pinch-off from a nozzle in air at microscale. The unity exponent might confirm the important effect of viscous force in the final pinch-off stage. With regard to the exponent transition from 0.43 or 0.35 to unity, similar results can be evidenced in microbubble pinch-off. Van Hoeve *et al.* (van Hoeve et al., 2011) investigated the microbubble pinch-off in a flow-focusing device and observed that at first, the neck collapses with a scaling exponent of 1/3; in the final stage, the pinch-off is characterized by a scaling exponent of 2/5. While Lu *et al.* (Lu et al., 2014) argued that the pinch-off exponent evaluated from initially 1/3 to eventually 1/2 through observing Taylor bubble in microfluidic flow-focusing device.

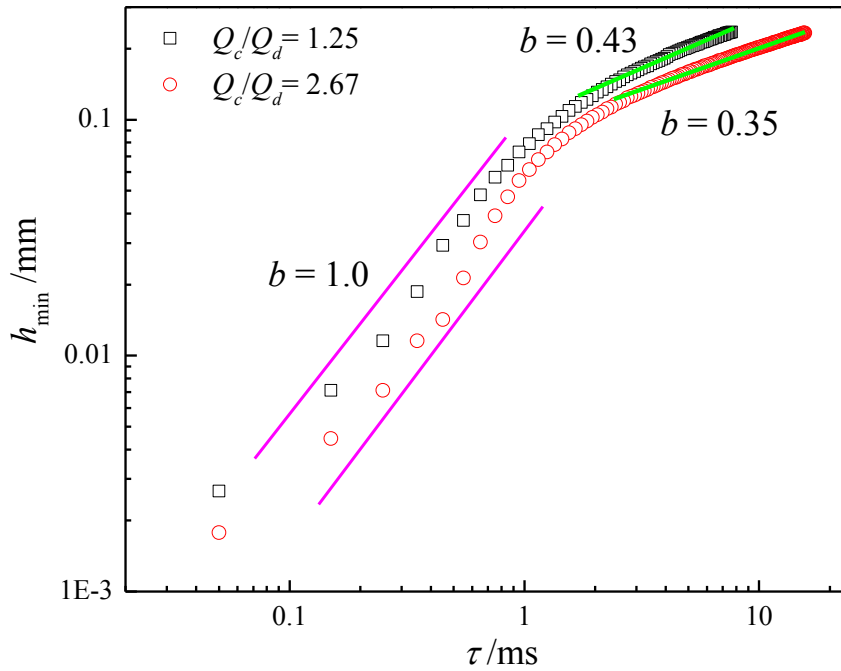


Figure I.31. Log-log plot of minimum neck diameter vs. time-to-pinch-off for two flowrate ratios at microscale.

I.6.2 Velocity distribution in the liquid neck

Though, drop pinch-off is scaled down to micrometers and the new exponent of unity is obtained through magnified visualization in micro-channel. The inner velocity field and the instantaneous and local fluid flow, especially near the pinch-off point are still scarce. There are several studies investigated the flow field in microchannel (Cheung and Qiu, 2012; Dietrich et al., 2008; Fu et al., 2012b; Funfschilling et al., 2009; Lindken et al., 2006; van Steijn et al., 2007; Xiong et al., 2007), which almost focused on the flow field of continuous phase. Here, the flow field of dispersed phase was measured as shown in Figure I.32.

In the slow thinning period, the flow field in the liquid thread of dispersed phase is unidirectional, as $t = 3.6$ ms (Figure I.32a) and $t = 2.7$ ms (Figure I.32b) for two different flowrate ratios. While during the transitional stage, a bifurcation occurs: reverse flow is observed at $t = 1.2$ ms (Figure I.32a) and unidirectional flow persists at $t = 1.2$ ms (Figure I.32b). In Figure I.32a, the left part of dispersed liquid thread retracts and flows back while the right part continues to flow downstream, due to the rapidly changing interface curvature. In this situation, the seeding particles are rejected to both sides. But no obvious changes were observed in Figure I.32b, as the left and right part of dispersed water thread all flows to

the downstream direction. The difference is certainly derived from the interaction between the internal and external flows. When the flowrate of continuous oil phase is very large, the thinning effect of continuous phase on the dispersed water phase is pronounced and the internal flow is largely obstructed. Thus the left part connected by the water thread of Figure I.32a is smoothly spherical and that of Figure I.32b is elongated conical. Once entering into the final pinch-off stage, the liquid thread undergoes nothing differently, just the continuous thinning until the pinch-off point.

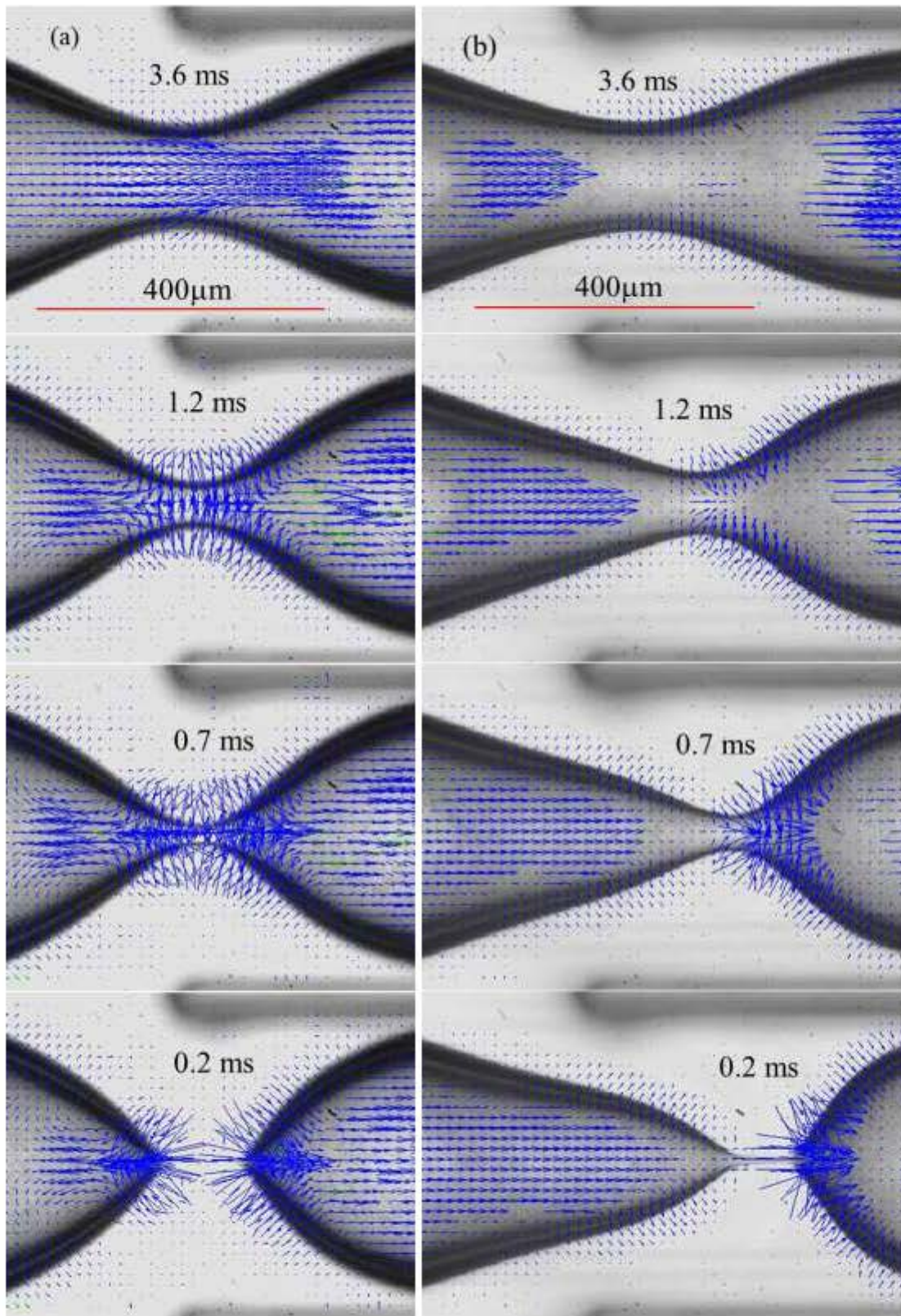


Figure I.32. In-plane velocity field of dispersed water droplet pinch-off in confined microchannel. (a) $Q_c/Q_d = 2.67$, with reverse flow; (b) $Q_c/Q_d = 1.25$, without reverse flow.

The reverse flow was once observed by van Steijn *et al.* (van Steijn *et al.*, 2009) in the gutters between the channel wall and the gaseous thread for microbubbles formed in a T-junction and they argued that the reverse flow initiated the nonlinear collapse of the gaseous thread. Figure I.33 shows the flow regime diagram for droplet pinch-off in a flow-focusing microchannel, where the flow rate of continuous oil phase Q_c and dispersed water phase Q_d are chosen as independent variables and dependent variables, respectively. In the present experiments, Q_c is ranged between 4 mL·hr⁻¹ and 30 mL·hr⁻¹, and Q_d is varied between 1.5 mL·hr⁻¹ and 24 mL·hr⁻¹. As shown in Figure I.33, the flow field is dramatically dependent of the dispersed phase flowrate Q_d . When the Q_d is less than a threshold value, saying between 8 – 12 mL·hr⁻¹, the reverse flow exists and vice versa.

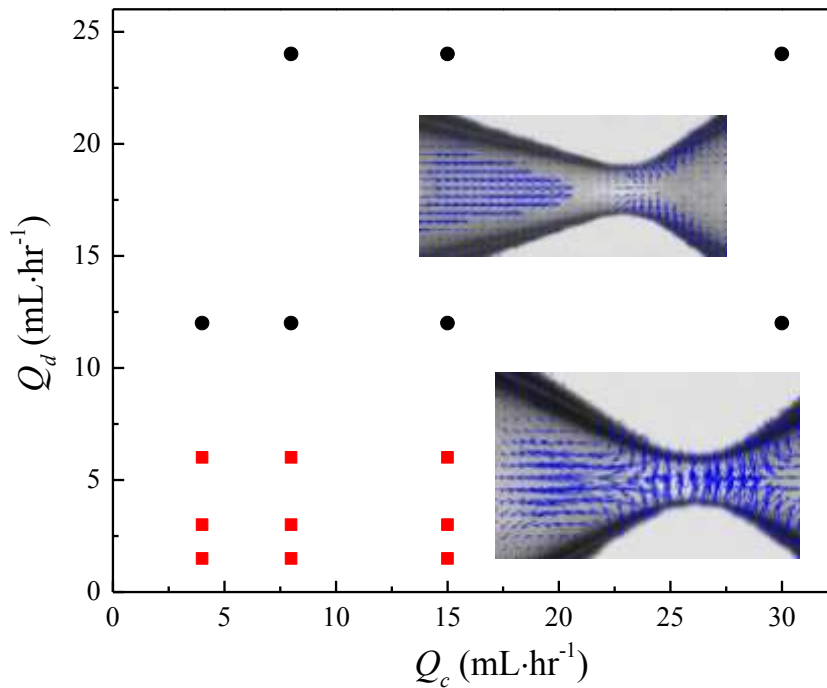


Figure I.33. Operating diagram of droplet behaviors with reverse flow or without reverse flow by plotting the flow rate Q_c of dispersed phase and Q_d of continuous phase.

I.7 Conclusion

In this part, the pinch-off dynamics was exhaustively investigated under various experimental conditions: ranging from gas-liquid to liquid-liquid, from homogenous to heterogeneous fluids, from macro-scale to micro-scale, from without external field to with external field and from gravity-superimposed to gravity-compensated.

Firstly, air bubble pinch-off in Newtonian and non-Newtonian fluids was studied both experimentally and numerically. The experimental results show that in the pinch-off region, the gas inertia, the viscous liquid drag and the surface tension reach certain equilibrium. The scaling law exponent for bubble pinch-off in Newtonian fluids of low viscosity is 0.5; in non-Newtonian fluids of low viscosity ranges from 0.5 to 1, and in Newtonian fluids of high viscosity is close to 1. For highly shear-thinning non-Newtonian fluids, a transition point occurs and deviates from the universal and self-similar character. Our experimental results are well validated through the numerical simulation. In addition, the two ends immediately after pinch-off is “plane” for Newtonian fluids of low viscosity, “cusp” for Newtonian fluids of high viscosity and special “tail” for all non-Newtonian fluids.

Secondly, two-fluid drop pinch-off from a free surface flow was investigated. For drops of Newtonian fluids, we proved that the universal self-similar behavior significantly depends on the viscosity ratio: at intermediate λ ($55.56 \leq \lambda \leq 638.89$), the drop pinch-off is universal and self-similar with the characteristics of two pinch-off points and a chain of droplets evolving into one; when $\lambda < 0.061$ and $\lambda \geq 3305.56$, drop pinch-off is non-universal and non-self-similar with various pinch-off points along the thread and a primary satellite drop sandwiched by two irregular arrays of smaller droplets. The viscosity effect is mainly accomplished by the interaction of external and internal fluids. In addition, our experiments reveal that the non-Newtonian drop pinch-off in both air and viscous external fluids fails to exhibit a self-similar behavior with the formation of exceptionally long filament and beads-on-string.

Furthermore, an external magnetic field was added to manipulate the formation and breakup of heterogeneous solid-liquid ferrofluids. Through varying the magnetic field direction and strength, the gravity is compensated (UM) and superimposed (DM) and the primary pinch-off points under UM and DM were observed to be invariant to the applied direction of magnetic force. The results show that the volume, shape as well as formation frequency of ferrofluid drops could be actively controlled by the external magnetic field. We demonstrate that there exist three regimes during the neck breakup process: linear regime,

transient regime and final self-similar pinch-off regime. The presence of the magnetic field shortens the duration of transient regime and prolongs the linear regime especially at a higher magnetic flux density. For the radial thinning, the primary pinch-off exponent is within the range of 0.70 – 0.80 while for the axial elongation, the exponent remains close to unity. Overall, the formation process and the breakup dynamics in presence of a magnetic field differ significantly from their counterparts without a magnetic field and we exclude the effect of the initial conditions, especially the direction of the magnetic field, on the self-similar pinch-off behavior.

Lastly, considering the limitation of optical camera ($\sim 20 \mu\text{m}$), we go further to study the droplet pinch-off at micro-scale where the gravity is negligible. The minimum neck diameter can be lowered to $\sim 1 \mu\text{m}$ and the final pinch-off is scaled with a power law of exponent $b = 1$. The flow field was measured in the dispersed water droplet and it shows that there is reverse flow in the water thread near pinch-off and seeding particles in the water thread are rejected to two sides. The flow pattern diagram is then obtained, showing the reverse flow is dramatically dependent of the flowrate of dispersed water phase. The pinch-off dynamics at microscale is quite similar to that at macroscale and we exclude the gravity effect. At macro-scale, the local flow field is unknown and especially for suspension ferrofluids, whether it is the liquid or solid that breaks up at the singularity point. Here, the droplet pinch-off at micro-scale maybe gives some insights.

To conclude, this part proved that the final pinch-off dynamics is affected by the interactions between internal and external fluids. And the effect of buoyancy, magnetic force and gravity on the final pinch-off dynamics is excluded. However, as we know once the neck thins to quasi molecular limit, the macroscopic physics fails to describe the phenomena at micro-scale or even molecular level which hinders the progress of pinch-off researches. Thus the development of new technical solutions to relieve the limitations of optical visualization and then further investigating the pinch-off process at microscale would be still required. This is the partial objective of the third part of this thesis.

PART II: Drop manipulation by superhydrophobicity

II.1 Literature review

Drop manipulation and mobility is strongly dependent of the interactions between drops and supporting surfaces and it has received widespread attention due to the various applications such as spray coating, inkjet printing, dropwise condensation, self-cleaning, anti-icing, biomedical devices and so on (Khalil et al., 2014). The common surfaces like glass, timber and soil are hydrophilic and a wetting drop is not possible to be manipulated. In order to manipulate an intact drop, superhydrophobic interface immerges and enjoys an increasing attention no matter in industrial applications and academic research.

II.1.1 Wetting and superhydrophobicity

Wetting is a ubiquitous phenomenon involving a liquid maintaining contact with a solid surface. When a liquid meets a smooth solid surface, a contact angle (θ_c) will be formed at the three-phase contact line, see Figure II.1. Here we use γ_{LG} , γ_{SL} and γ_{SG} , to signify the surface tension between liquid-gas interface, the solid-liquid interface and the solid-gas interface, respectively. In equilibrium, the liquid shape is thus the result of the energy minimization of the three tension forces. The wetting condition is then characterized by the Yong's relation:

$$\gamma_{SG} = \gamma_{SL} + \gamma_{LG} \cos \theta_c \quad (\text{II.1})$$

This equation can also be used in liquid-liquid-solid system and predict the contact angle (θ_c) of a liquid drop on a solid surface which varies between 0° to 180° . $\theta_c = 0^\circ$ means the completely wetting while $\theta_c = 180^\circ$ stands for the completely non-wetting. A contact angle less than 90° usually indicates the favorable wetting and a large area of liquid spreading on the solid surface. By contrast, contact angles greater than 90° generally means the unfavorable wetting of the surface and the liquid will minimize contact with the surface and form a compact liquid drop.

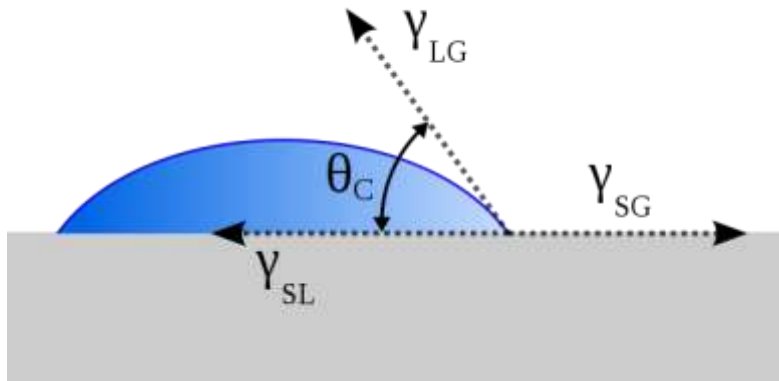


Figure II.1. Contact angle around the three-phase contact line.

While for a liquid drop on rough solid surface, the wetting state is directly affected by the roughness of the solid surface. In 1936, Wenzel (Wenzel, 1936) firstly investigated the relationship between the surface roughness and liquid wetting, and proposed that the adding surface roughness enhanced the wettability. As Wenzel model in Figure II.2a, the base liquid completely fills into the grooves. In 1944, Cassie and Baxter (Cassie and Baxter, 1944) then demonstrated that porous surfaces can impart superhydrophobicity, as Cassie - Baxter model in Figure II.2b that liquid does not penetrate into the grooves. However, when the base liquid partially penetrates into the grooves, the Cassie–Baxter to Wenzel transition occurs (Figure II.2c).

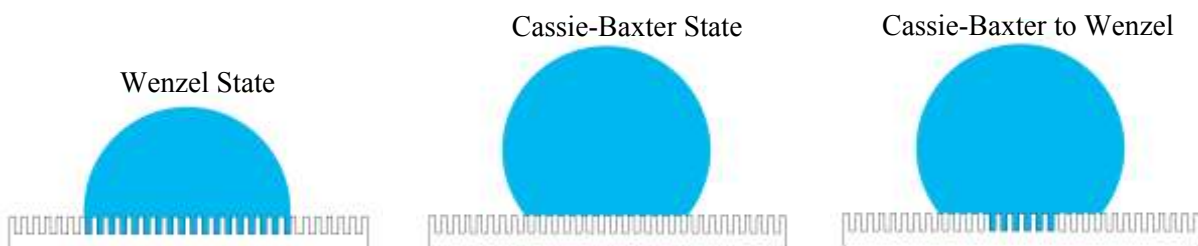


Figure II.2. Contact models of a liquid drop on a rough surface.

The lotus leaf is the most common non-wetting surface which exhibits a Cassie - Baxter state for water drops. Local structures on lotus leaves (inset of Figure II.3a) trap air and form air pockets between the solid surface and liquid, leading to the superhydrophobic mystery. Beside the lotus leaves, there are many superhydrophobic surfaces, such as spider leg, butterfly wings, legs of water striders and gecko's feet and so on as shown in Figure II.3

(Berthier, 2007). Inspired by mimicking the nature (Darmanin and Guittard, 2015), superhydrophobicity now has attracted a lot of interest due to its wide applications, like self-cleaning and anti-icing. Superhydrophobic surface exhibits the high apparent contact angle ($> 150^\circ$) and low contact angle hysteresis ($< 5^\circ$). When slightly tilting the surface, water drops will bead or roll off, which provides the surface with extreme water repellency and self-cleaning characteristics. The tilting angle for triggering the motion of drops on the slope is just defined as contact angle hysteresis. The lower the hysteresis is, the easier the motion for drops, and then the stronger the superhydrophobicity.

Nowadays artificial superhydrophobicity can be usually obtained by modifying surface structures to create superhydrophobic pearl-like drops or dressing the drops to form armored marbles (Bormashenko et al., 2010b). Recently, some researchers even manipulate the drops to be self-propelled through gradient methods like chemical (Chaudhury and Whitesides, 1992; Jiang et al., 2005; Plummer et al., 2003; Smith et al., 2004), thermal (Dupeux et al., 2013; Linke et al., 2006) and energy gradient (Olin et al., 2015). For example, Leidenfrost drop can be formed on heated substrate and even self-propelled when the surface equipped with ratchets (Quéré, 2013). Thus superhydrophobic surface is an ideal interface to investigate drop behavior under various situations, for example, drop evaporation (Ramos et al., 2015), drop delivery (Guo et al., 2006; Nguyen et al., 2010a; Sheng and Zhang, 2011; Vuong et al., 2015), drop squeeze (Bormashenko and Bormashenko, 2011) and drop impact (Bird et al., 2013; LeClear et al., 2016; Yeong et al., 2014) and so on.

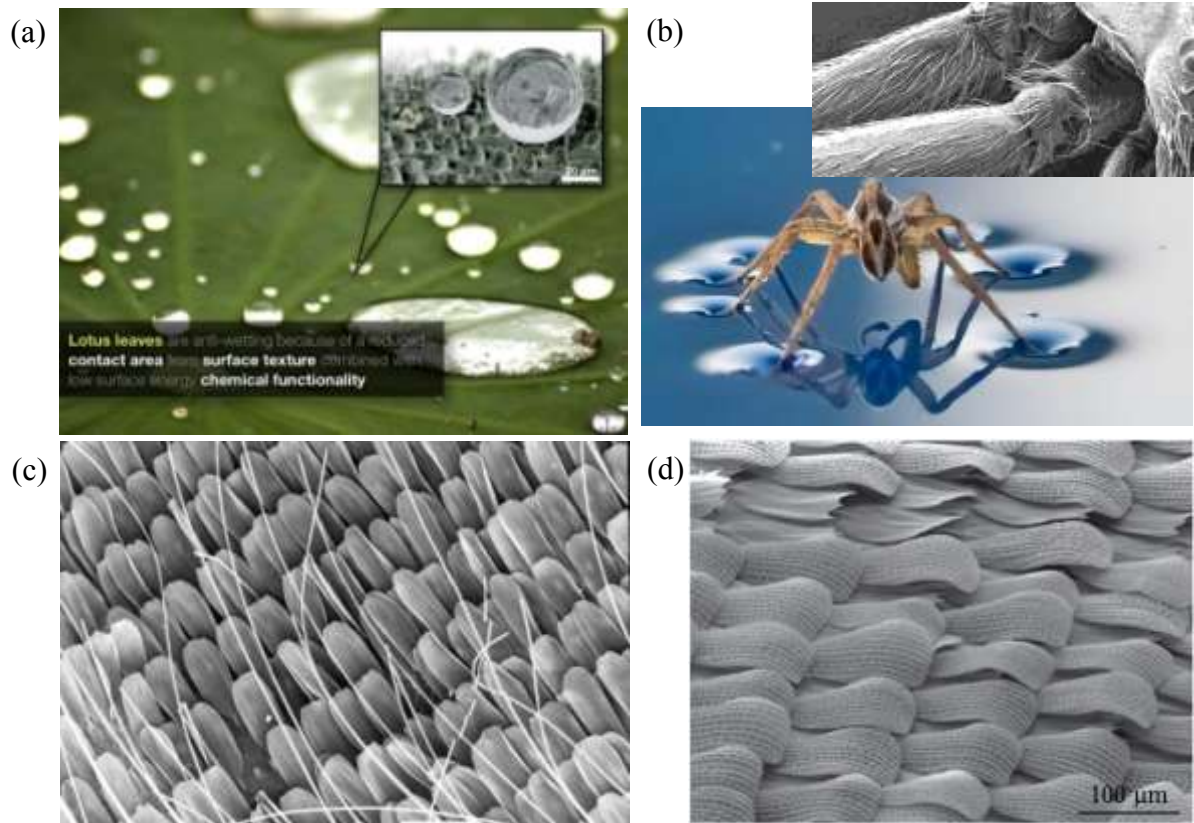


Figure II.3. (a) Lotus leaf; (b) spider walking on water; (c) SEM image of a butterfly wings, <http://www.bath.ac.uk/ceos/insects3.html>; (d) wings of *Papilio Ulysses* (Berthier, 2007).

II.1.2 Drop motion on barrier-attached surface

Drops' motion and manipulation on a solid surface is a long-term scientific topic that lies behind various applications, such as self-cleaning, anti-icing, biomedical devices, spray coating, inkjet printing, dropwise condensation, liquid transportation and so on (Li et al., 2016; Semprebon and Brinkmann, 2014; Sheng and Zhang, 2011; van Dam and Le Clerc, 2004; Vance et al., 2000; Wang et al., 2015; Wisdom et al., 2013; Yarin, 2006).

The defects on a solid surface are ubiquitous, arising from mechanical damage, fabrication imperfection or purely artificial textures and barriers. These defects can be advantageous depending on their size, shape and profile. For example, the patterned microscale defects can lead to nonstick drops (Lv et al., 2016) and could be applied to self-cleaning technology; while the line-shaped defects can result in the trapping effect (Olin et al., 2015) and could be applied to the raindrop collection. Most previous studies of drops on solid surfaces with defects all focus on drop wetting and impact phenomena ('t Mannetje et

al., 2013; Bird et al., 2013; Frank et al., 2015; Gao and McCarthy, 2009; Gauthier et al., 2015; Josserand et al., 2005; Varagnolo et al., 2016). With regard to the dynamical impact, Bird *et al.* (Bird et al., 2013) experimentally and theoretically proved the presence of microscale roughness can reduce the contact time and Josserand *et al.* (Josserand et al., 2005) experimentally and numerically demonstrated the small barrier such as layers of adhesive tape can trigger the splashing. To our best knowledge, few studies have been conducted on the drop motion on a barrier-attached solid surface. 't Mannetje *et al.* ('t Mannetje et al., 2014) conducted experiments to capture sliding drops on an inclined plane that is equipped with electrically tunable wetting defects. Dupeux *et al.* (Dupeux et al., 2011) decelerated and even trapped Leidenfrost drops through crenelated surfaces. The present work aims at investigating the capacity of liquid drops of different properties to pass through millimeter-scale barriers of various geometries on superhydrophobic surfaces. Unlike human being, drops cannot anticipate barriers and the only possibility is just head-on confrontation, by deforming themselves to adapt to the environment. Whether their spatio-temporal deformation facilitates their crossing or not and how they behave themselves under various conditions, that is the main topic we considered here.

II.1.3 Liquid marble

In the early 20th century, stabilized interfaces by particles were conceptualized due to Pickering emulsions (Pickering, 1907; Ramsden, 1903). Nowadays, particles can be employed to stabilize an individual liquid drop which is firstly named as “*liquid marble*” by Aussillous and Quéré (Aussillous and Quéré, 2001). Liquid marbles are non-stick water drops encapsulated with micro- or nano- metrically superhydrophobic particles, as shown in Figure II.4. The presence of outside particles forms a shell to directly prevent the inside liquid from evaporation and contamination. And the particles separate the liquid-gas and liquid-substrate by air pockets so that the friction between the marble and solid substrate is largely reduced (Biance et al., 2003; Planchette et al., 2012). Thus liquid marbles make it possible to conserve biological samples and liquid assays, or even to transport them through a certain distance without leaving behind any trail. In the past decades, many interests were focused on liquid marbles due to their various applications such as micro-reactors (Arbatan et al., 2012; Xue et al., 2010), micro-pumps (Bormashenko et al., 2010a), gas sensor (Tian et al., 2010), blood typing (Arbatan et al., 2012), electrowetting (Newton et al., 2007), optical

probing (Zhao et al., 2012), cell culture (Tian et al., 2013), to name only a few. The state-of-the-art studies on properties and applications of liquid marbles were covered in several review articles (Aussillous and Quéré, 2006; Bormashenko, 2011; McHale and Newton, 2011).

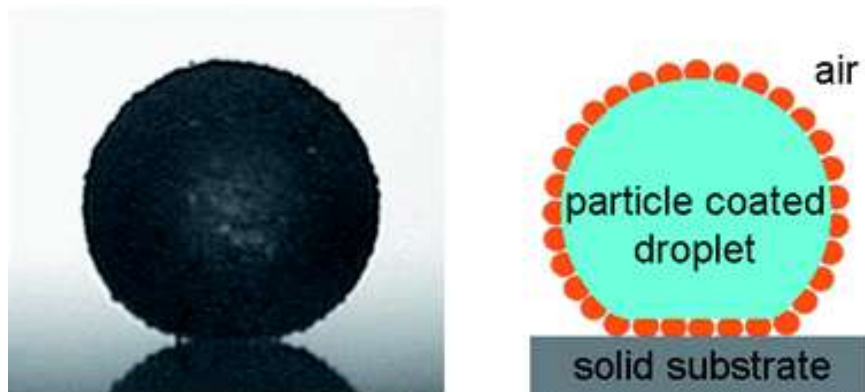


Figure II.4. Image and model of a liquid marble (McHale and Newton, 2011).

Liquid marble fabrication is usually achieved by depositing a liquid drop on a bed of particles and then moving it gently to produce an interface covered by particle layers. These particles can be hydrophobic (lycopodium, silica nanoparticles, PTFE, Latex, PE, OTFE) or hydrophilic (graphite, carbon black, PVDF) (Hashmi et al., 2012) and the inside liquid can be usually pure water, water/glycerol (Bormashenko et al., 2012c), water/alcohol (Bormashenko et al., 2012a; Bormashenko et al., 2015), organic solutions (Xue et al., 2010), ionic liquid (Gao and McCarthy, 2007), liquid metal (Sivan et al., 2013), magnetic fluids (Xue et al., 2010; Zhao et al., 2010), electrolyte solutions (Ooi and Nguyen, 2015). Due to their long-term stability, liquid marbles can roll on solid surfaces (Aussillous and Quéré, 2001; Ooi and Nguyen, 2015), float over liquid surfaces (Ooi et al., 2015) or even descend in liquid phase (Bormashenko et al., 2012c) without breaking the integrity. Recently, various methods like light sensitive (Paven et al., 2016), pH sensitive (Dupin et al., 2009; Fujii et al., 2010), magnetic field (Zhao et al., 2010) and electric field (Bormashenko et al., 2012b), etc., were proposed to actively control the motion and reverse coating of liquid marbles, even the redistribution of particles on the surface of a drop. Zang *et al.* (Zang et al., 2015) suggested the switchable closing and opening a liquid marble via ultrasonic levitation. Zhao *et al.* (Zhao et al., 2010) investigated the reversible self-removing and self-recovering of particle layer on liquid marbles through a magnetic field.

Besides the academic curiosity, liquid marbles are mainly studied for their transportation through a certain distance without adhesion to the solid substrate. However, the post biomedical analyses and other sensing systems require breaking down the interface of liquid marbles, either removing outside particles or abstracting inside liquid samples. The effective and efficient removing of the coating was realized by means of some stimulus-responsive systems as above-mentioned, but the challenge remains unaddressed for those systems without any stimulus possibility like inert particles. To our best knowledge, the dynamics of undressing hydrophobic particles around water marbles by an oil film has never been reported. This work aims at investigating how water marbles move on oil film and to what extent enveloping particles can be progressively undressed to immobilize finally the drop by liquid-liquid friction contact.

II.1.4 Slope motion through superhydrophobic interphase

Controlling the drop motion is especially fundamental for droplet-based microfluidic, a rapid growing interdisciplinary combined fluid mechanics, soft matter, biomedicine, biochemistry and microsystem engineering (Seemann et al., 2012; Squires and Quake, 2005). So far, several methods have been proved to actuate the drop motion. For most common fluids, drop actuation can be achieved by the ultrasonic surface acoustic wave and surface vibration (Brunet et al., 2007, 2009; Dong et al., 2006; John and Thiele, 2010; Noblin et al., 2009). For those volatile liquids, the thermal gradients can lead to the Leidenfrost phenomenon (Biance et al., 2003; Linke et al., 2006; Quéré, 2013), i.e. the levitation of liquid drop through a cushion of vapor when they are brought into contact with a heat solid surface. For polar fluids, electrowetting is an efficient method to drive drops to move (‘t Mannetje et al., 2011; Kuo et al., 2003). For magnetic fluids, drop motion can be actively actuated and controlled by an additional magnetic field (Afkhani et al., 2008; Bormashenko et al., 2008; Guo et al., 2006; Nguyen et al., 2010a). However, the most simple and direct way is to actuate the drop motion on the superhydrophobic surface through a slope.

In fact, the superhydrophobicity derives from the existence of the air pockets between the solid surface and liquid (Barthlott and Neinhuis, 1997). From solid surface modification, the bio-inspired patterned structures or artificial roughness can lead to the superhydrophobicity (Cottin-Bizonne et al., 2003; Lei et al., 2014; Suzuki et al., 2008). From liquid surface modification, the superhydrophobic particles can be used to wrap the

liquid drop and result in non-stick drops (Aussillous and Quéré, 2001; Bormashenko et al., 2015; Bormashenko et al., 2009; Gao and McCarthy, 2007; Ooi and Nguyen, 2015). One would wonder what the difference is between the two kinds of superhydrophobic interphases during the drop motion.

In contrast to the symmetric spreading and impacting, a lot of previous studies are devoted to the drop motion on a superhydrophobic slope, following the gravity gradient (Suzuki et al., 2008). Sheng and Zhang (Sheng and Zhang, 2011) studied the drop motion on an inclined ratchet-like superhydrophobic surfaces. Richard and Quéré (Richard and Quéré, 1999) studied the viscous drops moving on a tilted non-wettable solid and demonstrated the rolling motion instead of sliding. Some authors designed the slope with anisotropic wettability and run a drop through alternating stripes (Buehrle et al., 2002; Morita et al., 2005; Sbragaglia et al., 2014; Suzuki et al., 2008). Even the uphill droplet transportation on an inclined superhydrophobic surface was performed with airflow (Chung et al., 2015) or vibration (Benilov and Billingham, 2011; Brunet et al., 2007). Nevertheless, the motion of liquid marbles on a solid slope is less documented. Aussillous and Quéré (Aussillous and Quéré, 2001) was first to study the rolling motion of liquid marbles and they found that the larger slope can lead to strong deformation, like peanut, doughnut and disk shapes. Recently, the disintegration of liquid marbles by moving on oil film attached to a tilted slope was investigated by our group (Jiang et al., 2017). However, to our best knowledge, the comparison of two kinds of superhydrophobicity, either the side of a flat surface or the curved side of a drop, has never been done. In this work, we will investigate and compare the drop motion on superhydrophobic interface of two different methods.

II.2 Experimental details

II.2.1 Experimental method for drop hurdling

Aluminum, stainless steel and resin were three materials that we adopted to produce the basic surfaces with barriers on. Three geometries of the same base w ($w = 1$ and 2 mm respectively) — semicircle, equilateral triangle and square (Figure II.5a-c) were prepared as barriers on flat surfaces and a slope was added to release drops. The distance from the slope bottom to the barriers were 10 mm for $w = 1$ mm and 20 mm for $w = 2$ mm. These surfaces were fabricated with precise milling for aluminum and stainless steel or by 3D printing for resin and then coated with the commercial product NeverWetTM (Rust-Oleum Corporation, USA) consisting of superhydrophobic nanoparticles dispersed in volatile solvents. The spray was conducted by two procedures: firstly base coating and then top coating. After solvent evaporation, a thin film, about two hundred micrometers, was attached on the substrates as well as the barriers. Both the flat substrates and barriers share the similarly superhydrophobic properties (Figure II.5d) and the static contact angle is about 160° for pure water drops (Figure II.5e). The superhydrophobicity of the surfaces were regularly verified through contact angle measurements and renewed if some diminution was observed.

In order to make sure the drops could slide on the superhydrophobic surface and barriers, the slope was set to be 15° . The drop was released from the micro-syringe (volume range: 10 μL , 50 μL , and 100 μL with the maximum deviation of ± 1 μL). The initial velocity (v_1) in the vicinity of the barriers could be varied by adjusting the height position where the drop was released from the slope. It is worth mentioning that we only record the situations that drops can slide to cross the barriers, not roll or fly over the barriers as that happens sporadically. Therefore every experiment must be preceded dozens of times. One scenario of a water drop hurdling the semicircle protrusion was given in Figure II.5f.

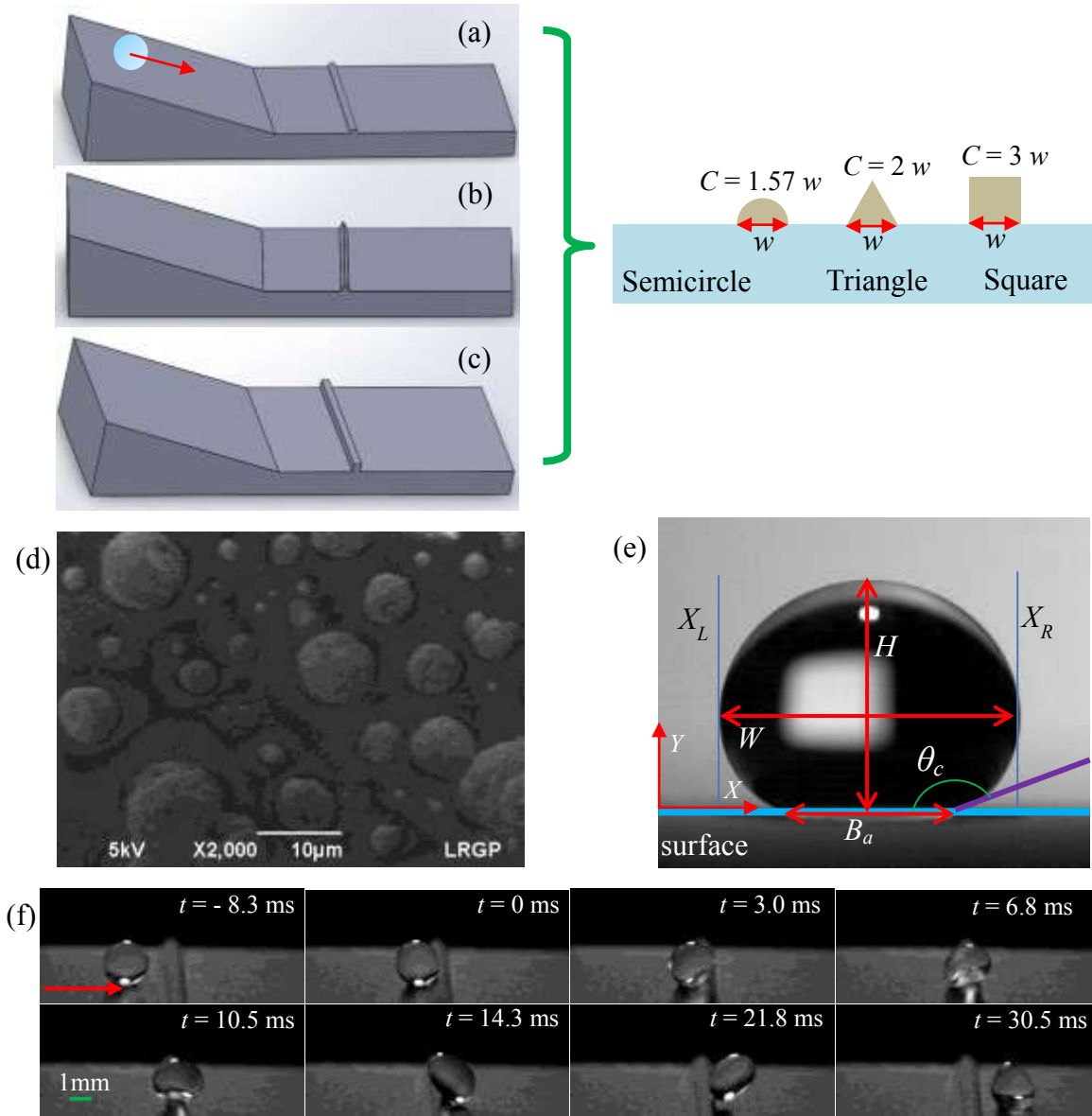


Figure II.5. Experimental setup and materials. Base surfaces with various barriers. The cross-section shapes of these barriers are semicircle (a), equilateral triangle (b) and square (c). The length of base substituted by the barriers in the direction of drop motion is defined as w . Thus the convex path length ‘ C ’ covers the barriers’ surface. (d), Scanning electron microscope (SEM) for surfaces treated with the commercial spray NeverWet™. (e), Shape parameters. ‘ H ’, ‘ W ’ and ‘ B_a ’ stand for the height, width and base of liquid drops. ‘ X_L ’ and ‘ X_R ’ means the left and right position relative to the given coordinate. ‘ θ_c ’ is the contact angle. (f), Sequence of a $10 \mu\text{L}$ water drop hurdling the semicircle protrusion ($w = 1 \text{ mm}$). t is defined as the difference between the instantaneous time and the contact time with the barrier.

II.2.2 Experimental method for undressing water marbles

Lycopodium particles are hydrophobic and the mean diameter of these particles is around 20 – 50 μm (Figure II.6a). Water drops of given volumes controlled by a precise microdosing syringe (range: 0 - 100 μL) were released to a bed of superhydrophobic and superoleophilic lycopodium particles placed in a hemi-spherical clock glass. By gently shaking the hemi-spherical clock glass, water drops rolled over the powder back and forth so that these particles automatically self-enwrapped and self-assembled on the surface of water drops in a very short term. The formed liquid marbles were superhydrophobic and the static apparent contact angle reached 155° on glass (Figure II.6b). The inset of Figure II.6b indicates a fluffy appearance of the liquid profile of a particle-wrapped marble and this rough structure enables the liquid marble to withstand some mechanical impact and deformation (Bormashenko and Bormashenko, 2011).

In order to investigate the undressing dynamics of a liquid marble on an oil film, a rolling experimental device was designed as shown in Figure II.6c. Through a small spoon, the newly formed liquid marble could be transferred to a glass slide. The slope of the glass slide (total length is 7.6 cm) was set to be $\alpha = 10^\circ$ and a thin layer of silicone oil was brushed gently with a tissue. The thickness of the brushed oil film estimated about 50 μm by weighting.

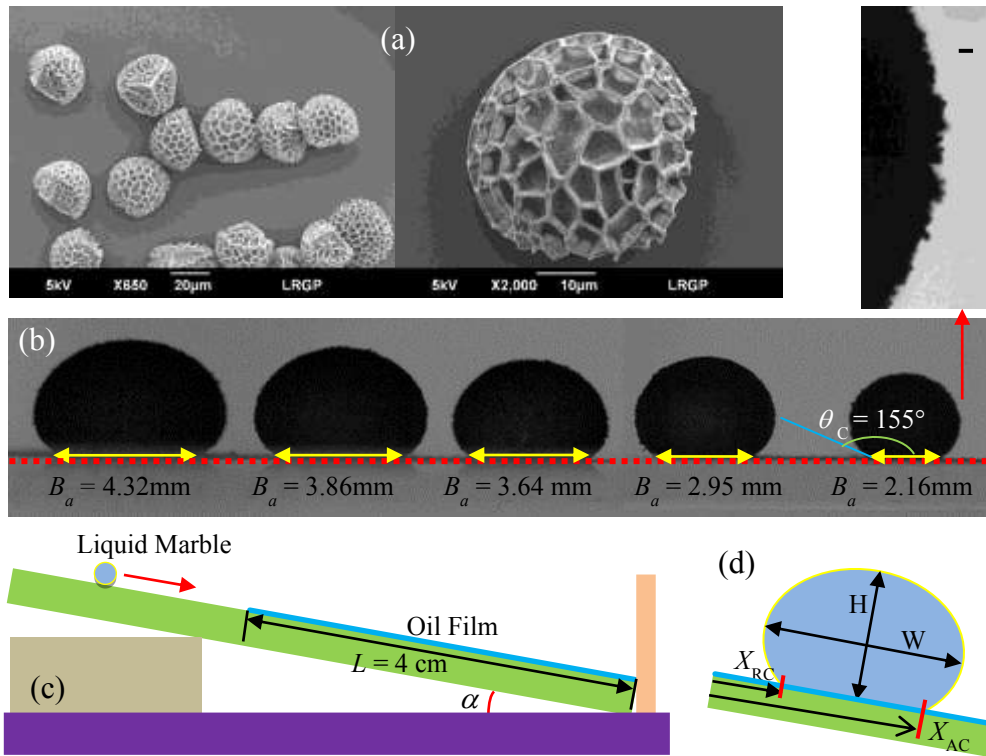


Figure II.6. (a) SEM of lycopodium particles. (b) Static water marbles on glass substrate, from left to right: 50 μL , 40 μL , 30 μL , 20 μL , 10 μL . The top-right scale bar in the locally magnified image represents 100 μm . (c) Experimental setup. (d) Shape description of water marble during the downhill process.

II.2.3 Experimental method for slope motion

The superhydrophobic substrate through spraying coating and the liquid marble through wrapping superhydrophobic particles were prepared as stated in the above section: II.2.1 and II.2.2. The slope in Figure II.5 is used to initiate the drop motion. One slope is coated for liquid drops. While the other one is preconditioned with a piece of glass slide and the tilting angle remains $\alpha = 15^\circ$. The experimental setup for liquid drops and liquid marbles is given in Figure II.7. Quantitative details of liquid drops and marbles on the slope is the same with the Figure II.6.

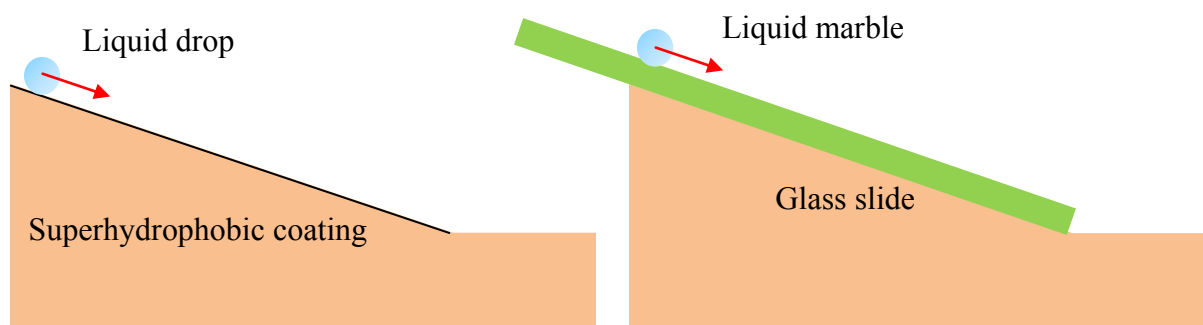


Figure II.7. (a) Liquid drop downhill on a superhydrophobic slope; (b) Liquid marble downhill on a glass slide slope without oil film. The tilting angle remains $\alpha = 15^\circ$ for both (a) and (b).

II.2.4 Physical properties of working fluids

The properties of the work fluids were gathered in Table II.1. For drops hurdling experiments, water was the basic and SDS and glycerol aqueous solutions were prepared to change the surface tension and viscosity, respectively. For liquid marble undressing on oil film, water was enwrapped with lycopodium particles and four silicone oils of different viscosities: SO 5, SO 10, SO 50 and SO 100, were simply applied to form the oil film. Silicone oils share the same molecular structure with different chain lengths and importantly, we can widely change the viscosity of silicone oils and simultaneously keep the surface tension constant.

Table II.1. Properties of various liquids used in our experiments. SDS stands for the sodium dodecyl sulfate.

	$\rho/ (\text{kg}\cdot\text{m}^{-3})$	$\eta/ (\text{mPa}\cdot\text{s})$	$\sigma/ (\text{mN}\cdot\text{m}^{-1})$
Liquid drops hurdling various barriers or slope motion			
Water	996	1.0	72.5
0.1wt% SDS + Water	996	1.0	50.3
45wt% glycerol + Water	1121	5.5	69.0
60wt% glycerol + Water	1157	12.0	67.0
70wt% glycerol + Water	1184	25.0	66.0
80wt% glycerol + Water	1211	64.0	65.0
85wt% glycerol + Water	1227	138.7	64.8
Undressing water marbles on oil film			
Water	996	1.0	72.5
Silicone oil 5 (SO 5)	915	5.8	18.5
Silicone oil 10 (SO 10)	920	11.5	19.7
Silicone oil 50 (SO 50)	955	59.5	20.1
Silicone oil 100 (SO 100)	960	112.8	20.2

II.2.5 Imaging analysis

The processes for both drops hurdling over various barriers and undressing water marbles on oil film were recorded by our Phantom v7.11 camera (Vision Research, USA). For hurdling experiments, the visualized speed and resolution was typically 8000 fps (frames of second) and 656×256 pixels. The exposure time was $5 \mu\text{s}$. For the motion of water marbles on the slope, the visualized speed was 2000 fps and the resolution was 1280×400 pixels. The exposure time was $10 \mu\text{s}$. While for the slope motion, the resolution was 704×256 pixels and 752×304 pixels for liquid drops and liquid marbles, respectively. The visualized speed was 6000 fps and the exposure time is $5 \mu\text{s}$.

The images were analyzed through a home-made Matlab program. For the horizontal surface motion, the gray images were firstly transferred into binary images by applying a threshold value which is similar to Part I. Secondly, remove the non-involved part in the image and select the surface as the basic line. Then hide the barriers and calculate the left, right and up line by batch processing. Finally, the width, height, base and even the velocities as shown in Figure II.5e can be quantitatively obtained. However, the motion of liquid marble on a slope can be converted to a horizontal surface by rotating the whole image. Then the processing method by Matlab is identical to the previous one. It is worth noting that all the parameters are relative to the slope coordinate and the velocities were calculated by the advancing and receding point as shown in Figure II.6d.

II.3 Drop hurdling barriers of various geometries

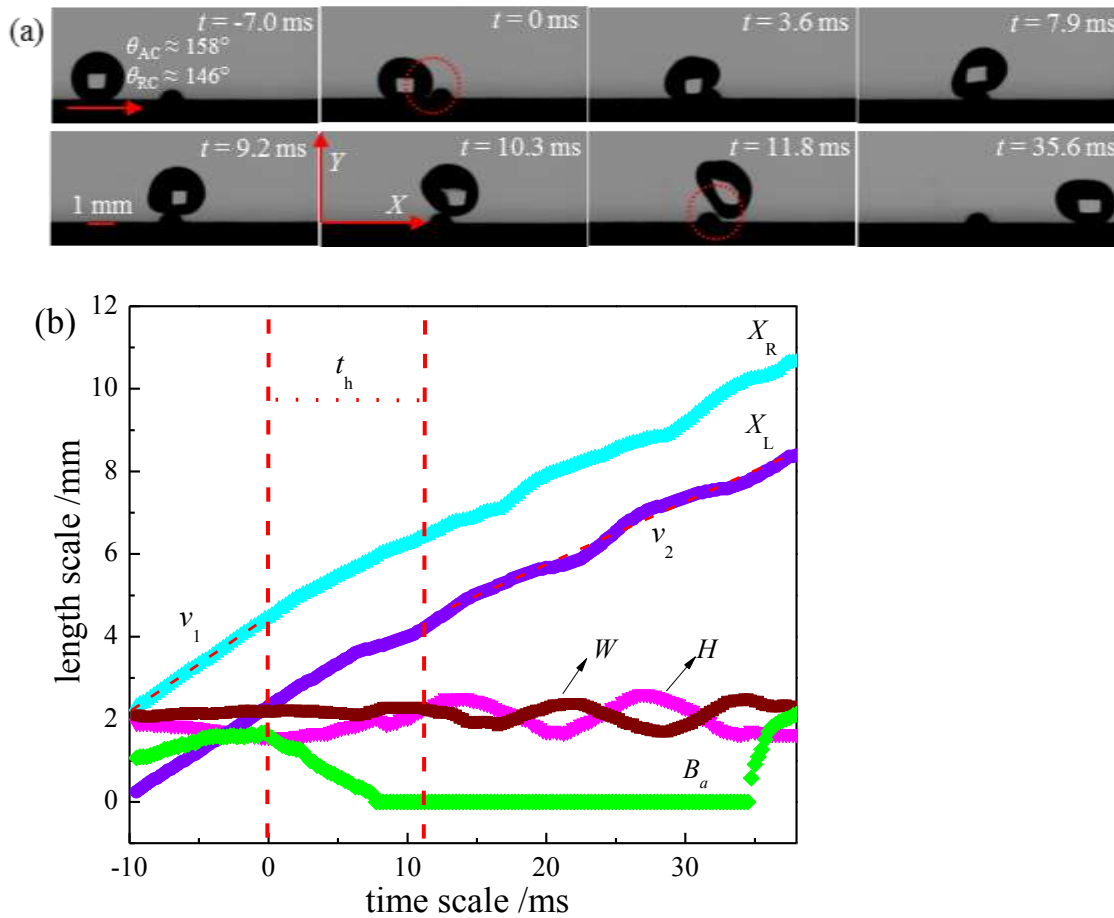
II.3.1 Hurdling dynamics

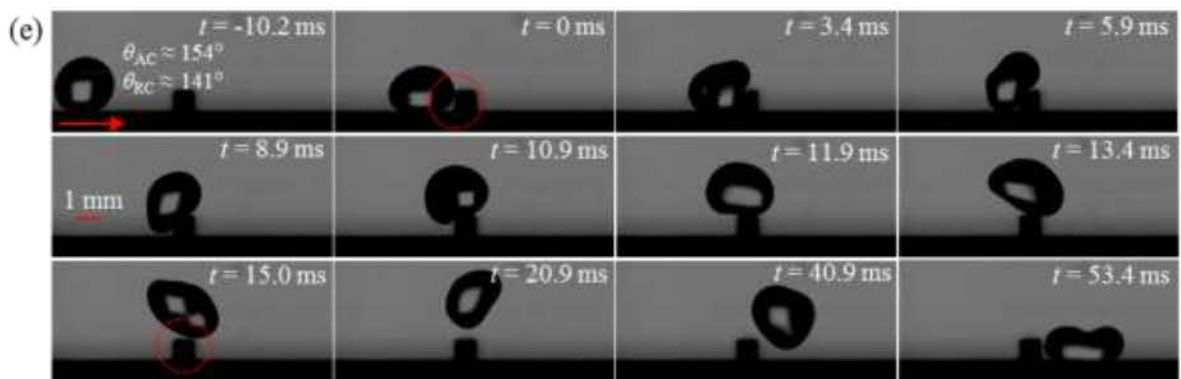
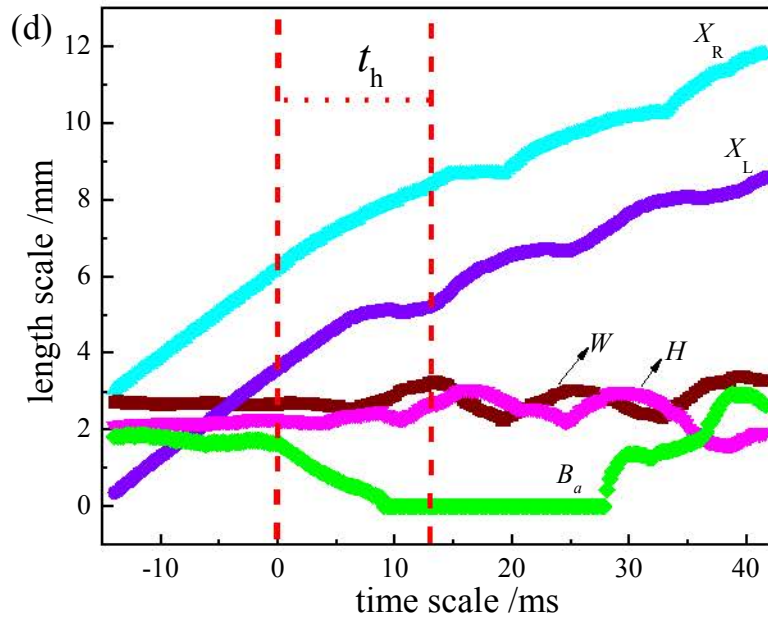
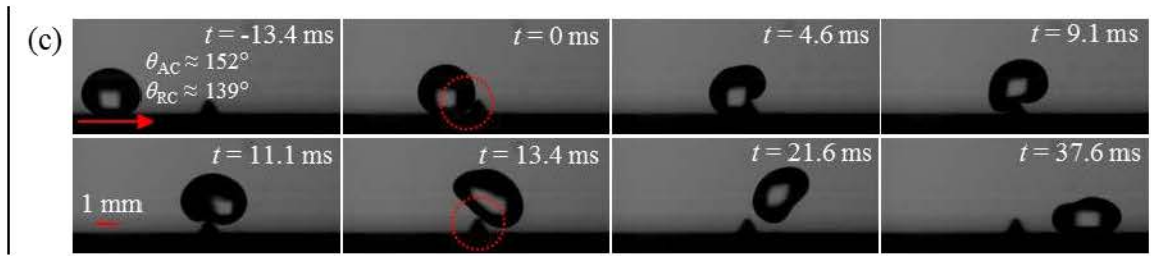
Figure II.8a – f presents water drops ($V = 10 \mu\text{L}$) to hurdle three barriers (see Video AII.1-3). Drops roll down from the slope due to the gravitation and once reaching the flat surface, they will be flattened by the interplay between the inertial force, drag and repelling force by the superhydrophobic surface. After several shape oscillations, drops reach a steady state and a clear hysteresis between the advancing angle (θ_{AC}) and receding angle (θ_{RC}) can be observed in the first images of Figure II.8a, c and e. The hysteresis is mainly determined by the triple contact line and resists to the motion of drops (Gao and McCarthy, 2006). The hysteresis maintains order of ten degrees for three barriers of geometry, this implies the comparable surface condition after being coated. Moreover, each hurdling experiment was consecutively repeated three to five times and no noticeable deviation was observed. Of course, as many superhydrophobic surfaces, the superhydrophobicity diminishes by absorbing the ambient humidity after a certain period so that a new surface should be coated to keep the similar surface properties. At $t = 0$ ms, drops begin to touch the barriers and the contact positions all locate in the middle-to-top part of the facing surface. Due to the quasi spherical shape of drops with high contact angle, there exists a tiny slot between the drops and the barriers. Then, the leading part of water drops is obstructed while the trailing part continues to go ahead, resulting in the disappearance of these slots. The upper part of water drops which is higher than the barriers, is pushed forward to climb barriers and remains a smooth hypersurface. Gradually, the front-end drags the back-end and detaches from the horizontal surface. The whole drop continues to move forward and at one moment, the whole drop stands on the barriers to form a “mushroom” shape, except the square barrier which is partially occupied by the water drop. Thereafter, drops leave the barriers due to both the inertia and asperities and rotate in air. A slight difference can be observed among three geometries. After the summit of the semicircle and triangle barrier, water drops downhill along the right-side surface of barriers before detaching while the water drop directly take off from the platform of the square barrier due to the large intercept area.

In fact, rigid solid spheres of comparable sizes and different densities, such as steel beads, were also tested on the same superhydrophobic surface. The results show that solid spheres are more likely to rebound (Figure II.8g) or fly over the barriers instead of sliding due to the point-to-point contact without any shape deformation. We note that no matter the

take-off appears at the downhill surface (Figure II.8a and c) or just on the platform (Figure II.8e), a rotation in the air always follows. After the rotations, drops undergo a somewhat slight impact when landing on the horizontal surface. Later on, the drops adapt their shape and continue to move forward. In particular, the drop with a higher viscosity (Figure II.8h) maintains a smooth shape during the barrier-crossing process compared to the frequent and easy deformation of a pure water drop (Figure II.8a). Obviously, the shape fluctuation is attenuated by viscous forces (Olin et al., 2013).

Usually, small drops tend to take-off and rotate in the air while the larger ones are more likely to climb over these protrusions. The W and H evolution in Figure II.8b, d and f, imply that the shape deformation happens more frequently for the square barrier. While the X_R and X_L evolution indicates that the velocity difference of the semicircle barrier is the lowest. The characteristic hurdling time t_h indicated in Figure II.8b, d and f is quantitatively in the order: semicircle < triangle < square, implying the increasing hurdling difficulty under the given conditions.





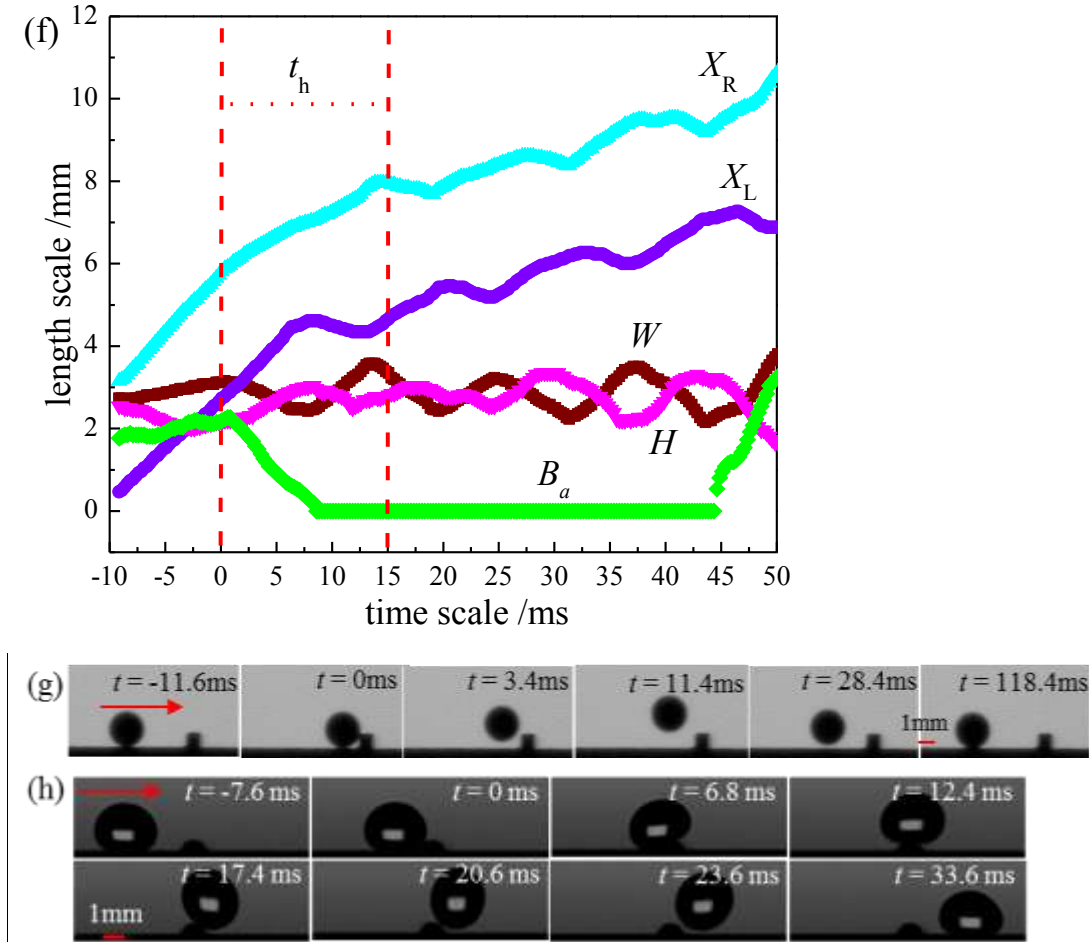
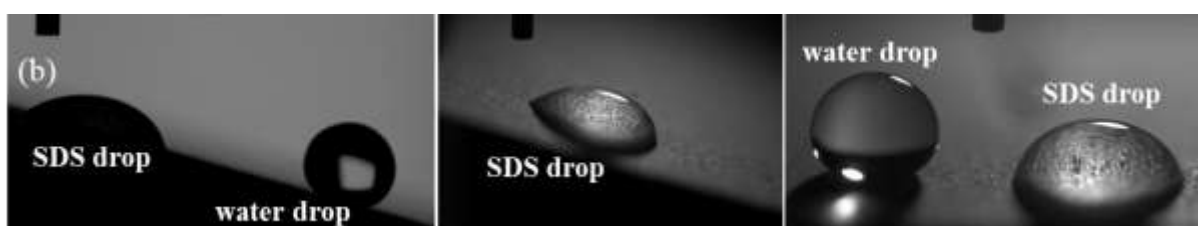
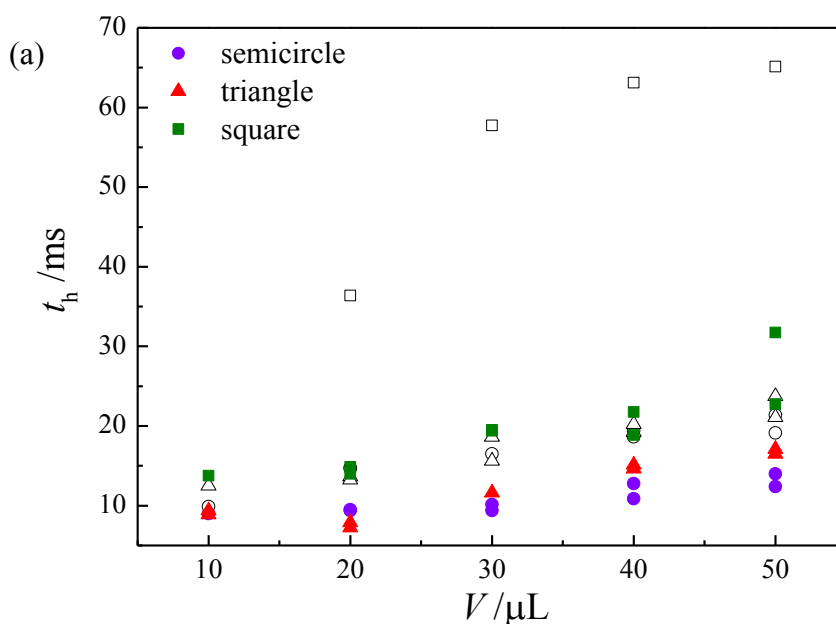


Figure II.8. Dynamical hurdling behavior. (a), (c) and (e) are the blowups of 10 μ L water drops hurdling the semicircle, triangle and square barriers ($w = 1$ mm), respectively and (b), (d) and (f) are their corresponding quantitative characterization of shape evolutions in two dimensions. The ' X_R ' and ' X_L ' are calculated from the left side of each image. The hurdling time t_h is defined as the difference between the first contact and the last leave on the barriers (as indicated with red circles). The initial velocity (v_1) and final velocity (v_2) of the drop can be obtained from the ' X_R ' or ' X_L '. In fact, the initial velocity in Fig. 2(a-b), (c-d), (e-f), are: $0.22 \text{ m}\cdot\text{s}^{-1}$ (semicircle), $0.23 \text{ m}\cdot\text{s}^{-1}$ (triangle) and $0.23 \text{ m}\cdot\text{s}^{-1}$ (square). (g), Blowups of a steel bead (diameter = 2.5 mm, density = $7850 \text{ kg}\cdot\text{m}^{-3}$) failing to hurdle the square protrusion ($w = 1$ mm). (h), Sequence of a 10 μ L glycerol drop with the viscosity $\eta = 64 \text{ mPa}\cdot\text{s}$ crossing the semicircle barrier ($w = 1$ mm).

II.3.2 Hurdling time

In Figure II.9a, the hurdling time t_h increases with the drop volume and decreases with the drop's initial velocity, under a given barrier geometry. Intuitively, a higher initial kinetic energy should take less time to hurdle the barriers. But due to the complex pattern of the triple line contact as well as the drop deformation, bigger drops can occupy more contact areas and generate more friction with the solid surface (Olin et al., 2013). For the same drop volume and initial velocity, the hurdling time t_h increases from semicircle to triangle and to square barriers, implying the increasing hurdling difficulty. From the morphological point of view, the shape and height of the barriers are the most significant parameters. The semicircle barrier with its curvature makes the drop to quickly and easily adapt while the square barrier with a 90° facing surface confronts to obstruct the drop's motion in the horizontal direction. With the same base length, the barrier's heights are: 0.5 mm (semicircle), 0.866 mm (triangle) and 1 mm (square), respectively, which exactly corresponds to the increasing trend of the potential energy required.



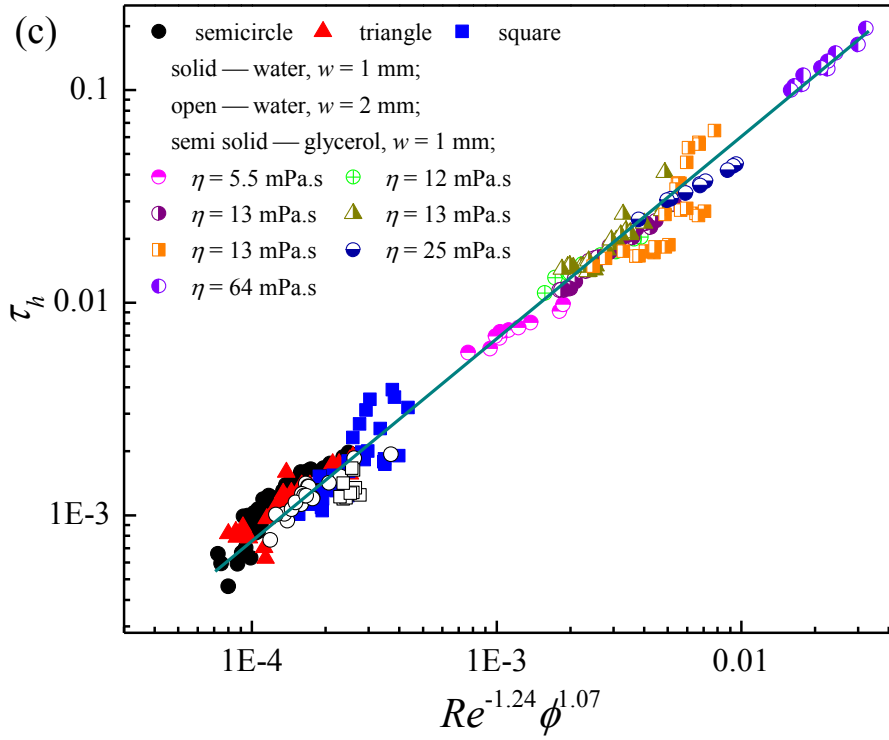


Figure II.9. The hurdling time t_h under various conditions. (a), Water drops released from two height positions of the slope on the three geometries ($w = 1$ mm). t_h is the dimensionless hurdling time and V is the volume of drops. The solid symbols refer to the higher releasing position ($v_1 = 0.30$ m·s⁻¹) while the open symbols stand for the lower releasing position ($v_1 = 0.20$ m·s⁻¹). (b), Pure water drops ($\sigma = 72.5$ mN·m⁻¹) and 0.1% sodium dodecyl sulfate (SDS) aqueous drops ($\sigma = 50.3$ mN·m⁻¹) of the same volume $V = 20$ μ L on the superhydrophobic slope or plane. The nozzle is set as a reference (out diameter = 0.91 mm). (c), Log-Log plot of dimensionless hurdling time τ_h vs. $Re^{-1.24} \phi^{1.07}$ for all the conditions investigated. Re is the Reynolds number and ϕ the shape dependent factor. The fitting error of eqn. (II.1) was given in Figure AII.1.

Except the above, other factors like barrier's size, liquid viscosity and surface tension, were also considered (see Figure AII.2). For a given barrier, the larger barrier size means the increasing difficulty for drops to hurdle. And the hurdling time is more pronouncedly increased for 80% glycerol solution. It is worth mentioning that all these parameters should be chosen to make sure that drops could hurdle barriers without leaving behind any trail. If the viscosity or the barrier size continues to increase, liquid drops could no longer hurdle the barriers due to the insufficient kinetic energy in our present conditions. With the variation of

viscosity, the surface tension of glycerol solutions was also slightly reduced. Similarly, the drops of even lower surface tension were tested and more likely to stick and spread on the superhydrophobic surface due to lower surface tension (Figure II.9b) without motion ability. Thus, the surface tension should be limited to a relatively narrow range in avoid spreading and adhesion on solid surfaces.

In order to generalize all these parameters, we firstly define the dimensionless shape factor as $\phi = C / L_\sigma$, to describe the effect of the barrier's geometry, and the Reynolds number $Re = \rho v_1 d / \eta$. Here $L_\sigma = \sqrt{\sigma / \rho g}$ is the capillary length of the drop fluid, and C is the convex path length shown in Figure 1a, g is the gravitational acceleration. d is the equivalent diameter of liquid drops, $d = \sqrt[3]{6V / \pi}$, v_1 , ρ and η are respectively the velocity, density and dynamic viscosity of hurdling drops. Furthermore, the viscous relaxation time (Rohlfis et al., 2014), $t_r = \rho d^2 / \eta$, is introduced to define a dimensionless hurdling time. Thus, a scaling law based on the best fitting (Figure II.9c) is given as follows:

$$\tau_h = \frac{t_h}{t_r} = 5.90 Re^{-1.24} \phi^{1.07} \quad (\text{II.1})$$

It is worth noting that the dynamic viscosity covers a wide range from 1 to 64 mPa.s in the present work as shown in Table II.1. The quantified effect of viscosity is significant enough with respect to the experimental errors which would not exceed 5%. In fact, when a drop touches the barrier, the liquid-solid collision mainly results in the shape deformation. Classical friction of liquid on solid surface is drastically reduced due to the superhydrophobic properties in the Cassie-Baxter state. The key role of viscosity is just to resist the shape deformation. To our best knowledge, there is no work on drops hurdling patterned obstacles. A similitude could be drawn with the exhaustively investigated drop impact on a solid surface. In particular, the deformation of a drop impacting on the solid surface is usually defined by the spreading factor β that is the ratio of the maximum radius to the initial one. A scaling with the Reynolds number $\beta \propto Re^{1/5}$ is often found except for high impact velocities implying high Weber numbers (Josserand and Thoroddsen, 2016). In the present work, the sliding velocity is quite low so that the scaling obtained in Eqn. II.1 is comparable to that for drop impact: the hurdling time $t_h \propto \eta^{0.24}$ due to more difficult deformation with higher viscosity here while the maximum radius for drop impact $R \propto \eta^{-0.2}$ owing to the easy deformation with lower viscosity.

II.3.3 Energy dissipation

A moving drop on superhydrophobic surface usually dissipates energy by viscous friction in the triple contact line and in the bulk, by pinning and depinning from the surface and by adsorption and detachment of liquid molecules (Butt et al., 2017). However, liquid drops hurdling barriers turn out to be more complicated. Firstly, in order to climb the barriers, drops need to overcome the potential energy in the vertical direction by converting a part of horizontal kinetic energy. Secondly, the soft liquid drops move to pass over the static barriers, which definitely lead to the shape deformation accompanied by internal viscous dissipation. Thirdly, the triple contact line is three-dimensional and in some cases, drops can take off by leaving temporarily the barriers (Figure II.8a, c and e). In view of the hurdling complexity and limited measurable parameters, the kinetic energy loss of drops immediately before and after hurdling the barriers is employed to quantify the energy dissipation.

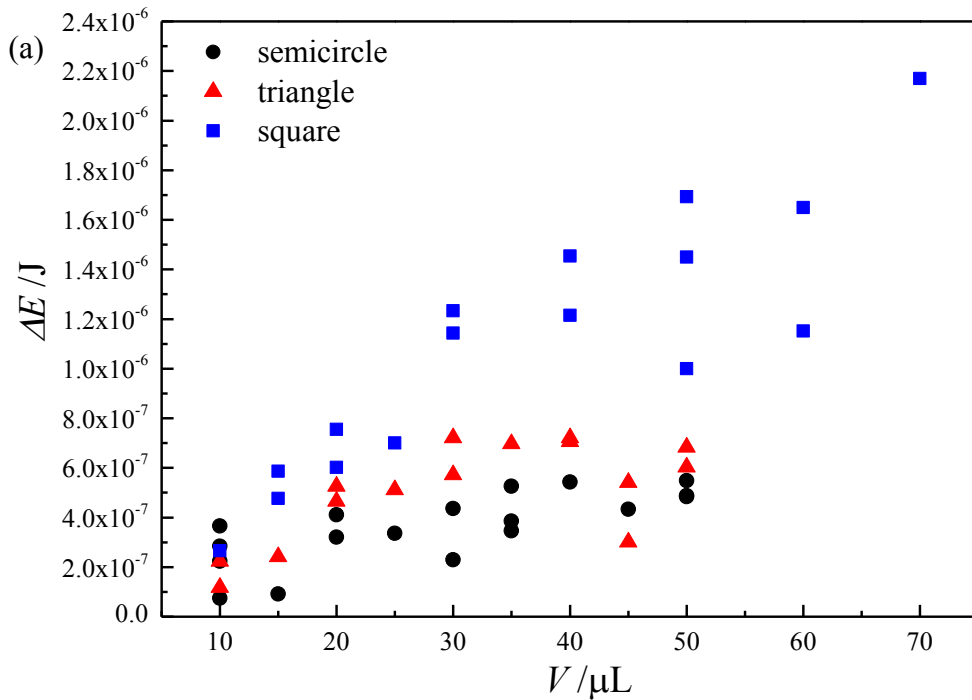
Without an enough initial kinetic energy, the drop cannot hurdle these barriers, especially the square protrusions (see Video AII.4). Thus, the kinetic energy loss is also an important parameter to characterize the efficiency of barrier-hurdling process. The kinetic energy loss before and after the barrier-hurdling $\Delta E = (v_1^2 - v_2^2)m/2$ vs. the drop volume V is plotted in Figure II.10a. Here, m is the mass of the drop. Obviously, ΔE increases from the semicircle to the triangle and to the square barrier, implying the square barrier is the most laborious geometry while the semicircle barrier is the easiest. In reality, the kinetic energy loss increases with the barrier size and the larger drop viscosity leads to larger viscous dissipation. It is worth mentioning that the liquid dynamic viscosity also has a more significant effect on the initial velocity due to the friction of drops approaching the barriers on the flat surface (Maali and Bhushan, 2008; Wang et al., 2009).

Similarly, the dimensionless kinetic energy loss based on the viscous dissipation $\Omega = \Delta E / (\eta v_1 d^2)$ vs. combination of Reynolds number Re and dimensionless shape factor ϕ is plotted in Figure II.10b. A scaling law allows gathering together all experimental data under a wide range of experimental conditions:

$$\Omega = \frac{\Delta E}{\eta v_1 d^2} = 0.41 Re^{0.85} \phi^{0.57} \quad (\text{II.2})$$

Even if other dimensionless numbers such as Weber number We , Capillary number Ca as well as Ohnesorge number Oh (Castrejon-Pita et al., 2015; Chen et al., 2002; McKinley,

2005) were considered to correlate the data of the loss of the dimensionless kinetic energy Ω and the dimensionless shape factor ϕ , the similar argument with respect to the drop impact mechanism is still reliable as for the dimensionless hurdling time stated before. In fact, the kinetic energy loss in the horizontal direction is scaled to the dynamic viscosity as $\Delta E \propto \eta^{0.15}$: higher viscosity, higher kinetic energy loss. This is comparable to the facilitated maximum deformation of a drop impacting on solid surface scaled as $R \propto \eta^{-0.2}$: higher viscosity, smaller deformation. Of course, drops hurdling a barrier through both 3D deforming and sliding mechanisms are still different from axisymmetric drop impact. Moreover, the narrow range of the surface tension is also a limited factor for our liquid drops otherwise they cannot slide and move on the solid surfaces due to the adhesion. Based on a stimulus-response principle, the dimensionless shape factor ϕ comparing the ratio between the barrier's inherent path length and the drop's capillary length is naturally responsible for the kinetic energy loss as well as the hurdling time.



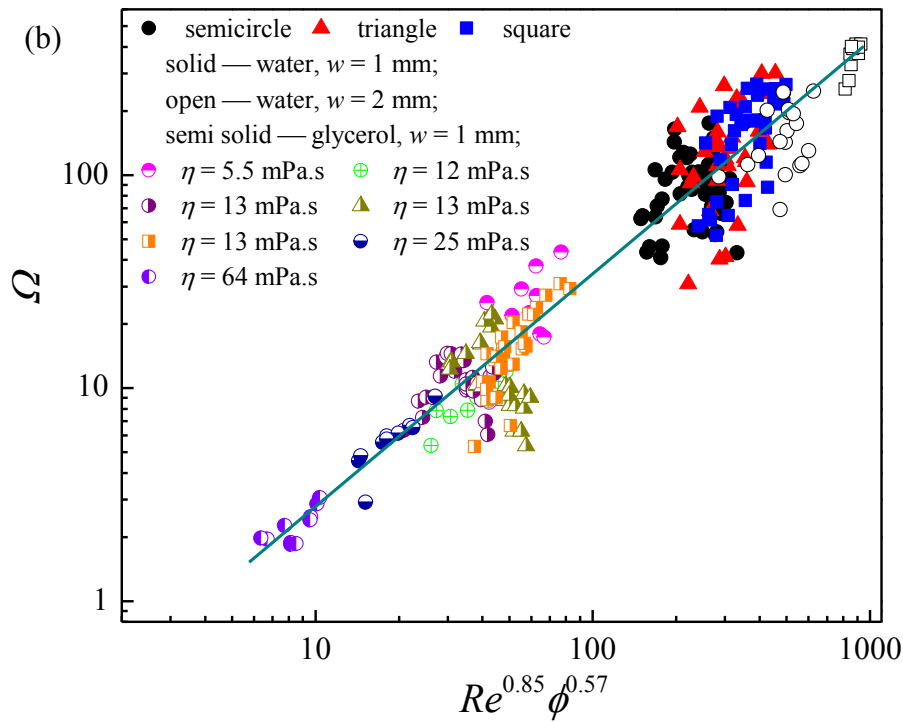


Figure II.10. Kinetic energy loss during the barrier-hurdling processes. (a), Water drops hurdling the three geometries with $w = 1$ mm. (b), Log-Log plot of dimensionless kinetic energy loss Ω vs. $Re^{0.85} \phi^{0.57}$ for all the conditions investigated. The fitting error of eqn. (II.1) was given in Figure AII.1.

II.4 Undressing water marbles on oil film

The static shape of liquid marbles on a solid surface is mainly subjected to the interplay of gravity and surface tension and marbles always attempt to minimize its surface free energy. For a given volume of inside water, the equivalent radius is $R = \sqrt[3]{3V / 4\pi}$ and the corresponding capillary length is $L_\sigma = \sqrt{\sigma / \rho g}$. Here, g is the gravitational acceleration, ρ and σ are the density and surface tension of water, respectively. When R is smaller than L_σ , liquid marbles are quasi-spherical (Figure II.6b) and the radius of contact area ($B_d/2$) is proportional to $R^2 L_\sigma^{-1}$ (Mahadevan and Pomeau, 1999; McEleney et al., 2009). While when R is larger than L_σ , liquid marbles are flattened due to the gravity and the radius of contact area ($B_d/2$) is proportional to $R^{1.5} L_\sigma^{-0.5}$ (Aussillous and Quéré, 2006). In the present work, R is controlled to be less than L_σ so that gravity is smaller than surface tension and liquid marbles are all quasi-spherical. Figure II.11 presents the static base width (B_d) of water drops and water marbles on different oil films. Obviously, water drops occupy a much larger area compared to water marbles as the former has a liquid-liquid contact and the latter's interface is covered by particles which separate the two liquids. With the increasing volume, the contact area increases no matter for water drops and water marbles.

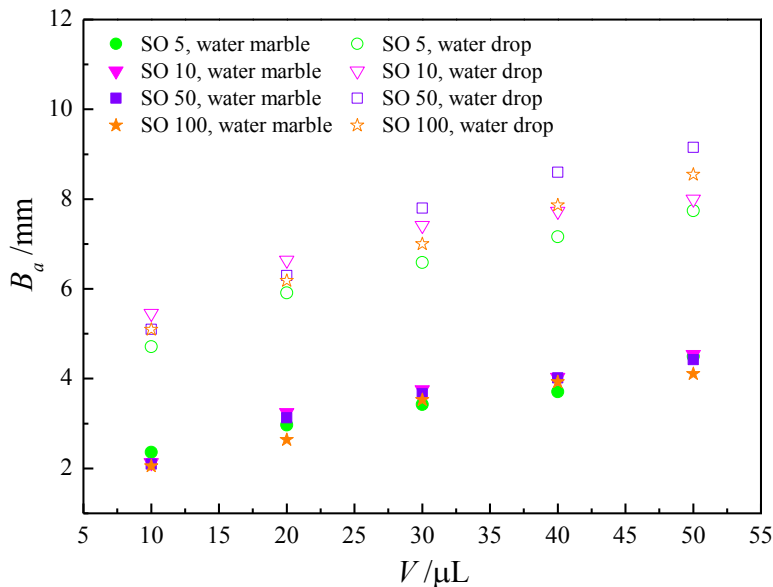
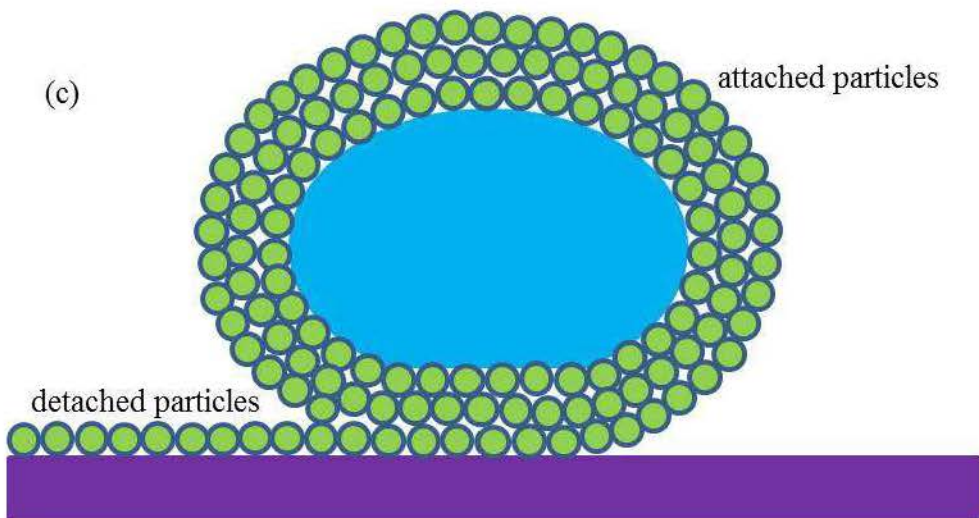
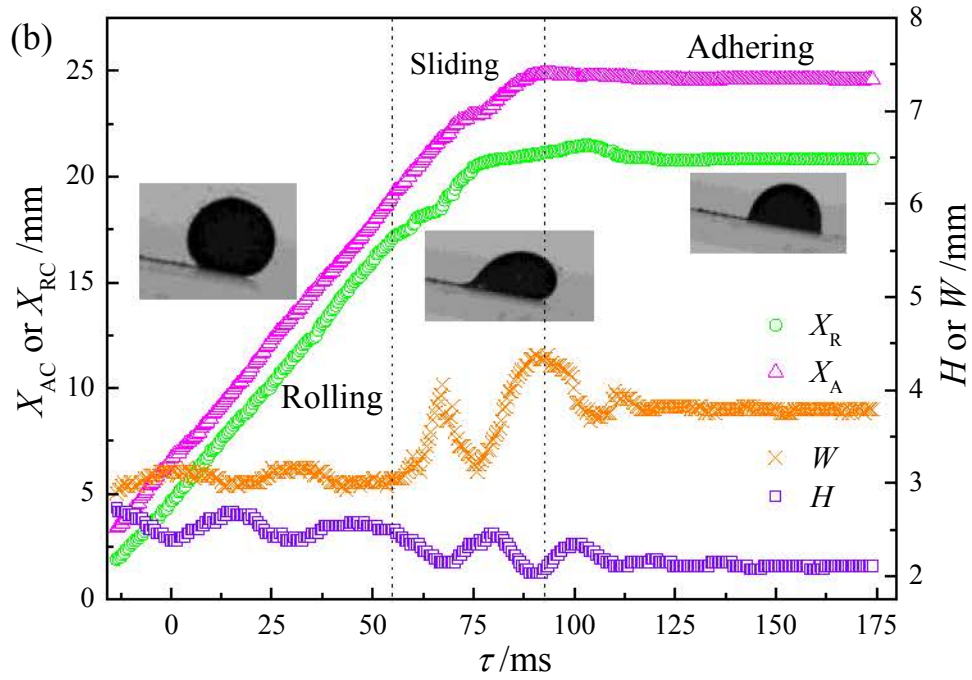
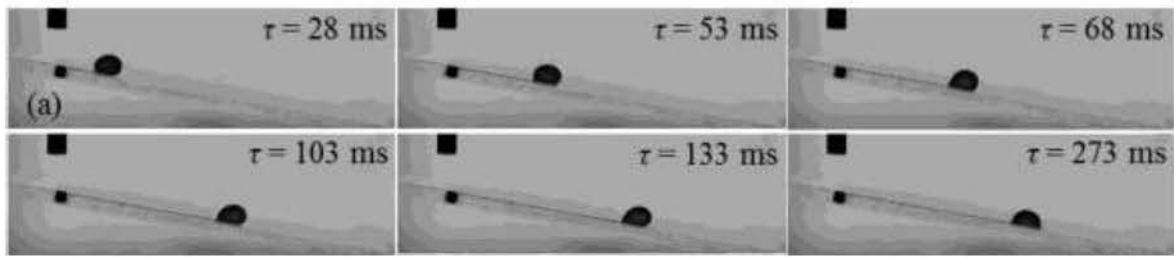


Figure II.11. The base width (B_d) of static water marbles and pure water drops on different surfaces covered by an oil film. “SO 5, water marble” means that a water marble stand static on oil film of SO 5. The experimental error is within ± 0.09 mm.

When the substrate is tilted, liquid marbles roll down along the slope (glass slide) instead of sliding, due to the solid-solid contact. This kind of rolling motion is well evidenced in previous studies (Bormashenko, 2011; Mahadevan and Pomeau, 1999; Richard and Quéré, 1999). Liquid marbles are soft solid and the rolling pattern is different from a rigid solid ball. A rolling marble can move laterally on the inclined solid surface, or even deform into a disk or a peanut under fast rotation (Aussillous and Quéré, 2001).

Figure II.12a gives an example of side view of a water marble moving on the preconditioned oil film. When water marble touches the oil film, the superoleophilic particles are wetted then captured by oil film and gradually leave from the water interface. Liquid marble remains intact in the initial moving stage on oil film, indicating that the inside water is well shielded by superhydrophobic and superoleophilic particles of multilayers. In fact, the energy of a hydrophobic particle detaching from the liquid bulk is absolutely lower than that of an oleophilic particle detaching from the oil film. With the rolling motion, particles become less and less and a distinct trail of particles leaves over the oil film. At one moment, water marble is dragged and superhydrophobic particles are finally captured by the oil film at the base of the marble at least so that there is a direct contact between the water drop and the oil film. The efficient contact friction between water and oil can then immobilize the water marble which adopts a stable state over the oil film after some shape oscillations.



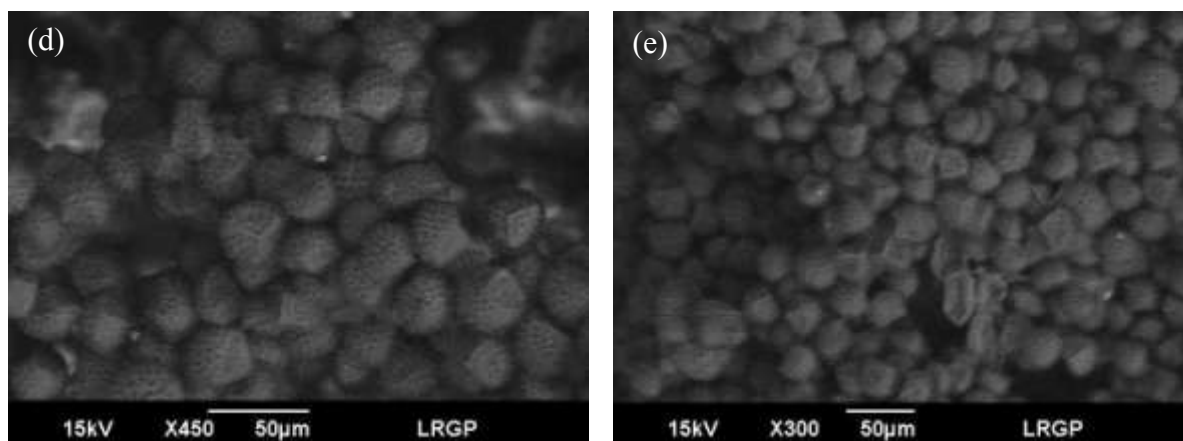


Figure II.12. Dynamical undressing process. (a) A 10 μL water marble releasing from a slope rolls down to touch the oil film (SO 100). τ is the remaining time ($\tau = t - t_0$, t is real time and t_0 is contact time). The nozzle (outside diameter 2.5 mm) in each image is set as a reference. (b) Corresponding dynamical position evolution of a water marble during its motion on SO 100 film. The velocity obtained from the rolling stage is $0.23 \text{ m}\cdot\text{s}^{-1}$. X_{AC} (X_{RC}) means the distance between the advancing (receding) point and the starting point in the image and H and W stands for the height and width of liquid marble relative to the slope (given in Figure II.6d). (c) The analytical model of the linear motion of water marble on oil film. (d) and (e) The surface image of a water marble by SEM. Due to the vacuum circumstance, the water marble is collapsed with time.

We recorded quantitatively the motion position of a water marble by means of a high-speed camera in function of time in Figure II.12b. We set time zero as the moment when the liquid marble begins to touch the oil film. Clearly, there exist three distinct stages during the marble-capturing process: linear stage (rolling), transient stage (sliding) and attaching stage (adhering). The advancing or receding position X_{AC} or X_{RC} evolves in a linear relationship with the remaining time which implies that water marble is rolling, instead of sliding, on oil film before it's captured and more importantly, the superhydrophobic particles around the water marble are certainly multilayer rather than monolayer. This is confirmed through the roughness of the drop interface by image in Figure II.6b or by the SEM in Figure II.12d and e. The constant descent velocity can be stretched back to the work of previous authors while the multilayer structure of liquid marble is well evidenced with the scanning electron microscopy imaging of marbles (Bormashenko, 2011; Richard and Quéré, 1999). The stability of liquid marbles results from particle-particle interactions and particle-liquid bulk

interactions (Nguyen et al., 2010b). The particle-liquid bulk interaction helps the liquid bulk to avoid contacting with the substrate and leads to non-stick drops while the particle-particle interaction leads to the multilayer structure of liquid marble. As indicated by the schematic diagram in Figure II.12c, the superhydrophobic particles are progressively undressed and captured by the oil film for a rolling water marble. A near constant rolling velocity is maintained until a physical contact between water and oil film when superhydrophobic particles begin to be removed at the base of the liquid marble.

At the transient stage, particles continuously detach and multilayers become locally monolayer, especially at the base of the liquid marble. Under this circumstance, the water marble sliding over the oil film and some fluctuation can be observed. Logically, H decreases and W increases during the whole sliding stage. However, it needs mentioning that W and H undergo two local extrema. This can be explained that the elongated tail corresponding to the first extremum is released quickly due to the inertia and at this case, W decreases and H increases. Then a new tail forms with the marble advancing downhill and W increases and H increases again until the second local extrema. This time, the tail covers a longer distance compared to the first local extrema, revealing the tendency of being captured. Once again, the tail retracts a little and W decreases and H increases. With the increase of the occupation region of the monolayer, water marble is captured due to an efficient water-oil friction. After several times of advancing and receding shape dumping, water marbles spread on oil film in a form of a cap. The similar peeling dynamics is observed in our other sequences. In Figure II.13a, the final shape of captured water marble is quite similar to that of a pure water drop on oil film and the apparent contact angles are almost the same. This reveals a physical water-oil contact. Compared to newly-formed water marbles standing static on oil film or glass substrate, the distinct small contact angle of captured water marble implies that the particles in the bottom of water marble should be undressed almost totally. Such transparent bottom of water marble without particles leads to promising application of the optical probing and sensing in medical, biological and chemical analyses.

In addition, the trails were recorded after one day evaporation of captured marbles. From Figure II.13b, numerous particles are effectively captured once it moves on oil film. The uniform trail indicates that water marble undergoes limited shape deformation and the contact area almost remains unchanged. Due to the complex interactions between different phases, the final trail of attached marbles is asymmetrical to the particle-discharging path. The non-spherical shape of superhydrophobic particles could also play a role in this phenomenon.

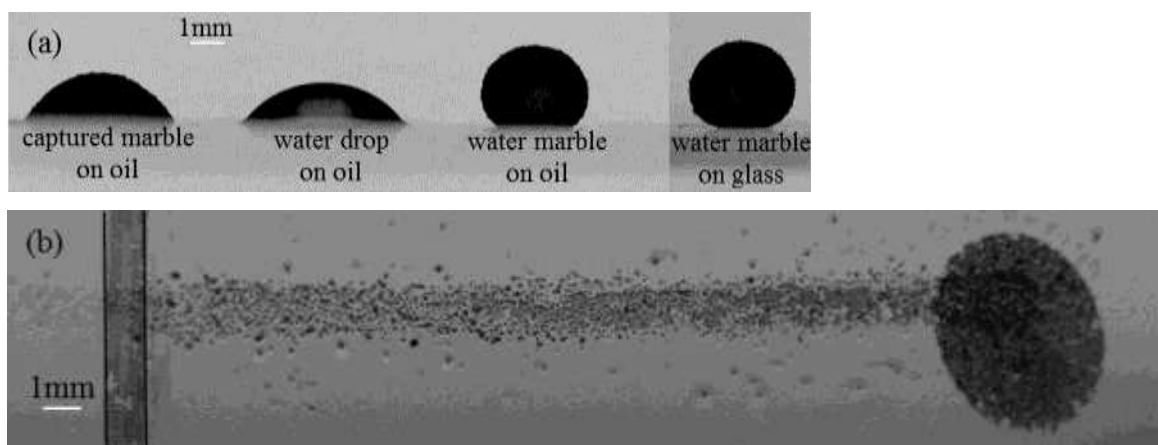
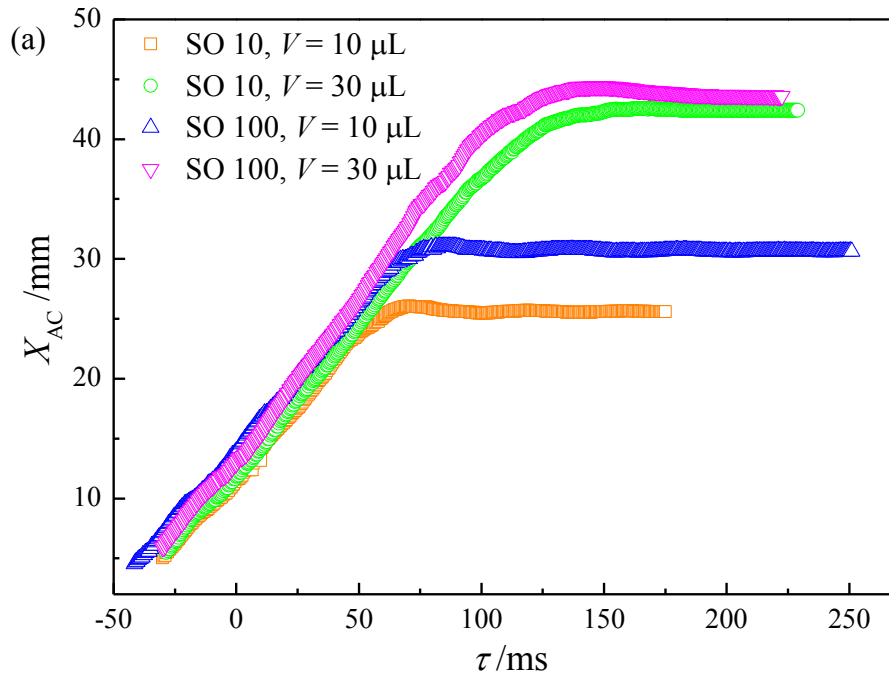


Figure II.13. (a) Apparent contact angles of a 10 μL water marble captured by the SO 100 film (53°), a 10 μL water drop wetting on SO 100 film (45°), a newly-formed 10 μL water marble resting on SO 100 film (141°) and a newly-formed 10 μL water marble resting on glass substrate (155°). (b) The trail after evaporation of a 10 μL water marble moving on SO 100 film.

As the initial coating of a water marble is quite difficult to be controlled perfectly, such as for the number of particle layers and their organization, it is delicate to compare quantitatively the capture length required for immobilizing the water marble on oil films. Moreover, neither the shape nor size of particles shown in Figure II.6a is completely homogeneous. Basically, for the same oil film, the larger volume of water marbles tends to cover a longer distance (Figure II.14a). In fact, the number of revolution of water marbles on oil film can be roughly estimated through the ratio of their covered length and their apparent perimeter. The results reveal that whatever the volume of drops, the revolution number remains quite similar, typically ranging from 3 to 3.5 and confirmed by the camera visualization. However, the oil viscosity plays obviously a role in the final liquid–liquid friction for immobilizing the water marble (Figure II.14b). The rolling stage undergoes more quickly to the adhering stage when the oil film is increasingly viscous. This deceleration dynamics can be described by an exponential decrease function $\exp(-k\eta\tau)$ where η and τ are the viscosity of oil film and the remaining time, respectively. The solid lines representing the exponential decay as shown in Figure II.14b describe satisfactorily the experimental observations of the deceleration. This observation can be argued that when marbles are undressed to the last layer, the more viscous the oil film, the larger the drag force due to

classical viscous friction. It can be concluded that the capture efficiency of water marbles tends to increase with the oil viscosity and decreases with the drop volume.

Finally, several experimental evidences support the assumption that the water marble would display a locally monolayer structure of particles when its motion is switched from rolling to sliding: the comparable value of the contact angle between the captured marble on the oil film (Figure II.13a) and a conventional water–oil system; the particles' trails behind the liquid marble shown in Figure II.13a reveal a progressive dynamics of undressing multiplayer enveloping the marble; the similar rolling number described above whatever the marble volume seems to confirm a multilayer structure.



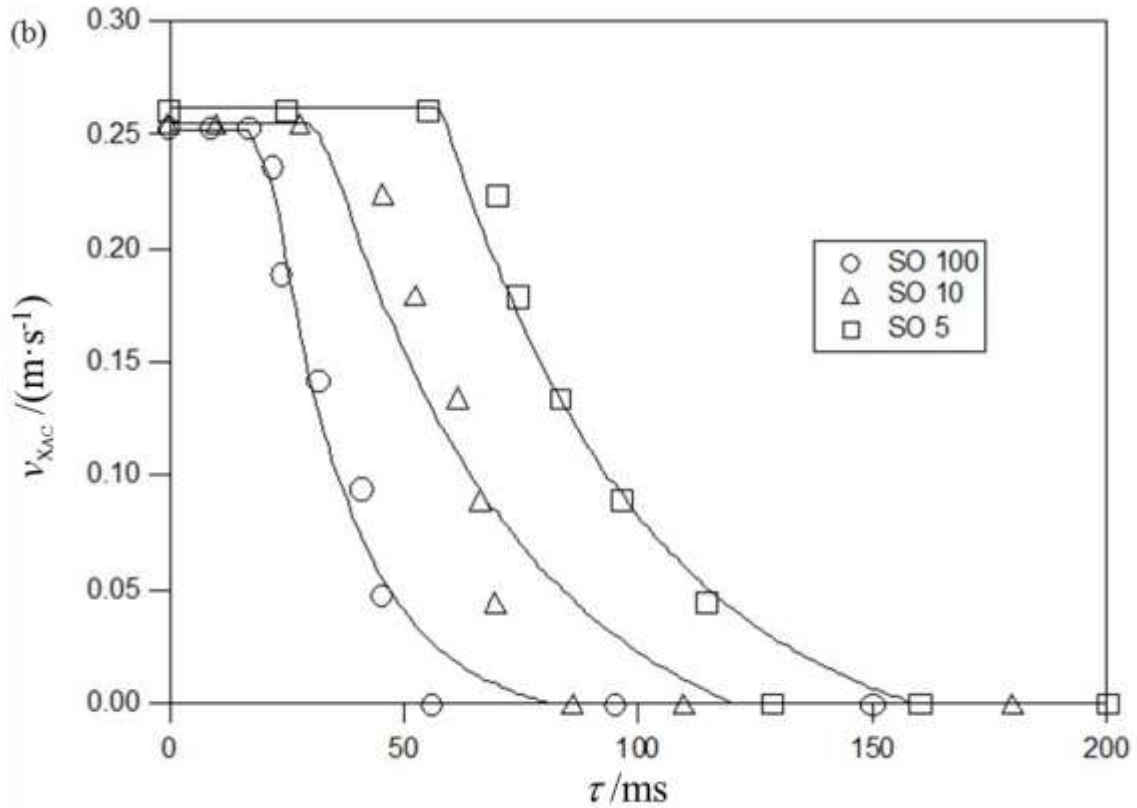


Figure II.14. The position a) X_{AC} and b) velocity $v_{X_{AC}}$ of water marbles running down on oil films. The solid lines represent the modelling by an exponential decay $\exp(-k\eta\tau)$.

II.5 Slope motion of liquid drops and liquid marbles

II.5.1 Drops downhill on superhydrophobic surface

Figure II.15 presents the dynamics of liquid drops moving on the superhydrophobic slope with a 15° angle. After released from the exit of the needle, the drops start to move due to the gravitation on the slope. The largely reduced friction on the slope makes the drops downhill the slope easily. Though drops will continue to move on the horizontal surface, it's beyond our interest. Thus we set the moment that the base of drops approaching the end of the slope as $t = 0$ ms. During the downhill process, drops also undergo deformation: sometimes oblate, sometimes plump. From Figure II.15a, b and c, the larger the drops, the more obvious the deformation; and the more viscous the drops, the less the deformation. In addition, the large viscosity leads to time-consuming downhill process.

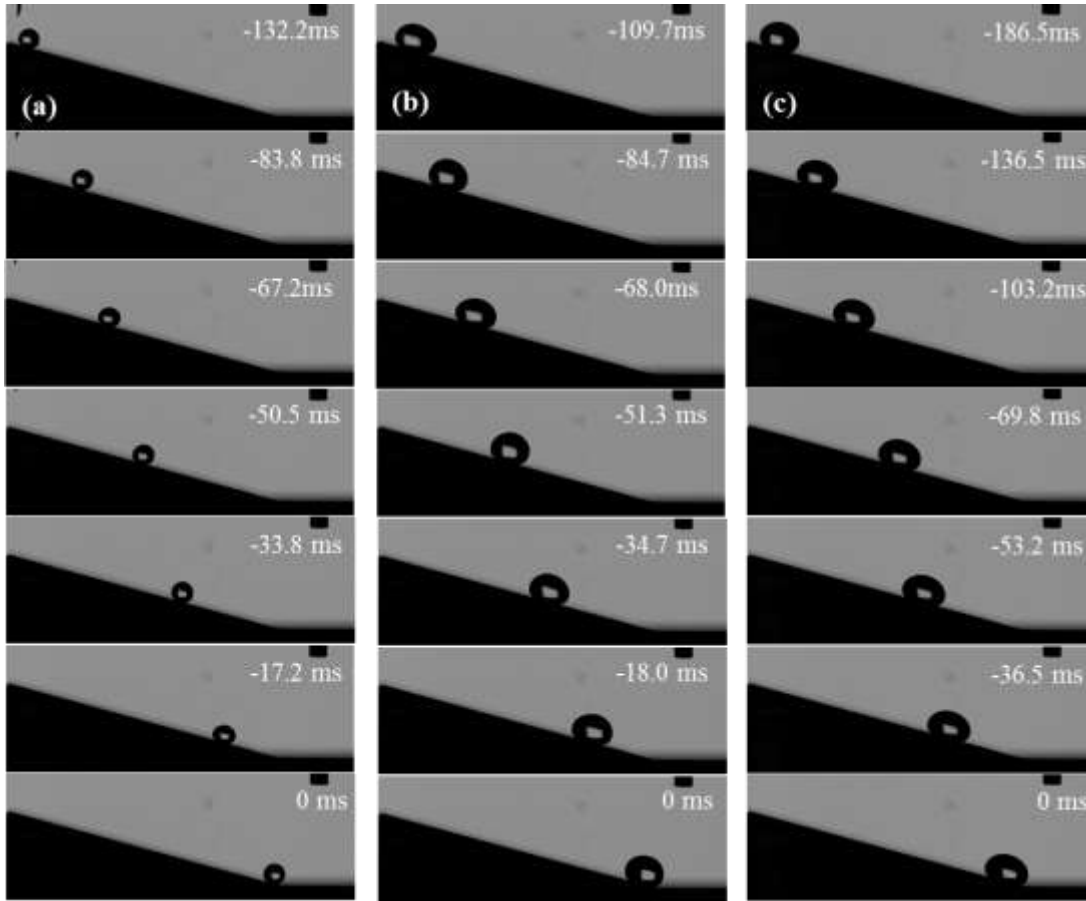
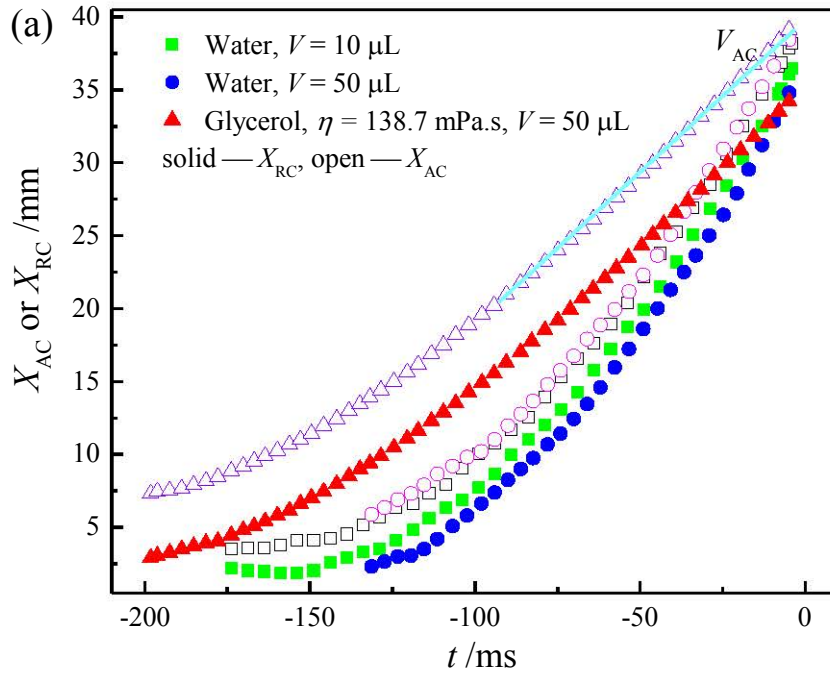


Figure II.15. (a) 10 μL water drop downhill on the superhydrophobic surface, $Oh = 0.0023$; (b) 50 μL water drop downhill on the superhydrophobic surface, $Oh = 0.0017$; (c) 50 μL 85% glycerol drop downhill on the superhydrophobic surface, $Oh = 0.2301$.

Figure II.16 shows the quantitative characterization of drops moving on the superhydrophobic slope. The evolution of X_{RC} or X_{AC} indicates that drops accelerate in the initial stage until the final steady state where the velocity is constant. The constant speed implies the rolling instead of sliding motion which can be evidenced in several previous works (Allen and Benson, 1975; Mahadevan and Pomeau, 1999; Richard and Quéré, 1999). The final stationary velocity decreases with the increasing liquid viscosity and this will be detailed analyzed in the later part. In Figure II.16a, the difference between X_{RC} or X_{AC} implies that the base of drops contacting the slope is large when the drop volume is large. Figure II.16b gives the spatial width and height of drops in two dimensions relative to the slope. The smaller drop deforms more frequently and the viscous drop almost remains the same shape. Furthermore, the deformation factor F_{max} in Figure II.16c confirms directly this

point. Here, F_{\max} is defined as the maximum ratio between the width and height, i.e. $F_{\max} = \max(W/H)$.



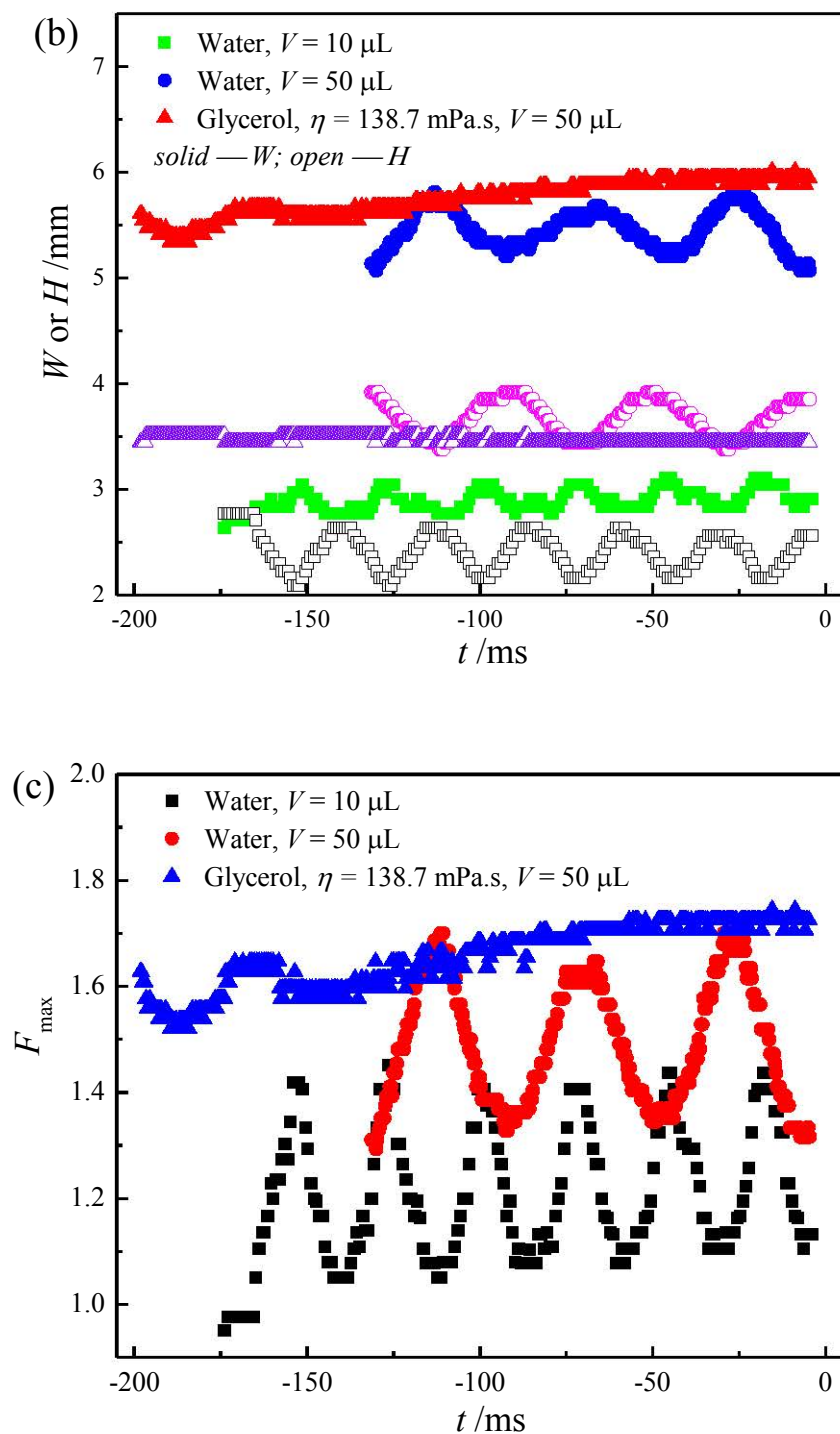


Figure II.16. (a) X_{AC} and X_{RC} evolution of liquid drops down-hilling the slope; (b) W and H evolution of liquid drops down-hilling the slope; (c) F_{\max} evolution of liquid drops down-hilling the slope.

II.5.2 Liquid marbles downhill on a glass slide

Similarly, liquid marbles moving on the glass slide are displayed in Figure II.17. The glass slide is of no oil film with a tilting angle of 15° . The time $t = 0$ ms and other variables share the same definition with the above liquid drops. Water marbles deform to go ahead in the similar way with liquid drops, except a small difference in the trails that are left behind on the glass slide due to the fluffy structure of liquid marbles. Taking a close look at the particles on the surface of marble (as marked in Figure II.17b), a rotating motion can be observed. Bormashenko *et al.* (Bormashenko et al., 2009) once tried a chemical reaction to characterize the rolling motion of liquid marbles and found that there is no contact between the liquid filling the marble and the solid, and the rolling motion of liquid marbles resembles mechanical bearings.

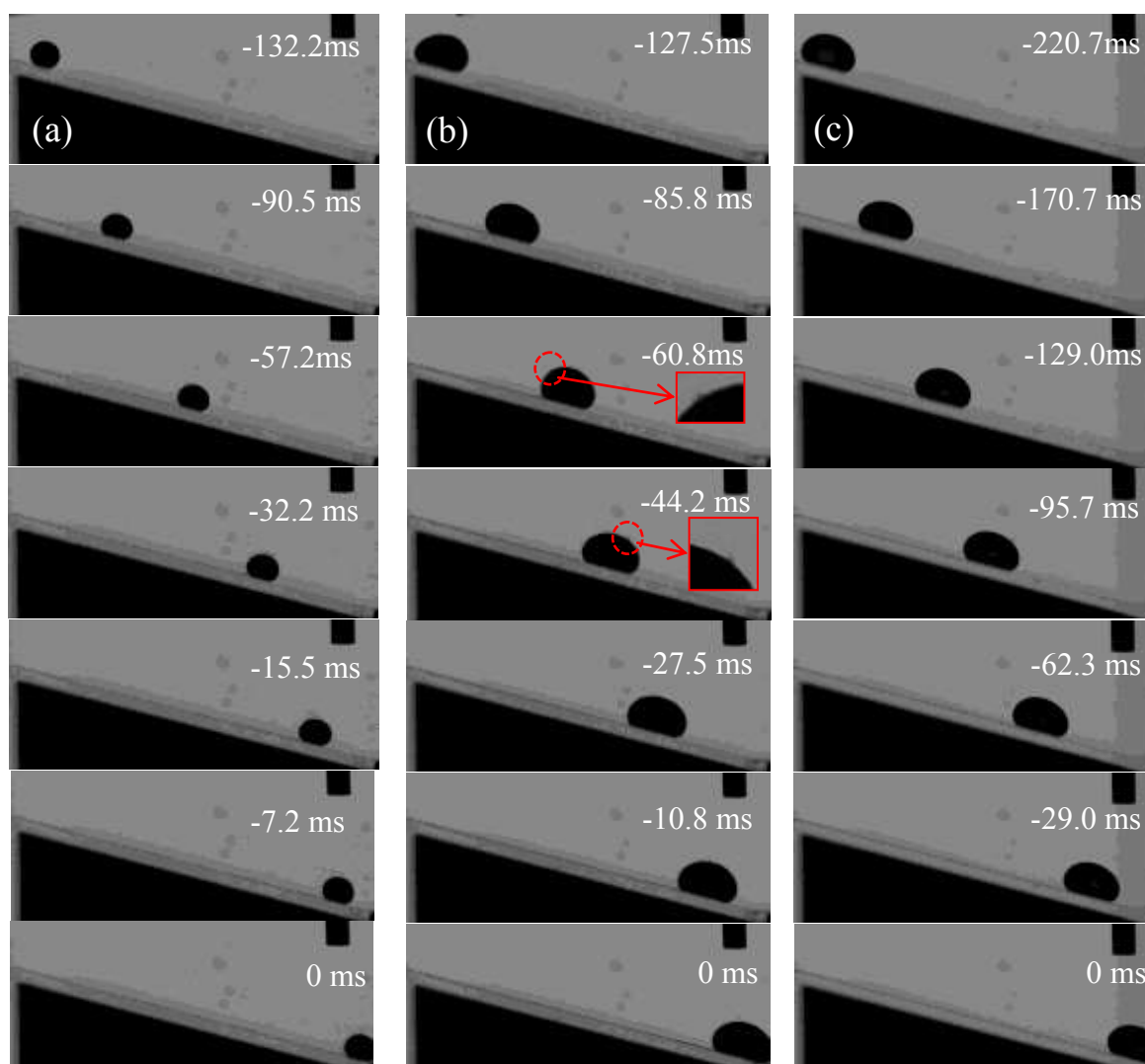
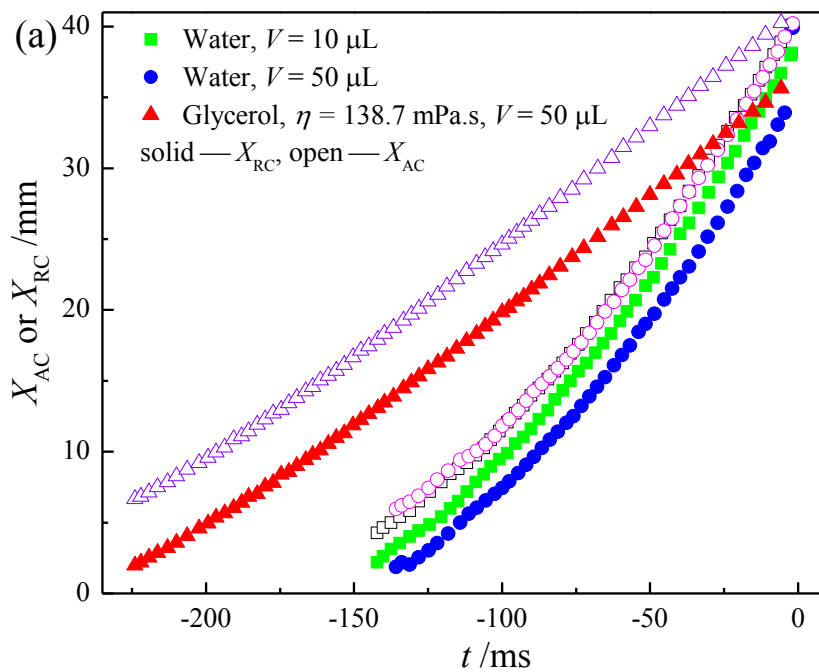


Figure II.17. (a) $10\ \mu\text{L}$ water marble downhill on the glass slide; (b) $50\ \mu\text{L}$ water marble downhill on the glass slide; (c) $50\ \mu\text{L}$ 85% glycerol marble downhill on the glass slide.

The motion dynamics of water marbles is quite similar to that of liquid drops. From Figure II.18a, the water marbles firstly undergo an obvious acceleration and then reach a stationary velocity. While glycerol marbles rapidly enter into constant-velocity stage. Now, the rolling motion is also proved for liquid marbles. Figure II.18b implies that the small viscosity of the inner liquid results in more deformation. In the same way, the deformation factor F_{\max} in Figure II.18c demonstrates directly that the smaller marble undergoes less deformation.



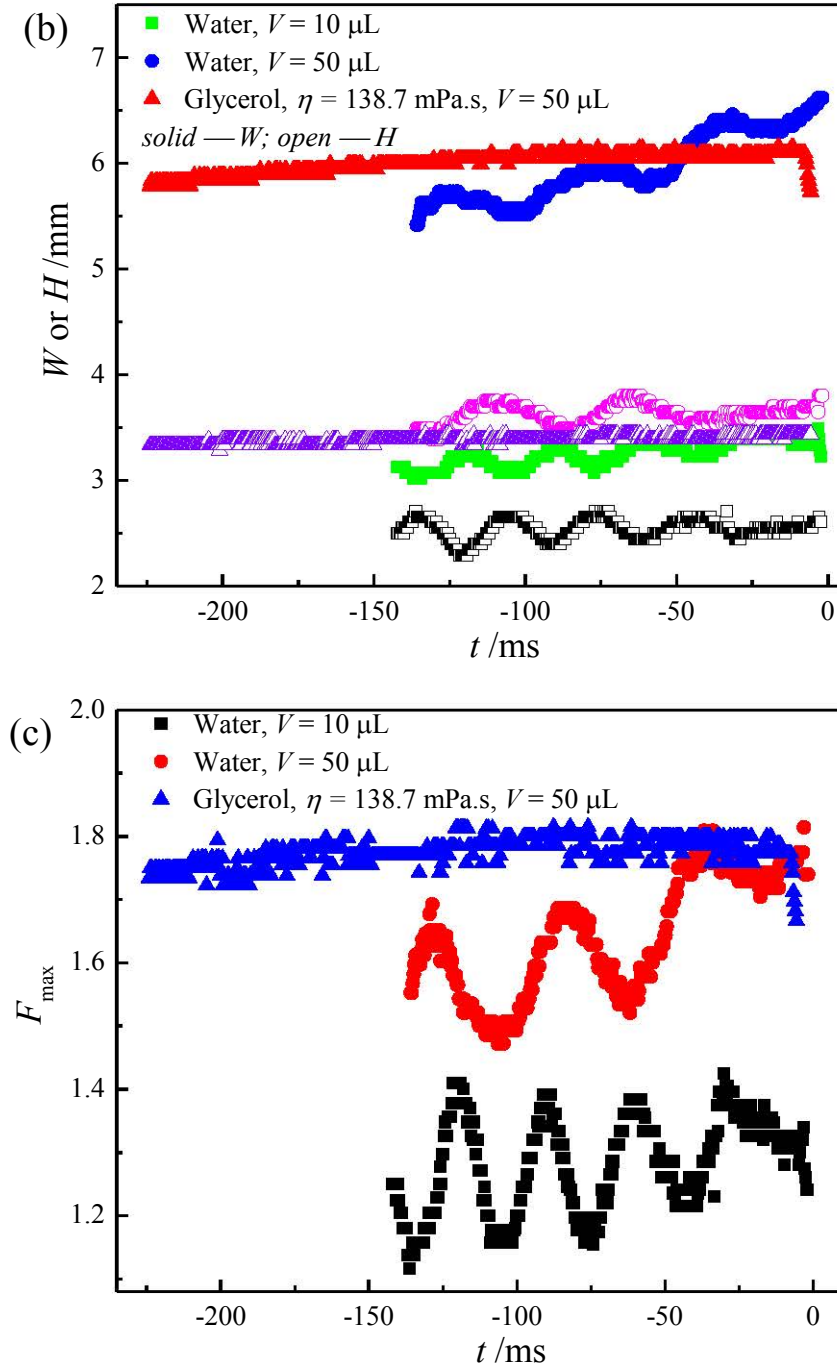


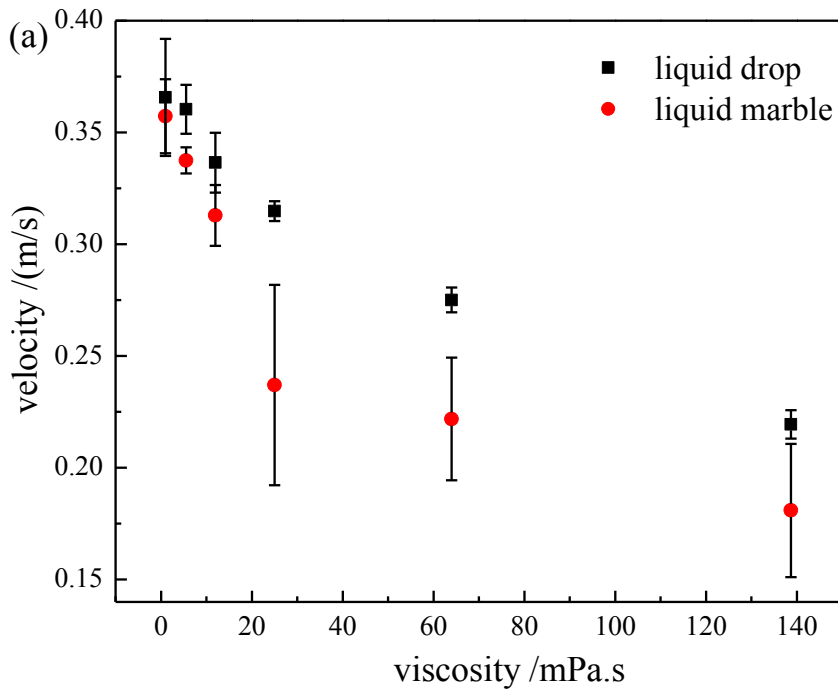
Figure II.18. (a) X_{AC} and X_{RC} evolution of liquid marbles down-hilling the glass slide; (b) W and H evolution of liquid marbles down-hilling the glass slide; (c) F_{\max} evolution of liquid marbles down-hilling the glass slide.

II.5.3 Stable velocity and deformation

According to the above results, both liquid drops and marbles exhibit a stationary moving velocity on the slope. With the increasing volume, the stationary velocity tends to

decreases. The mean stationary velocity of liquid drops and marbles of various viscosities is summarized in Figure II.19a. Clearly, the final velocity of both liquid drops and marbles decreases with the viscosity. Surprisingly, the velocity of liquid drops is obviously larger than liquid marbles, implying that the contact of liquid marble with the glass surface induces more friction than that between drops and the superhydrophobic coating. This can be rationalized that liquid drops are directly exposed to the superhydrophobic surface and the strong repellency makes the friction between liquid and solid largely reduced. While for liquid marbles, the enveloping superhydrophobic particles contact directly with the glass slide, leading to the solid-solid friction.

It is observed that F_{\max} increases with the increasing volume. Furthermore, the mean F_{\max} versus the fluid viscosity is plotted in Figure II.19b. Overall, F_{\max} of liquid marbles tends to be larger compared to liquid drops. The more the deformation, the more the energy dissipation. The friction of solid-solid is larger than solid-liquid, which naturally leads to the difference of sliding velocity.



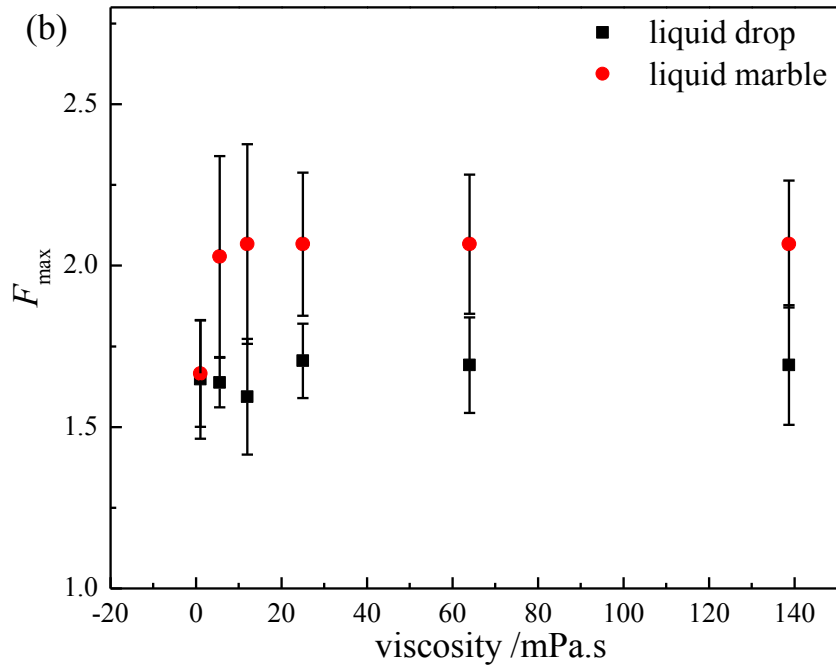


Figure II.19. Velocities (a) and F_{\max} evolution (b) of liquid drops and marbles during the down-hilling process for various liquids of different viscosity.

II.6 Conclusion

In this part, the manipulation of drops was accomplished by modifying either the solid surface or liquid interface.

Firstly, through the spraying-coated superhydrophobic substrate, the complex dynamics of drops hurdling different barriers was experimentally investigated under various conditions including noticeable drops' nature and barriers' geometry. Compared to a rigid solid ball, drops' deformation is just their self-adjustment to the external stimulus and is significantly advantageous to their hurdling process. However, it is still delicate to quantify exactly the drop deformation during the hurdling process due to the three-dimensional and complex spatio-temporary shape patterns. Two empirical relationships are proposed to describe the key hurdling parameters, i.e. hurdling time and kinetic energy loss, which reveal the main hurdling dynamics and reflect partially the shape deformation during the hurdling process. Irregular solid surfaces with even obstacles exist everywhere and affect the liquid motion involving triple contact lines. The topic of drops hurdling obstacles by deforming themselves not only generates fascinating academic behavior but also promises numerous potential applications, such as directional drop transportation, self-propulsion, self-cleaning and anti-icing surfaces, coating and spraying.

Then, by enveloping superhydrophobic particles on a water drop's surface, the undressing motion of water marbles on a thin oil film was preceded. In all cases, water marbles firstly undergo a linear motion stage to remove progressively the outside loose particles; followed by the transient stage where the compact particles are further undressed; finally water marbles are immobilized and adherent to the oil film when nearly all particles at the base of the water marble are removed. The contact angle of captured marbles after undressing is similar to that of static water drops on oil film, providing evidence that the bottom of water marbles is nearly void of particles to display a water-oil direct contact. In addition, we found that the larger the liquid volume, the longer the distance for marbles to undergo; the larger the oil viscosity, the quicker the transient stage to immobilize liquid marbles. Our experimental results gain insight into the understanding of rapid coating process of liquid marbles as well as developing potential applications in medicine, pharmaceuticals, cosmetics and home and personal care products.

Finally, with the aim of comparing the two different approaches to generating superhydrophobicity, the downhill motion was conducted on the slope of the same tilting angle: liquid drops on a superhydrophobic surface and water marbles on a hydrophilic

surface. Both liquid drops and liquid marbles pass through an acceleration towards a stationary sliding. No matter for liquid drops and liquid marbles, the stationary velocity decreases with the liquid viscosity and the more viscous the less deformation. Importantly, the stationary velocity of liquid marbles is lower than that of liquid drops and vice versa for F_{\max} . Our experimental results illustrate that both the drops rolling on non-stick surface and non-stick marbles on solid substrate share similarities and differences and the superhydrophobicity of spraying coating is proved to be more efficient for the sliding than enveloping particles.

PART III: Manipulation of dripping-on-substrate (DoS)

In the first part, the pinch-off instability of an interface was introduced and in the second part, the stability of interfaces was obtained by superhydrophobic properties and then manipulated under different contexts. However, the initial contact followed by wetting of a liquid drop on a substrate and the pinch-off of a liquid drop are both rapid phenomena behind a lot of applications. The former concerns the bridging of two different phases while the later evolves the rupture of a continuous medium. How the contact or breakup singularity point is established at microscale or even molecular scale? Considering the resolution limitation of high-speed cameras, an electrical approach can give some indicative information in the very vicinity of the breakup or contact point. In this part, both of them will be discussed through designing a dripping-on-substrate system with the detecting methods combining the high-speed camera and high-speed electric device.

III.1 Literature review

III.1.1 Drop spreading

The wetting and spreading of liquids on a surface have been investigated by a lot of researchers due to the academic interests and their wide applications, such as the raindrop on the windshield, removal dirt by detergent solutions, inkjet printing (Basaran, 2002; Yarin, 2006), spray coating (Weinstein and Ruschak, 2004), painting, drop-wise condensation and pesticide deposition (Bergeron et al., 2000; Roux and Cooper-White, 2004). In early times, Huh and Scriven (Huh and Scriven, 1971) considered the exceptionally complicated hydrodynamic problem of flow near the triple line of a liquid spreading on a solid surface. Since then, much work has been performed on the wetting and spreading dynamics and a classic review is given by de Gennes (de Gennes, 1985).

When a liquid drop deposited on a solid surface, a microscopic precursor film propagates ahead of the drop and then the interfacial force drives drop spreading until it reaches the final equilibrium contact angle (Wang et al., 2014). For a completely wetting surface, the initial spreading is mainly dominated by the inertia, while the later spreading is dominated by the viscous force (Biance et al., 2004; Bird et al., 2008). The initial spreading is faster than the later one (Saritha et al., 2005; Tanner, 1979). While for partially wetting surface such as hydrophobic surfaces for aqueous drops, spreading is usually an integral part of impact process (Lv et al., 2016). Lavi and Marmur (Lavi and Marmur, 2004) proposed a

stretched exponential power law which described very well the kinetics of partial drop spreading.

Previous studies experimentally, theoretically or numerically, devoting to the wetting and spreading of liquids on solid surface, considered the effect of liquid properties (density, viscosity and surface tension), solid state (roughness, elasticity, material) and operating conditions (temperature, pressure, spontaneous or impact) (Bertola, 2013; Chen et al., 2013; Jarecka et al., 2015; Josserand and Thoroddsen, 2016; Liang et al., 2009; Marmur and Lelah, 1980; Ravi et al., 2013; Sun et al., 2013; Wang et al., 2014; Yoo and Kim, 2015). The main findings include that aqueous drops spread faster on the hydrophilic surfaces than they do on the hydrophobic surfaces and larger drops spread faster than smaller drops. For small drops with radius (R) below the capillary length, $\lambda_c = (\sigma/\rho g)^{0.5}$, the spreading radius (r) evolves with the relationship $r \sim R(\sigma/\eta R)^{1/10} t^{1/10}$, which is called Tanner's law (Lavi and Marmur, 2004). Here, ρ is the liquid density, g is the gravity acceleration, σ is the surface tension and η is the dynamic viscosity. While for drops with radius $R > \lambda_c$, the gravity effect becomes important and the spreading radius follows another power-law $r \sim R(R\rho g/\eta)^{1/8} t^{1/8}$, which is called Huppert's law (Cazabat and Stuart, 1986; Huppert, 1982; Lopez et al., 1976).

However, emphasis is turned to the very initial dynamics of drop spreading on a surface. Bird *et al.* (Bird et al., 2008) studied the early stage of drop wetting on a solid surface and demonstrated that the spreading radius of drops followed a power law whose exponent is only dependent of the equilibrium contact angle of the liquids on the surface, i.e. the surface wettability. This point is lately demonstrated numerically by Thampi *et al.* (Thampi et al., 2016). Chen *et al.* (Chen et al., 2011; Chen et al., 2013) investigated the drop wetting on a soft surface and further confirmed that the early stage of spreading is also dominated by the inertia and the wetting dynamics mainly depends on the wettability, but not on softness. They derived a similar scaling law with exponent ranging from 1/5 to 1/2. Cazabat and Stuart (Cazabat and Stuart, 1986) considered the effect of surface roughness on liquid wetting and proposed that the spreading dynamics followed a power-law with exponent ranging from 0.25 to 0.40. Recently, Mitra and Mitra (Mitra and Mitra, 2016) found that a viscous regime $r \sim t$ went before the well-established inertial regime $r \sim t^{1/2}$ by experimentally observing the spreading of a liquid drop on a substrate kept submerged in another liquid medium.

Some authors tried to approach to the very early regime of spreading by a high-speed camera even with synchronized bottom and side views (Eddi et al., 2013; Mitra and Mitra,

2016), the initial contact and spreading of a liquid drop on a substrate is still elusive due to the very fast phenomenon involved. Winkels *et al.* (Winkels et al., 2012) accessed previously unexplored length and time scales, using two complementary methods: molecular dynamics (MD) simulations and high-speed imaging, and provided a detailed picture on how the initial contact between the liquid drop and the partially wetting surface was established. In this part, we design a dripping-on-substrate (DoS) system to investigate the initial contact and spreading of an electrolyte solution through capturing both the images from a high-speed camera and the electric signals from an ultra-high-speed electric device.

III.1.2 Bottleneck of pinch-off investigation

The previous authors observed that the pinch-off of drops and bubbles exhibits a universal self-similar behavior and the curvature-induced interfacial velocity increases and diverges up to the limit where the continuous approach is still valid. The minimum neck width decreased in time as a power law with an exponent of $2/3$ for the low-viscosity liquids and an exponent of 1 for the viscous liquids in air, both of which showed to be consistent with the Rayleigh-Plesset equation. However, it has been confirmed that the final pinch-off reach up to the nanometer scale by conducting fluid (Burton et al., 2004), cannot be measured by optical devices.

Provided molecular dimensions are not reached first, viscous effect would come into play when the minimum neck width reached to the scale of viscous length. For water, the viscous length scale l_η is just 10 nanometers, far below the present resolution of optical devices. For viscous fluids like glycerol, the viscous length scale l_η is in the order of centimeter which is easily observable through camera. Especially, viscous effect on two-fluid drop pinch-off is embodied in viscosity ratio between the internal and external fluids. These details about drop pinch-off were discussed in our Part I.

Though a lot of attention has been devoted to this area, there still exists challenge to both simulation and experimentation. So far, most numerical methods are based on the approximations to the Navier-Stokes (NS) equations, through modeling the dynamics by one-dimensional slender jet analysis (Eggers and Dupont, 2006) and boundary element analysis (Bechtel et al., 1992). Some researchers demonstrated the change of scaling law as pinch-off approached by numerical methods. However, in the vicinity of singularity point, the NS equation is no longer valid.

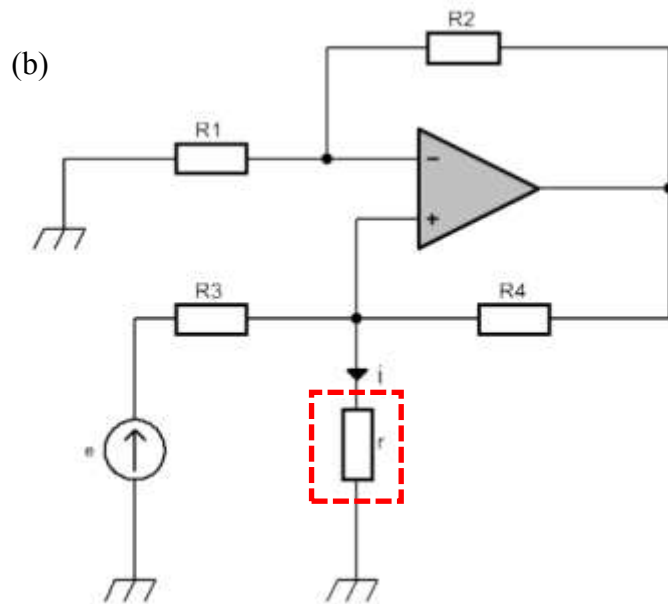
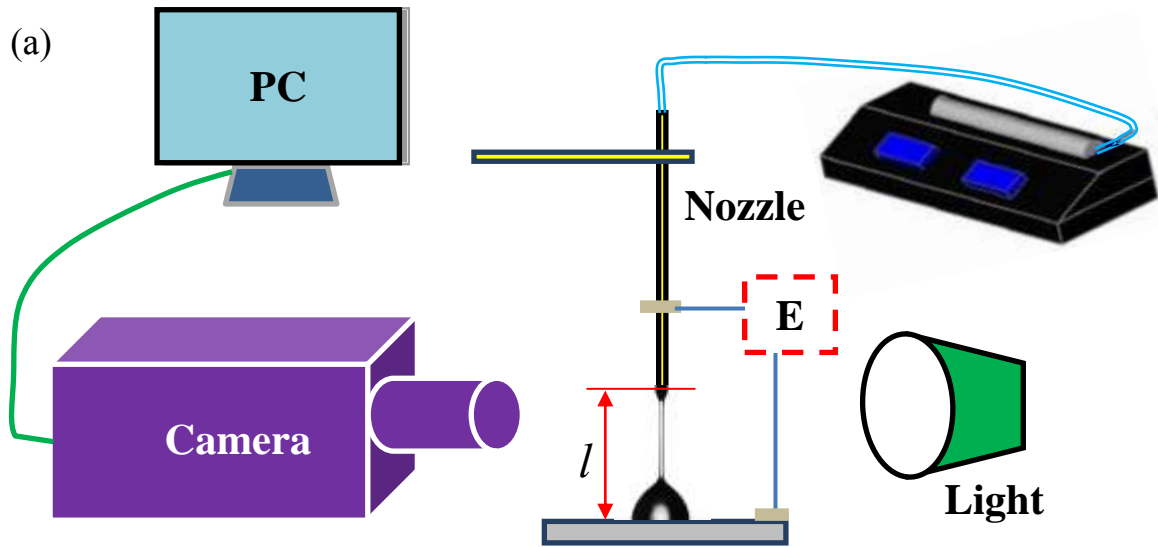
Meanwhile, experimental studies of drop pinch-off are also challenging due to the small length and short time scales in such a fast phenomenon. Optical visualization is the most common method to experimentally study the pinch-off dynamics in these years. The presently most sophisticated high-speed camera can reach to the length scale of μm with the help of a microscopy and time scale of μs . Considering the resolution limitation of optical camera, Burton *et al.* (Burton et al., 2004) tried to measure the electric resistance of a mercury bridge as it undergoes pinch-off. Their electric measurements could probe the region of the singularity point down to nanosecond time scale and nanometer length scale and demonstrated that the resistance of the liquid bridge diverges as $t^{-2/3}$, as expected for inviscid pinch-off.

The application of electric field in studying drop pinch-off provides a new approach to access the fast phenomenon (Guo et al., 2015; Zhang et al., 2015). Thus, in this part, the pinch-off dynamics of common fluids would be further investigated through the combining methods of optical and electric devices. In addition, the thinning of non-Newtonian fluids would also be tried considering the complicated long cylindrical filament and bear-on-strings characteristics.

III.2 Experimental details

The experiment setup of dripping-on-substrate (DoS) system was illustrated in Figure III.1a. The stainless steel nozzle (inner diameter $d=0.6$ mm and outside diameter $d'=0.97$ mm) were used to generate drops through a syringe pump. A round plate of stainless steel or bronze with dimensions of 4 (diameter) \times 0.4 (thickness) cm, was horizontally placed under the nozzle. The distance (l) between the nozzle and the plate was adjusted to maintain the non-natural drop formation, i.e. the connection of the circuit. The electric voltage of fluid-plate bridge (marked as red 'E') was measured using an ultra-high-speed data acquisition system developed by the electronical service SIEL of our laboratory. The electrical circuit was given in Figure III.1b and the DC current intensity was precisely controlled to be constant $I=0.1$ mA. One electrode was connected to the nozzle and the other one was connected to the plate, so that the fluid serves as a liquid wire in the circuit.

The stainless steel and bronze were fabricated with high-precision milling in our mechanical workshop. The scanning electron microscope (SEM) of the surface state for stainless steel and bronze was given in Figure III.1c. Bronze is less hard compared to the stainless steel and thus there exist fault texture. Particularly, the atomic force microscopy (AFM) in Figure III.2 gives a more clear structure of the surface roughness. The maximum height of the roughness is within 1 μm , implying the smaller roughness of both stainless steel and bronze. In addition, bronze surface is indeed rougher than the stainless steel surface as there are local ups and downs.



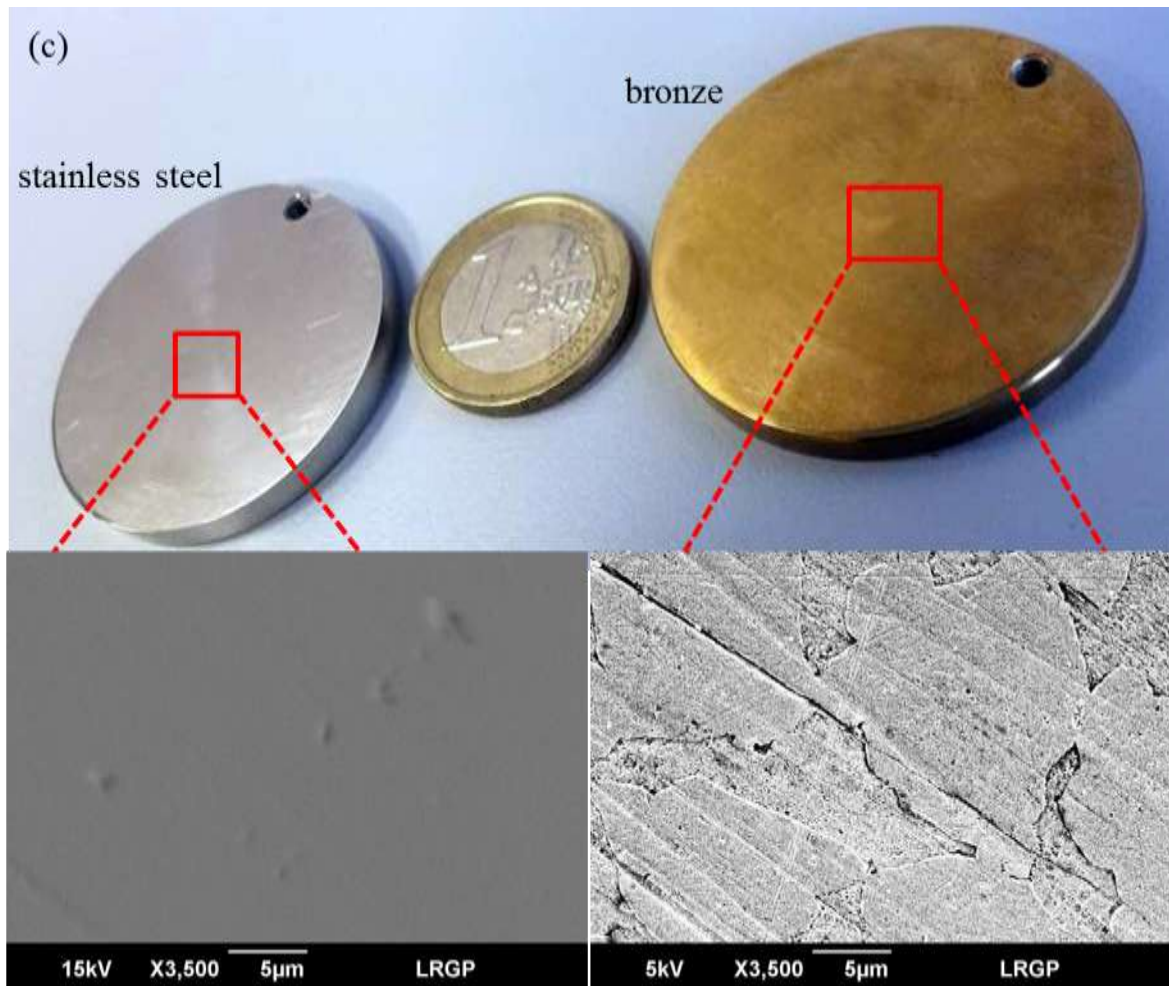
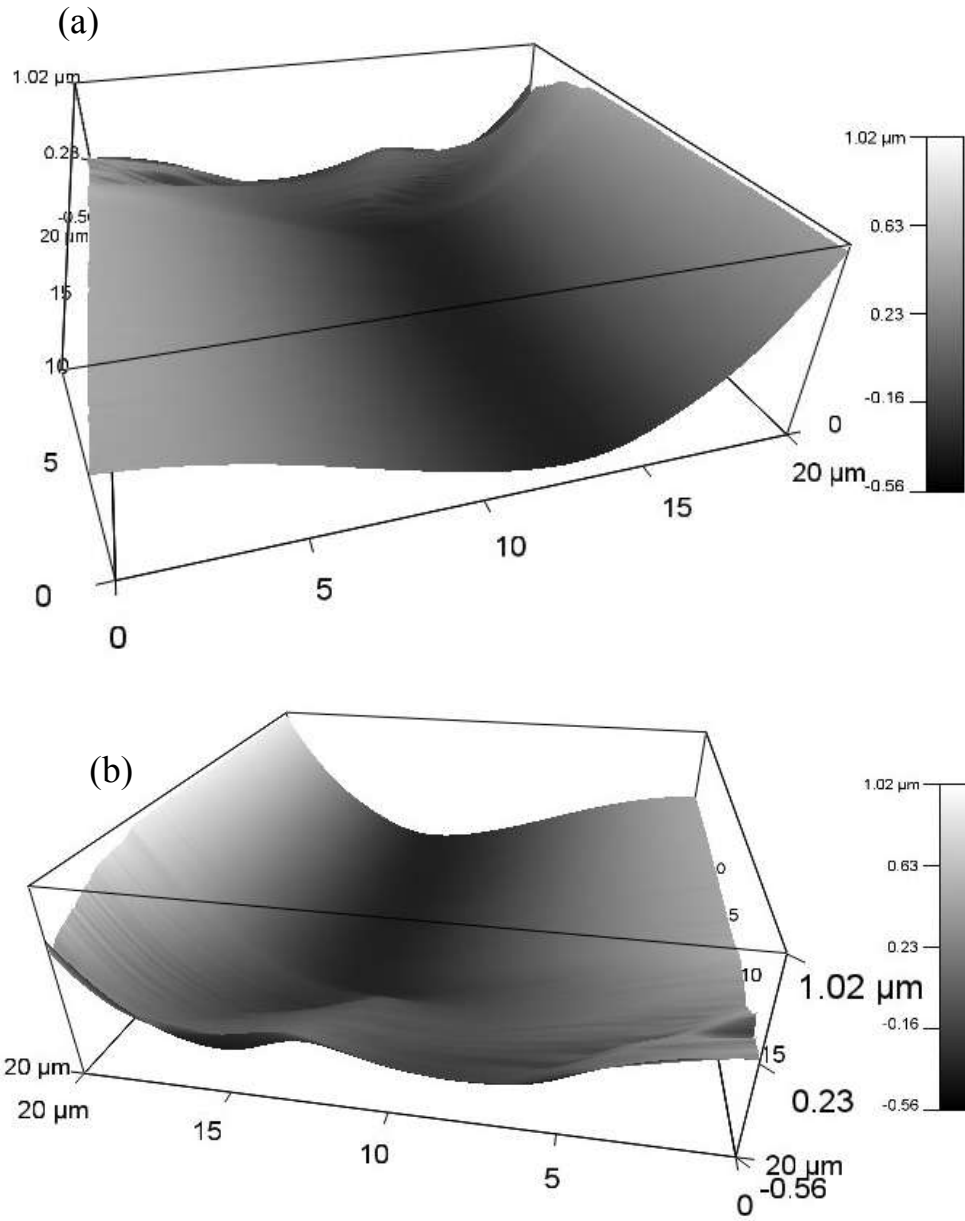


Figure III.1. (a) Experimental setup, inside is an example of viscoelastic liquid filament; (b) The electrical circuit; (c) Scanning Electron Microscope (SEM) of substrate surface of stainless steel and bronze, respectively.



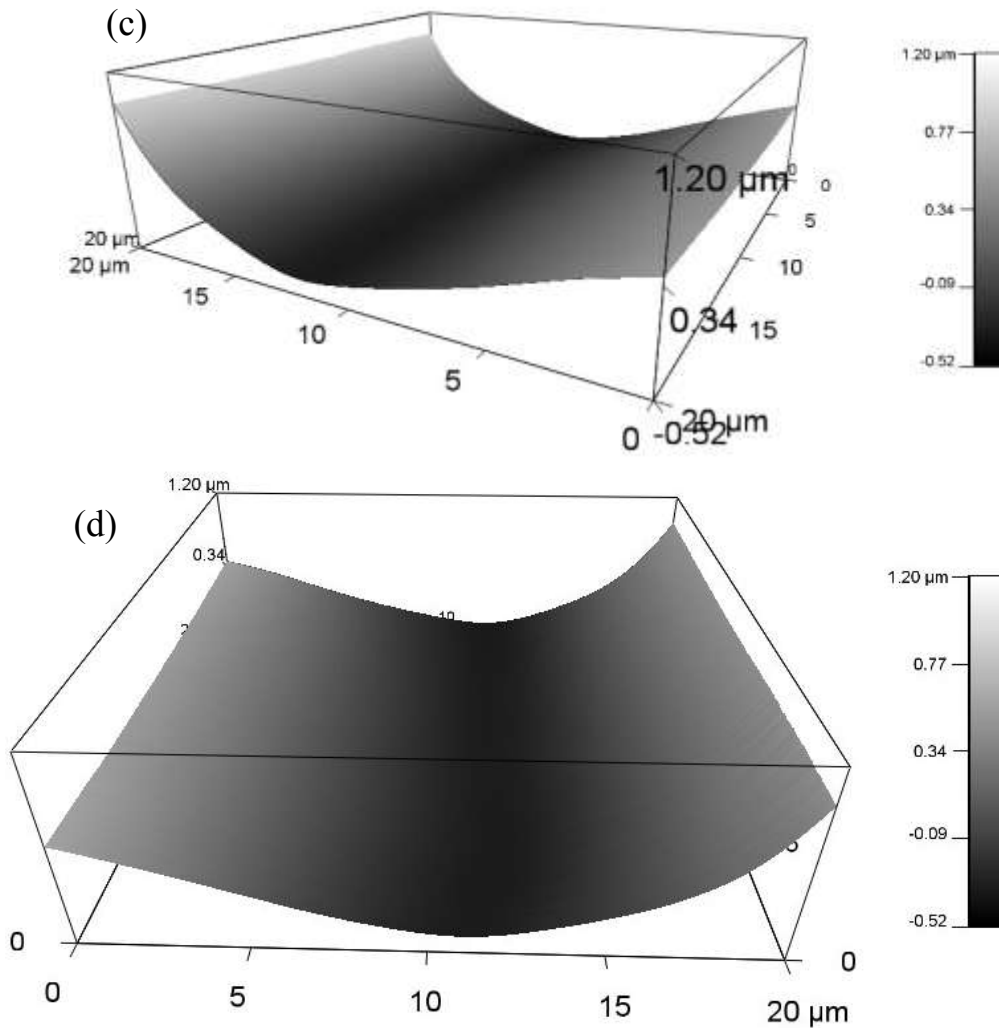


Figure III.2. Atomic force microscopy (AFM) of substrate surface of bronze (a and b) and stainless steel (c and d), respectively.

The fluids in our experiments consisted of both Newtonian and non-Newtonian fluids: water, sodium chloride aqueous solutions (NaCl), emkarox HV 45 aqueous solutions (Emkarox) and polyacrylamide (PAAm, AN 905 SH, SNF Floerger, France). The physical properties of fluids were given in Table III.1. The conductivity was measured by a Multi-parameter analysers C3030 (Consort, Belgium). As the deionized water was firstly tried in the pretest, no electric signal was obtained. Thus all solutions were prepared by tap water in order to improve the conductivity. It needs to note that in 35% emkarox aqueous solution, electric signal is no longer detected. PAAm (molecular mass: $\sim 1 - 1.3 \times 10^4$ kg/mol) dissolved in tap water was used as non-Newtonian fluid. In order to test the effect of salt in non-Newtonian fluid, 10% NaCl were also added into the PAAm aqueous solutions. Figure

III.3 gives the rheological properties of both PAAm solutions and their salt solutions, measured by our rheometer. Clearly, PAAm solutions exhibited a shear-thinning effect. And the presence of NaCl obviously decreases the viscosity of PAAm solutions due to the electrostatic effect. The similar power-law model ($\eta = K\dot{\gamma}^{n-1}$) could be applied to fit the viscosities, where η is the viscosity, K is the consistency, $\dot{\gamma}$ is the shear rate and n is the flow index.

Table III.1. Properties of work fluids at 293.15K.

Dripping-on-Substrate system	$\rho/(\text{kg/m}^3)$	$\sigma/(\text{mN/m})$	$\eta/(\text{mPa}\cdot\text{s})$	$\gamma' (\text{mS/cm})$
Short-time spreading and final pinch-off				
Water	996	72.50	1.0	0.466
25wt% NaCl+ Water	1188.7	82.13	18.53	10.84
5wt% Emkarox+water	996	66.00	4.25	0.417
10wt% Emkarox+water	996	49.00	14.79	0.346
20wt% Emkarox+water	996	40.20	71.80	0.270
35wt% Emkarox+water	996	37.9	427.01	0.109
Filament thinning of non-Newtonian fluids				
0.5wt% PAAm+Water	996	69.3	$\eta = 0.77\dot{\gamma}^{-0.55}$	1.125
0.1wt% PAAm+Water	996	67.7	$\eta = 3.96\dot{\gamma}^{-0.63}$	1.290
2.0wt% PAAm+Water	960	66.2	$\eta = 20.52\dot{\gamma}^{-0.73}$	2.540
(0.5wt% PAAm+Water) +10wt% NaCl	996	--	$\eta = 0.30\dot{\gamma}^{-0.42}$	153.4
(2.0wt% PAAm+Water)+ 10wt% NaCl	996	--	$\eta = 8.44\dot{\gamma}^{-0.64}$	144.7

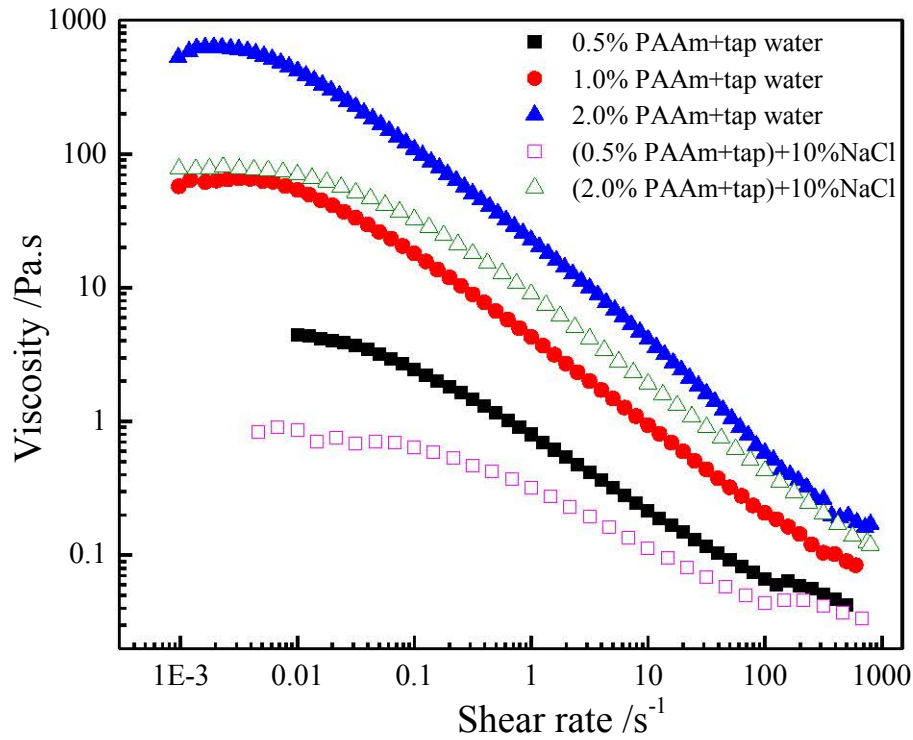


Figure III.3. Rheological properties of PAAm solutions. Here, ‘tap’ means the tap water.

The sampling speed of electric signal is always kept constant as 1.25×10^6 Hz, i.e. a temporary interval of $0.8 \mu\text{s}$. For the initial contact and spreading and final pinch-off of Newtonian fluids, the first drop formation is captured by the camera with 60017 fps, resolutions 256×256 pixels and exposure time $10 \mu\text{s}$. But for the filament thinning of non-Newtonian fluids, the feeding of liquid is stopped after the first drop due to the spinning behavior of viscoelastic fluids, so that the filament will break at last. And the visualized speed of filament thinning is mainly 500 fps. A syringe pump (10 mL, Hamilton, Germany) was adopted to control the flowrate ($Q = 0.1 \text{ mL/min}$). The obtained images were analyzed frame by frame through the self-programmed Matlab.

III.3 Results and discussion

To obtain the effective electric signals, three main kinds of non-natural drop formation were designed as illustrated in Figure III.4. When the distance between the nozzle and the plaque surface (l) is relatively small (Figure III.4a), no liquid neck occurs in the beginning and the formation and pinch-off of liquid drops is largely obstructed. At this situation, the electric signals can give the information of the initial contact and spreading dynamics of drops on the metal surface. When the distance between the nozzle and the metal surface (l) is large (Figure III.4b), liquid neck occurs in the beginning and the formation and pinch-off of liquid drops is slightly obstructed and nearly in a natural way as the drop formation presented in Part I. Once the diameter of bottom contact area becomes larger than that of the upper liquid neck, the electric signals can directly reflect the pinch-off dynamics of fluids. While the distance (l) is relatively large (Figure III.4c), liquid filament forms before the liquid-solid contact and the electric signals can directly reflect the thinning dynamics of viscoelastic fluids.

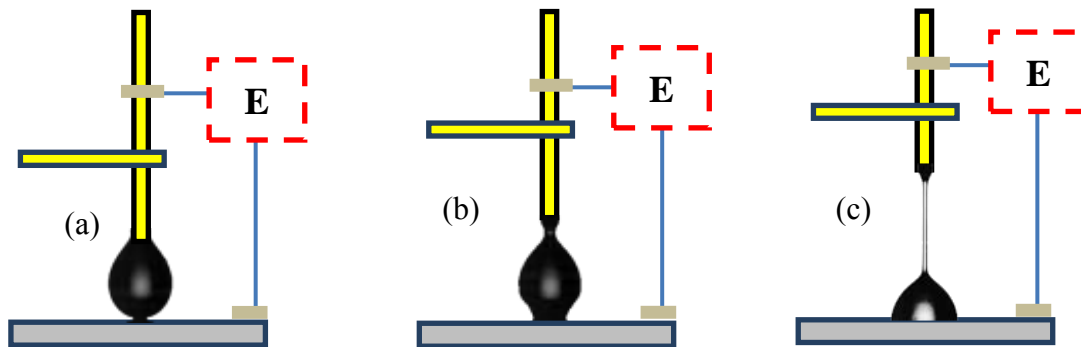


Figure III.4. (a) Short distance dripping-on-substrate for investigation of initial contact and spreading; (b) Long distance dripping-on-substrate for investigation of drop pinch-off of Newtonian fluids; (c) Extreme long distance dripping-on-substrate for investigation of filament thinning of non-Newtonian fluids.

III.3.1 Initial contact and spreading

The short-distance dripping-on-substrate behavior is given through the visualized images coupling with the corresponding electric signals (Figure III.5). Here, we define the time zero ($t - t_s = 0$ ms) as the moment when the first contact is observed in the image and the first decreasing point of voltage is found in electric signals. Here, t is the actual time and

t_s is the first contact time. Due to the constant DC current intensity $I = 0.1$ mA, the decreasing voltage reflects the decreasing electric resistance of the liquid bridge. But the resistance largely depends on the narrowest part of the liquid where the motion of electrons is largely obstructed, i.e. the smaller the minimum neck width, the larger the resistance.

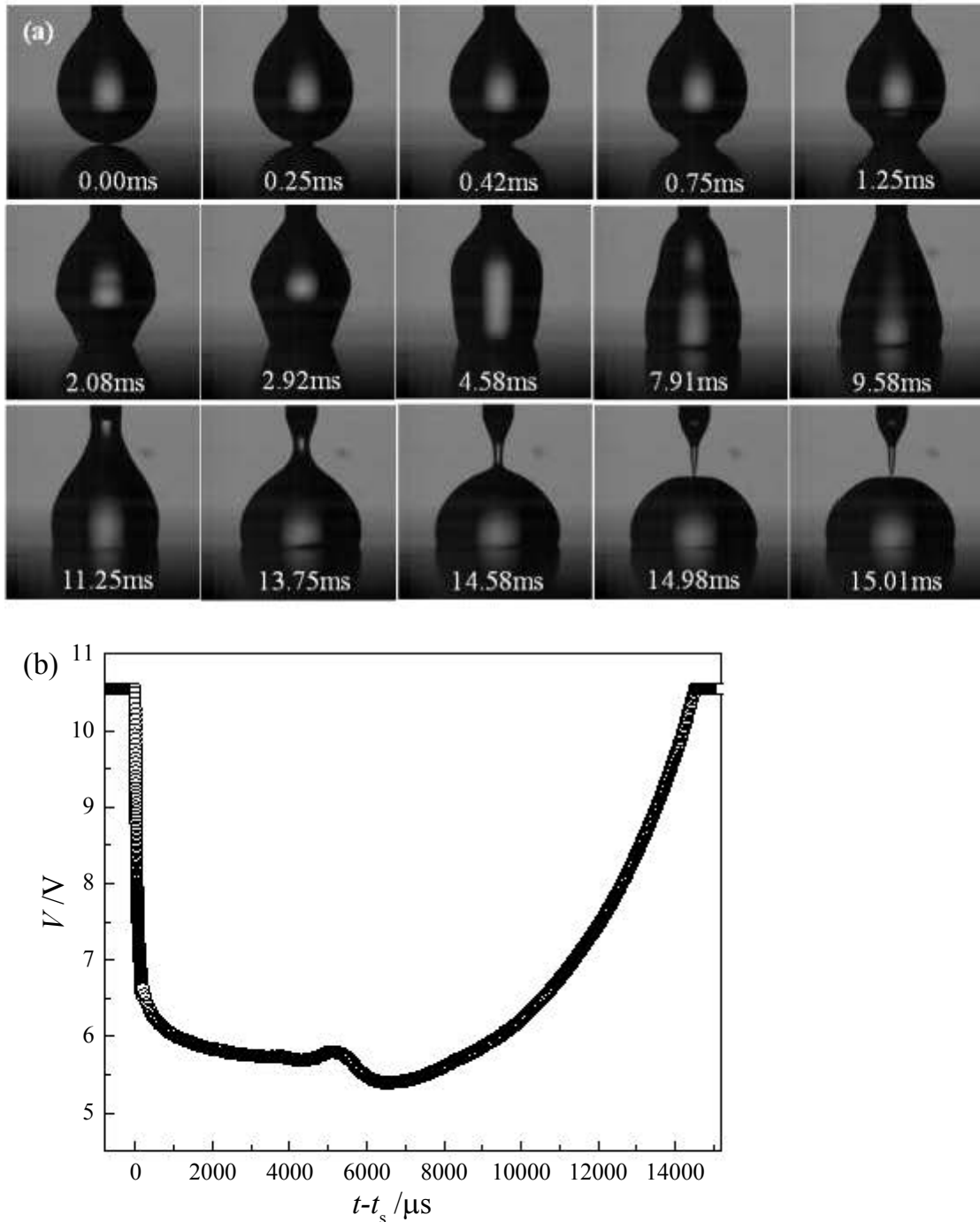
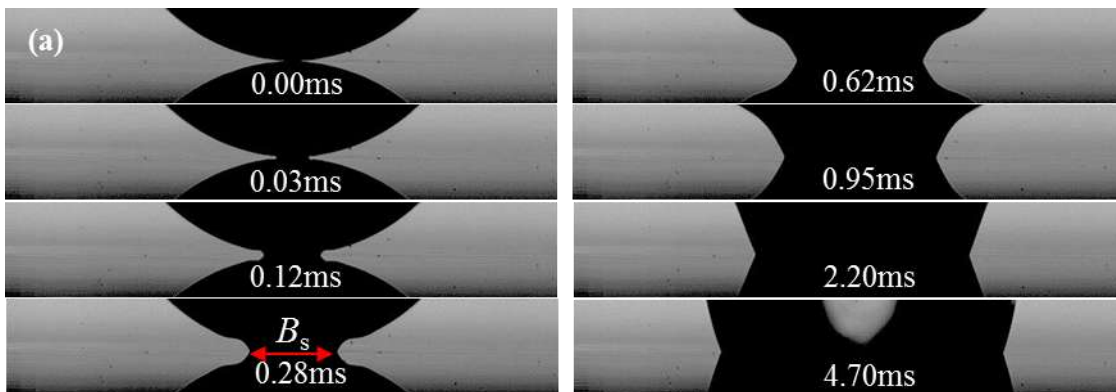


Figure III.5. Short-distance dripping-on-substrate behavior of tap water on stainless steel surface, (a) optical images; (b) electric signals.

At $t - t_s = 0$ ms, the pendant water drop begins to touch the surface (Figure III.5a) and the voltage decreases sharply due to the conducting liquid bridge in the circuit (Figure III.5b). From the images of $t - t_s = 0.25$ ms to $t - t_s = 0.42$ ms, the diameter of contact area increases but the drop body remains a smooth surface. The voltage decreases gently compared to the very initial contact. With the spreading of liquid base, a capillary wave occurs and propagates along the surface of the drop and electric signals decrease slowly. The bottom part of drop begins to be trapezoid and the upper part is still quite smooth. At $t - t_s = 2.92$ ms, the drop is much like a vase and the largest width symmetrically lies in the middle. Later on, with the continuous spreading and filling, the drop evolves like a uniform cylinder, a calabash and a conical flask and the voltage undergoes local extremums. Since then, the liquid drop begins to thin and rupture and the voltage increases until the disconnection of the circuit.

Now we focus firstly on the dynamics of the initial contact and spreading on the metal surface. Figure III.6a presents magnified details of the initial contact and spreading of a water drop on stainless steel surface and Figure III.6b and c plot the short-time contact dynamics from both image analyses ($0 - 3.5$ ms) and electric signals ($0 - 140 \mu\text{s}$). From Figure III.6a, once the gas film between the liquid and the solid is rejected, a contact point establishes and rapidly expands. The capillary wave is pronounced after $t = 0.28$ ms. Then, power-laws, $B_s \propto (t - t_s)^b$ and $V \propto (t - t_s)^c$, are applied to describe the dynamics of short-time spreading from imaging and electric signals, respectively. Figure III.6b indicates that the initial spreading follows a power-law relationship with an exponent of 0.42. However, in Figure III.6c, the electric signals exhibit an exponent of -0.15.



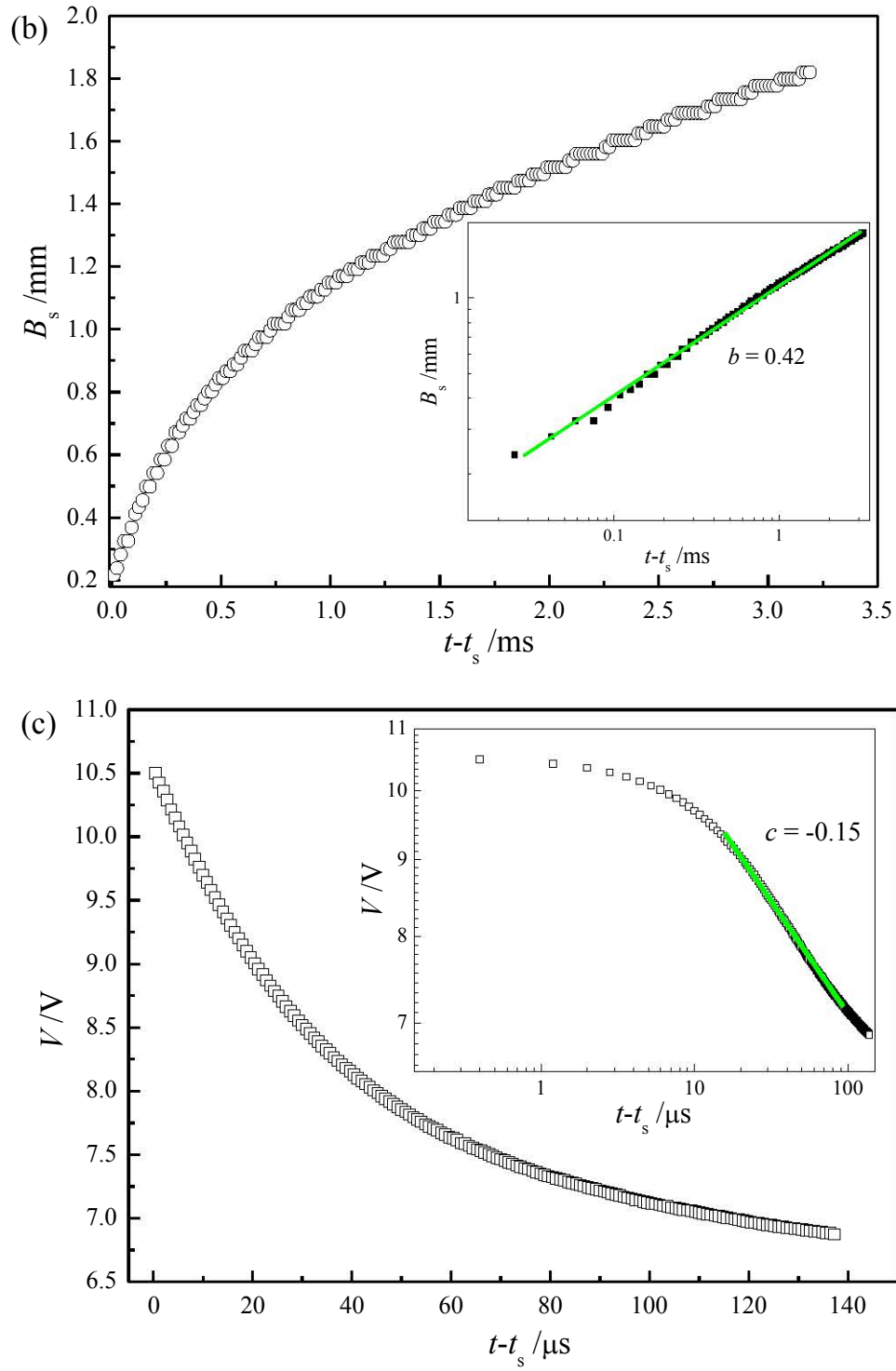
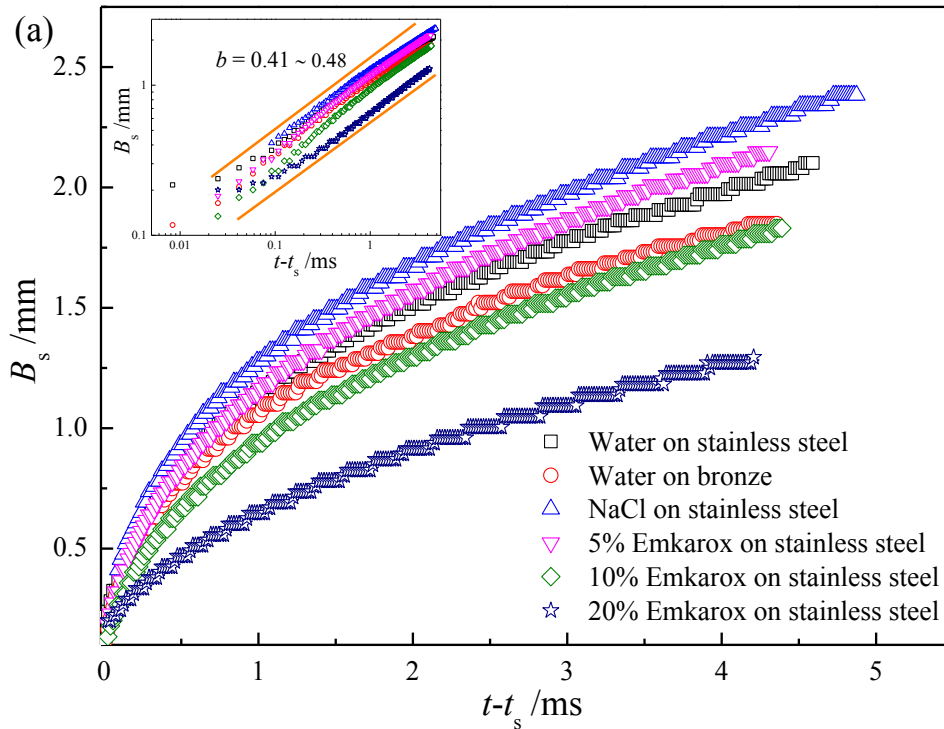


Figure III.6. (a) Close-up of short-time contact and spreading of tap water on stainless steel surface; (b) and (c) dynamics of short-time contact and spreading from visualized images and electric signals, inside is their corresponding log-log plots.

To further study the short-time contact and spreading, we change the surface material as well as the fluid properties and the results are presented in Figure III.7. In Figure III.7a, after $t - t_s = 1$ ms, the spreading of tap water drops on stainless steel surface is relatively faster than that on bronze surface, due to the more roughness on bronze surface. Sodium chloride aqueous solutions (NaCl) spreads slightly faster than tap water and it's noted that the higher the viscosity of Emkarox solutions, the slower the spreading behavior. But the log-log plot of the imaging data in Figure III.7a shows that the initial spreading follows a power-law relationship with the exponent ranging from 0.41 to 0.48, for all solutions investigated no matter on stainless steel or on bronze surface. The exponents are quite close to the previous results of inertial spreading (Cazabat and Stuart, 1986; Chen et al., 2013).

As some authors proved that the inertial spreading dynamics is only dependent of the surface wettability. Though the roughness of stainless steel surface and bronze surface shows observable difference (Figure III.1c and Figure III.2), the initial spreading dynamics from images is quite the same. This can be further observed in Figure III.7b, where the electric signals of initial spreading is nearly superimposed for tap water on stainless steel surface and bronze surface.



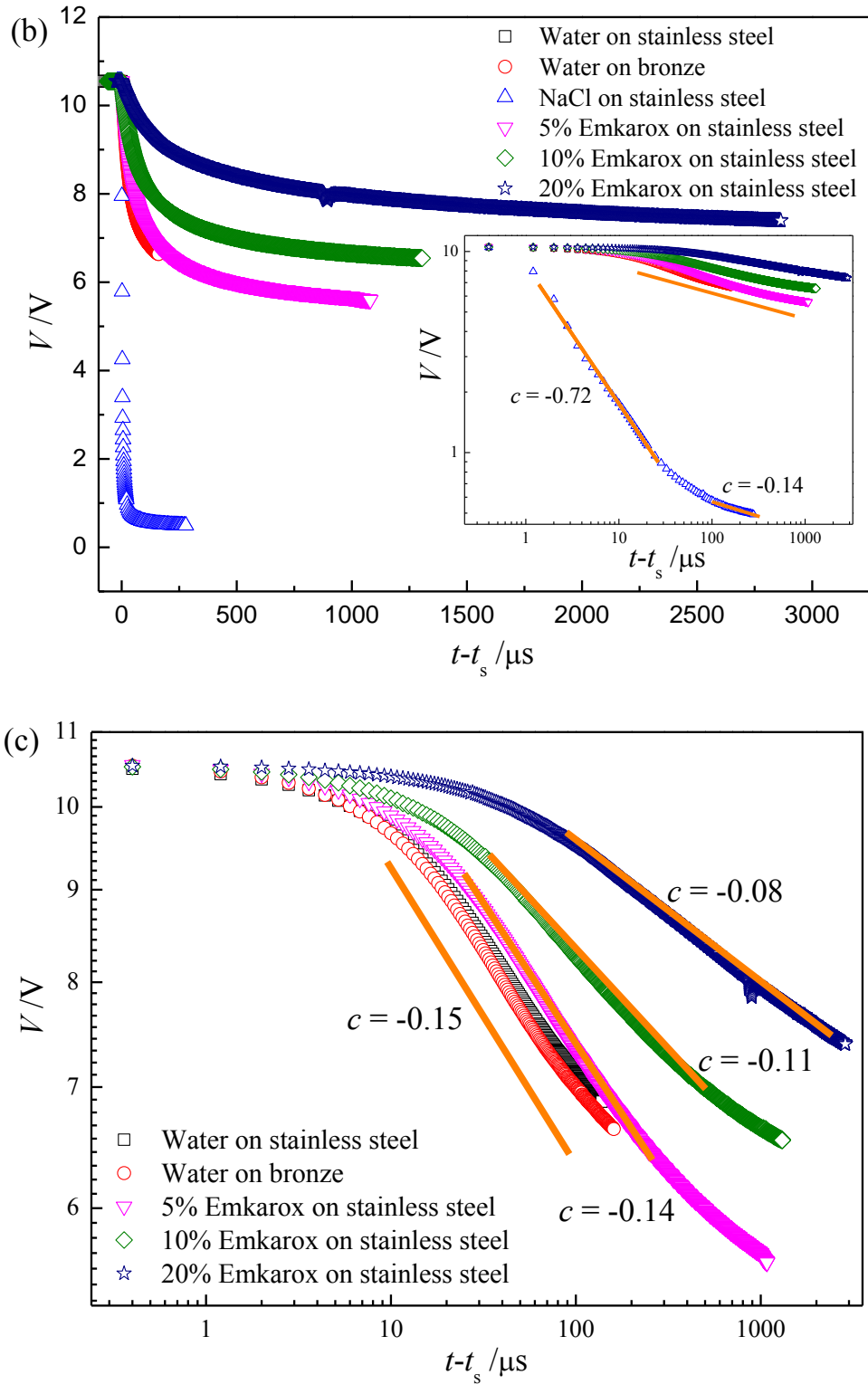


Figure III.7. Dynamics of short-time contact and spreading from visualized images (a) and electric signals (b) & (c) for all Newtonian fluids; insides are their corresponding log-log plots.

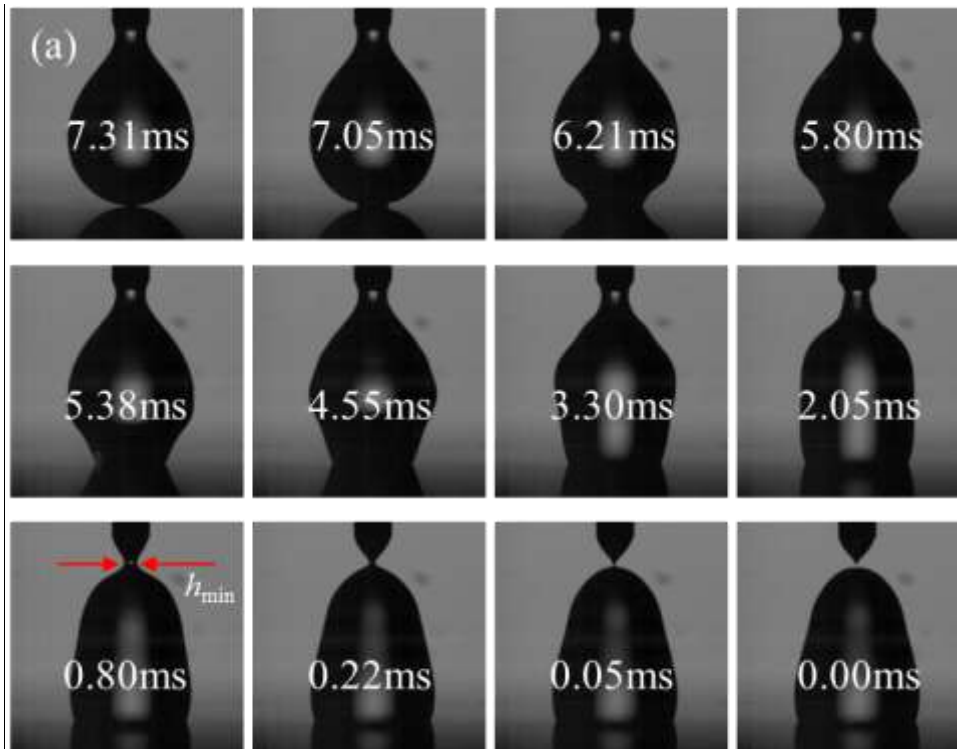
From Figure III.7b, the voltage firstly undergoes a rapid decreasing stage and then a slow decreasing stage. In the first decreasing stage, the voltage decreases dramatically for sodium chloride aqueous solutions (NaCl), compared to the other solutions. That is probably resulted from the high conductivity of NaCl solutions. And we note that the higher the viscosity of Emkarox solutions, the slower the voltage decreases. In the second decreasing stage, the voltage of water on both stainless steel surface and bronze surface is almost the same and the voltage of NaCl solution is extremely low. And the higher the viscosity of Emkarox solutions, the higher the voltage. Considering the negative relationship between the voltage and spreading base, these results are in a good agreement with the above imaging analyses.

Similarly, a power-law, $V \propto (t - t_s)^c$, is applied to the voltage evolution during the initial contact and spreading process and the exponents are all negative and given in Figure III.7b and c. The exponent c is -0.08 to -0.15 for the water and Emkarox solutions investigated. Surprisingly, the exponent of NaCl solutions is firstly -0.72 within $\sim 20 \mu\text{s}$ and then -0.14 after $100 \mu\text{s}$. The special exponent of -0.72 indicates that once the liquid and solid contact, the voltage of NaCl solutions decreases extremely rapid. While the exponent -0.14 means that the short-time spreading is as slow as the other solutions. The change of scaling law is mainly due to the high conductivity of NaCl solutions which is a very sensitive parameter in our electric device. However, the exponent of -0.14 is compatible to the range of -0.08 to -0.15 for the water and Emkarox solutions, implying that the short-time spreading dynamics is similar.

In all, the exponents of short-time spreading 0.41 to -0.48 and -0.08 to -0.15 are obtained for imaging and electrical analyses, respectively. The effect of fluid properties especially the conductivity, on the exponent is excluded and the electric device reaches a much finer time-scale dynamics of initial contact and spreading. The different mechanism between the two exponents is still difficult to be explained at this stage. Besides the difference in liquid wetting and conducting properties on these solid surfaces, a more important difficulty arises from the topology of the liquid bridge during the initial contact and spreading process: the narrowest neck of liquid drop contributes significantly to the resistance but is not the whole. So the voltage is not possible to exhibit a simple linear or square relationship with the drop base. Thus in the near future, the application of electric device in studying the fast spreading behavior still requires further investigation to clarify the relationship between the topology of the liquid bridge and the electric resistance signals.

III.3.2 Pinch-off of Newtonian fluids

Figure III.8a and b presents the images and electric signals of water drop pinch-off on the steel surface. Here, we define the time as $(t_0 - t)$, as t_0 is the breakup time and t is the actual time. Before the pendent liquid drop touching the substrate, a neck comparable to the nozzle diameter occurs. In Figure III.8a, at $t_0 - t = 7.31$ ms, liquid drop contacts the steel surface. At this time, the voltage in Figure III.8b decreases rapidly due to the establishment of the contact between liquid and solid. Then the base of liquid drop expands on the surface and the voltage continues to decrease. Once the liquid base becomes wider than the neck connecting to the nozzle outlet, the electric signal reflects no longer the spreading of liquid base but the pinch-off of the liquid neck. After $t_0 - t = 7.05$ ms, the base of liquid drop spreads on the surface and liquid body evolves in same way as the previous Figure III.5a. However, the liquid neck nearly remains the same and the corresponding voltage changes very slowly. At $t_0 - t = 2.05$ ms, the liquid body evolves to be uniform cylinder and around this time scale, the voltage undergoes the local extremums. Since then, the liquid neck begins to thin and the voltage increases rapidly. Eventually, the liquid neck breaks up into two parts and the electric circuit is broken.



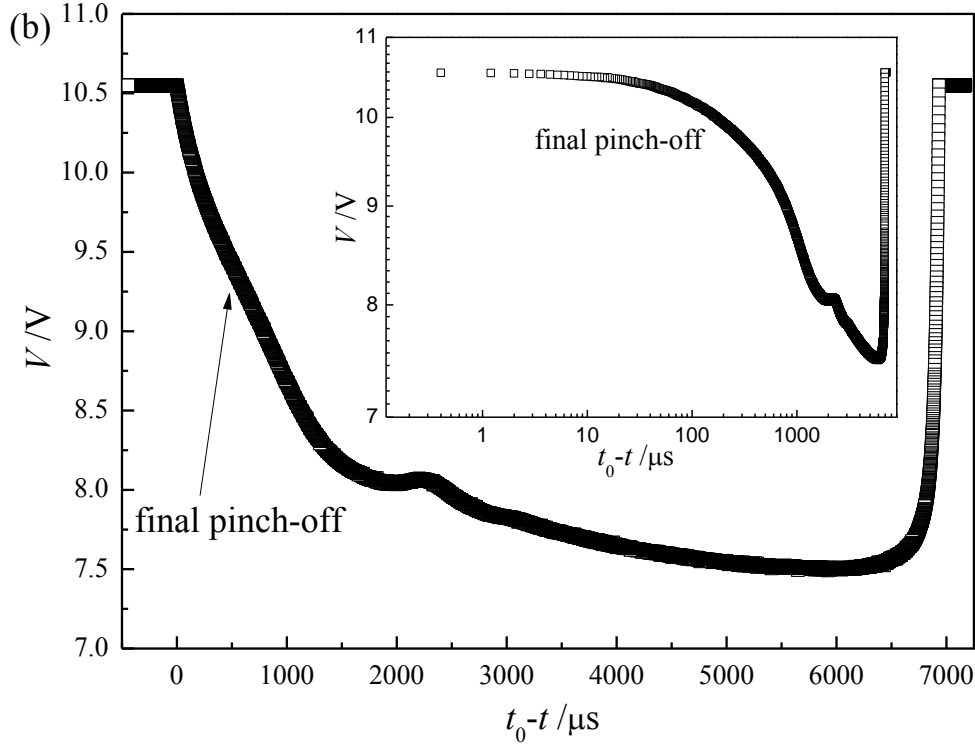
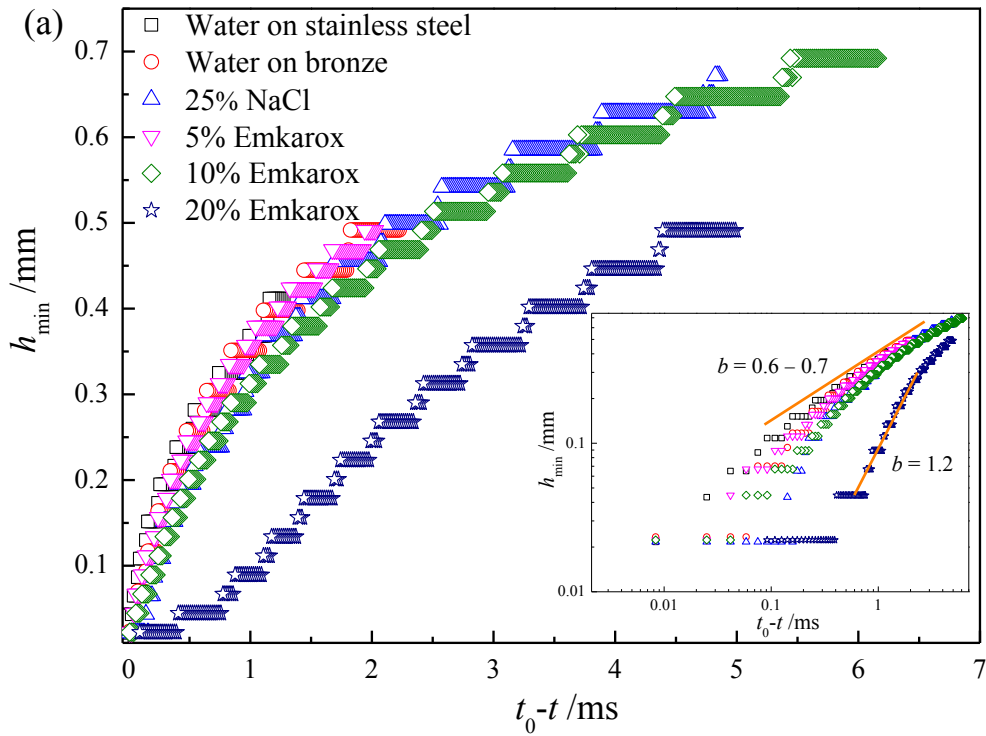


Figure III.8. (a) Long-distance evolution of tap water on stainless steel surface; (b) electrical signals.

Figure III.9a presents the final pinch-off dynamics from image analyses. Except 20% Emkarox solution, the rest are almost superimposed. To keep accordance with previous pinch-off studies in Part I, the similar scaling law, $h_{\min} \propto (t_0 - t)^b$, is adopted to fit the final pinch-off region. Here, h_{\min} is the minimum neck diameter as shown in Figure III.8a. The exponent is (0.6 – 0.7) for water, NaCl, 5% Emkarox and 10% Emkarox solutions. But a larger exponent 1.2 is observed for 20% Emkarox solution. This changing of scaling law is mainly derived from the effect of viscosity, which we have discussed in Part I.

The electric signals in Figure III.9b show that with the approaching of pinch-off point, the voltage increases due to the increasing resistance in the liquid thread. Quite similar to the initial contact and spreading, the surface material makes no big difference in the voltage of water on stainless steel surface and bronze surface. Among the Emkarox solutions, the larger viscosity leads to a higher voltage. It is found that the voltage of NaCl solution is lowest and near the pinch-off point, the voltage increases dramatically. This behavior is reminiscent of the previous sharp decreasing voltage of NaCl solution during the initial contact and spreading and they are all resulted from the high conductivity.

The similar scaling-law, $V \propto (t_0 - t)^c$, is applied to describe the pinch-off dynamics. The exponent of NaCl solution is negatively large, i.e. -3.0 within $\sim 50 \mu\text{s}$ and then -0.10 after $200 \mu\text{s}$ (Figure III.9b). The voltage of 20% Emkarox evolves with the exponent of -0.02 while the rest solutions exhibit an exponent ranging from -0.07 to -0.08 after $200 \mu\text{s}$ (Figure III.9c). Here, we can conclude that the very final pinch-off ($< 100 \mu\text{s}$) from electric signals is dependent of the conductivity of liquids due to the sensitivity of the electric devices. But the final pinch-off ($> 100 \mu\text{s}$) is mainly dependent of liquid viscosity.



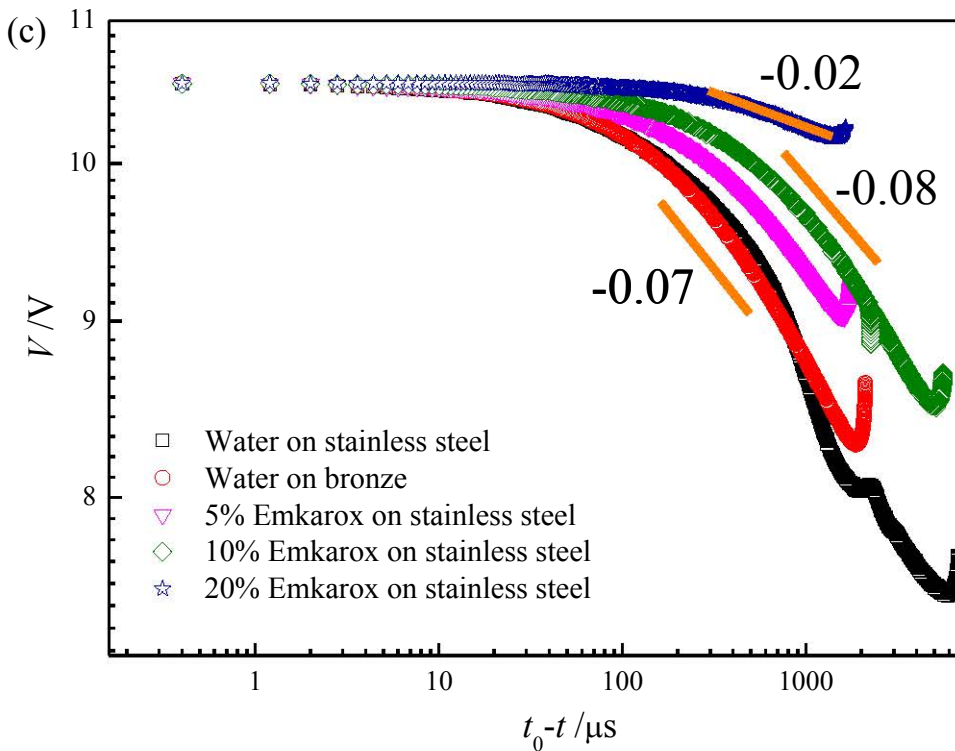
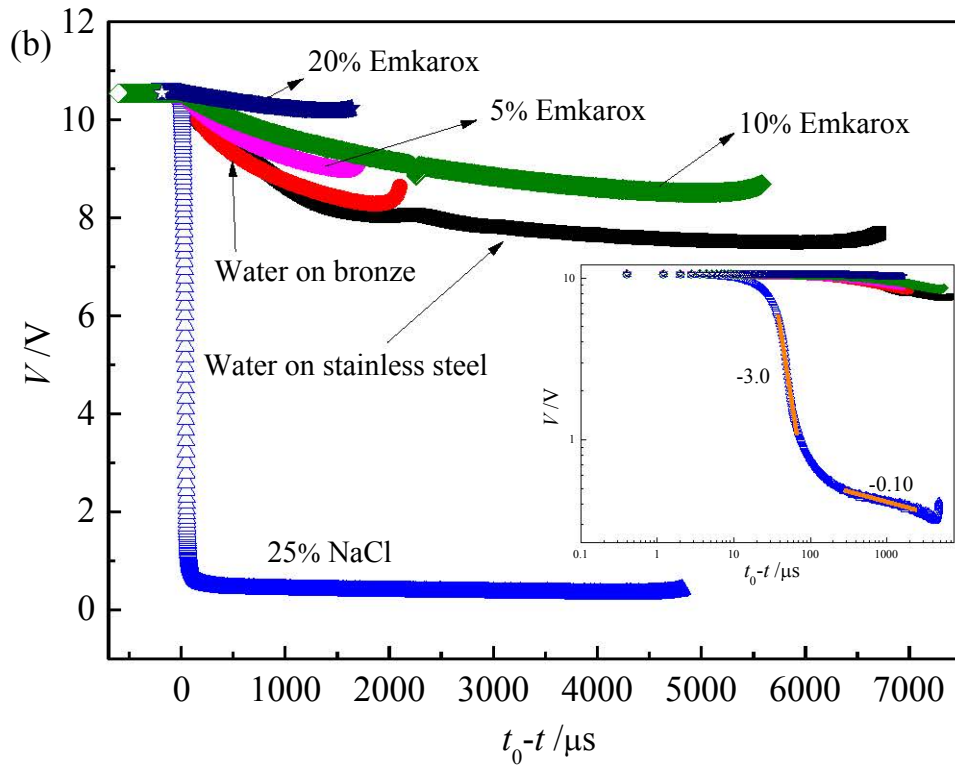


Figure III.9. Dynamics of final pinch-off from visualized images (a) and electric signals (b) & (c) for all Newtonian fluids; insides are their corresponding log-log plots.

Actually, when the liquid viscosity is much higher, the liquid neck exhibits a cylindrical column rather than a conical shape near the pinch-off point. Figure III.10a shows the pinch-off sequence and electric signals of 20% Emkarox solutions. The long thread differs from the conventional conical pinch-off and the above discussions proved that 20% Emkarox evolves differently from the others no matter imaging methods or electric signals. More importantly, electric signals in Figure III.10b become no longer smooth and oscillating fluctuations occur. And it is found that the overall time of Figure III.10a is larger than that of Figure III.10b, implying that the some particular dynamics lies behind the pinch-off of a liquid filament. This motivates our further investigation in the following section.

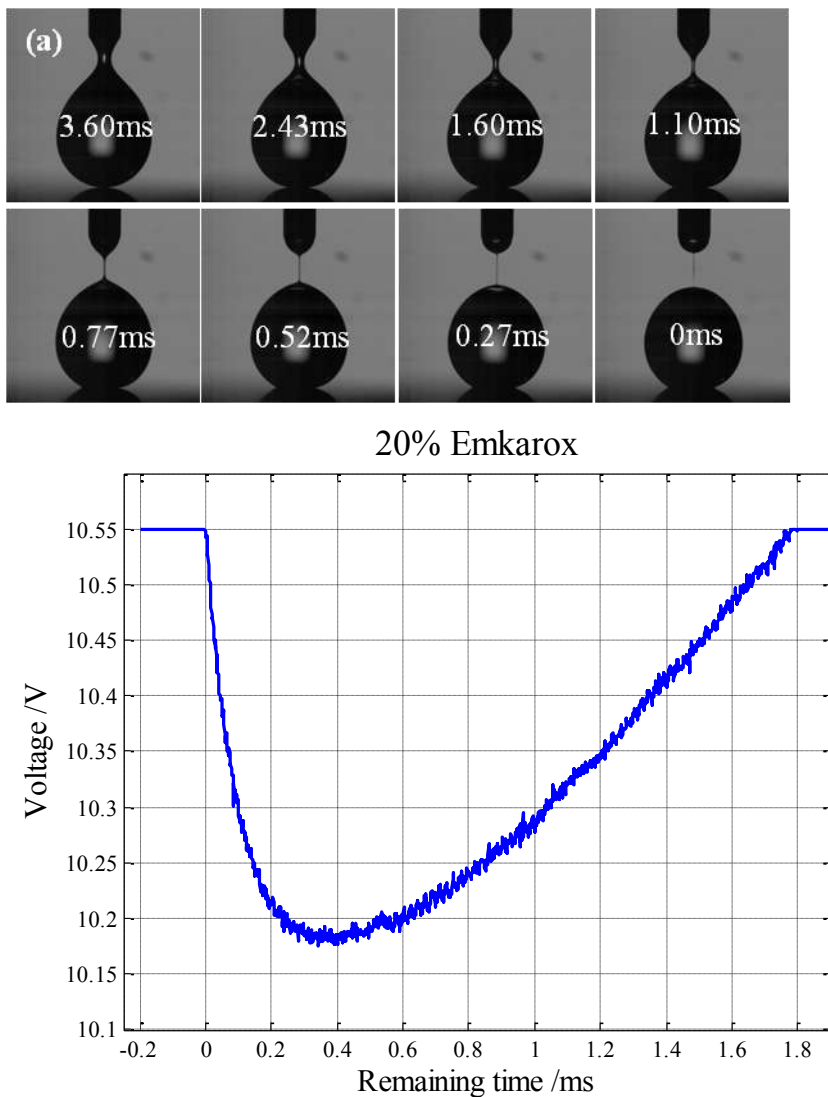


Figure III.10. Final pinch-off of 20% Emkarox aqueous solution from visualized images (a) and electric signals (b).

III.3.3 Filament thinning of non-Newtonian fluids

Considering the difficulty of determining the exact breakup time of spinning non-Newtonian fluids, we define the time as $(t - t_s)$, as t is the actual time and t_s is the contact time. Figure III.11 – 13 shows the filament thinning of (PAAm + tap water) solutions from both images and electric signals. A long filament forms before it touches the substrate due to the viscoelastic properties of PAAm solutions. When the drop touches the substrate, the electric signal decreases sharply until the spreading base is larger than the diameter of the liquid filament. Then the continuous spreading of the drop base is no longer the determining factor for the resistance of the measuring system. At that time, the electric signal increases, implying that the thinning of liquid filament becomes a dominant source for the resistance increase.

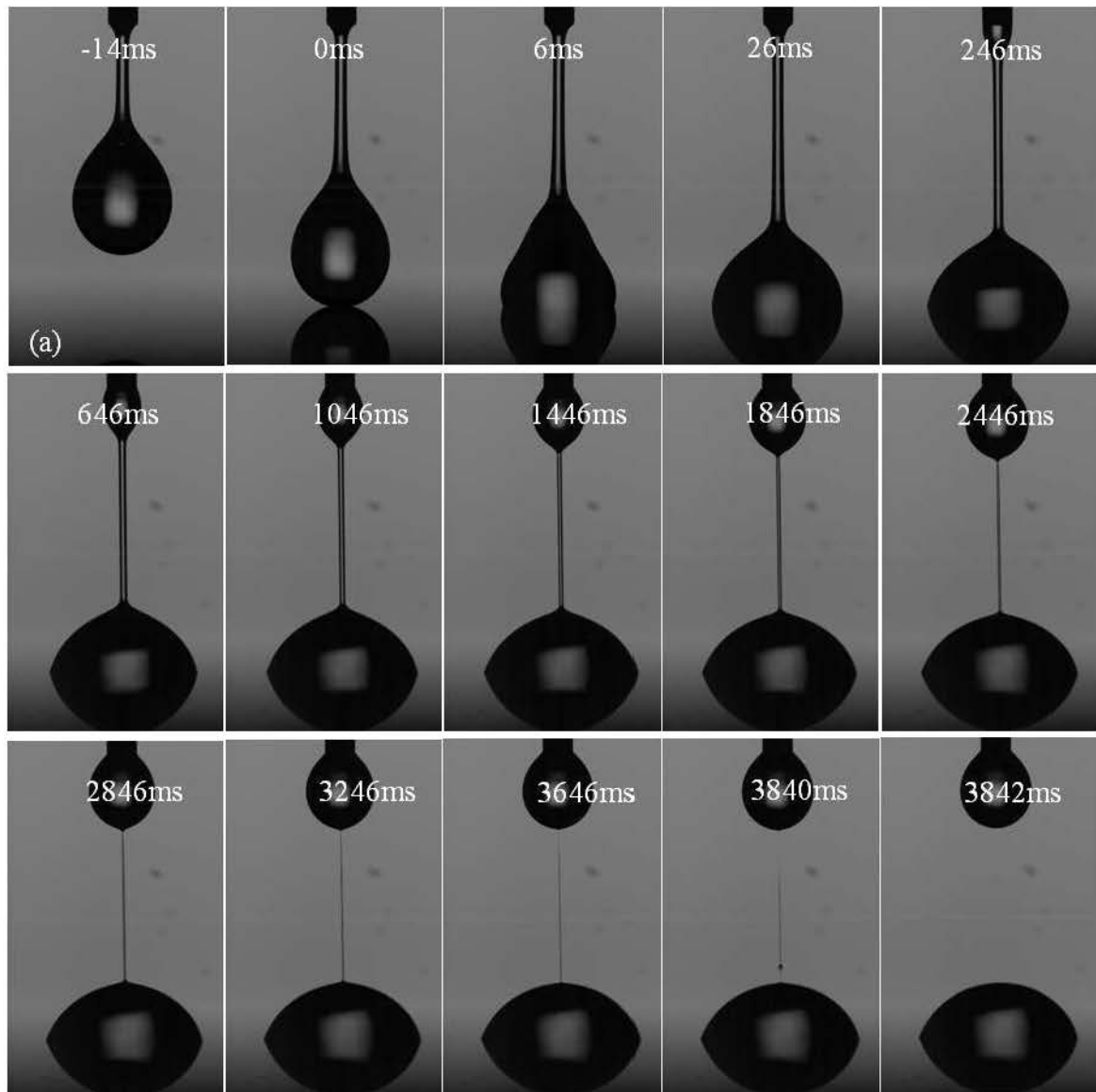
The previous studies both numerically or experimentally showed that the long filament, the bear-on-string behavior and the multiple singularities are the principal characteristics of thinning of viscoelastic fluids. In our work, the same phenomena are observed in visualized images by the camera. And the lifetime for the thinning process is found to increase sensitively with the concentration of PAAm solutions no matter for images or electric signals. The increasing stability of the filament significantly derives from the increasing viscous stress under extensional flow (Cooper-White et al., 2002). Then we focus mainly on the electric signals.

For Newtonian fluids, the electric signal increases until the occurrence of the final pinch-off point where the voltage returns to the maximum $V = 10.54$ V. Here, we found several surprising differences for the thinning filament of non-Newtonian fluids. Firstly, the global minimum voltage of 0.5% PAAm aqueous solution is the largest ($V = 10.35$ V) and that of 2% PAAm aqueous solution is the lowest ($V = 8$ V). This indicates that the global extremum of voltage is dependent on the concentration, to be exact, the conductivity of PAAm solutions. It is worth noting that the effect of viscosity on the global extremum of voltage is excluded due to the disappearance of electric signals for 35% Emkarox solutions which is mentioned in the experimental section. Secondly, no matter for 0.5%, 1.0% or 2% PAAm aqueous solutions, the voltage evolution cannot follow the time scale of images. This means that the overall time of electric signals is much shorter than that of the image sequence. Thirdly, the voltage evolution is not as smooth as the pinch-off of Newtonian fluids and peak signal occurs for three concentrations of PAAm aqueous solutions.

In fact, when the electric signal no longer changes, the filament diameter is about 200 μm according to the camera, still observable for our naked eyes. Normally, the ultra-fast acquisition system can reach very low time and length scales than the classic imaging system. The capturing electric signals here fail in delivering a corresponding electric signal even with a width of 200 μm . This surprising phenomenon uniquely occurs for the thinning of viscoelastic fluids in our various experiments. Absolutely, it is not directly related to the conductivity of fluids. We realize that it is related to the special structure of viscoelastic fluids itself and this will be further studied by our group.

The signal displaying regular peaks not only exists in the evolution that the voltage increasing to the maximum, but also exists in the saturation part of the electric circuit after the voltage returns to $V = 10.54$ V. More importantly, the occurrence of this kind peak signal increases with the concentration of PAAm aqueous solutions. In Figure III.11b, there mainly exist four peaks and the close-up of these peaks is given in Figure III.11c. Except for the peak 1, the rest peaks all occur in the plateau line instead of the evolution curve. Both peak 1 and peak 2 show two extremums and only one extremum is observed in peak 3 and peak 4. The corresponding voltage (V_{ep}) of peak 1 is quite small. However, the peak voltage decreases from peak 2 to peak 3 and then peak 4, as indicated in Figure III.11b. In addition, the number of points in each peak tends to decrease.

More surprisingly, it can be found that the time interval between two neighboring peaks (T_{dp}) is almost the same, $\approx 20\text{ms}$, as shown in Figure III.11b, the inset of Figure III.12b and Figure III.13b. In order to investigate the characteristics of the peaks, we here analyze the peaks of 1% PAAm aqueous solutions.



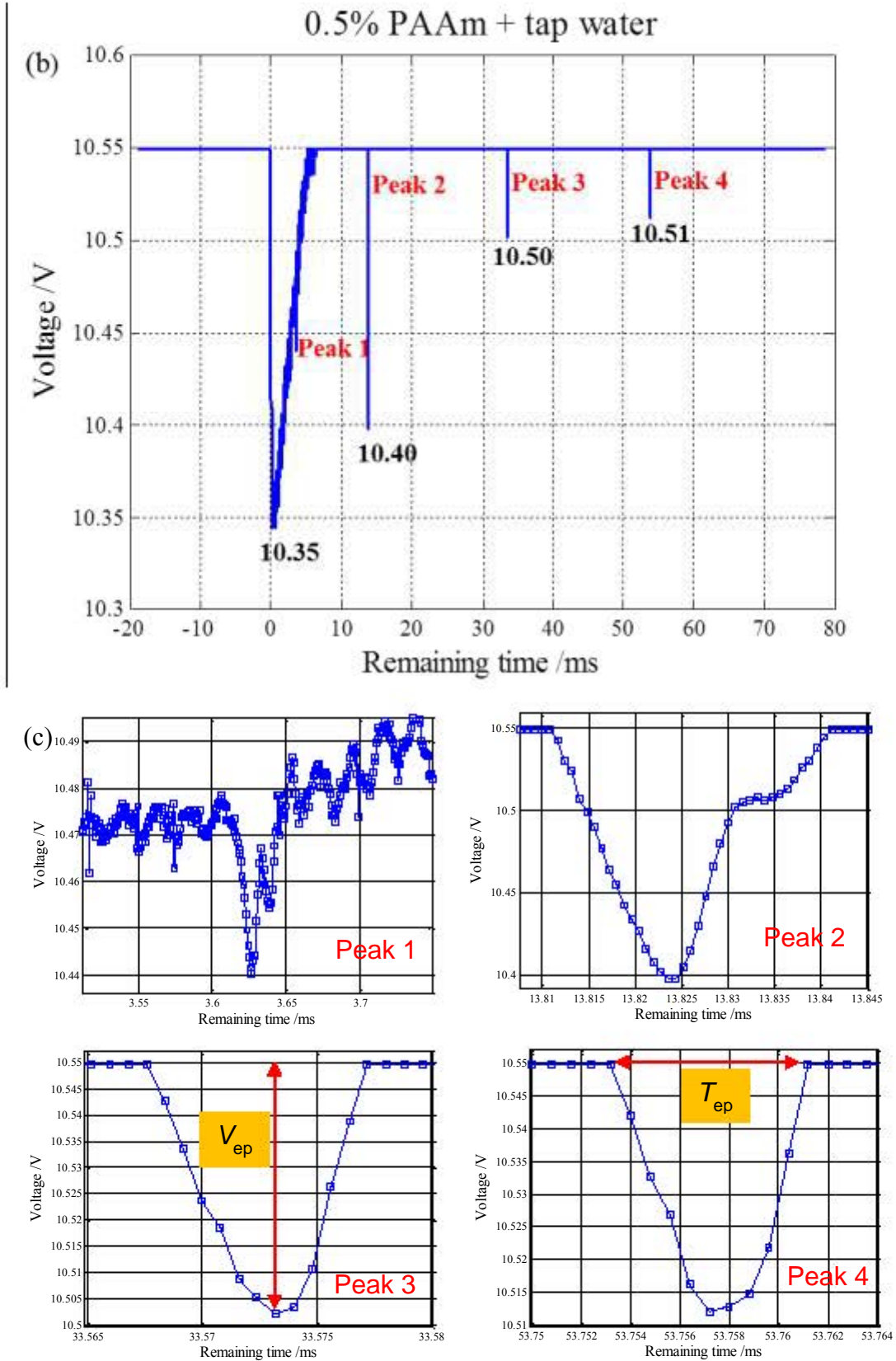
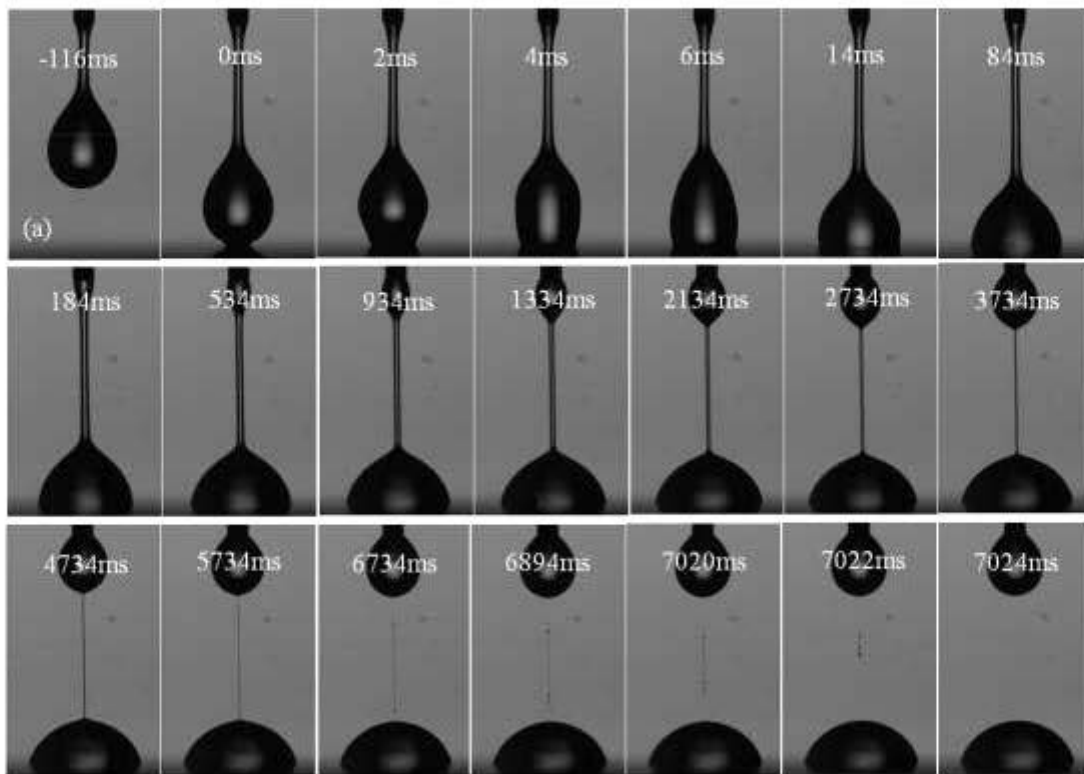


Figure III.11. Filament thinning of 0.5% PAAm aqueous solution on stainless steel surface, (a) optical images and (b) electric signals. (c) Close-up of four peaks in (b).



1.0% PAAm + tap water

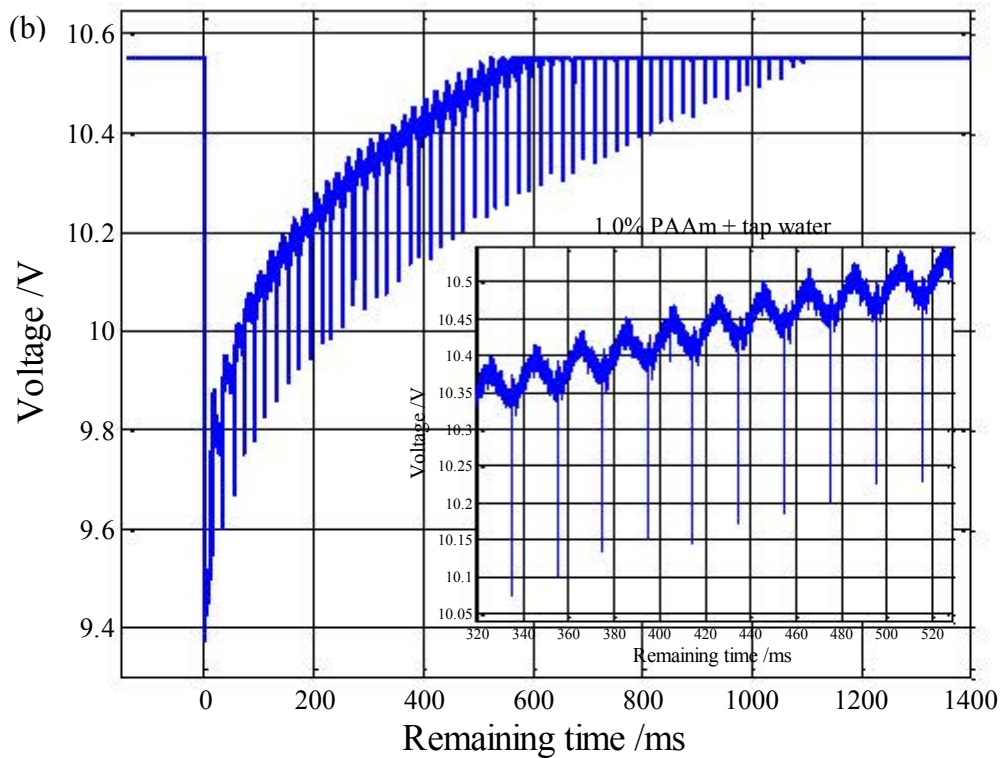
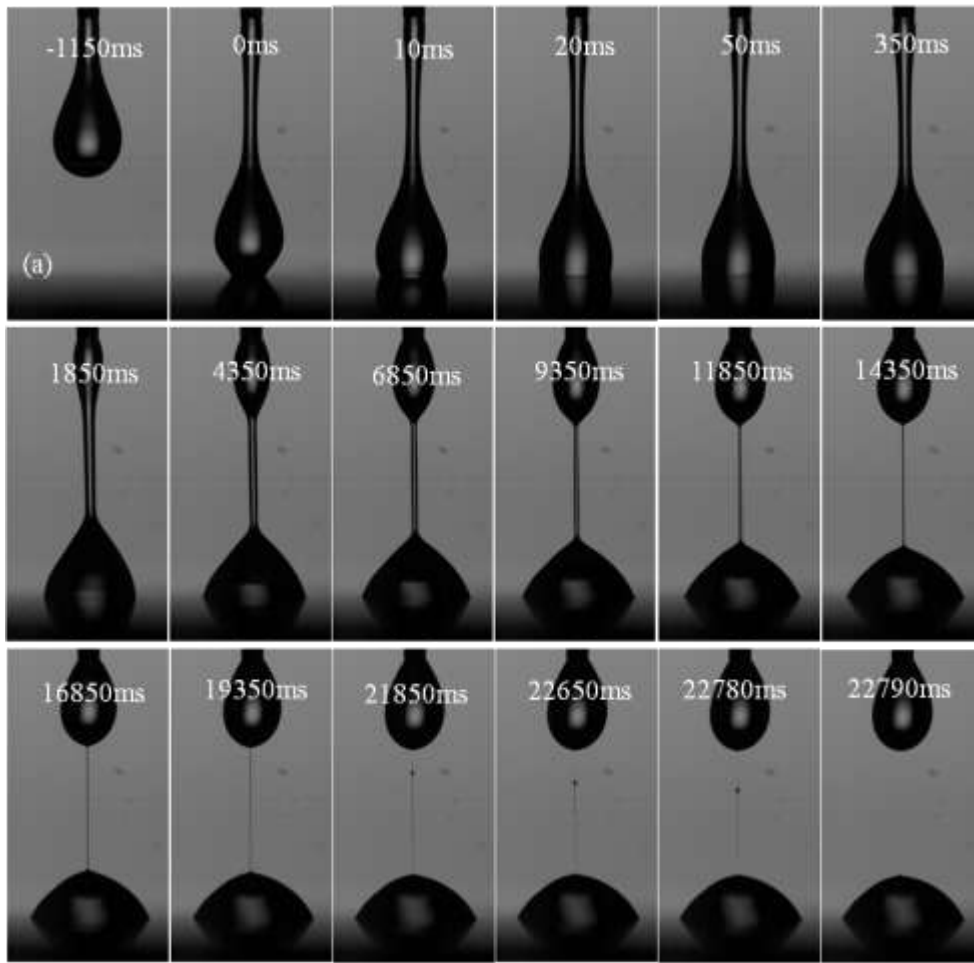


Figure III.12. Filament thinning of 1.0% PAAm solution on stainless steel surface, (a) optical images; (b) electric signals.



2.0% PAAm + tap water

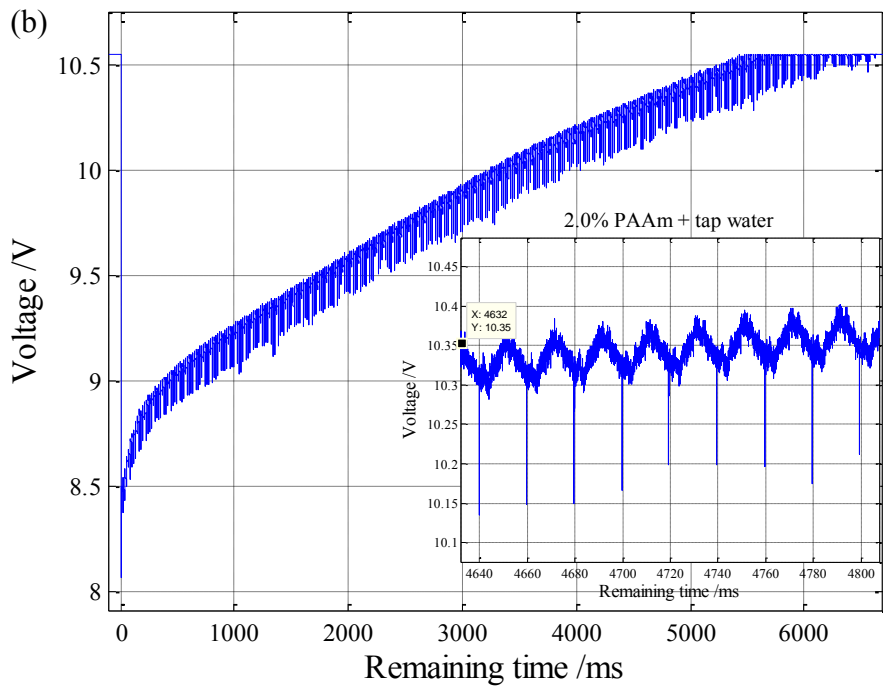
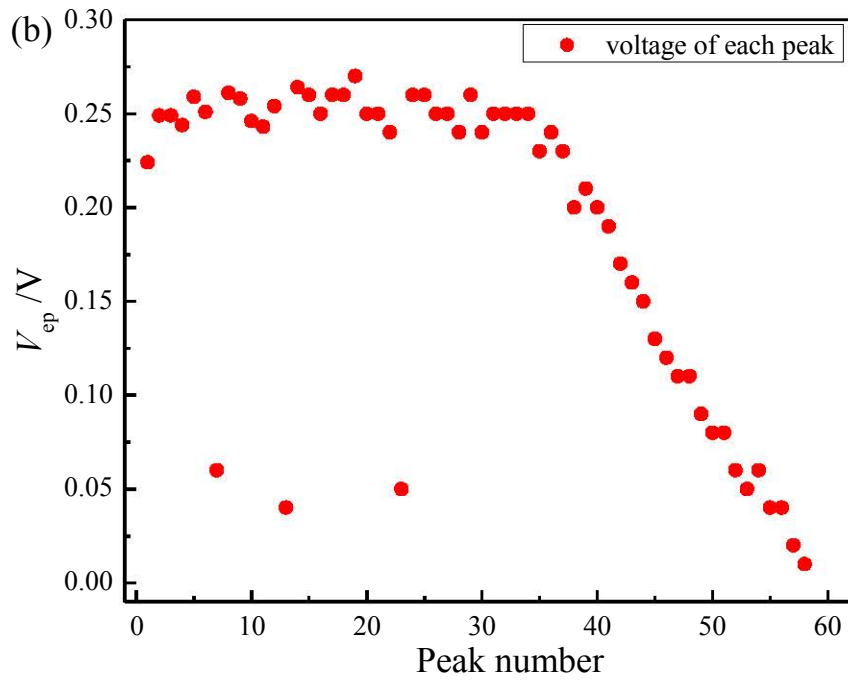
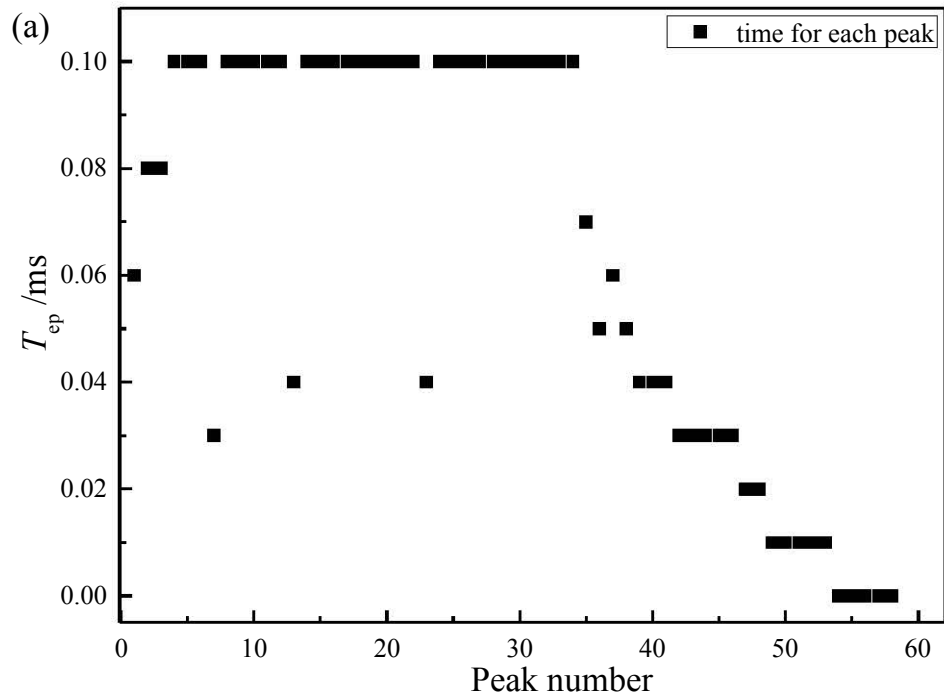


Figure III.13. Filament thinning of 2.0% PAAm solution on stainless steel surface, (a) optical images; (b) electric signals.

The quantitative results of peak characteristics for the representative 1% PAAM aqueous solutions are shown in Figure III.14. The total number of peaks is 58. Firstly, the time duration between each peak (T_{ep}) is found to be constant, $T_{ep} = 0.1$ ms, in the beginning (Figure III.14a). But after Peak 34, T_{ep} decreases until nearly zero, implying the disappearance of the electric signals. Secondly, Figure III.14b shows the similar evolution of the voltage for each peak (V_{ep}) which already defined in Figure III.11c and the transition also locates in Peak 34. Thirdly, the number of points (N_{ep}) in each peak is roughly constant and later on, it decreases (Figure III.14c). Here, we found that for each peak, the transition of T_{ep} , V_{ep} and N_{ep} , occurs after Peak 34 which corresponds to $(t - t_s) = 615$ ms. However, the time $(t - t_s) = 615$ ms, is just roughly corresponding to the end of the main curve and the beginning of the line evolution of the voltage. At this time, the liquid neck is still about 200 μm by observing the images in Figure III.12a. This leads to wonder that there exists a threshold neck width below which the electric signal in each peak occurs similarly, but above which the electric signal decays until the final disappearance.

The evolution of T_{ep} , V_{ep} and N_{ep} for three concentrations of PAAM aqueous solutions is similar. In Figure III.14d, the time interval between two neighboring peaks (T_{dp}) is constant, $T_{dp} = 20$ ms, no matter in main curve or in the line evolution of the voltage. The same value of T_{dp} is also observed before. This feature stimulates us to imagine that the liquid filament acts as a valve which regularly adjusts the transportation of the conducting medium, i.e. controlling the local conductivity. We wonder whether the conductivity is dynamically changing like the viscosity in PAAM solutions. Thus we go further to try to add the sodium chloride to the 0.5% and 2% PAAM aqueous solutions. The results are shown in Figure III.15 and Figure III.16.



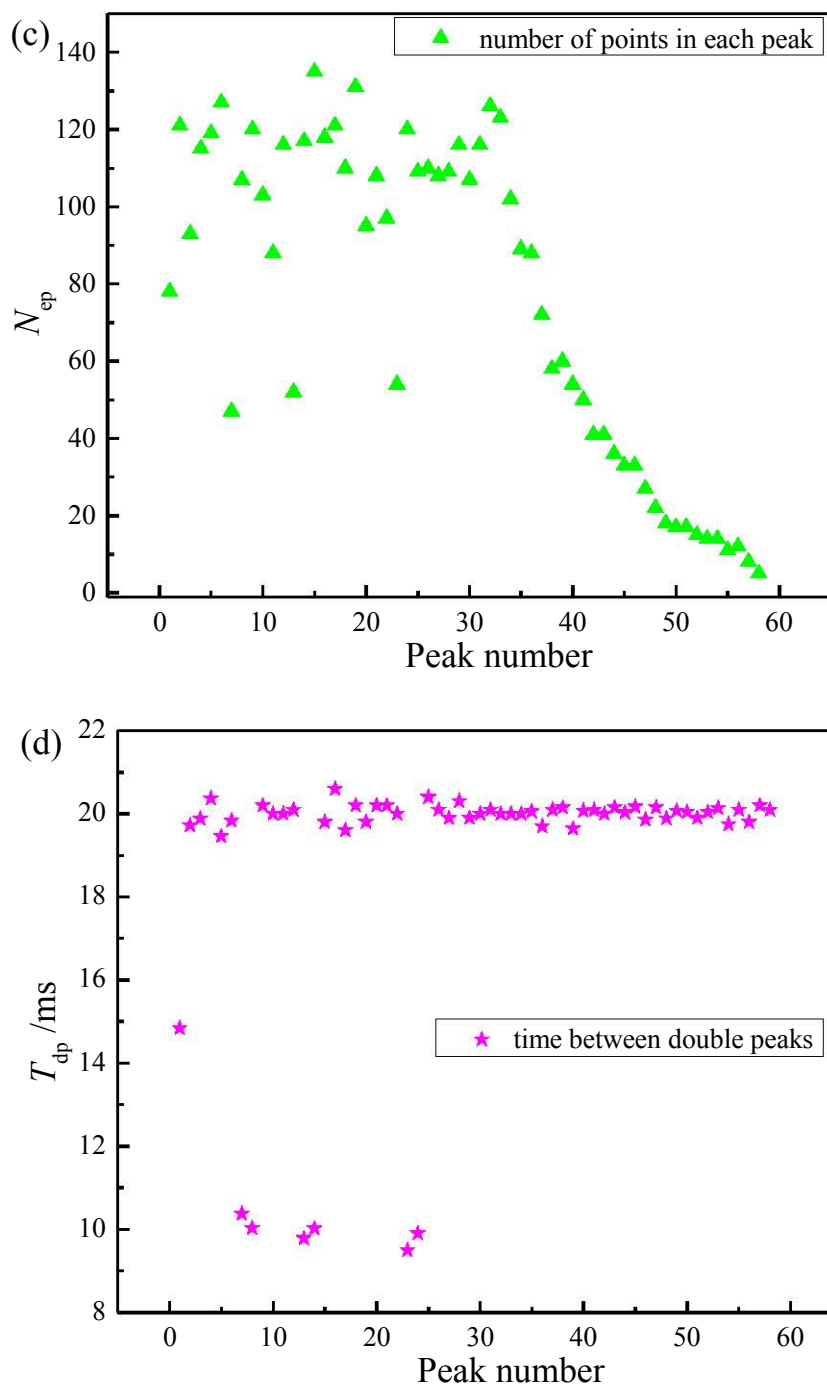
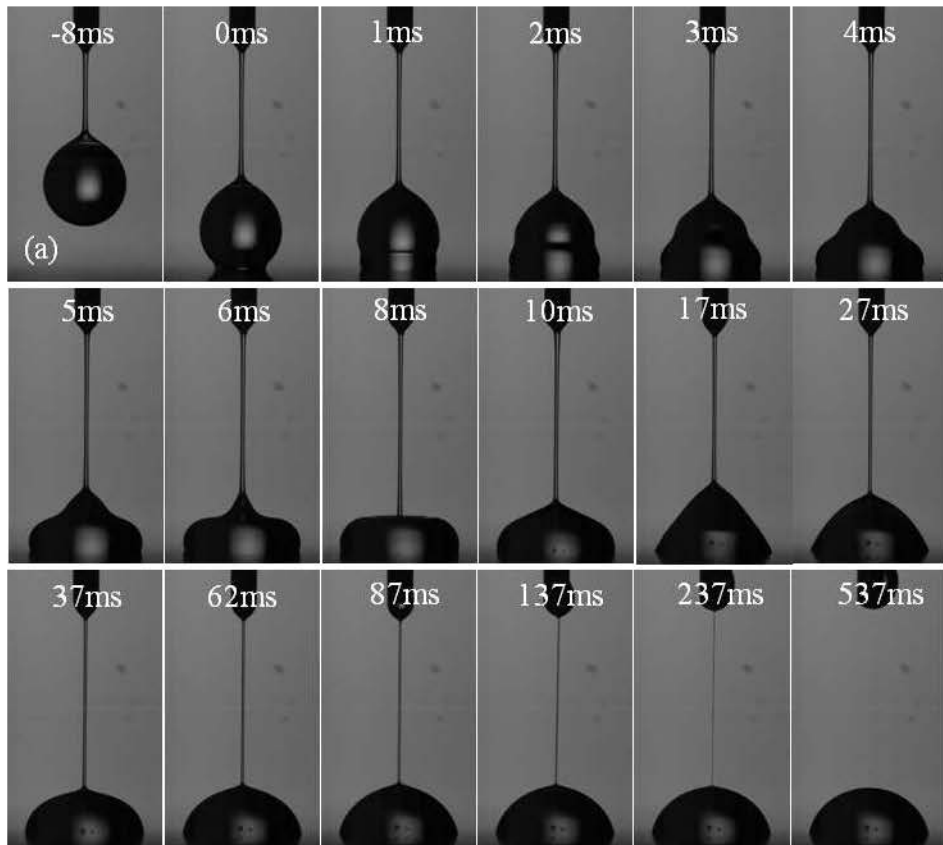


Figure III.14. Peak characteristics of 1.0% PAAm solution on stainless steel surface, (a) time duration for each peak; (b) voltage change for each peak; (c) number of points in each peak; (d) time interval for two neighboring peaks.

Indeed, the measured rheological property in Figure III.3 shows that the presence of NaCl not only leads the viscosity decrease rapidly as the spatial organization of polymer group changes, but also leads the conductivity increases significantly. Thus the global extremum in Figure III.15 and Figure III.16, decreases dramatically to 2 V and 1 V for (0.5%PAAm +water) + 10% NaCl and (2.0%PAAm +water) + 10% NaCl solutions, respectively. The total time for the thinning process is found to be comparable between the imaging and optical methods. However, a bifurcation occurs. Compared to the PAAm aqueous solutions without adding NaCl, the time for the whole thinning process in Figure III.15a and Figure III.16a decreases a lot, while that in Figure III.15b and Figure III.16b increases significantly. The shortening time in images is because of the decreasing viscosity and the prolonging time in electric signals is due to the increasing conductivity. Here, we prove that the loss of electric signal at about 200 μm and failure to catch up the imaging time in PAAm aqueous solutions is perhaps due to the insufficient conductivity.

The peaks are still observed in Figure III.15 and Figure III.16 and the peaks are more than their corresponding solutions without NaCl. If the increasing viscosity leads to the increasing number of peaks (like in PAAm aqueous solutions), then the decreasing viscosity by adding NaCl should result in fewer peaks. Thus it is only logical that the peaks are affected by the fluid conductivity as the increasing conductivity makes more peaks. What's more, the peaks mostly locate in the main curve of voltage. Due to the dramatically decreasing global voltage, the peaks are not as so pronounced as they are in pure PAAm aqueous solutions. In addition, the time interval between two neighboring peaks (T_{dp}) is constant, $T_{ep} = 10$ ms for (0.5%PAAm +water) + 10%NaCl solutions and $T_{dp} = 20$ ms for (2.0%PAAm +water) + 10%NaCl solutions.



(0.5% PAAm+ water) + 10% NaCl

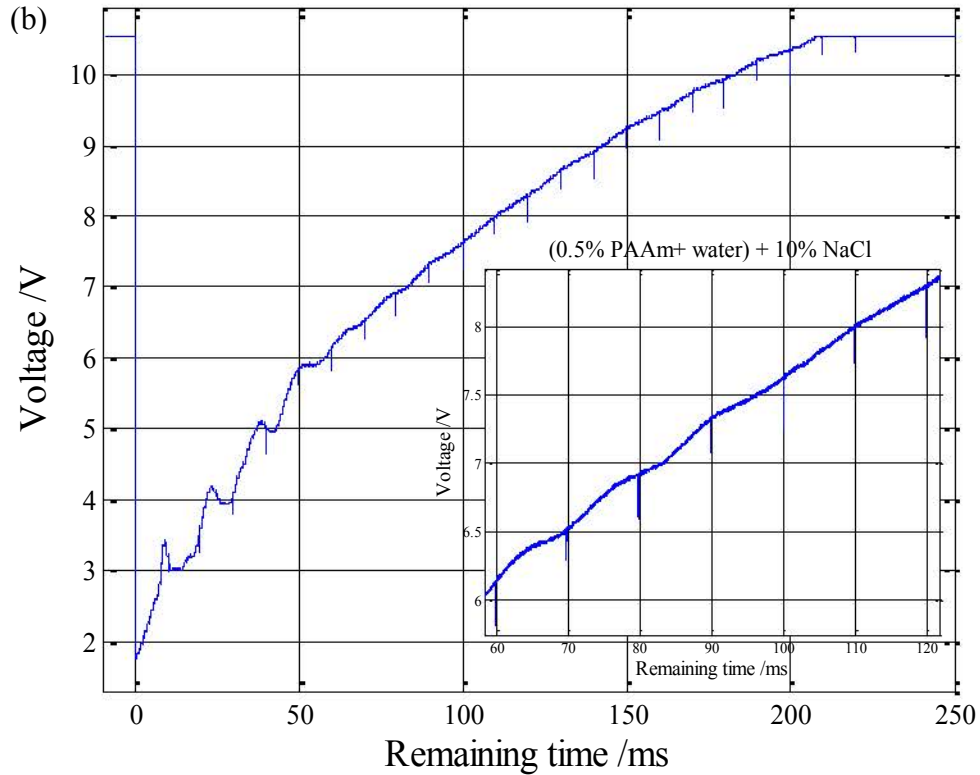
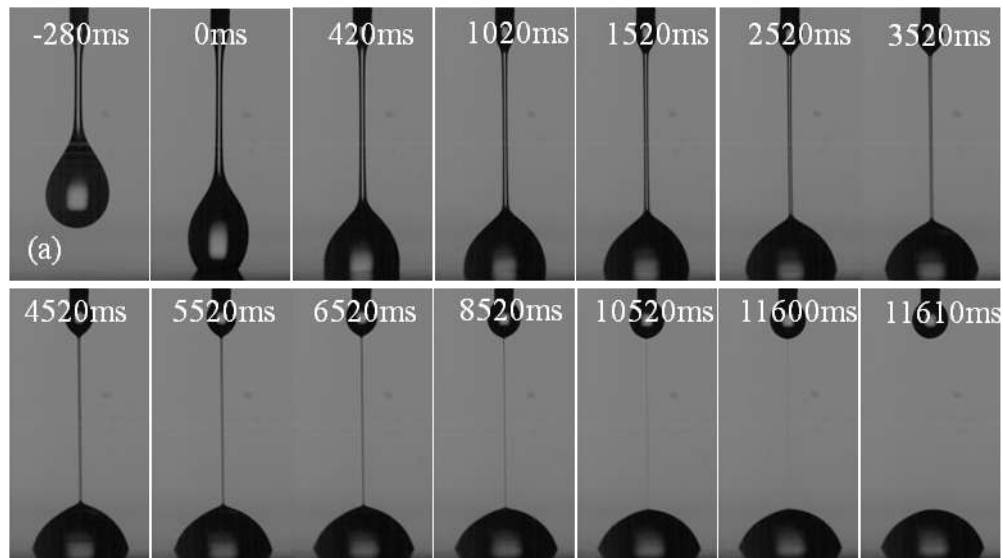


Figure III.15. Filament thinning of (0.5% PAAm + tap water) + 10% NaCl solution on stainless steel surface, (a) optical images; (b) electric signals.



(2.0% PAAm + water) + 10% NaCl

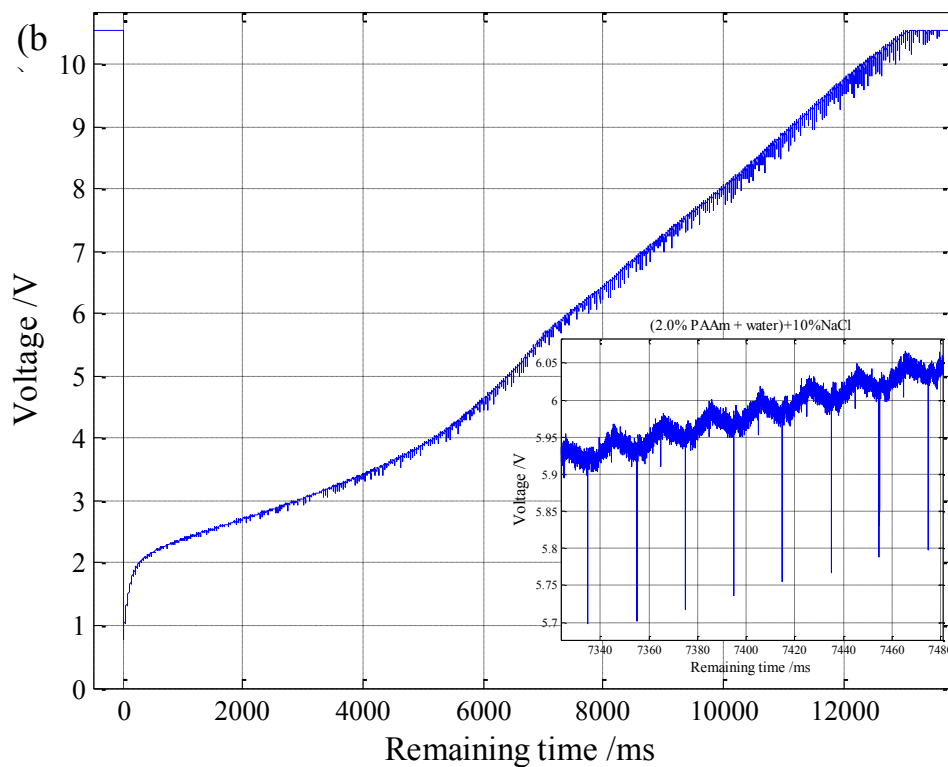


Figure III.16. Filament thinning of (2.0% PAAm + tap water) + 10% NaCl solution on stainless steel surface, (a) optical images; (b) electric signals.

In fact, the time duration of each peak (T_{ep}) in the curve remains roughly the same, $T_{ep} = 0.1$ ms. The points in each peak decreases compared to the before PAAm aqueous

solutions. However, the voltage for each peak (V_{ep}) fluctuates and eventually disappears, which is a little bit different from the previous results.

Finally, the quantitative results from images are plotted in Figure III.17. The liquid filament is uniform cylindrical and here we also define the minimum neck diameter as h_{\min} . No matter with or without adding NaCl into PAAm aqueous solutions, the minimum neck diameter of the filament decreases with the contact time ($t - t_s$) until the final pinch-off. Obviously, the thinning dynamics is accelerated by the adding NaCl into PAAm aqueous solutions.

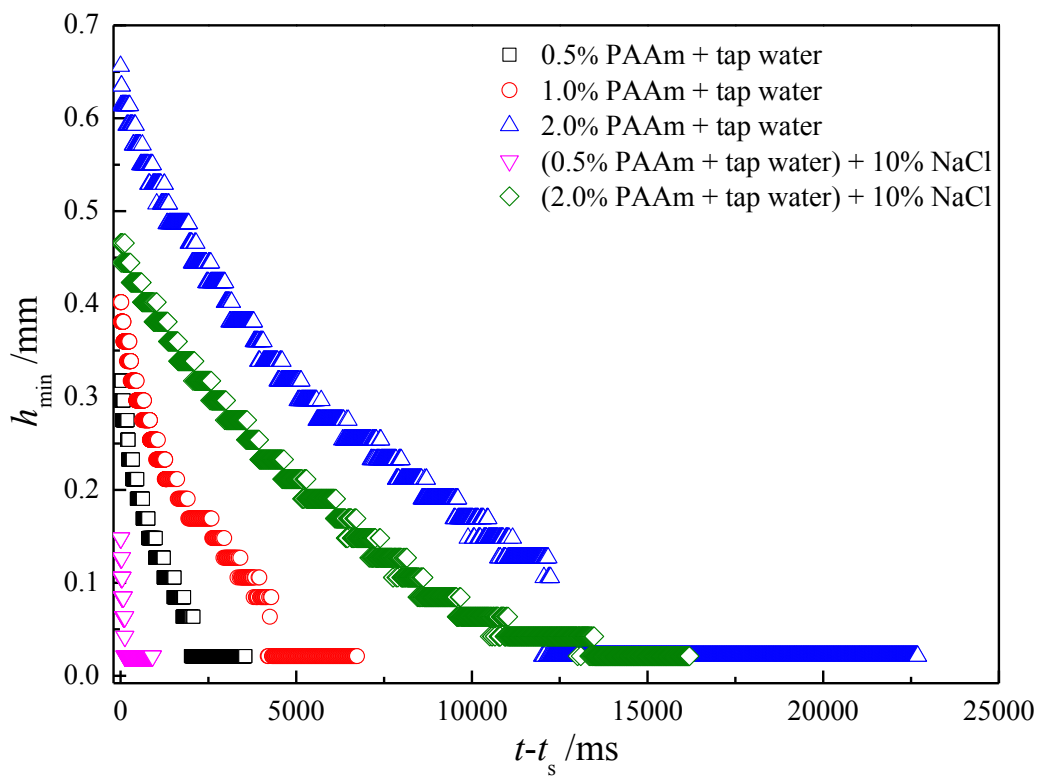


Figure III.17. Thinning dynamics from visualized images for viscoelastic fluids with or without NaCl. Here, h_{\min} is the minimum neck diameter of liquid filament.

III.4 Conclusion

The initial contact and spreading on a flat surface, pinch-off of Newtonian fluids and filament thinning of non-Newtonian fluids were studied through the combining electrical and optical approaches on a dripping-on-substrate system (DoS).

The electrical device reaches a much lower time-scale dynamics of initial contact and spreading and the effect of substrate material and fluid properties especially the conductivity, on the exponent is excluded for the short-time spreading. The imaging analysis gives an exponent of around 0.41 to 0.48, which is quite compatible to the previous results. By applying the similar power-law, $V \propto (t - t_s)^c$, the exponent of -0.08 to -0.15 is obtained from the ultra-high-speed electric signals.

With regard to the pinch-off of Newtonian fluids, the exponent is 0.6 to 0.7 for low-viscosity Newtonian fluids. But a larger exponent 1.2 is observed for high-viscosity Newtonian fluids. While by applying the similar scaling-law, $V \propto (t_0 - t)^c$, the voltage of 20% Emkarox evolves with the exponent of -0.02 and the rest solutions exhibit an exponent ranging from -0.07 to -0.10. This different scaling law no matter in images or electric signals is derived from the effect of viscosity.

Lastly, the thinning of liquid filament shows special phenomena in electric signals. Firstly, the peak regularly occurs during the thinning of non-Newtonian fluids and they are affected by the conductivity and concentration. To be precise, the number of peaks increases with the fluid conductivity and concentration. Secondly, the real time for the whole thinning process is directly related to the fluid viscoelasticity. Furthermore, we find that the conductivity directly determines the global extremum of voltage.

In all, except the strong conductivity disturbance of NaCl in the very initial contact and the very final pinch-off, the obtained dynamics of short-time spreading and pinch-off is similar between imaging and electrical methods. However, the special peaks are found through electric signals during the filament thinning of non-Newtonian fluids. Due to the unclear quantitative relationship between the electric signals and optical images, the further investigation will be required in this area, especially the peak feature.

PART IV: General conclusions and perspectives

IV.1 General conclusions

This thesis mainly focuses on the interfacial phenomena involved in drops and bubbles, including the pinch-off of drops and bubbles, manipulation of drops on superhydrophobic interface and initial contact and spreading of a drop on a solid surface. These investigations of drop and bubble manipulations not only deepen the understanding of the interfacial phenomena but also facilitate the possibly industrial applications like spray-coating, inkjet printing and liquid transportation. The main conclusions of the thesis are summarized as follows:

Part I involves the breakup of an interface, i.e. instability of interface. The pinch-off dynamics was firstly investigated by a bubble generated from a submerged nozzle. The buoyancy takes effect in the initial stage but in the pinch-off region, the gas inertia, the viscous liquid drag and the surface tension reach a certain equilibrium. The exponent of the scaling power-law indicates that bubble pinch-off in Newtonian fluids and non-Newtonian fluids of low viscosity is self-similar, but bubble pinch-off in Newtonian fluids of high viscosity deviates from the universal and self-similar character. These experimental results were well validated through numerical simulations. Secondly, the two-fluid drop pinch-off from a free surface flow was investigated. We proved that the universal self-similar behavior significantly depends on the viscosity ratio between the internal and external fluids. Furthermore, the formation and breakup dynamics of ferrofluid drops was studied under either upward or downward magnetic fields to counterbalance or amplify the gravity. The results show that the volume, shape as well as formation frequency of ferrofluid drops could be actively controlled by the external magnetic field. But the gravity-compensated and gravity-superimposed magnetic fields don't affect the self-similar pinch-off behavior. Last but not least, the droplet pinch-off at micro-scale was further studied considering negligible gravity in a horizontal micro-device. The self-similar pinch-off was demonstrated at a lower length scale with a unity exponent. The flow field was obtained and reverse flow in the water thread near pinch-off was found. In all, the pinch-off dynamics is studied comprehensively and we prove that the final pinch-off is affected by the viscosity ration between internal and external fluids and we exclude the effect of buoyancy and gravity on the self-similar behavior.

Part II involves the manipulation of superhydrophobic interfaces. On the one hand, the superhydrophobic interface is accomplished by spraying-coating on a solid substrate. Then the non-wetting water drops hurdling different barriers were experimentally investigated. Unlike solid spheres, drops' deformation is just their self-adjustment to the external barriers and is significantly advantageous to their hurdling process. Two empirical relationships were proposed to describe the key hurdling parameters, i.e. hurdling time and kinetic energy loss, which reveal the main hurdling dynamics and reflect partially the shape deformation during the hurdling process. On the other hand, the superhydrophobic interface is obtained by wrapping water drops with non-wetting particles. Water marbles then could be manipulated and their undressing motion on a thin oil film was performed. We found that water marbles undergo three distinct stages: a linear motion stage to remove progressively the outside loose particles; transient stage where the compact particles are further undressed; adherent stage that liquid marbles are finally immobilized and adherent to the oil film. The similar contact angle of captured marbles and static water drops on oil film, indicates that the bottom of water marbles is nearly void of particles to display a water-oil direct contact. In addition, we found that the larger the liquid volume, the longer the distance for marbles to travel; the larger the oil viscosity, the quicker the transient stage to immobilize water marbles.

Part III further investigates the interfacial phenomena through optical and electrical methods for the initial contact and of drops on a solid metallic surface as well as the pinch-off of the resulting liquid film. The ultra-high-speed electric device reaches a much lower time-scale and gives the dynamical details of the initial contact and spreading pinch-off of Newtonian fluids and filament thinning of non-Newtonian fluids on a dripping-on-substrate system. The effect of substrate material and fluid properties especially the conductivity, on the short-time spreading exponent is obtained both optically and electrically. With regard to the pinch-off of Newtonian fluids, the exponent ranges from 0.6 to 0.7 for low-viscosity Newtonian fluids. But a larger exponent 1.2 is observed for high-viscosity Newtonian fluids. The changing of scaling law is also observed in electrical signals, which is derived from the effect of viscosity. For the pinch-off of non-Newtonian fluids, the long filament and bead-on-string were previously observed, but here a special phenomenon exists in electric signals. The peaks occur regularly during the thinning of non-Newtonian fluids and the larger the conductivity, the more the peaks. Additionally, the real time for the whole thinning process

was demonstrated to be directly related to the viscosity and the global extremum of voltage was determined by the conductivity of fluids.

IV.2 Perspectives

The breakup of interface, drop manipulation, short-time spreading and filament thinning were studied in this thesis. But some perspectives still remain open.

- (1) Bubble pinch-off in highly shear-thinning non-Newtonian fluids deviates from the universal and self-similar character. And the two ends immediately after pinch-off is “plane” for Newtonian fluids of low viscosity, “cusp” for Newtonian fluids of high viscosity and special “tail” for all non-Newtonian fluids. This stimulates us to wonder whether it is resulted from the elasticity and other effect like fluid intrinsic structure. The special pinch-off dynamics and these spatially modulated geometries require further investigations in accordance with fluid properties like viscoelastic non-Newtonian fluids of either high-viscosity or structure such as suspensions and emulsions.
- (2) During the drop pinch-off of ferrofluids, the gravity-compensated and gravity-superimposed effect is excluded. However, whether the final pinch-off takes place in pure liquid or in chains of magnetic particles, is still unknown. Though we added seeding particles into the dispersed phase at microscale in the micro-device and the results obtained by the micro-PIV showed that the seeding particles in the water thread are rejected to two sides, the seeding particle size of 0.88 μm is quite large compared to magnetic particles in ferrofluids, typically about 10 nm. Thus in the near future, the pinch-off of suspension drops or emulsion drops needs further attention.
- (3) The fast phenomena of drop or bubble pinch-off require further study as the molecular level is finally reached when the breakup takes place. The numerical simulation based on molecular dynamics (MD) would be necessary instead of the classical Navier-Stokes equation for the singularity breaking point. And experimental studies of pinch-off are still limited by the resolution of high-speed camera. Though we tried to reveal the dynamics of the breakup point through ultra-high-speed electrical device, the behind

quantitative relationship between the electrical signals and optical images still needs to establish.

- (4) Ferrofluid drops can exhibit a conical shape under a magnetic field. The conical to-conical coalescence has never been reported in the literature. Especially, when a ferrofluid drop from a continuous feeding nozzle and a small amount of ferrofluid on a substrate are exposed to the same magnetic field, the periodic phenomenon of coalescence and breakup would occur. Such kind of self-sustained system needs further works.



Figure IV.1. Self-sustained coalescence and breakup of ferrofluid droplets.

- (5) The manipulation of superhydrophobic surface can be extended to the topic that liquid drops impact on superhydrophobic surface with various geometries which will facilitate the applications like self-cleaning and spray-coating.

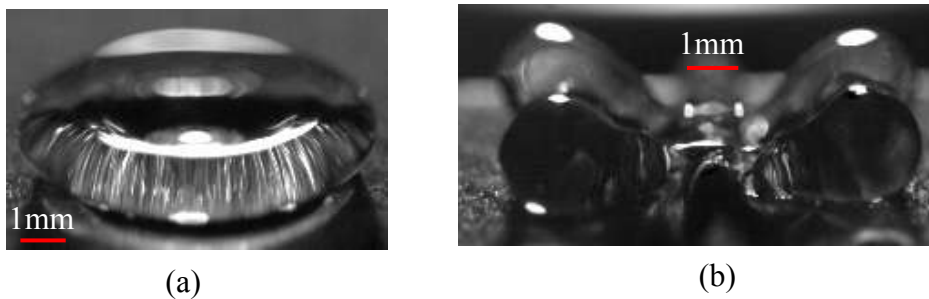


Figure IV.2. Drops impact on the flat superhydrophobic surface (a) and the barrier-attached superhydrophobic surface (b).

- (6) The coalescence between two drops could be performed on superhydrophobic surfaces, especially a water drop and a ferrofluid drop. The conventional studies about drop coalescence are conducted by two semi-spherical drops on the vertical direction. Here, on superhydrophobic surface, the dynamics of coalescence can be investigated on horizontal direction considering the size and fluid properties of two drops. One drop is triggered through a slope or external fields like a magnetic field to approach the fixed drop. Especially, the ferrofluid drop can be actively controlled to approach a water drop and the mixing dynamics is possible to be obtained by analyzing the black and white boundary.

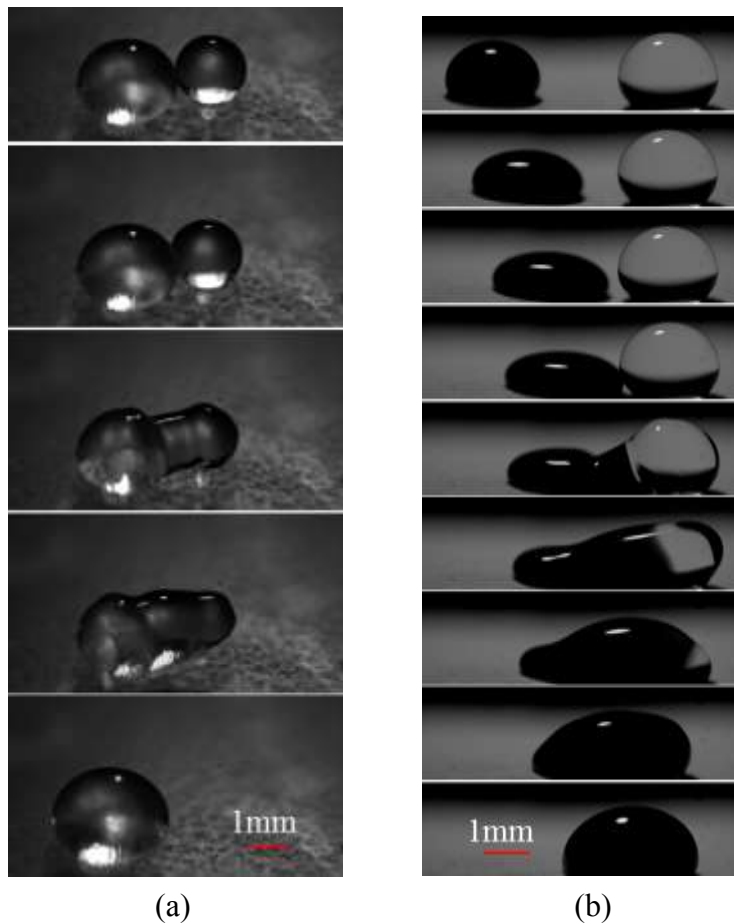


Figure IV.3. Coalescence of water-water drops (a) and water-ferrofluid drops (b) on superhydrophobic surface.

- (7) The peak characteristics in the filament thinning of non-Newtonian fluids captured by the electrical device motivates the future work of Boger fluids whose viscosity is constant and the elasticity effect would be particularly studied.
- (8) The ultra-high-speed electrical acquisition system can be employed to investigate the coalescence of two conducting drops. Or one pendant drop coalesces with a flat liquid sheet.

Nomenclature

Latin Symbols

Part I

a	prefactor [$\text{m}\cdot\text{s}^{-b}$]
b	exponent
B	magnetic flux density [T]
C_D	drag coefficient
d	inner diameter of a nozzle [m]
d'	outside diameter of a nozzle [m]
D_{max}	maximum bubble diameter [m]
D_0	orifice diameter [m]
f	frequency [s^{-1}]
g	gravitational acceleration [$\text{m}\cdot\text{s}^{-2}$]
h_{min}	minimum neck diameter of primary pinch-off [m]
h'_{min}	minimum neck diameter of secondary pinch-off [m]
K	consistency [$\text{Pa}\cdot\text{s}^n$]
l_η	viscous length scale, $l_\eta = \eta^2 / (\sigma\rho)$
P_L	static liquid pressure [Pa]
P_B	gas pressure [Pa]
P_u	pressure due to the viscous drag of fluid [Pa]
Q	fluid flowrate [$\text{m}^3\cdot\text{s}^{-1}$]
Q_c	flowrate of continuous phase [$\text{m}^3\cdot\text{s}^{-1}$]
Q_d	flowrate of dispersed phase [$\text{m}^3\cdot\text{s}^{-1}$]
R	equivalent radius of bubble or drop [m]
R', R''	local radii of curvature [m]
\dot{R}, \ddot{R}	first derivative ($\text{m}\cdot\text{s}^{-1}$) and second derivative [$\text{m}\cdot\text{s}^{-2}$]
t	real time [s]
t_0	breakup time [s]
V_B	volume of bubble [m^3]
U_B	rising velocity of bubble [$\text{m}\cdot\text{s}^{-1}$]

Nomenclature

x	distance from the center axis of the magnet [m]
z'	relative neck position [m]
z	real position in a specific plane [m]
z_0	position corresponding to h_{\min} [m]
Part II	
w	base width of barriers [m]
C	convex path length [m]
X_L	left position of liquid drops [m]
X_R	right position of liquid drops [m]
X_{AC}	advancing position of liquid marbles [m]
X_{RC}	receding position of liquid marbles [m]
H	height of liquid drops or marbles [m]
W	width of liquid drops or marbles [m]
F_{max}	maximum deformation of drops and marbles
B_a	base of liquid drops or marbles [m]
v_1	initial velocity of drops hurdling barriers [$\text{m}\cdot\text{s}^{-1}$]
v_2	final velocity of drops hurdling barriers [$\text{m}\cdot\text{s}^{-1}$]
V	drop volume [m^3]
t_h	hurdling time [s]
L_σ	capillary length of the drop fluid, $L_\sigma = \sqrt{\sigma / \rho g}$ [m]
t_r	viscous relaxation time, $t_r = \rho d^2 / \eta$ [s]
Part III	
R	drop radius [m]
g	gravitational acceleration [$\text{m}\cdot\text{s}^{-2}$]
r	spreading radius [m]
l_η	viscous length scale, $l_\eta = \eta^2 / (\sigma \rho)$
d	inner diameter of a nozzle [m]
d'	outside diameter of a nozzle [m]
l	distance between the nozzle and the plate [m]
I	current intensity [A]

K	fluid consistency [Pa.s ⁿ]
n	flow index
Q	flowrate [m ³ ·s ⁻¹]
t	real time [s]
t_s	the first contact time during initial spreading [s]
V	voltage [V]
B_s	spreading base [m]
t_0	breakup time [s]
h_{\min}	minimum neck diameter [m]
T_{ep}	time for each peak [s]
V_{ep}	voltage for each peak [V]
N_{ep}	number of points in each peak
T_{dp}	the time between two neighboring peaks [s]

Greek Symbols

Part I

τ, τ'	time-to-pinch-off [s]
η_{ext}	viscosity of external fluids [Pa.s]
ρ	density [kg·m ⁻³]
ρ_G	density of gas [kg·m ⁻³]
ρ_L	density of liquid [kg·m ⁻³]
η	viscosity [Pa.s]
η_{air}	viscosity of air [Pa.s]
η_1, η_2	viscosity of SO 50 and SO 100 [Pa.s]
η_{in}	viscosity of internal fluid [Pa.s]
η_{ex}	viscosity of external fluid [Pa.s]
λ	viscosity ratio
λ_1	viscosity ratio of drops in SO 50
λ_2	viscosity ratio of drops in SO 100
σ	surface tension [N·m ⁻¹]
σ_1	interfacial tension of drops in SO 50 [N·m ⁻¹]
σ_2	interfacial tension of drops in SO 100 [N·m ⁻¹]

Nomenclature

$\dot{\gamma}$	shear rate [s^{-1}]
τ_{rr}	normal shear stress in the r direction [Pa]
θ	the angle between the normal to the bubble surface [$^{\circ}$]
θ_a	cone angle [$^{\circ}$]
θ_{up}	up cone angle [$^{\circ}$]
θ_{down}	bottom cone angle [$^{\circ}$]
Φ	diameter of the NdFeB magnet [m]
χ	initial susceptibility of the ferrofluid

Part II

θ_c	contact angle [$^{\circ}$]
γ_{LG}	liquid-gas surface tension [$N \cdot m^{-1}$]
γ_{SL}	solid-liquid surface tension [$N \cdot m^{-1}$]
γ_{SG}	solid-gas interface tension [$N \cdot m^{-1}$]
θ_{AC}	advancing angle [$^{\circ}$]
θ_{RC}	receding angle [$^{\circ}$]
τ_h	dimensionless hurdling time,
ϕ	dimensionless shape factor, $\phi = C / L_{\sigma}$
β	spreading factor
ΔE	kinetic energy loss, $\Delta E = (v_1^2 - v_2^2)m / 2$ [J]
Ω	dimensionless kinetic energy loss, $\Omega = \Delta E / (\eta v_1 d^2)$
α	tilting angle [$^{\circ}$]

Part III

ρ	density [$kg \cdot m^{-3}$]
η	viscosity [Pa.s]
λ_c	capillary length, $\lambda_c = (\sigma / \rho g)^{0.5}$ [m]
γ	conductivity [S/m]
$\dot{\gamma}$	shear rate [s^{-1}]

Dimensionless groups

Part I

Bo	Bond number, $Bo = \rho g d^2 / (\sigma)$
We	Weber number, $We = \rho u^2 R / \sigma$
Ca	Capillary number, $Ca = \eta u / \sigma$

Part II

Re	Reynolds number, $Re = \rho v_1 d / \eta$
Oh	Ohnesorge number, $Oh = \eta / \sqrt{\rho \sigma d}$

Abbreviations

Part I

PMMA	poly(methyl methacrylate)
SDS	sodium dodecyl sulfate
PAAm	polyacrylamide, AN 905 SH
SO 10	silicone oil 10
SO 50	silicone oil 50
SO 100	silicone oil 100
fps	frame per second
NdFeB	neodymium iron boron
NM	no magnetic field
UM	upward magnetic field
DM	downward magnetic field
μ -PIV	micro-particle image velocimetry system

Part II

SEM	scanning electron microscope
-----	------------------------------

Part III

NS	Navier-Stokes
DoS	dripping-on-substrate
AFM	atomic force microscopy
SIEL	service instrumentation & électronique du laboratoire

References

- 't Mannetje, D., Banpurkar, A., Koppelman, H., Duits, M.H., van den Ende, D., Mugele, F., 2013. Electrically tunable wetting defects characterized by a simple capillary force sensor. *Langmuir* 29, 9944-9949.
- 't Mannetje, D., Ghosh, S., Lagraauw, R., Otten, S., Pit, A., Berendsen, C., Zeegers, J., van den Ende, D., Mugele, F., 2014. Trapping of drops by wetting defects. *Nature Communications*. 5, 3559.
- 't Mannetje, D.J.C.M., Murade, C.U., van den Ende, D., Mugele, F., 2011. Electrically assisted drop sliding on inclined planes. *Applied Physics Letters* 98, 014102.
- Afkhami, S., Renardy, Y., Renardy, M., Riffle, J.S., St Pierre, T., 2008. Field-induced motion of ferrofluid droplets through immiscible viscous media. *Journal of Fluid Mechanics* 610, 363.
- Afzal, A., Kim, K.-Y., 2014. Flow and mixing analysis of non-Newtonian fluids in straight and serpentine microchannels. *Chemical Engineering Science* 116, 263-274.
- Albadawi, A., Donoghue, D.B., Robinson, A.J., Murray, D.B., Delauré, Y.M.C., 2013. Influence of surface tension implementation in Volume of Fluid and coupled Volume of Fluid with Level Set methods for bubble growth and detachment. *International Journal of Multiphase Flow* 53, 11-28.
- Allen, R.F., Benson, P.R., 1975. Rolling drops on an inclined plane. *J Colloid Interface Sci* 50, 250-253.
- Amirnia, S., de Bruyn, J.R., Bergougnou, M.A., Margaritis, A., 2013. Continuous rise velocity of air bubbles in non-Newtonian biopolymer solutions. *Chemical Engineering Science* 94, 60-68.
- Arbatan, T., Li, L., Tian, J., Shen, W., 2012. Liquid marbles as micro-bioreactors for rapid blood typing. *Adv Healthc Mater* 1, 80-83.
- Aubin, J., Prat, L., Xuereb, C., Gourdon, C., 2009. Effect of microchannel aspect ratio on residence time distributions and the axial dispersion coefficient. *Chemical Engineering and Processing: Process Intensification* 48, 554-559.
- Aussillous, P., Quéré, D., 2001. Liquid marbles. *Nature* 411, 924-927.
- Aussillous, P., Quéré, D., 2006. Properties of liquid marbles. *Proc. R. Soc. A* 462, 973-999.
- Barthlott, W., Neinhuis, C., 1997. Purity of the sacred lotus, or escape from contamination in biological surfaces. *Planta* 202, 1-8.

- Basaran, O.A., 2002. Small-scale free surface flows with breakup: drop formation and emerging applications. *AIChE Journal* 48.
- Bashir, S., Bashir, M., Rees, J.M., Zimmerman, W.B.J., 2014. Dynamic wetting in microfluidic droplet formation. *BioChip Journal* 8, 122-128.
- Bechtel, S.E., Cao, J.Z., Forest, M.G., 1992. Practical application of a higher order perturbation theory for slender viscoelastic jets and fibers. *Journal of Non-Newtonian Fluid Mechanics* 41, 201-273.
- Benilov, E.S., Billingham, J., 2011. Drops climbing uphill on an oscillating substrate. *Journal of Fluid Mechanics* 674, 93-119.
- Bergeron, V., Bonn, D., Martin, J.Y., Vovelle, L., 2000. Controlling droplet deposition with polymer additives. *Nature* 405, 772-775.
- Bergmann, R., van der Meer, D., Stijnman, M., Sandtke, M., Prosperetti, A., Lohse, D., 2006. Giant bubble pinch-off. *Physical Review Letters* 96.
- Berthier, S., 2007. Iridescences: the physical colors of insects. *New York: Springer*.
- Bertola, V., 2013. Dynamic wetting of dilute polymer solutions: the case of impacting droplets. *Advances in Colloid and Interface* 193, 1-11.
- Biance, A.L., Clanet, C., Quere, D., 2004. First steps in the spreading of a liquid droplet. *Physical Review E* 69, 016301.
- Biance, A.L., Clanet, C., uéré , D., 2003. Leidenfrost drops. *Physics of Fluids* 15, 1632.
- Bird, J.C., Dhiman, R., Kwon, H.M., Varanasi, K.K., 2013. Reducing the contact time of a bouncing drop. *Nature* 503, 385-388.
- Bird, J.C., Mandre, S., Stone, H.A., 2008. Short-time dynamics of partial wetting. *Physical Review Letters* 100, 234501.
- Bormashenko, E., 2011. Liquid marbles: Properties and applications. *Current Opinion in Colloid & Interface Science* 16, 266-271.
- Bormashenko, E., Balter, R., Aurbach, D., 2010a. Micropump based on liquid marbles. *Applied Physics Letters* 97, 091908.
- Bormashenko, E., Balter, R., Aurbach, D., 2012a. Formation of liquid marbles and wetting transitions. *J Colloid Interface Sci* 384, 157-161.
- Bormashenko, E., Bormashenko, Y., 2011. Non-stick droplet surgery with a superhydrophobic scalpel. *Langmuir* 27, 3266-3270.
- Bormashenko, E., Bormashenko, Y., Gryniov, R., Aharoni, H., Whyman, G., Binks, B.P., 2015. Self-propulsion of liquid marbles: leidenfrost-like levitation driven by marangoni flow. *The Journal of Physical Chemistry C* 119, 9910-9915.

- Bormashenko, E., Bormashenko, Y., Musin, A., Barkay, Z., 2009. On the mechanism of floating and sliding of liquid marbles. *Chemphyschem* 10, 654-656.
- Bormashenko, E., Bormashenko, Y., Oleg, G., 2010b. On the nature of the friction between nonstick droplets and solid substrates. *Langmuir* 26, 12479-12482.
- Bormashenko, E., Pogreb, R., Balter, R., Gendelman, O., Aurbach, D., 2012b. Composite non-stick droplets and their actuation with electric field. *Applied Physics Letters* 100, 151601.
- Bormashenko, E., Pogreb, R., Bormashenko, Y., Musin, A., Stein, T., 2008. New investigations on ferrofluidics: ferrofluidic marbles and magnetic-field-driven drops on superhydrophobic surfaces. *Langmuir* 24, 12119–12122.
- Bormashenko, E., Pogreb, R., Musin, A., 2012c. Stable water and glycerol marbles immersed in organic liquids: from liquid marbles to Pickering-like emulsions. *J Colloid Interface Sci* 366, 196-199.
- Brenner, M.P., Eggers, J., Joseph, K., Nagel, S.R., Shi, X.D., 1997. Breakdown of scaling in droplet fission at high Reynolds number. *Physics of Fluids* 9, 1573-1590.
- Brenner, M.P., Shi, X.D., Nagel, S.R., 1994. Iterated instabilities during droplet fission. *Physical Review Letters* 73, 3391-3394.
- Brunet, P., Eggers, J., Deegan, R.D., 2007. Vibration-induced climbing of drops. *Physical Review Letters* 99, 144501.
- Brunet, P., Eggers, J., Deegan, R.D., 2009. Motion of a drop driven by substrate vibrations. *The European Physical Journal Special Topics* 166, 11-14.
- Buehrle, J., Herminghaus, S., Mugele, F., 2002. Impact of line tension on the equilibrium shape of liquid droplets on patterned substrates. *Langmuir* 18, 9771-9777.
- Burton, J.C., Rutledge, J.E., Taborek, P., 2004. Fluid pinch-off dynamics at nanometer length scales. *Physical Review Letters* 92, 244505.
- Burton, J.C., Rutledge, J.E., Taborek, P., 2007. Fluid pinch-off in superfluid and normal He4. *Physical Review E* 75, 036311.
- Burton, J.C., Taborek, P., 2007. Role of dimensionality and axisymmetry in fluid pinch-off and coalescence. *Physical Review Letters* 98, 224502.
- Burton, J.C., Taborek, P., 2008. Bifurcation from bubble to droplet behavior in inviscid pinch-off. *Physical Review Letters* 101, 214502.
- Burton, J.C., Waldrep, R., Taborek, P., 2005. Scaling and instabilities in bubble pinch-off. *Physical Review Letters* 94, 184502.

- Butt, H.J., Gao, N., Papadopoulos, P., Steffen, W., Kappl, M., Berger, R., 2017. Energy dissipation of moving drops on superhydrophobic and superoleophobic surfaces. *Langmuir* 33, 107-116.
- Carrier, O., Funfschilling, D., Li, H.Z., 2014. Effect of the fluid injection configuration on droplet size in a microfluidic T junction. *Physical Review E* 89, 013003.
- Cassie, A.B.D., Baxter, S., 1944. Wettability of porous surfaces. *Trans. Faraday Soc.* 40, 546-551
- Castrejon-Pita, J.R., Castrejon-Pita, A.A., Thete, S.S., Sambath, K., Hutchings, I.M., Hinch, J., Lister, J.R., Basaran, O.A., 2015. Plethora of transitions during breakup of liquid filaments. *Proceedings of the National Academy of Sciences* 112, 4582-4587.
- Cazabat, A.M., Stuart, M.A.C., 1986. Dynamics of wetting: effects of surface roughness. *The Journal of Physical Chemistry* 90, 5845-5849.
- Chaudhury, M.K., Whitesides, G.M., 1992. How to make water run uphill. *Science* 256, 1539-1541.
- Chen, A.U., Notz, P.K., Basaran, O.A., 2002. Computational and experimental analysis of pinch-off and scaling. *Physical Review Letters* 88, 174501.
- Chen, C.Y., Chen, C.H., Lee, W.F., 2009. Experiments on breakups of a magnetic fluid drop through a micro-orifice. *Journal of Magnetism and Magnetic Materials* 321, 3520-3525.
- Chen, L., Auernhammer, G.K., Bonaccorso, E., 2011. Short time wetting dynamics on soft surfaces. *Soft Matter* 7, 9084.
- Chen, L., Bonaccorso, E., Shanahan, M.E., 2013. Inertial to viscoelastic transition in early drop spreading on soft surfaces. *Langmuir* 29, 1893-1898.
- Chen, Y.J., Steen, P.H., 1997. Dynamics of inviscid capillary breakup: collapse and pinchoff of a film bridge. *Journal of Fluid Mechanics* 341, 245-267.
- Chen, Z., Ata, S., Jameson, G.J., 2015. Breakup and re-formation of bubble clusters in a flotation cell. *Minerals Engineering* 71, 16-20.
- Cheung, Y.N., Qiu, H., 2012. Droplet pinch-off in acoustically actuated flow-focusing devices. *Journal of Micromechanics and Microengineering* 22, 125003.
- Christopher, G.F., Anna, S.L., 2007. Microfluidic methods for generating continuous droplet streams. *Journal of Physics D: Applied Physics* 40, R319-R336.
- Chung, D.C.K., Katariya, M., Huynh, S.H., Cheong, B.H.-P., Liew, O.W., Muradoglu, M., Ng, T.W., 2015. Uphill airflow transport of drops on superhydrophobic inclines. *Colloids and Interface Science Communications* 6, 1-4.

- Cohen, I., Brenner, M.P., Eggers, J., Nagel, S.R., 1999. Two fluid drop snap-off problem: experiments and theory. *Physical Review Letters* 83, 1147-1150.
- Cooper-White, J.J., Fagan, J.E., Tirtaatmadja, V., Lester, D.R., Boger, D.V., 2002. Drop formation dynamics of constant low-viscosity, elastic fluids. *Journal of Non-Newtonian Fluid Mechanics* 106, 29-59.
- Corkidi, G., Rojas, A., Pimentel, A., Galindo, E., 2012. Visualization of compound drops formation in multiphase processes for the identification of factors influencing bubble and water droplet inclusions in oil drops. *Chemical Engineering Research and Design* 90, 1727-1738.
- Cottin-Bizonne, C., Barrat, J.-L., Bocquet, L., Charlaix, E., 2003. Low-friction flows of liquid at nanopatterned interfaces. *Nat Commun* 2, 237-240.
- Cubaud, T., Mason, T.G., 2008. Capillary threads and viscous droplets in square microchannels. *Physics of Fluids* 20, 053302.
- Darmanin, T., Guittard, F., 2015. Superhydrophobic and superoleophobic properties in nature. *Materials Today* 18, 273-285.
- Davidson, J.F., Schuler, B.O.G., 1960. Bubble formation at an orifice in a viscous liquid. *Trans. Inst. Chem. Eng.* 38, 105-115.
- Day, R.F., Hinch, E.J., Lister, J.R., 1998. Self-similar capillary pinchoff of an inviscid fluid. *Physical Review Letters* 80, 704-707.
- de Gennes, P.G., 1985. Wetting: Statics and dynamics. *Reviews of Modern Physics* 57, 827-863.
- Dietrich, N., Mayoufi, N., Poncin, S., Li, H.Z., 2013a. Experimental investigation of bubble and drop formation at submerged orifices. *Chemical Papers* 67, 313-325.
- Dietrich, N., Mayoufi, N., Poncin, S., Midoux, N., Li, H.Z., 2013b. Bubble formation at an orifice: a multiscale investigation. *Chemical Engineering Science* 92, 118-125.
- Dietrich, N., Poncin, S., Midoux, N., Li, H.Z., 2008. Bubble formation dynamics in various flow-focusing microdevices. *Langmuir* 24, 13904-13911.
- Dollet, B., van Hoeve, W., Raven, J.P., Marmottant, P., Versluis, M., 2008. Role of the channel geometry on the bubble pinch-off in flow-focusing devices. *Physical Review Letters* 100, 034504.
- Dong, L., Chaudhury, A., Chaudhury, M.K., 2006. Lateral vibration of a water drop and its motion on a vibrating surface. *Eur. Phys. J. E* 21, 231-242.

- Doshi, P., Cohen, I., Zhang, W., Siegel, M., Howell, P., Basaran, O.A., Nage, S.R., 2003. Persistence of memory in drop breakup: the breakdown of universality. *Science* 302, 1185-1188.
- Du, W., Fu, T., Zhang, Q., Zhu, C., Ma, Y., Li, H.Z., 2016. Breakup dynamics for droplet formation in a flow-focusing device: Rupture position of viscoelastic thread from matrix. *Chemical Engineering Science* 153, 255-269.
- Dupeux, G., Baier, T., Bacot, V., Hardt, S., Clanet, C., Quéré, D., 2013. Self-propelling uneven Leidenfrost solids. *Physics of Fluids* 25, 051704.
- Dupeux, G., Le Merrer, M., Clanet, C., Quere, D., 2011. Trapping leidenfrost drops with crenelations. *Physical Review Letters* 107, 114503.
- Dupin, D., Armes, S.P., Fujii, S., 2009. Stimulus-responsive liquid marbles. *Journal of the American Chemical Society* 131, 5386–5387.
- Eddi, A., Winkels, K.G., Snoeijer, J.H., 2013. Short time dynamics of viscous drop spreading. *Physics of Fluids* 25, 013102.
- Eggers, J., 1993. University pinching of 3D axisymmetric flow. *Physical Review Letters* 71, 3458-3460.
- Eggers, J., 1997. Nonlinear dynamics and breakup of free-surface flows. *Reviews of Modern Physics* 69, 865-929.
- Eggers, J., Dupont, T.F., 2006. Drop formation in a one-dimensional approximation of the Navier–Stokes equation. *Journal of Fluid Mechanics* 262, 205.
- Eggers, J., Fontelos, M.A., Leppinen, D., Snoeijer, J.H., 2007. Theory of the collapsing axisymmetric cavity. *Physical Review Letters* 98, 094502.
- Eggers, J., Villermaux, E., 2008. Physics of liquid jets. *Reports on Progress in Physics* 71, 036601.
- Frank, X., Charpentier, J.-C., Ma, Y., Midoux, N., Li, H.Z., 2012. A multiscale approach for modeling bubbles rising in non-Newtonian fluids. *Industrial & Engineering Chemistry Research* 51, 2084-2093.
- Frank, X., Li, H.Z., 2005. Complex flow around a bubble rising in a non-Newtonian fluid. *Physical Review E* 71, 036309.
- Frank, X., Li, H.Z., 2006. Negative wake behind a sphere rising in viscoelastic fluids: a lattice Boltzmann investigation. *Physical Review E* 74, 056307.
- Frank, X., Li, H.Z., Funfschilling, D., Burdin, F., Ma, Y.G., 2003. Bubble motion in non-newtonian fluids and suspensions. *The Canadian Journal of Chemical Engineering* 81, 483-490.

- Frank, X., Perre, P., Li, H.Z., 2015. Lattice Boltzmann investigation of droplet inertial spreading on various porous surfaces. *Physical Review E* 91, 052405.
- Fu, T., Funfschilling, D., Ma, Y., Li, H.Z., 2010. Scaling the formation of slug bubbles in microfluidic flow-focusing devices. *Microfluidics and Nanofluidics* 8, 467-475.
- Fu, T., Ma, Y., Funfschilling, D., Li, H.Z., 2011. Bubble formation in non-Newtonian fluids in a microfluidic T-junction. *Chemical Engineering and Processing: Process Intensification* 50, 438-442.
- Fu, T., Ma, Y., Funfschilling, D., Zhu, C., Li, H.Z., 2012a. Breakup dynamics of slender bubbles in non-newtonian fluids in microfluidic flow-focusing devices. *AIChE J.* 58, 3560-3567.
- Fu, T.T., Wu, Y.N., Ma, Y.G., Li, H.Z., 2012b. Droplet formation and breakup dynamics in microfluidic flow-focusing devices: from dripping to jetting. *Chemical Engineering Science* 84, 207-217.
- Fujii, S., Kameyama, S., Armes, S.P., Dupin, D., Suzuki, M., Nakamura, Y., 2010. pH-responsive liquid marbles stabilized with poly(2-vinylpyridine) particles. *Soft Matter* 6, 635-640.
- Fujii, T., 2002. PDMS-based microfluidic devices for biomedical applications. *Microelectronic Engineering* 61 907-914.
- Funfschilling, D., Debas, H., Li, H.Z., Mason, T.G., 2009. Flow-field dynamics during droplet formation by dripping in hydrodynamic-focusing microfluidics. *Physical Review E* 80, 015301.
- Funfschilling, D., Li, H.Z., 2001. Flow of non-Newtonian fluids around bubbles PIV measurements and birefringence visualisation. *Chemical Engineering Science* 56, 1137-1141.
- Gao, L., McCarthy, T.J., 2006. Contact angle hysteresis explained. *Langmuir* 22, 6234-6237.
- Gao, L., McCarthy, T.J., 2007. Ionic liquid marbles. *Langmuir* 23, 10445-10447.
- Gao, L., McCarthy, T.J., 2009. Wetting 101 degrees. *Langmuir* 25, 14105-14115.
- Garstecki, P., Stone, H.A., Whitesides, G.M., 2005a. Mechanism for flow-rate controlled breakup in confined geometries: A route to monodisperse emulsions. *Physical Review Letters* 94, 164501.
- Garstecki, P., Stone, H.A., Whitesides, G.M., 2005b. Mechanism for flow-rate controlled breakup in confined geometries: a route to monodisperse emulsions. *Physical Review Letters* 94, 164501.

- Gauthier, A., Symon, S., Clanet, C., Quéré, D., 2015. Water impacting on superhydrophobic macrottextures. *Nat Commun* 6, 8001.
- Ghaini, A., Kashid, M.N., Agar D.W., 2010. Effective interfacial area for mass transfer in the liquid–liquid slug flow capillary microreactors. *Chemical Engineering and Processing: Process Intensification* 49, 358–366.
- Gordillo, J.M., Sevilla, A., Rodríguez-Rodríguez, J., Martínez-Bazán, C., 2005. Axisymmetric bubble pinch-off at high reynolds numbers. *Physical Review Letters* 95.
- Guo, C., He, L., Xin, Y., 2015. Deformation and breakup of aqueous drops in viscous oil under a uniform AC electric field. *Journal of Electrostatics* 77, 27-34.
- Guo, Z.G., Zhou, F., Hao, J.C., Liang, Y.M., Liu, W.M., Huck, W.T.S., 2006. “Stick and slide” ferrofluidic droplets on superhydrophobic surfaces. *Applied Physics Letters* 89, 081911.
- Habera, M., Fabian, M., Šviková, M., Timko, M., 2013. The influence of magnetic field on free surface ferrofluid flow. *Magnetohydrodynamic*. 49, 402-406.
- Hashmi, A., Strauss, A., Xu, J., 2012. Freezing of a liquid marble. *Langmuir* 28, 10324-10328.
- Hemmati, A., Torab-Mostaedi, M., Shirvani, M., Ghaemi, A., 2015. A study of drop size distribution and mean drop size in a perforated rotating disc contactor (PRDC). *Chemical Engineering Research and Design* 96, 54-62.
- Henderson, D.M., Pritchard, W.G., Smolka, L.B., 1997. On the pinch-off of a pendant drop of viscous fluid. *Physics of Fluids* 9, 3188-3200.
- Herbst, D.C., 2012. Pinch-off of underwater air bubbles with up--down asymmetry. *arXiv preprint arXiv 1210, 7826*.
- Herbst, D.C., Zhang, W.W., 2011. Underwater bubble pinch-off: Transient stretching flow. *Physical Review E* 84.
- Huh, C., Scriven, L.E., 1971. Hydrodynamic model of steady movement of a solid/liquid/fluid contact line. *J Colloid Interface Sci* 35, , 85–101.
- Huppert, H.E., 1982. The propagation of two-dimensional and axisymmetric viscous gravity currents over a rigid horizontal surface. *Journal of Fluid Mechanics* 121, 43-58.
- Jarecka, D., Jaruga, A., Smolarkiewicz, P.K., 2015. A spreading drop of shallow water. *Journal of Computational Physics* 289, 53-61.

- Jiang, X., Xu, Q., Dertinger, S.K., Stroock, A.D., Fu, T.M., Whitesides, G.M., 2005. A general method for patterning gradients of biomolecules on surfaces using microfluidic networks. *Anal Chem* 77, 2338-2347.
- Jiang, X.F., Li, H.Z., 2015. Self-similar pinch-off mechanism and scaling of ferrofluid drops. *Physical Review E* 92, 061003(R).
- Jiang, X.F., Zhu, C., Ma, Y., Li, H.Z., 2017. Undressing a water marble on oil film. *Advanced Materials Interfaces* 4, 1700193.
- John, K., Thiele, U., 2010. Self-ratcheting Stokes drops driven by oblique vibrations. *Physical Review Letters* 104, 107801.
- Josephides, D.N., Sajjadi, S., 2015. Increased drop formation frequency via reduction of surfactant interactions in flow-focusing microfluidic devices. *Langmuir* 31, 1218-1224.
- Josserand, C., Lemoine, L., Troeger, R., Zaleski, S., 2005. Droplet impact on a dry surface: triggering the splash with a small obstacle. *Journal of Fluid Mechanics* 524, 47-56.
- Josserand, C., Thoroddsen, S.T., 2016. Drop impact on a solid surface. *Annual Review of Fluid Mechanics* 48, 365-391.
- Kazhan, V.A., Korovin, V.M., 2003. Capillary instability of a cylindrical interface of viscous magnetic and nonmagnetic fluids subjected to an axial magnetic field. *Journal of Magnetism and Magnetic Materials* 260 222-230.
- Keim, N.C., Møller, P., Zhang, W.W., Nagel, S.R., 2006. Breakup of air bubbles in water memory and breakdown of cylindrical symmetry. *Physical Review Letters* 14, 144503.
- Keller, J., Miksis, M., 1983. Surface tension driven flows. *SIAM J. Appl. Math.* 43, 268-277.
- Khalil, K.S., Mahmoudi, S.R., Abu-dheir, N., Varanasi, K.K., 2014. Active surfaces: ferrofluid-impregnated surfaces for active manipulation of droplets. *Applied Physics Letters* 105, 041604.
- Krebs, F.C., 2009. Fabrication and processing of polymer solar cells: A review of printing and coating techniques. *Solar Energy Materials & Solar Cells* 93, 394-412.
- Kulkarni, A.A., Joshi, J.B., 2005. Bubble formation and bubble rise velocity in gas-liquid. *Industrial & Engineering Chemistry Research* 44, 5873-5931.
- Kuo, C.C., Dennin, M., 2013. Scaling behavior of universal pinch-off in two-dimensional foam. *Physical Review E* 87, 052308.
- Kuo, J.S., Spicar-Mihalic, P., Rodriguez, I., Chiu, D.T., 2003. Electrowetting-induced droplet movement in an immiscible medium. *Langmuir* 19, 250-255.

- Lan, W., Li, S., Wang, Y., Luo, G., 2014. CFD simulation of droplet formation in microchannels by a modified level set method. *Industrial & Engineering Chemistry Research* 53, 4913-4921.
- Lavi, B., Marmur, A., 2004. The exponential power law: partial wetting kinetics and dynamic contact angles. *Colloids and Surfaces A: Physicochemical and Engineering Aspects* 250, 409-414.
- LeClear, S., LeClear, J., Abhijeet, Park, K.C., Choi, W., 2016. Drop impact on inclined superhydrophobic surfaces. *J Colloid Interface Sci* 461, 114-121.
- Lee, B.S., Cho, H.J., Lee, J.G., Huh, N., Choi, J.W., Kang, I.S., 2006. Drop formation via breakup of a liquid bridge in an AC electric field. *J Colloid Interface Sci* 302, 294-307.
- Lei, W., Jia, Z.h., He, J.C., Cai, T.M., 2014. Dynamic properties of vibrated drops on a superhydrophobic patterned surface. *Appl. Therm. Eng.* 62, 507-512.
- Lesage, F.J., Marios, F., 2013. Experimental and numerical analysis of quasi-static bubble size and shape characteristics at detachment. *International Journal of Heat and Mass Transfer* 64, 53-69.
- Leshansky, A.M., Pismen, L.M., 2009. Breakup of drops in a microfluidic T junction. *Physics of Fluids* 21, 023303.
- Li, D., Xue, Y., Lv, P., Huang, S., Lin, H., Duan, H., 2016. Receding dynamics of contact lines and size-dependent adhesion on microstructured hydrophobic surfaces. *Soft Matter* 12, 4257-4265.
- Li, H.Z., 1999. Bubbles in non-Newtonian fluids: formation, interactions and coalescence. *Chemical Engineering Science* 54, 2247-2254.
- Li, H.Z., Mouline, Y., Midoux, N., 2002. Modelling the bubble formation dynamics in non-Newtonian fluids. *Chemical Engineering Science* 57, 339-346.
- Li, Y., Sprittles, J.E., 2016. Capillary breakup of a liquid bridge: identifying regimes and transitions. *Journal of Fluid Mechanics* 797, 29-59.
- Li. Huai Z., Mouline, Y., Midoux, N., 2002. Modelling the bubble formation dynamics in non-Newtonian Fluids. *Chemical Engineering Science* 57, 339-346.
- Liang, Z.P., Wang, X.D., Lee, D.J., Peng, X.F., Su, A., 2009. Spreading dynamics of power-law fluid droplets. *Journal of Physics. Condensed Matter* 21, 464117.
- Liao, Y.C., Subramani, H.J., Franses, E.I., Basaran, O.A., 2004. Effects of soluble surfactants on the deformation and breakup of stretching liquid bridges. *Langmuir* 20, 9926-9930.

- Lind, S.J., Phillips, T.N., 2010. The effect of viscoelasticity on a rising gas bubble. *Journal of Non-Newtonian Fluid Mechanics* 165, 852-865.
- Lindken, R., Westerweel, J., Wieneke, B., 2006. Stereoscopic micro particle image velocimetry. *Experiments in Fluids* 41, 161-171.
- Linke, H., Aleman, B.J., Melling, L.D., Taormina, M.J., Francis, M.J., Dow-Hygelund, C.C., Narayanan, V., Taylor, R.P., Stout, A., 2006. Self-propelled Leidenfrost droplets. *Physical Review Letters* 96, 154502.
- Liontas, R., Ma, K., Hirasaki, G.J., Biswal, S.L., 2013. Neighbor-induced bubble pinch-off: novel mechanisms of in situ foam generation in microfluidic channels. *Soft Matter* 9, 10971.
- Lister, J.R., Stone, H.A., 1998a. Capillary breakup of a viscous thread surrounded by another viscous fluid. *Physics of Fluids* 10, 2758-2764.
- Lister, J.R., Stone, H.A., 1998b. Capillary breakup of a viscous thread surrounded by another viscous fluid. *Physics of Fluids* 10, 2758-2764.
- Longmire, E.K., Norman, T.L., Gefroh, D.L., 2001. Dynamics of pinch-off in liquid/liquid jets with surface tension. *International Journal of Multiphase Flow* 27, 1735-1752.
- Longuet-Higgins, M.S., Kerman, B.R., Lunde, K., 1991. The release of air bubbles from an underwater nozzle. *Journal of Fluid Mechanics* 230, 365-390.
- Lopez, J., Miller, C.A., Ruckenstein, E., 1976. Spreading kinetics of liquid drops on solids. *J Colloid Interface Sci* 56, 460-468.
- Loubière, K., Hébrard, G., 2004. Influence of liquid surface tension (surfactants) on bubble formation at rigid and flexible orifices. *Chemical Engineering and Processing: Process Intensification* 43, 1361-1369.
- Louvet, N., Bonn, D., Kellay, H., 2014. Nonuniversality in the pinch-off of yield stress fluids: role of nonlocal rheology. *Physical Review Letters* 113, 218302.
- Lu, Y., Fu, T., Zhu, C., Ma, Y., Li, H.Z., 2013. Pinch-off mechanism for Taylor bubble formation in a microfluidic flow-focusing device. *Microfluidics and Nanofluidics* 16, 1047-1055.
- Lu, Y., Fu, T., Zhu, C., Ma, Y., Li, H.Z., 2014. Scaling of the bubble formation in a flow-focusing device: Role of the liquid viscosity. *Chemical Engineering Science* 105, 213-219.
- Lv, C., Hao, P., Zhang, X., He, F., 2016. Drop impact upon superhydrophobic surfaces with regular and hierarchical roughness. *Applied Physics Letters* 108, 141602.

- Maali, A., Bhushan, B., 2008. Nanorheology and boundary slip in confined liquids using atomic force microscopy. *Journal of Physics: Condensed Matter* 20, 315201.
- Mahadevan, L., Pomeau, Y., 1999. Rolling droplets. *Physics of Fluids* 11, 2449-2453.
- Marmur, A., Lelah, M.D., 1980. The dependence of drop spreading on the size of the solid surface. *J Colloid Interface Sci* 78, 262-265.
- McCreery, G.E., Stoots, C.M., 1996. Drop formation mechanisms and size distributions for spray plate nozzles. *International Journal of Multiphase Flow* 22, 431-452.
- McEleney, P., Walker, G.M., Larmour, I.A., Bell, S.E.J., 2009. Liquid marble formation using hydrophobic powders. *Chemical Engineering Journal* 147, 373-382.
- McHale, G., Newton, M.I., 2011. Liquid marbles: principles and applications. *Soft Matter* 7, 5473-5481.
- McKinley, G.H., 2005. Dimensionless groups for understanding free surface flows of complex fluids. *Soc. Rheol. Bull.* 74, 6-14.
- Milosevic, I.N., Longmire, E.K., 2002. Pinch-off modes and satellite formation in liquid/liquid jet systems. *International Journal of Multiphase Flow* 28, 1853-1869.
- Miskin, M.Z., Jaeger, H.M., 2012. Droplet formation and scaling in dense suspensions. *Proceedings of the National Academy of Sciences* 109, 4389-4394.
- Mitra, S., Mitra, S.K., 2016. Understanding the early regime of drop spreading. *Langmuir* 32, 8843-8848.
- Moon, D., Im, D.J., Lee, S., Kang, I.S., 2014. A novel approach for drop-on-demand and particle encapsulation based on liquid bridge breakup. *Experimental Thermal and Fluid Science* 53, 251-258.
- Morita, M., Koga, T., Otsuka, H., Takahara, A., 2005. Macroscopic-wetting anisotropy on the line-patterned surface of fluoroalkylsilane monolayers. *Langmuir* 21, 911-918.
- Mounir, A., Jose, P., Shahidzadeh-Bonn, N., Moulinet, S., Wagner, C., Amarouchene, Y., Eggers, J., Bonn, D., 2013. Drop formation in non-newtonian fluids. *Physical Review Letters* 110.
- Newton, M.I., Herbertson, D.L., Elliott, S.J., Shirtcliffe, N.J., McHale, G., 2007. Electrowetting of liquid marbles. *J. Phys. D: Appl. Phys.* 40, 20-24.
- Nguyen, N.T., Zhu, G.P., Chua, Y.C., Phan, V.N., Tan, S.H., 2010a. Magnetowetting and sliding motion of a sessile ferrofluid droplet in the presence of a permanent magnet. *Langmuir* 26, 12553-12559.
- Nguyen, T.H., Hapgood, K., Shen, W., 2010b. Observation of the liquid marble morphology using confocal microscopy. *Chemical Engineering Journal* 162, 396-405.

- Noblin, X., Kofman, R., Celestini, F., 2009. Ratchetlike motion of a shaken drop. *Physical Review Letters* 102, 194504.
- Nooranidoost, M., Izbassarov, D., Muradoglu, M., 2016. Droplet formation in a flow focusing configuration: Effects of viscoelasticity. *Physics of Fluids* 28, 123102.
- Notz, P.K., Chen, A.U., Basaran, O.A., 2001. Satellite drops: unexpected dynamics and change of scaling during pinch-off. *Physics of Fluids* 13, 549-552.
- Oguz, H.N., Prosperetti, A., 1993. Dynamics of bubble growth and detachment from a needle. *Journal of Fluid Mechanics* 251, 111-145.
- Olin, P., Lindstrom, S.B., Pettersson, T., Wagberg, L., 2013. Water drop friction on superhydrophobic surfaces. *Langmuir* 29, 9079-9089.
- Olin, P., Lindstrom, S.B., Wagberg, L., 2015. Trapping of water drops by line-shaped defects on superhydrophobic surfaces. *Langmuir* 31, 6367-6374.
- Ooi, C.H., Nguyen, N.T., 2015. Manipulation of liquid marbles. *Microfluidics and Nanofluidics* 19, 483-495.
- Ooi, C.H., Vadivelu, R.K., St John, J., Dao, D.V., Nguyen, N.T., 2015. Deformation of a floating liquid marble. *Soft Matter* 11, 4576-4583.
- Otten, A., Koster, S., Struth, B., Snigirev, A., Pfohl, T., 2005. Microfluidics of soft matter investigated by small-angle X-ray scattering. *J Synchrotron Radiat* 12, 745-750.
- Ozen, O., Aubry, N., Papageorgiou, D.T., Petropoulos, P.G., 2006. Monodisperse drop formation in square microchannels. *Physical Review Letters* 96, 144501.
- Pamme, N., 2006. Magnetism and microfluidics. *Lab on a Chip* 6, 24-38.
- Papageorgiou, D.T., 1995. On the breakup of viscous liquid threads. *Physics of Fluids* 7, 1529-1544.
- Paven, M., Mayama, H., Sekido, T., Butt, H.J., Nakamura, Y., Fujii, S., 2016. Light-driven delivery and release of materials using liquid marbles. *Advanced Functional Materials* 26, 3199-3206.
- Peregrine, D.H., Shoker, G., Symon, A., 2006. The bifurcation of liquid bridges. *Journal of Fluid Mechanics* 212, 25.
- Pickering, S.U., 1907. Emulsions. *J. Chem. Soc.* 91 2001-2021.
- Planchette, C., Biance, A.L., Lorenceau, E., 2012. Transition of liquid marble impacts onto solid surfaces. *EPL (Europhysics Letters)* 97, 14003.
- Plummer, S.T., Wang, Q., Bohn, P.W., 2003. Electrochemically derived gradients of the extracellular matrix protein fibronectin on gold. *Langmuir* 19, 7528-7536.
- Quéré, D., 2013. Leidenfrost Dynamics. *Annual Review of Fluid Mechanics* 45, 197-215.

- Ramos, S.M., Dias, J.F., Canut, B., 2015. Drop evaporation on superhydrophobic PTFE surfaces driven by contact line dynamics. *J Colloid Interface Sci* 440, 133-139.
- Ramsden, W., 1903. Separation of solids in the surface-layers of solutions and 'suspensions'. *Proc. R. Soc. London* 72, 156-164.
- Ravi, V., Jog, M.A., Manglik, R.M., 2013. Effects of pseudoplasticity on spread and recoil dynamics of aqueous polymeric solution droplets on solid surfaces. *Interfacial Phenomena and Heat Transfer* 1, 273–287.
- Ray, B., Biswas, G., Sharma, A., 2012. Bubble pinch-off and scaling during liquid drop impact on liquid pool. *Physics of Fluids* 24, 082108.
- Rayleigh, L., 1892. On the stability of a cylinder of viscous fluid under a capillary force. *Philos. Mag.* 34, 145-154.
- Richard, D., Quéré, D., 1999. Viscous drops rolling on a tilted non-wettable solid. *Europhys. Lett.* 48, 286-291.
- Roché, M., Aytouna, M., Bonn, D., Kellay, H., 2009. Effect of surface tension variations on the pinch-off behavior of small fluid drops in the presence of surfactants. *Physical Review Letters* 103, 264501.
- Rohlf, W., Ehrenpreis, C., Haustein, H., Kneer, R., 2014. Influence of viscous flow relaxation time on self-similarity in free-surface jet impingement. *International Journal of Heat and Mass Transfer* 78, 435-446.
- Rosensweig, R.E., 1985. Ferrohydrodynamics. *Cambridge University Press*.
- Rothert, A., Richter, R., 1999. Experiments on the breakup of a liquid bridge of magnetic fluid. *Journal of Magnetism and Magnetic Materials* 201, 324-327.
- Rothert, A., Richter, R., Rehberg, I., 2001. Transition from symmetric to asymmetric scaling function before drop pinch-off. *Physical Review Letters* 87, 084501.
- Rothert, A., Richter, R., Rehberg, I., 2003. Formation of a drop: viscosity dependence of three flow regimes. *New Journal of Physics* 5, 59.51–59.13.
- Roux, D.C., Cooper-White, J.J., 2004. Dynamics of water spreading on a glass surface. *J Colloid Interface Sci* 277, 424-436.
- Rueger, P.E., Calabrese, R.V., 2013. Dispersion of water into oil in a rotor–stator mixer. Part 1: drop breakup in dilute systems. *Chemical Engineering Research and Design* 91, 2122-2133.
- Sackmann, E.K., Fulton, A.L., Beebe, D.J., 2014. The present and future role of microfluidics in biomedical research. *Nature* 507, 181-189.

- Saritha, S., Zhang, X., Neogi, P., 2005. Wetting kinetics of films containing nonadsorbing polymers. *J Chem Phys* 122, 244711.
- Savage, J.R., Caggioni, M., Spicer, P.T., Cohen, I., 2010. Partial universality: pinch-off dynamics in fluids with smectic liquid crystalline order. *Soft Matter* 6, 892.
- Sbragaglia, M., Biferale, L., Amati, G., Varagnolo, S., Ferraro, D., Mistura, G., Pierno, M., 2014. Sliding drops across alternating hydrophobic and hydrophilic stripes. *Physical Review E* 89, 012406.
- Seemann, R., Brinkmann, M., Pfohl, T., Herminghaus, S., 2012. Droplet based microfluidics. *Reports on Progress in Physics* 75, 016601.
- Semprebon, C., Brinkmann, M., 2014. On the onset of motion of sliding drops. *Soft Matter* 10, 3325-3334.
- Séro-Guillaume, O.E., Zouaoui, D., Bernardin, D., Brancher, J.P., 1992. The shape of a magnetic liquid drop. *Journal of Fluid Mechanics* 241, 215-232.
- Sheng, X., Zhang, J., 2011. Directional motion of water drop on ratchet-like superhydrophobic surfaces. *Applied Surface Science* 257, 6811-6816.
- Shi, X.D., Brenner, M.P., Nagel, S.R., 1994. A cascade of structure in a drop falling from a faucet. *Science* 265, 219-222.
- Simmons, J.A., Sprittles, J.E., Shikhmurzaev, Y.D., 2015. The formation of a bubble from a submerged orifice. *European Journal of Mechanics* 53, 24-36.
- Sivan, V., Tang, S.-Y., O'Mullane, A.P., Petersen, P., Eshtiaghi, N., Kalantar-zadeh, K., Mitchell, A., 2013. Liquid metal marbles. *Advanced Functional Materials* 23, 144-152.
- Smith, J.T., Tomfohr, J.K., Wells, M.C., Thomas P. Beebe, J., Kepler, T.B., Reichert, W.M., 2004. Measurement of cell migration on surface-bound fibronectin gradients. *Langmuir* 20, 8279-8286.
- Smolka, L.B., Belmonte, A., 2003. Drop pinch-off and filament dynamics of wormlike micellar fluids. *Journal of Non-Newtonian Fluid Mechanics* 115, 1-25.
- Squires, T.M., Quake, S.R., 2005. Microfluidics: Fluid physics at the nanoliter scale. *Reviews of Modern Physics* 77.
- Stone, H.A., Lister, J.R., Brenner, M.P., 1999. Drops with conical ends in electric and magnetic fields. *Proc. R. Soc. Lond. A.* 455, 329-347.
- Sun, R., Bai, H., Ju, J., Jiang, L., 2013. Droplet emission induced by ultrafast spreading on a superhydrophilic surface. *Soft Matter* 9, 9285.

- Suryo, R., Doshi, P., Basaran, O.A., 2004. Non-self-similar, linear dynamics during pinch-off of a hollow annular jet. *Physics of Fluids* 16, 4177-4184.
- Suzuki, S., Nakajima, A., Tanaka, K., Sakai, M., Hashimoto, A., Yoshida, N., Kameshima, Y., Okada, K., 2008. Sliding behavior of water droplets on line-patterned hydrophobic surfaces. *Applied Surface Science* 254, 1797-1805.
- Tan, S.H., Nguyen, N.T., Yobas, L., Kang, I.S., 2010. Formation and manipulation of ferrofluid droplets at a microfluidic T-junction. *Journal of Micromechanics and Microengineering* 20, 045004.
- Tanner, L.H., 1979. The spreading of silicone oil drops on horizontal surfaces. *J. Phys. D: Appl. Phys.* 12, 1473-1484.
- Taylor, G., 1964. Disintegration of water drops in an electric field. *Proc. R. Soc. London, Ser. A.* 280, 383-397.
- Terry, S.C., Jerman, J.H., Angell, J.B., 1979. A gas chromatographic air analyzer fabricated on a silicon wafer. *IEEE Trans. Electron. Dev.* 26, 1880-1886.
- Thampi, S.P., Pagonabarraga, I., Adhikari, R., Govindarajan, R., 2016. Universal evolution of a viscous-capillary spreading drop. *Soft Matter* 12, 6073-6078.
- Theberge, A.B., Courtois, F., Schaerli, Y., Fischlechner, M., Abell, C., Hollfelder, F., Huck, W.T., 2010. Microdroplets in microfluidics: an evolving platform for discoveries in chemistry and biology. *Angew Chem Int Ed Engl* 49, 5846-5868.
- Thoroddsen, S.T., Etoh, T.G., Takehara, K., 2007. Experiments on bubble pinch-off. *Physics of Fluids* 19, 042101.
- Tian, J., Arbatan, T., Li, X., Shen, W., 2010. Liquid marble for gas sensing. *Chem Commun (Camb)* 46, 4734-4736.
- Tian, J., Fu, N., Chen, X.D., Shen, W., 2013. Respirable liquid marble for the cultivation of microorganisms. *Colloids Surf B Biointerfaces* 106, 187-190.
- Tomotika, S., 1935. On the instability of a cylindrical thread of a viscous liquid surrounded by another viscous fluid. *Proc. R. Soc. Lond. A* 150, 322.
- Torres-Díaza, I., Rinaldi, C., 2014. Recent progress in ferrofluids research: novel applications of magnetically controllable and tunable fluids. *Soft Matter* 10, 8584-8602.
- Tzounakos, A., Karamanev, D.G., Margaritis, A., Bergougnou, M.A., 2001. Effect of the surfactant concentration on the rise of gas bubbles in power-law non-Newtonian liquids. *Industrial & Engineering Chemistry Research* 43, 5790-5795.

- Utada, A.S., Fernandez-Nieves, A., Stone, H.A., Weitz, D.A., 2007. Dripping to jetting transitions in coflowing liquid streams. *Physical Review Letters* 99, 094502.
- Utada, A.S., Lorenceau, E.L., Link, D.R., Kaplan, P.D., Stone, H.A., Weitz, D.A., 2005. Monodisperse double emulsions generated from a microcapillary device. *Science* 308, 537-541.
- van Dam, D.B., Le Clerc, C., 2004. Experimental study of the impact of an ink-jet printed droplet on a solid substrate. *Physics of Fluids* 16, 3403-3414.
- van Hoeve, W., Dollet, B., Versluis, M., Lohse, D., 2011. Microbubble formation and pinch-off scaling exponent in flow-focusing devices. *Physics of Fluids* 23.
- van Steijn, V., Kleijn, C.R., Kreutzer, M.T., 2009. Flows around confined bubbles and their importance in triggering pinch-off. *Physical Review Letters* 103, 214501.
- van Steijn, V., Kreutzer, M.T., Kleijn, C.R., 2007. m-PIV study of the formation of segmented flow in microfluidic T-junctions. *Chemical Engineering Science* 62, 7505-7514.
- Vance, B., Daniel, B., Yves, M.J., Louis, V., 2000. Controlling droplet deposition with polymer additives. *Nature* 405, 772-775.
- Varagnolo, S., Basu, N., Ferraro, D., Tóth, T., Pierno, M., Mistura, G., Fois, G., Tripathi, B., Brazil, O., Cross, G.L.W., 2016. Effect of hair morphology and elastic stiffness on the wetting properties of hairy surfaces. *Microelectronic Engineering* 161, 74-81.
- Visconti, R.P., Kasyanov, V., Gentile, C., Zhang, J., Markwald, R.R., Mironov, V., 2010. Towards organ printing: engineering an intra-organ branched vascular tree. *Expert Opinion on Biological Therapy* 10, 409-420.
- Vuong, T., Cheong, B.H., Huynh, S.H., Muradoglu, M., Liew, O.W., Ng, T.W., 2015. Drop transfer between superhydrophobic wells using air logic control. *Lab on a Chip* 15, 991-995.
- Waelchli, S., Rudolf von Rohr, P., 2006. Two-phase flow characteristics in gas-liquid microreactors. *International Journal of Multiphase Flow* 32, 791-806.
- Wang, N., Xiong, D., Li, M., Deng, Y., Shi, Y., Wang, K., 2015. Superhydrophobic surface on steel substrate and its anti-icing property in condensing conditions. *Applied Surface Science* 355, 226-232.
- Wang, X., Chen, L., Bonaccorso, E., 2014. Comparison of spontaneous wetting and drop impact dynamics of aqueous surfactant solutions on hydrophobic polypropylene surfaces: scaling of the contact radius. *Colloid and Polymer Science* 293, 257-265.

- Wang, Y., Bhushan, B., Maali, A., 2009. Atomic force microscopy measurement of boundary slip on hydrophilic, hydrophobic, and superhydrophobic surfaces. *Journal of Vacuum Science & Technology A* 27, 754-760.
- Wehking, J.D., Gabany, M., Chew, L., Kumar, R., 2013. Effects of viscosity, interfacial tension, and flow geometry on droplet formation in a microfluidic T-junction. *Microfluidics and Nanofluidics* 16, 441-453.
- Weinstein, S.J., Ruschak, K.J., 2004. Coating flows. *Annual Review of Fluid Mechanics* 36, 29-53.
- Wenzel, R.N., 1936. Resistance of solid surfaces to wetting by water. *Industrial & Engineering Chemistry* 28, 988-994.
- Whitesides, G.M., 2006. The origins and the future of microfluidics. *Nature* 442, 368-373.
- Whitney, R.S., 2013. Nonlinear thermoelectricity in point contacts at pinch off: A catastrophe aids cooling. *Physical Review B* 88, 064302.
- Winkels, K.G., Weijs, J.H., Eddi, A., Snoeijer, J.H., 2012. Initial spreading of low-viscosity drops on partially wetting surfaces. *Physical Review E* 85, 055301.
- Wisdom, K.M., Watson, J.A., Qu, X., Liu, F., Watson, G.S., Chen, C.H., 2013. Self-cleaning of superhydrophobic surfaces by self-propelled jumping condensate. *Proceedings of the National Academy of Sciences* 110, 7992-7997.
- Wu, Y.N., Fu, T.T., Ma, Y.G., Li, H.Z., 2013. Ferrofluid droplet formation and breakup dynamics in a microfluidic flow-focusing device. *Soft Matter* 9, 9792-9798.
- Wu, Y.N., Fu, T.T., Ma, Y.G., Li, H.Z., 2015. Active control of ferrofluid droplet breakup dynamics in a microfluidic T-junction. *Microfluidics and Nanofluidics* 18, 19-27.
- Xiong, R., Bai, M., Chung, J.N., 2007. Formation of bubbles in a simple co-flowing micro-channel. *Journal of Micromechanics and Microengineering* 17, 1002-1011.
- Xu, C., Huang, Y., Fu, J., Markwald, R.R., 2014a. Electric field-assisted droplet formation using piezoactuation-based drop-on-demand inkjet printing. *Journal of Micromechanics and Microengineering* 24, 115011.
- Xu, C., Zhang, M., Huang, Y., Ogale, A., Fu, J., Markwald, R.R., 2014b. Study of droplet formation process during drop-on-demand inkjetting of living cell-laden bioink. *Langmuir* 30, 9130-9138.
- Xue, Y., Wang, H., Zhao, Y., Dai, L., Feng, L., Wang, X., Lin, T., 2010. Magnetic liquid marbles: a "precise" miniature reactor. *Adv Mater* 22, 4814-4818.
- Yang, G.Q., Du, B., Fan, L.S., 2007. Bubble formation and dynamics in gas-liquid-solid fluidization—A review. *Chemical Engineering Science* 62, 2-27.

- Yarin, A.L., 2006. Drop impact dynamics: splashing, spreading, receding, bouncing. *Annual Review of Fluid Mechanics* 38, 159-192.
- Yeong, Y.H., Burton, J., Loth, E., Bayer, I.S., 2014. Drop impact and rebound dynamics on an inclined superhydrophobic surface. *Langmuir* 30, 12027-12038.
- Yıldırım, Ö.E., Basaran, O.A., 2006. Dynamics of formation and dripping of drops of deformation-rate-thinning and -thickening liquids from capillary tubes. *Journal of Non-Newtonian Fluid Mechanics* 136, 17-37.
- Yoo, H., Kim, C., 2015. Experimental studies on formation, spreading and drying of inkjet drop of colloidal suspensions. *Colloids and Surfaces A: Physicochemical and Engineering Aspects* 468, 234-245.
- Yuan, J., Li, Y., Zhou, Y., 2014. Effect of contact angle on bubble formation at submerged orifices. *Journal of Materials Science* 49, 8084-8094.
- Zang, D., Li, J., Chen, Z., Zhai, Z., Geng, X., Binks, B.P., 2015. Switchable opening and closing of a liquid marble via ultrasonic levitation. *Langmuir* 31, 11502-11507.
- Zhang, D., Men, L., Chen, Q., 2011. Microfabrication and applications of opto-microfluidic sensors. *Sensors* 11, 5360-5382.
- Zhang, D.F., Stone, H.A., 1997. Drop formation in viscous flows at a vertical capillary tube. *Physics of Fluids* 9, 2234-2242.
- Zhang, L., He, L., Ghadiri, M., Hassanpour, A., 2015. Effect of surfactants on the deformation and break-up of an aqueous drop in oils under high electric field strengths. *Journal of Petroleum Science and Engineering* 125, 38-47.
- Zhang, W.W., Lister, J.R., 1999a. Similarity solutions for capillary pinch-off in fluids of differing viscosity. *Physical Review Letters* 83, 1151-1154.
- Zhang, W.W., Lister, J.R., 1999b. Similarity solutions for capillary pinch-off in fluids of differing viscosity. *Physical Review Letters* 83, 1151.
- Zhao, L., Yan, K.C., Yao, R., Lin, F., Sun, W., 2016. Modeling on microdroplet formation for cell printing based on alternating viscous-inertial force jetting. *Journal of Manufacturing Science and Engineering* 139, 011005.
- Zhao, Y., Fang, J., Wang, H., Wang, X., Lin, T., 2010. Magnetic liquid marbles: manipulation of liquid droplets using highly hydrophobic Fe₃O₄ nanoparticles. *Adv Mater* 22 707-710.
- Zhao, Y., Xu, Z., Parhizkar, M., Fang, J., Wang, X., Lin, T., 2012. Magnetic liquid marbles, their manipulation and application in optical probing. *Microfluidics and Nanofluidics* 13, 555-564.

- Zhu, G.P., Nguyen, N.T., Ramanujan, R.V., Huang, X.Y., 2011. Nonlinear deformation of a ferrofluid droplet in a uniform magnetic field. *Langmuir* 27, 14834-14841.
- Zhu, P., Kong, T., Lei, L., Tian, X., Kang, Z., Wang, L., 2016. Droplet breakup in expansion-contraction microchannels. *Scientific Reports*. 6, 21527.

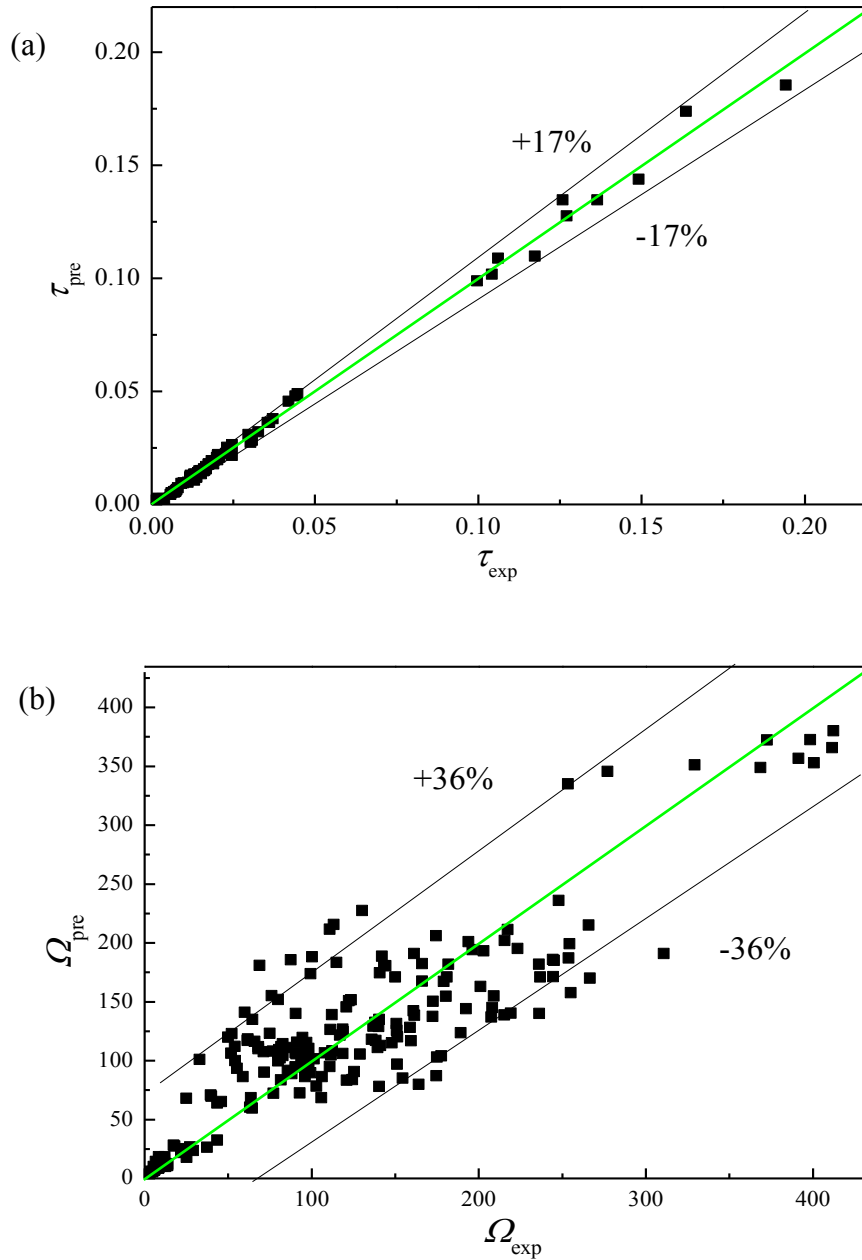
Annexes**Annexes of Part II. Liquid drop hurdling behavior and characteristics**

Figure AII.1. Comparisons of the dimensionless time τ (a), and dimensionless kinetic energy loss Ω (b), between the predicted values from Eqn. (II.1) and Eqn. (II.2) and the experimental data.

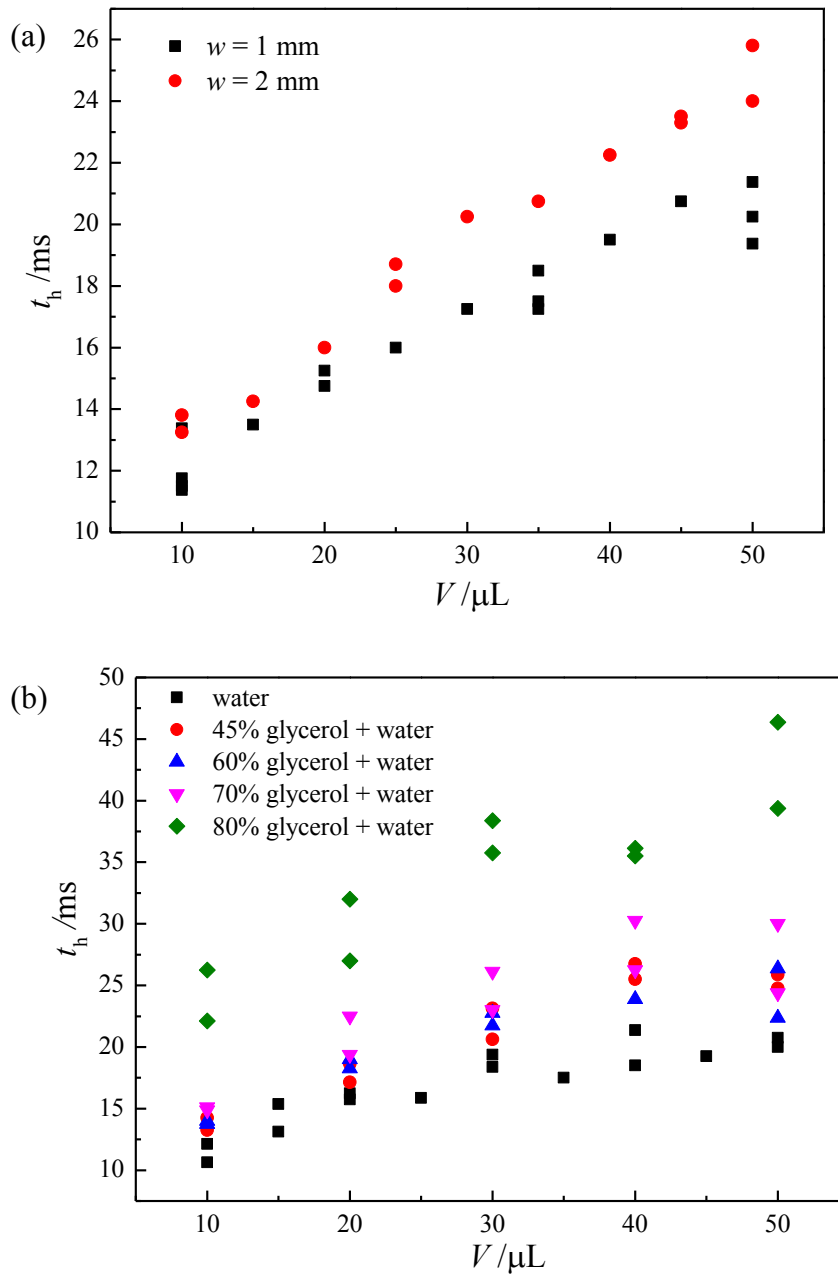


Figure AII.2. Effect of barrier's size and liquid properties on the hurdling time. (a), Water drops released from the slope on the semicircle barriers with $w = 1 \text{ mm}$ and $w = 2 \text{ mm}$. (b), Water drops and glycerol drops released almost from the same position of the slope on the semicircle barrier ($w = 1 \text{ mm}$).

Video AII.1

A water drop of 10 μL hurdling a barrier of semicircular geometry.



10 μL semicircle.avi

Video AII.2

A water drop of 10 μL hurdling a barrier of triangular geometry.



10 μL triangle.avi

Video AII.3

A water drop of 10 μL hurdling a barrier of square geometry.



10 μL square.avi

Video AII.4

A water drop of 10 μL failing in hurdling a square barrier.



10 μL square no cross.avi

Publications issued from this thesis

- [1]. Xiao F. Jiang, Huai Z. Li, Self-similar pinch-off mechanism and scaling of ferrofluid drops. *Physical Review E*, 2015, 92 (6), 061003.
- [2]. Xiao F. Jiang, Yi N. Wu, Youguang Ma, Huai Z. Li, Formation and breakup dynamics of ferrofluid drops. *Chem. Eng. Res. Des.* 2016,115, 262-269.
- [3]. Xiao F. Jiang, Chun Y. Zhu, Huai Z. Li, Bubble pinch-off in Newtonian and non-Newtonian fluids. *Chem. Eng. Sci.* 2017, 170, 98-104.
- [4]. Xiao F. Jiang, Chun Y. Zhu, Youguang Ma, Huai Z. Li, Undressing a water marble on oil film. *Adv. Mater. Interfaces.* 2017, 4(13), 1700193.
- [5]. Xiao F. Jiang, Huai Z. Li, Liquid drops hurdling over barriers of various geometries. *Adv. Mater. Interfaces.* 2017, 4, 1700516.
- [6]. Xiao F. Jiang, Huai Z. Li, Universality and non-universality of drop pinch-off in a surround fluid. (Under review)
- [7]. Xiao F. Jiang, Huai Z. Li, Initial contact and spreading of drop dripping-on-substrate (DoS). (In preparation)
- [8]. Xiao F. Jiang, Huai Z. Li, Filament thinning of non-Newtonian drop dripping-on-substrate (DoS) through optical and electric methods. (In preparation)

Phénomènes interfaciaux dans la manipulation des gouttes et des bulles

Résumé

Les phénomènes interfaciaux impliqués dans les écoulements polyphasiques existent dans de nombreux procédés industriels. Des gouttes et des bulles sont des éléments typiques pour comprendre les phénomènes interfaciaux. Ainsi, cette thèse étudie les gouttes (bulles) impliquées dans la manipulation d'une interface, y compris la rupture de l'interface, le mouvement d'une goutte sur une surface superhydrophobe et le contact sur un support solide à l'aide d'un système d'acquisition pour des signaux électriques. Dans la première partie, une caméra rapide est utilisée pour étudier la dynamique de pincement des fluides homogènes et des ferrofluides hétérogènes à travers des systèmes confinés et non-confinés liquide-liquide ou liquide-gaz. L'effet de compétition entre les différentes forces telles que la poussée d'Archimède, la force magnétique, la gravité et la tension interfaciale sur la rupture finale d'un fluide interne dans un environnement fluide externe est démontré et quantifié. La deuxième partie est consacrée à la manipulation d'une goutte aqueuse à l'aide d'une interface superhydrophobe sous deux angles distincts: saut d'obstacle de la goutte sur une surface solide revêtue d'une couche superhydrophobe; déshabillage d'une goutte enveloppée de particules superhydrophobes dite "marbre liquide" sur un film huileux. Le comportement dynamique du saut d'obstacle et du déshabillage des gouttes est quantifié et comparé dans des conditions opératoires très différentes telles que la viscosité, la tension interfaciale, la géométrie d'obstacle, etc. La troisième partie est dévolue au contact d'une goutte sur un support solide: contact initial, étalement, et pincement final des fluides tant newtoniens que non newtoniens, grâce à une méthodologie combinant la caméra rapide et un système d'acquisition ultra-rapide d'un signal électrique.

Mots clés: goutte, bulle, ferrofluide, pincement, superhydrophobe, saut d'obstacle, déshabillage, contact initial, étalement, filament

Interfacial phenomena involved in the manipulation of drops and bubbles

Abstract

The interfacial phenomena in multiphase flows widely exist in numerous industrial processes. Drops and bubbles are typical models to investigate these interfacial phenomena. Thus this thesis investigates the drop (bubble) involved interface manipulation, including the breakup of interface, drop's motion on superhydrophobic surface and Dripping-on-Substrate with an acquisition system of electric signals. In the first part, the pinch-off dynamics of homogenous fluids and heterogeneous ferrofluids, unconfined liquid-liquid (liquid-gas) or confined liquid-liquid systems was investigated by a high-speed camera. The effect of buoyancy, magnetic force, gravity and interface tension between internal and external fluids on the final pinch-off was demonstrated and quantified. The second part focuses on the drop manipulation on superhydrophobic interface through two distinct approaches: superhydrophobic coating on a substrate and superhydrophobic particles enveloping a liquid drop to form "liquid marble". The hurdling behavior of liquid drops on superhydrophobic obstacles and undressing dynamics of liquid marbles on oil films were discussed and the slope motion of liquid drops and liquid marbles were then compared. The third part concentrates on the Dripping-on-Substrate behavior: initial contact and spreading on a solid surface, final pinch-off of Newtonian fluids and filament thinning of non-Newtonian fluids, through a methodology combining the high-speed camera and ultra-high-speed acquisition device of an electric signal.

Key Words: drop, bubble, ferrofluid, pinch-off, superhydrophobic, hurdling, undressing, dripping-onto-substrate, initial contact, spreading, filament